ULTRA-WIDEBAND ELECTROMAGNETIC INDUCTION FOR UXO DISCRIMINATION

SERDP PROJECT CU 1122:

UXO DISCRIMINATION

BY MID-FREQUENCY ELECTROMAGNETIC INDUCTION

FINAL REPORT

Nov 30, 2002

Kevin O'Neill
USA CoE Engineer Research and Development Center (ERDC)
Hanover Site – Cold Regions Research and Engineering Laboratory
72 Lyme Rd
Hanover, NH 03755
koneill@CRREL.usace.army.mil

TABLE OF CONTENTS

LIST OF FIGURES

1. BACKGROUND, FOCUS OF INVESTIGATION, FINDINGS

1.1 The Nature of the Problem and the Focus of Investigation

This document reports the results from SERDP project 1102, "UXO Discrimination by Mid-frequency Electromagnetic Induction." The principal investigator and author of this report is Dr. Kevin O'Neill of the Army Corps of Engineers, Engineer Research and Development Center, Hanover Site. Other participants were the Thayer School of Engineering at Dartmouth College (Prof. Keith D. Paulsen); the MIT Center for Electromagnetic Theory and Application (Prof J-A. Kong); and Geophex, Ltd (Dr. I-J Won, President). At those institutions very substantial technical contributions came from Dr. Keli Sun and Dr. Fridon Shubitidze, and Research Engineers Irma Shamatava and Sherri Geimer, of the Thayer School; from Dr. Chi On Ao and Dr. Henning Braunisch, formerly of MIT; and from Dr. Bill Sanfilipo, Joe Siebert, Alex Oren and Dean Keiswetter (now, now, now, and formerly) of Geophex, Ltd. The executive summary at the end of this chapter contains a condensed rendering of the principal results of the project. The report contains no other sub-section with conclusions or recommendations. Subsequent chapters contain some of the details on which the findings and discussions in the executive summary are based

To explain the results obtained, we begin in this section and the next with some general background material, designed to make comprehensible the discussion of purposes, measures taken, and results. Both concepts and nomenclature are laid out. The introductory material and, for that matter, the entire report, is written for the "technical layman," meaning someone with a general engineering or science background, but not necessarily with any specialized experience in this field. More complete or more technical renderings of the material can be found in the journal articles and conference papers that have resulted from this project. Most of these can be identified in the references below because they are written in bold blue. A few others are appended to the references. As regards the material included here, some parts are more technical and mathematically detailed than others, and some are more difficult to understand than others. However, they are all designed so that, armed with an understanding of the introductory material, the technical layman can grasp the main points effectively. So, did I mention that you should *be sure to read the background material*? Let's just say that, if you skip much of that material and then can't understand subsequent parts of the report, *don't complain to me about it*.

The basic setup for electromagnetic induction (EMI) sensing as envisioned in this project is shown in Figure 1. The sensor consists of one or more loops around which currents circulate, generating the transmitted or "primary" magnetic field, H^{PR}. The primary field impinges upon a metallic object, inducing currents and polarization response in it. These in turn radiate a scattered or "secondary" magnetic field (H^s) back to the sensor. Just as the currents in the transmitter coils produced the original primary field, so, reciprocally, the transient scattered field passing through receiver loops induces currents in those coils. The measurement of those currents provides the recorded signal.

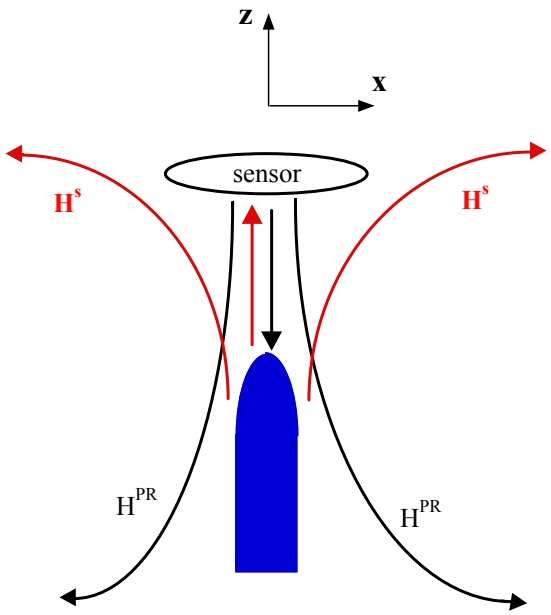

Figure 1. General paradigm for EMI sensing of UXO (blue object)

Variants on this system are possible, not covered by some details of the above paradigm. For example, as described, the receiver coil system responds to rates of change in H^s, not to H^s itself. It is possible to produce sensors that measure the magnetic field itself. However all the generally available systems with some demonstrated applicability (e.g. Geophex GEM and Geonics EM systems) function as described, and we will assume this in what follows. Within this constraint, many variations are possible in terms of number and arrangement of coils, as well as time domain (TD) or frequency domain (FD) operation.

Prior to this project, considerable effort had been expended in the realm of broadband, low frequency electromagnetic induction (LF-EMI) sensing of subsurface metallic objects [1, 2]. We may take LF to coincide roughly with the Geophex GEM-3 instrument's range (~30 Hz to ~ 20 kHz). At the time of the inception of this project, various renditions of the GEM-3 featured different upper limits of frequency, perhaps 22 kHz or 25 kHz. However we considered the signals to be reliable only up to about 18 to 20 kHz. Hence we will consider this to be the upper limit of practicable frequency that applied at the outset of our work. Our job was initially to evaluate the promise of the mid-frequency range (~20 kHz up to ~ 300 kHz), when it is added to the LF range. We term this higher frequency range "mid" instead of "high," to distinguish it from the zone above 300 kHz or 500 kHz, up through about 1 to 10 MHz. This very high frequency induction range draws in different physics, as explained in Section 2.1, and spans the transition from EMI to radar. This range is also somewhat problematical, from the point of view of both analysis and electrical engineering, and we do not address it here.

To the extent that measurement was a concern of this project, we place high priority on compatibility of any MF measurements with those carried out in the LF zone. That is, the purpose of adding data in the MF zone is to extend the picture in the LF range, to form a continuous, enlarged picture of target response. This presupposes a common calibration and, to some extent, similar processing, filtering, instrumental characteristics, etc, in the combined LF+MF larger band. While in principle this might be done using different devices or systems for different parts of the spectrum, for the most part it seemed clear that consistency would require a single, integrated, broader band instrumentation system. In any case, it was certainly desirable to produce and test such a system. As the project developed, we noted the arrival of a new generation of affordable network analyzers that could be used to produce and control signals all the way from a couple of Hz up through and beyond the MF range. This held out the possibility of producing a consistent system that would measure very low frequency (VLF) responses, as well as LF and MF responses. Further, early results in the research indicated that many of the signal features we considered essential in the LF and MF zones sometimes spread into the VLF zone. Thus to have the complete ultra-wideband (UWB) EMI picture, we need the complete VLF + LF + MF sub-bands. With SERDP concurrence, the scope of the project was broadened to include at least some investigation and measurement attempts in the VLF zone as well. That is, *the goal of the project became investigation of the full EMI UWB, i.e. the complete EMI response picture, from a few Hz up through some 100's of kHz.* The questions to be addressed were:

- Can one succeed in analyzing EMI phenomena over the newly expanded UWB range?
- Can one make consistent measurements over the UWB?
- Is it worth doing so? What does the expanded frequency range yield that might be useful for UXO discrimination?

Regarding the first item, we note that at the inception of this project it was not clear that some of the modeling issues that one confronted in the MF zone could be dealt with effectively. This is detailed below. Ultimately, the definition of project goals was taken as license to pursue and define any potentially useful, fundamental EMI response over the complete EMI UWB, particularly when the newly expanded UWB was required to see it. We did not restrict ourselves to the (almost impossibly narrow) field of phenomena visible *only* in the newly added MF and VLF zones. At same time, pains are taken in what follows to point out instances where the new sub-bands are vital for distinguishing signal characteristics of interest.

To pursue the basic questions enumerated above, over the newly assembled EMI UWB (VLF + LF + MF), we proceeded in a two-pronged effort:

- Analysis, which includes analytical and numerical modeling, combined with some interpretation or processing of data; and
- Measurement, which includes both new instrumentation design and construction as well as use of that instrumentation to make measurements in the MF band.

All of this entails tools and results of their application that have not been available before.

For discrimination of UXO, one seeks to identify characteristics in the secondary field signals – phase relations, frequency or temporal patterns, sensitivity to sensor location and orientation – that offer clues to the identity or basic characteristics of the unseen scatterer. In this project, the overwhelming focus is on the potential for such *discrimination*, as opposed to *detection*. By "detection," as that term is used here, we mean the perception of signal anomalies, relative to a background, which indicate the presence of metal objects, without regard to what those objects might be. "Discrimination" means here the ability to identify or classify the object that is the source of the response, given that detection has been achieved. The aim of this project is to pursue basic research that will contribute to a basis for improved EMI discrimination capability.

Did someone say “basic research”? That term means that we have not aimed to produce handy or fieldable tools at the conclusion of the work, whether in hardware or software (though, to some extent, that has been accomplished). Rather, we pursued basic science and engineering investigation to establish the fundamental phenomenology over an expanded EMI frequency band. Our analyses were designed to relate electromagnetic induction effects to the basic properties of targets, such as their shape, extent, orientation, interior (hollow vs solid) and material composition. Results show how and why real or hypothetical sensor responses occur, based on a first principles analysis of electromagnetic interactions with the target. In an analogous way, work on the instrumentation and measurement attacked basic problems of operation in the expanded frequency range, to achieve stable, repeatable, physically interpretable results. That said, we regard this project as being on the applied end of the basic research spectrum. The nature of our results reflects this orientation.

1.2 Basic EMI Phenomenology

Before proceeding to specific methods and results, we introduce some necessary concepts, terminology, and basic phenomenology. The induced polarization and current activity in a target, and hence the signals they produce, depend to a large extent on the kind of temporal changes in the primary field that are imposed by the sender. The change may be sudden, by design: in time domain (TD) systems one typically shuts off an initially steady primary field and then “listens” with the receiver on, after a sufficient interval. Cutting off the primary field stimulates electric currents on the target. Beginning on the target surface these eventually diffuse into its interior, where they decay while the signals they produce fade. In frequency domain (FD) systems one transmits an oscillating magnetic field at chosen frequencies and simultaneously measures the secondary fields, trying somehow to screen the primary field out of the sensor response. Often the avoidance of the primary field is accomplished by adding "bucking coils." These are designed to produce fields that counteract the primary field, canceling it as much as possible at the location of the receiver coil. A significant advantage of TD systems is that one is not constrained by bucking coil considerations, and thus has greater freedom in terms of instrument configuration, coil orientation, etc.

From the point of view of this project, the issue of time domain – frequency domain measurement is not very important. In principle both approaches contain the same information, viewed through different frameworks. In practice, available FD technology has generally covered a

wider equivalent time range than vice versa. At the inception of this project, the LF GEM-3 FD system recorded responses roughly equivalent to time transients on the order of tenths of a millisecond up to tenths of a second. No TD system available at that time came near furnishing that range. In recent years, TD systems at the research level have broadened their ranges. However concomitant expansions of the GEM system band have still kept it ahead of the TD world, in terms of equivalent time range. FD systems also offer greater control of response magnitude because, with some limitations, one can control or at least influence the magnitude of fields transmitted within particular frequency and equivalent time ranges. Results of FD systems are typically shown in terms of the target's impulse response, i.e. as if all contributing frequencies acted equally strongly, producing the most "democratic" representation of the target's scattering properties. TD systems, by contrast, only stimulate the target with the particular weighting of frequencies that is inherent in the step input of the primary field, and can only receive the frequency magnitudes that are present in sufficient strength as the signal fades over time. In practice, this "under-represents" the lowest frequency/ longest time portion of the spectrum. Many UXO produce key responses in the 100s of Hz, i.e. in the equivalent time range of several milliseconds, beyond what is typically measured in the TD. In addition, discrimination may benefit from identification of asymptotic signal values approaching the static limit. These often only appear below 100 Hz or further out in time than 0.01 s. Lastly, there are those of us who feel that signal characteristics and their physical connections are substantially more vivid in FD rendering, however the data were acquired. Still, we strive to be open minded, and follow current expansion of TD capabilities with keen interest [e.g. 3,4]. And some readers would doubtless take issue with the views expressed above, insisting that many of the alleged limitations of TD systems simply reappear in other forms in the FD (e.g. see discussion below of low frequency measurement). So, as an at least half-hearted confession of subjectivity, we'll regard this paragraph as an expression of "defensible prejudice." Most results below are presented in FD terms, while a detailed FD-TD translation tool is also provided (Section 2.6).

The essential electromagnetic properties of relevant targets that affect their EMI responses are electrical conductivity σ (S/m); relative magnetic permeability μ_r (dimensionless), which is the ratio of the magnetic permeability μ (H/m) of the target material to that of free space, μ_o; frequency f in Hz or angular frequency $\omega = 2\pi f$ in radians/s, and geometry. Targets with $\mu_r = 1$ are non-magnetic; those with $\mu_r > 1$ are magnetic. Steel is magnetic, with the exception of stainless steel. As explained below (Section 2.1), we assume here that soil properties are of secondary importance. Metallic targets such as UXO have σ values that are about nine orders of magnitude higher than soil. Also, soil is rarely significantly magnetic, though important exceptions do occur. Overall, while we may

have to modify this assumption in some instances, we will treat the soil surrounding the target as if it were transparent to EMI signals (i.e. unresponding).

Figure 2 shows something of a generic FD response from a discrete metallic object, in this case calculated from the analytical solution for EMI scattering from a sphere [e.g. 5]. Here and below, unless otherwise noted, we assume that the object is subjected to a uniform, positive primary field. The sign conventions in this plot are also explained below. While the curves were obtained for a specific case, they bear the essential traits of most EMI response plots. The picture presents the results scaled as if all input (primary field) frequencies had the same magnitude and phase, the latter calibrated to zero; thus the figure shows the impulse response. There are two components, one inphase with the transmitted field and the other in phase quadrature. These are alternatively designated as the I and Q components, or the (complex) real and imaginary parts of the response, respectively. In a sense explained below, the system displays resonance. The complex resonant frequency typically corresponds to a discrete point in the complex plane where the impulse response of the scatterer has a simple pole. In terms of real frequency, the peak in the quadrature component appears at the point on the real frequency axis, $f_{p,}$ directly below and closest to the pole in the complex frequency plane. For fundamental elucidation of EMI resonance, see [30].

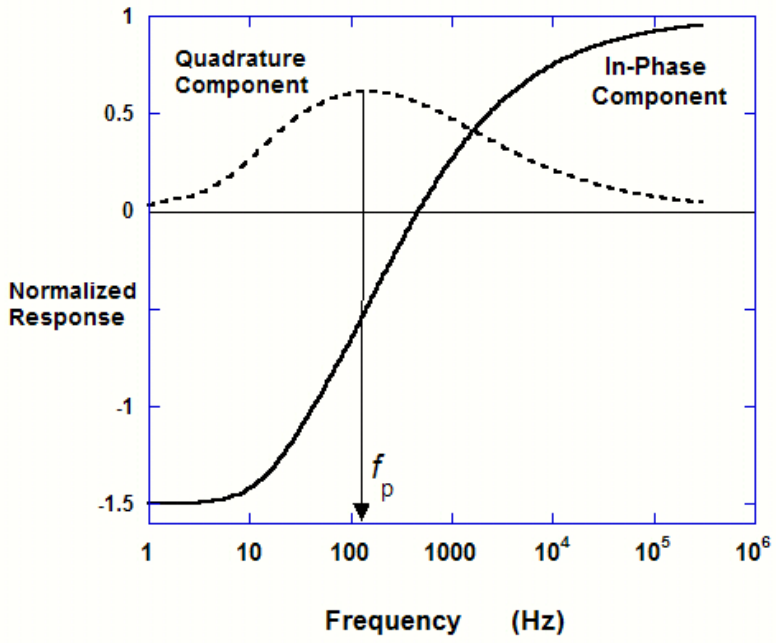

Figure 2. Typical EMI response spectrum from a magnetic object.

The quantity f_p is a fundamental item. A simple, single-mode exponential decay of the form e^{-bt} also corresponds more or less to a set of FD "relaxation curves" of the form seen in Figure 2, with the peak in the quadrature component at $\omega_p = 2\pi f_p = b$, where b is a constant. While complex structures may produce responses containing combinations of modes, it is often the case that a single, lowest mode dominates most of an object's response. In such instances one may infer b by observing f_p. Alternatively put, in terms of complex numbers, one can say that the system has a fundamental or characteristic "frequency" that is purely imaginary, equal to $i\omega_p$, so that $e^{i\omega_p t}$ produces pure decay, i.e. e^{-bt}.

Other notable features in the curves Figure 2 include the high and low frequency asymptotic limits of the I component, and the relation between the I and Q components. Each of these features reflects different aspects of the scatterer. Around the low frequency asymptote, approaching the static limit, the transmitted primary field penetrates the object essentially entirely. Generally speaking, the more magnetic the material is, the stronger (more non-zero) the quasi-static inphase response will be. In any case, the very low frequency signal ultimately queries the entire volume of the target, though it is indifferent to the electrical conductivity of the material. The quadrature component results from internally induced *volume currents*, i.e. currents that flow through at least some portion of the volume of the object. These are sensitive to both electrical conductivity and magnetic permeability, as well as geometry. The previous paragraph gives some indication of the significance of the shape of this Q component over frequency. The Q-related currents are null at the static limit, where there is no current activity. They are also absent at the high frequency limit, where all response is due to *surface* currents. The inphase high frequency response is entirely due to these surface currents, which are indifferent to the electrical and magnetic properties of the body's interior. Hence the response in that range reflects only the surface geometry and orientation. For magnetic materials, the high and low frequency I component limits will be of opposite sign. This is because around the static limit the induced polarization over the volume of the object lines up with that of the primary field, while at the high frequency end the induced surface currents act to oppose the primary field (Lentz' law). In terms of relation between the I and Q components, one notes the "resonance point" where the two curves cross, having equal magnitude. Also, the magnitude of the Q peak relative to either the high or low frequency I limit provides an inherent scaling of different response mechanisms relative to one another.

It is clear from the preceding paragraph that failure to perceive the complete EMI picture, from low frequency to high frequency limit, can deprive us of portions of the data specifically keyed to particular, fundamental material and geometrical properties of an object.

Focusing on the higher frequency region, note that transient electromagnetic fields have a hard time penetrating metallic objects, penetrating less when they vary rapidly in time. To the extent that they do penetrate, they usually decay rapidly from their values on the surface to much smaller values in the interior. Penetration by external fields is characterized in any particular conditions by a designation of a "skin depth" δ. That is, δ is the depth below the surface of a material over which the surface fields decay by a factor of $1/e \sim 0.37$. Over two δ the fields decay to about $e^{-2} \sim 0.14$ of their surface value; over 3 δ they decline to about 5%. Other things being equal, that is, for planar interfaces,

$$\delta = \frac{1}{\sqrt{\sigma\omega\mu/2}} \tag{1}$$

For non-planar geometries this quantity still provides a good rule-of-thumb measure of expected penetration and range of internal influence by external fields. Note that skin depth *decreases* as either conductivity, frequency, magnetic permeability, or their product *increases*.

As in the above equation, the parameters $\sigma\omega\mu$ frequently appear together in EMI analysis and in the display of results. Fundamental patterns of induction behavior are often a function of the single dimensionless quantity formed by the square root of this product times a characteristic dimension of the target, *a*. This *induction number* χ is defined as

$$\chi \equiv a\sqrt{\sigma\omega\mu} \tag{2}$$

The quantity χ is analogous to "*ka*" in higher frequency, e.g. radar bands. Showing results as a function of χ is approximately equivalent to displaying results as a function of the characteristic dimension of the target divided by skin depth, a/δ, because $\chi = \sqrt{2}\, a/\delta$.

At least when viewed from a few characteristic dimensions distance, a given object geometry in a fixed orientation will always produce the same curves as a function of induction number, for

fixed μ. That is, all cases with differing a, σ, and ω will produce exactly the same curves when they are plotted as a function of induction number, for a given permeability. For the special case of the sphere or any other compact object with essentially isotropic response, this means that a given permeability corresponds to a single, unique set of response curves relative to induction number. In this context, it is important to note that, beyond its influence through χ, magnetic permeability μ also has an independent effect on the response curves. Thus results are often presented in families of curves, each one a function of a/δ or of χ, with different curves for different values of μ_r. Note the example quadrature components in

Figure 3, obtained from the analytical solution for scattering from a sphere. The range of μ_r chosen is physically realistic. Note how the location of the peak value in this component, a fundamental discrimination signal feature, shifts over orders of magnitude in the relation between sphere size ($2a$) and the skin depth δ. Thus the figure shows that, to catch the fundamental mode of response, we must be prepared to analyze scattering behavior over an extreme range of induction numbers. In Section 3.1, information like that in the figure below is translated into specific examples, relative to frequency. Overall, the result is that methods of analysis and modeling must be able to treat extreme variation of spatial decay rate in the signal, relative to the geometry of the target. This problem arises whether or not one ventures into the MF zone, where skin depths are always small. Therefore addressing this problem is fundamental to modeling and analysis over virtually the entire EMI UWB.

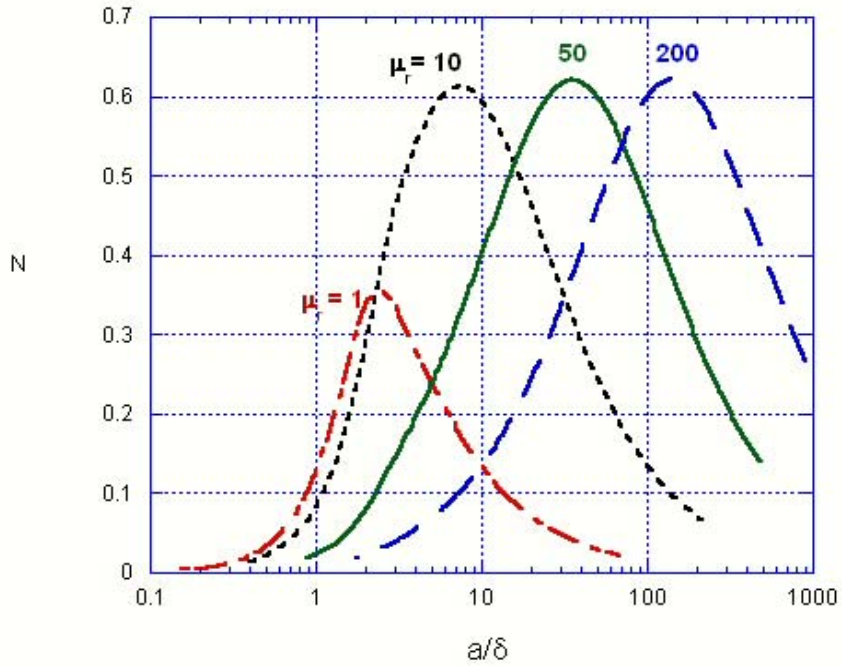

Figure 3. Variation of Q component vs a/δ ~ induction number, for spheres with different μ_r values.

Finally, by way of introduction, we motivate the expansion of the initially targeted frequency range to include very low frequency EMI (VLF-EMI). The instrumental considerations mentioned above gave the idea considerable allure. However this might still simply have provided an interesting technological curiosity if preliminary analysis had not suggested that important information was to be found in the VLF range. Some critics suggested that VLF values could just be obtained by extrapolation from higher frequency results, possibly relying on physically based modal representation of the response curves. While we provide more justification in the results in subsequent sections, for present purposes we show data from some rigorous numerical simulations in Figure 4. "Rigorous" means that all the relevant physics is included, with an algorithm that consistently produces results that match measurements (see Sections 2.2 and 3). The hypothetical scatterers are mildly magnetic metal cylinders that are "axially oriented," i.e. so that their long axes are aligned with the direction of the primary field. Curves are normalized by the "resonance" point, i.e. the values at the frequencies where the components are equal in magnitude. Different curves correspond to responses from different length cylinders, while the diameter (20 cm) and properties are held constant.

Could we infer the VLF responses from the higher frequency portions of the curves? Certainly not. We see both an *amount* and a *pattern* of VLF signal activity, not available without data specifically in the VLF range, linked to fundamental geometrical properties of the object. Have we chosen such hefty cylinders, perhaps larger than many UXO, so that we've artificially biased the response towards lower frequencies? No. Meaning, some UXO *are* in fact this large and, further, the value of μ_r used in the calculations is rather low. Common steels have μ_r values about an order of magnitude higher. This means that, even for smaller diameter cylinders, values of μ_r more typical of ferrous metals will push the response curves even *lower* in frequency (see Section 3.1). This and the further examples and results below indicate that we must include both the VLF and the MF ranges to define completely the EMI response, with all fundamental signal features that are potentially useful for discrimination.

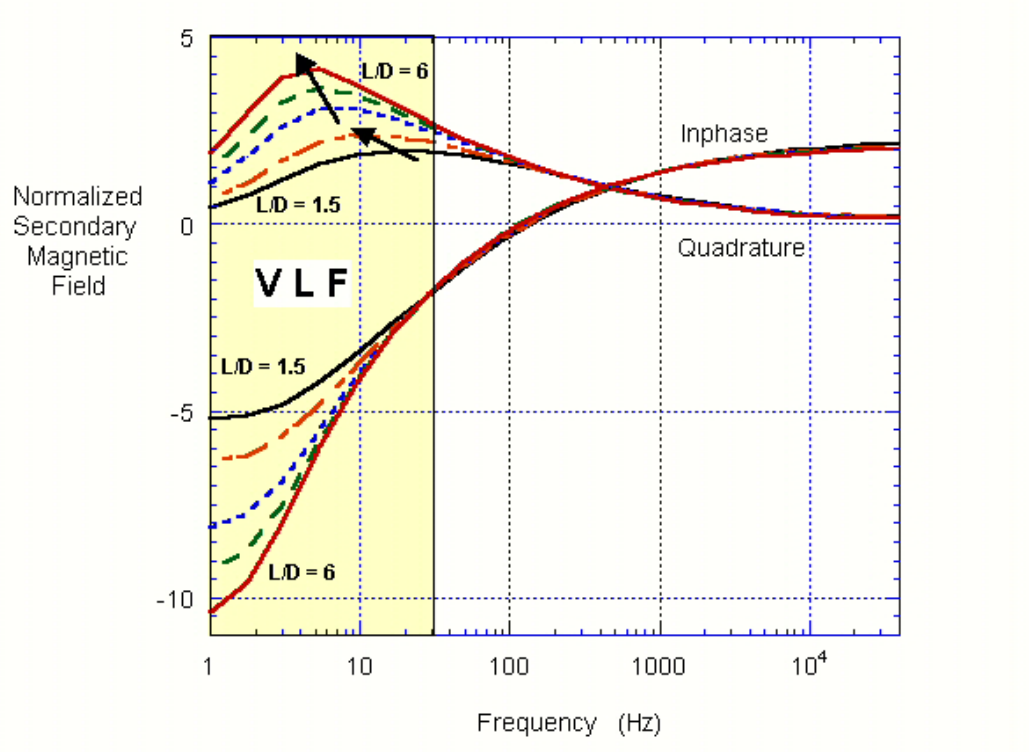

Figure 4. Response curves for cylinders with indicated length to diameter ratios, axially oriented, with $\mu_r = 10$, and $S = 10^7$ S/m.

1.3 Executive Summary and Conclusions

The material in this section consists of extracts from, summaries of, and comments on results that appear in more detail in the following chapters of the report. For the most part, literature references are not provided in this section, when they are present adequately in the more detailed report sections.

At the inception of the project, reliable, accurate means were needed to analyze EMI UWB target responses, both to identify phenomena in the new frequency frontiers and to integrate them into patterns continuing through the more familiar parts of the EMI band. Much was lacking in this regard in terms of both analytical and numerical models. To address this, formulations were developed to provide analytical solutions, for the first time, for basic non-spherical shapes (elongated and flattened spheroids). A parallel development was also undertaken in the numerical realm, designed to treat arbitrary shapes and material composition, in 3-D, from the low frequency limit to the high frequency limit. Work was successful in

both realms. All models were based on first-principles physics, in particular Maxwell's fundamental equations of electromagnetics. These are typically simplified somewhat in induction problems, as phenomena are justifiably treated as "quasi-magnetostatic" (MQS). In mathematical practice, this means that a term is eliminated that contains the time derivative of the electric field. At higher, e.g. radar frequencies, this term cannot be eliminated. The question immediately arises whether the addition of the MF sub-band raises the frequency limit to a point where this term can no longer be neglected. Analysis of the equations and of the magnitude of each term over the appropriate parameter space shows that this term may still be neglected here; relevant phenomena may be treated as MQS, both within and outside the target. Inside the target this means that phenomena are strictly diffusive in nature, and specifically are not true wave phenomena, even when highly damped "traveling wiggles" are stimulated by oscillation of an external field. Further analysis shows that outside the metallic target additional simplifications may be introduced, because the field is irrotational there. This means it can be expressed as the gradient of a scalar potential, reducing the exterior problem from a three-component vector problem to a much simpler scalar problem. In fact, the exterior field has all the structure of a truly magneto-static field, varying only in parallel with variation of boundary conditions or forcing functions.

The reductions of the original Maxwell's equations were put to work first to achieve a "library" of analytical solutions to cover virtually all basic shapes and material properties. New theory showed the way to express scattering from non-magnetic "parallel plates" (flat sides aligned with the impinging magnetic fields) and from non-magnetic cylinders in axial orientation (long axis aligned with the primary field), via approximate analytical solutions. These are valid when the observer is at least a couple of object dimensions away from them, and when the primary field is spatially smooth. Transverse cylinders, both magnetic and non-magnetic, can be approximated successfully by treating them as sections of infinite cylinders, for which analytical solutions already exist. Approximate analytical solutions for *magnetic* prolate and oblate spheroidal shapes were also obtained, for all orientations. Reviewing and organizing the above litany in terms of magnetic and non-magnetic cases, elongated and flattened shapes, axial and transverse orientation, reveals only a single general case for which we do not have a simple, easily evaluated analytical expression, namely the flattened, non-magnetic shape, subjected to "broadside" excitation (e.g. non-magnetic oblate spheroid for primary field aligned with its axis). Because the only variables for that case are the object's proportions and electrical conductivity, this case can be dealt with effectively via a look up table of complete numerical solutions. That is, results can easily be tabulated, indexed by axis ratio and plotted relative to an induction number based on either axis.

Beyond this, serious effort was devoted to obtaining complete, general analytical solutions for prolate and oblate spheroids, without the simplifications adduced for the approximate solutions and hence without their restrictions. The function evaluations required for this had been declared intractable by authorities in the field some fifty years ago, and progress since then had not been sufficient to provide the needed solutions. During the time frame of this project, the complete analytical solutions were indeed obtained for modest degrees of elongation or flatness, and for more extreme shapes when induction numbers are in the higher and lower reaches of the EMI UWB. Methods for rational approximations to bridge gaps between the high and low frequency results were also devised and demonstrated. Since the conclusion of this project, follow-on work at MIT, also supported by SERDP, has resolved the remaining difficulties. This means that we now have the prospect of complete analytical solutions for non-spherical basic shapes, in any orientation, with any material properties, for any primary field. Some of these are now being applied in inversion work, and documentation of the results should be available by Jan 03.

The real significance of these analytical solutions derives from another result of this project; see the sections below regarding fine surface features and inference of object aspect ratios. Specifically, for EMI modeling, basic shapes may be used effectively to represent more intricate geometries with the same overall proportions, so that an oblate spheroid successfully models a disk, and a prolate spheroid a cylinder, etc, even when the shape being approximated has sharp edges and ridges. Some limitations on this are noted, and their treatment explained. Since the completion of the project we have successfully modeled the detailed (measured) wideband EMI response from twisted pieces of scrap, simply by approximating them as spheroids with comparable dimensions. Because inversion programs typically require fast and easily manipulated forward solution algorithms, these analytical solutions are therefore of paramount importance. Probably the greatest limitation on the applicability to UXO lies in the assumption of material homogeneity, while many if not most UXO are heterogeneous. Ongoing basic EMI research on composite objects shows that we can usually model objects with sections made of different metals by assuming negligible electrical connection between pieces, that is, as if the sections of the object were extremely close together but not touching. This suggests that we might yet find application of the analytical spheroid solutions to composite objects by modeling them as collections of spheroids in very close proximity. Preliminary results suggest that, for two contiguous *magnetic* sections, the edge (tip) curvature of the representative spheroids may cause distortions when those edges (tips) are near one another. However the full implications here remain to be worked out, and should appear within the next year.

For full numerical solution of EMI UWB scattering from metallic objects with arbitrary characteristics, we developed and applied a new approach, using the Method of Auxiliary Sources (MAS). In the MAS, unknown fields are produced by arrays of fictitious sources located inside and outside the object. Each of these sources produces a field that constitutes an exact solution of the governing relations, and has unknown multiplicative coefficients associated with it. Application of the boundary conditions on the object provides the set of algebraic relations needed to obtain the coefficients, and hence the entire solution to the problem. The method has the advantage that the sources that mathematically produce the required fields are removed from the surface where boundary conditions are applied. Thus one does not encounter singularities in the course of calculations, in the way that most integral equation formulations do (e.g. Method of Moments, MoM). Separation of the sources from the real surface also spreads the fields that they produce more smoothly over that surface, so fewer irregularities appear and fewer coefficients are required for the approximation of smooth functions. Further, higher order testing and interpolation functions produce extremely efficient, Galerkin type formulations, capable of producing highly accurate solutions for complex problems, quickly, on a PC. Perhaps most important, because the only real approximation in the MAS involves application of the boundary conditions over the real surface, one can test, after the fact, to see how well those conditions have been met. That is, the method has a natural and easily implemented system for determination and location of error, and thus also provides a rational means for assessment and refinement of solutions. We know of no other general method that possesses this virtue. Tests of the MAS program against other solution methods validate it; tests against measured data, with complex objects and non-uniform primary fields, also show extremely accurate and efficient solutions.

In some cases, performance of the original MAS formulation may suffer, or even become unstable, when very high frequencies (induction numbers) are involved. This same problem appears in the established integral techniques based on Green functions (MoM), even within the LF-EMI region. For difference methods such as the finite element or finite difference method, the same difficulty simply appears in a different form. Viewed in one way, the issue is one of resolution. Discretization (mesh) requirements based on observations or recommendations in the literature are impossibly demanding, when fields of interest or Green functions decay over extremely short distances within the object, in absolute distance for high frequencies, and in relative terms for high induction numbers. Magnetic bodies with curved surfaces readily drive the most significant responses into the problem zones. That is, while this resolution problem comes to the fore immediately in the MF zone, it turns out that one frequently confronts it throughout much of the more traditional EMI band, particularly when magnetic materials are involved. This has indeed frustrated

modelers heretofore. Thus solving the problem had implications for general EMI investigations. To address matters, we developed special techniques analogous to impedance boundary condition systems, implemented numerically in formulations with the Thin Skin Approximation (TSA) and analytically in the Small Penetration Assumption (SPA). These techniques allow one to obtain accurate and extremely efficient EMI scattering solutions, from the realm where skin depths first become small (as frequency increases), up to any degree of infinitesimally small skin depth.

Most remarkably, for basic object shapes containing high permeability materials such as steel, and for smooth primary fields, the TSA/SPA formulations perform well over the *entire* EMI UWB, from around the static (low frequency) limit, up to the high frequency asymptotes. Using the TSA formulation, one can obtain accurate UWB solutions while solving for only a single scalar unknown at each numerical node, requiring only a mesh density that is sufficient to resolve the object geometry. This represents a very substantial advance of the state of the art. Among other things, it means that, when the TSA is combined with the MAS, highly efficient, reliable, and flexible numerical solutions can be obtained for complex (realistic) problems, on a PC. Theoretical analyses of the method also succeed in explaining why/how this unexpected breadth of applicability occurs. That is, however initially counter-intuitive, it has in the end a rational basis. As one product of this project, a user-friendly MAS-TSA program treating bodies of revolution has been made available, and is presently combined with a fast and accurate algorithm for translation of results from FD to TD.

Implementation of the SPA in analytical formulations has also produced readily usable programs for both elongated and flattened, high permeability (steel) spheroidal objects, applicable across the entire EMI UWB. As mentioned above, these extremely fast, analytically manipulable solutions are now being applied to inversion. Since the conclusion of this project, we have identified the limitations of the TSA/SPA system, when applied to high permeability, low induction number cases. Specifically, in cases with very irregular geometries and/or highly non-uniform primary fields, fields within the object may not converge to uniform distributions around the static limit, and the TSA/SPA formulations may not converge to the correct low frequency asymptote. However this is a minor limitation, as the methods were not really designed to be applied near the static limit. They do survive tests with irregular geometry and fields in their intended domain of application, above the proximity of the low frequency asymptote.

At the highest EMI frequencies, all induced currents flow only on the surface of the scattering body. Simulations at the high frequency, perfectly reflecting limit are actually easiest to perform. Results from such calculations provide current maps over the surface of an object, which continue to show at least

a reasonable representative of near surface current trajectories when penetration of the object is considerable, at lower frequencies. Thus the technique offers interesting diagnostic data, through which we can understand target responses. Simulations of pipe-like annuli show that we should expect approximately the same response from an intact open annulus and one with a longitudinal gap in its side. The induced currents contrive to pursue very much the same pattern, with and without the longitudinal cut. This situation holds until the lowest frequency regime, in which the cut pipe is essentially a broken circuit. Both measurements and simulations demonstrate this, and show a fall off of quadrature signal at the lowest frequencies for the annulus with gap. Thus being able to compare responses from the lowest to the highest frequencies may indicate whether a target is a continuous (open ended) shell, or whether it is a bent plate. Bending or unbending a plate has very little effect on its spectral response, when the primary field is aligned with its sides. Multiple viewing angles are required to find indications of bending.

Development of complete and flexible simulation tools permitted us to investigate the effects of geometrical and material properties on the character of secondary fields. No fundamental studies had been done previously, systematically exploring the sensitivity of EMI responses, much less UWB EMI responses, to comprehensive variation of fundamental parameters. Overall the magnitude of the low frequency limit is strongly influenced by magnetic content and object elongation. Also, under axial orientation, increasing the magnetic content and elongation push down the frequency range of peak response and principal signal activity. This also applies to magnetic bodies that are flattened (e.g. disk or oblate spheroid), when they are viewed edge-on by the sensor. A compact object, such as a sphere or very short cylinder in any orientation, or a longer transversely oriented cylinder, show the opposite sensitivity relative to permeability: increased values of μ_r push the principal signal activity up in frequency. This implies a strong orientation effect in the case of magnetic elongated or flattened bodies, which is absent for elongated non-magnetic bodies or modified for non-magnetic flattened shapes. Ultimately, the limiting response at high frequency depends only on object geometry; and the relation (e.g. crossing) of the inphase and quadrature components relates magnetic content, elongation, and does so differently for axial vs transverse orientation. Variation of parameters and combinations of parameters within ranges of interest here readily drives the principal signal activity into the VLF or MF zones. This means that any processing system that fails to access the complete UWB picture will lack some of the most fundamental response information on which classification can be based.

For some specific parameter sensitivities, the effects of *gross size* of the object are considered. Results here apply best when the object's response is linked to only a single

characteristic length, e.g. a compact object or an elongated object viewed only in transverse orientation, in which case only its diameter affects the response spectrum. Note that the response of an axially oriented, elongated magnetic object is affected significantly by *two* dimensions, namely its diameter and length, so its responses are not linked to "gross size." In terms of gross size, a relatively large (~ 20 cm diameter), non-magnetic object will produce responses very much in the VLF range. At the other extreme, a relatively small, lower conductivity, high permeability object (steel, ~ 2 cm diameter) produces response very much in the MF region. The parameters chosen in the second case correspond roughly to those that might apply to a 20 mm or 30 mm UXO, in transverse orientation, and indeed measurements show responses for such ordnance in the MF range. Note particularly that halving or doubling the characteristic dimension of the object does not take the frequency locale of response for these items out of the VLF or MF regions. Even if shifts in these parameters are sufficient to take the much of the Q pattern out of these regions, without the additional VL or MF information we might not be able to locate the peak very well, and wouldn't be able to define the *shape* of the Q curve, which contains potential discrimination information. For magnetic objects of interest here, it's unlikely that *gross size alone* will cause the main portion of the Q response to be in the VLF region. To define the asymptotic limit of the inphase response, however, one is very likely to need the VLF range for such an object. Recall also that an *elongated* magnetic object in axial orientation will readily produce its principal signal activity in the VLF.

As implied in the above paragraphs, and as is visible in many measurements, change in orientation of an elongated magnetic object produces a substantial shift in the frequency range of signal activity. Initially an explanation was proposed to the effect that, in horizontal (transverse) orientation, induced electric currents typically had to pass over sharp features, provoking higher frequency response. However, definitive tests indicate that this is not the reason for the frequency shift. Rather, it is a general consequence of aspect ratio, and the differently proportioned current loops that pass around the object in different orientations. Fine surface features such as sharp edges, corners, or points have little effect on the spectral response. Some intermediate scale features, such as a gradually converging nose cone, do indeed produce distinctive features; but in the cases considered this only appears in the higher frequency portion of the pattern. This underlines the need for adding that higher frequency zone to the EMI picture.

The results regarding fine surface features highlight the central role of overall aspect ratio (AR) in determining spectral response. Inference of AR for unseen targets would be extremely valuable for discrimination purposes, particularly because signatures based on detailed structure may

be neither possible nor desirable, given the variability of the objects of interest. We advance a new resonance-based theory for AR inference, which tests out extremely well for homogeneous, magnetic objects. The system is based on frequency characteristics of the response, in particular on the quantity $\sqrt{f_t / f_a}$, where f_t and f_a equal f_p for the transverse and axial orientations, respectively. These correspond to the principal (single-mode) decay rates in TD systems. For non-magnetic objects, the system must be supplanted by an amplitude-based approach, based on the ratio of the magnitude of the transverse and axial responses, β_t/β_a. Overall, we regard frequency-based (or decay rate based) AR inference systems as more desirable. This is because response corresponding to axial and transverse orientations must be estimated, in field situations, by moving the antenna around and inferring the necessary quantities through some sort of model-dependent inversion. Because slight changes in position often affect the signal magnitudes greatly, the necessary antenna movement adds uncertainty in the magnitude-based systems, but does not affect the frequency-based ones so much.

The complexities of measured data in real situations can make "peak picking" (i.e. f_p identification) a precarious basis on which to rest AR inference. The processing could be improved by finding a best fit between entire quadrature component shapes and single-mode response curves, to best estimate the underlying the resonant frequency f_p. Another approach making greater and perhaps more robust use of broadband information examines the magnitude ratio β_t/β_a. By using magnitudes from over the entire UWB, one may hope that the system will be more immune to disarrangement by uncertainties in any particular frequency regions. A characteristic reversal of the β_t/β_a value with increasing frequency, from less than one to greater than one, indicates the presence of an elongated magnetic target; this quantity remains a constant depending on elongation for non-magnetic targets. In many instances, seeing the characteristic shape of the ratio reversal for β_t/β_a, particularly its limiting high and low frequency values, will depend on availability of VLF and MF (or very late and very early time) information. Analysis of measurements and also modeling of more complicated, i.e. heterogeneous objects, shows that these frequency-based AR inference approaches may still work if the steel portion of the target dominates the response, but are unlikely to work if the non-magnetic portion plays a large role, e.g. is much closer to the sensor. The highest frequency portion of the MF sub-band (equivalent to very early time) is intriguing because the primary field in that range reflects from the target without penetrating, and the signal is therefore indifferent to metal type. This holds the possibility of AR inference without the hindrance of material heterogeneity. While results show that this is possible in theory, the required accuracy of data may be unlikely in practice. Overall,

more work is needed in the realm of composite targets, and more is being done in follow-on work under other auspices.

Either from isolated fragments or from UXO fins still attached to the ordnance, spectral effects may appear from non-magnetic "parallel plates," that is, from flat non-permeable metal plates, of uniform thickness, with the primary field oriented parallel to their flat surfaces and impinging on their edges. Analysis using our new, validated, approximate analytical solutions shows that peak responses may readily appear in the new MF zone. Measurements have shown marked effects when ordnance tail sections are facing and closer to the sensor than the rest of a UXO. This may well be caused by the plate-like fins, in conjunction with the rest of the tail section. The spectral responses from non-magnetic parallel plates is dominated by a single dimension, the plate thickness, regardless of the rest of its shape (rectangular, square, circular disk, etc), as long as all lateral dimensions are significantly greater than the thickness.

This is not the case for magnetic plates. We analyze them with detailed numerical simulation, and also analytical oblate spheroid solutions. Magnetic plates show a sensitivity reminiscent of elongated bodies of revolution (BOR), depending on the degree of elongation in the direction of the primary field, assumed to be the same as the direction of observation. Under parallel plate excitation, magnetic plates show a very distinctive relation between the inphase and quadrature components that indicates that the object is broadly flattened. Making a magnetic plate thinner, whatever its orientation, raises the frequency range of its signal activity. Keeping the plate thickness constant and enlarging the diameter drives the frequency range of its response down, whatever its orientation. It seems unlikely that enlargements of a flattened magnetic object, within the size range and parameter values of interest here, would shift its responses into the VLF range. However, modest changes in diameter and/or thickness can easily move some important spectral content further into the MF zone, and the MF zone will likely be needed to view the approach to the high frequency asymptote.

Analysis of multi-fin structures produces the surprising result that they behave like BORs. That is, even for two fins formed by a right angle bend in a plate, the spectral responses from both end (parallel plate) and side observations are essentially insensitive to rotations of the structure around an axis parallel to the plate, i.e. as if they were attached to a rotating UXO. This suggests that cylindrically symmetrical UXOs with fins, a rather general class, can be represented successfully in modeling and inversion as BORs, despite the marked directional geometry of the fins themselves.

The relevance of the EMI UWB is also assessed below in cases involving finite wall thickness, i.e. hollow objects as opposed to solids. As previously, the sphere provides a good benchmark case, among other things because we have an analytical solution for the hollow sphere, and implications carry over to the horizontal cylinder. In terms of our interest in the new regions of the EMI UWB, for non-magnetic cases the VLF will only be relevant to discrimination of wall thickness effects in large, thick-walled, high conductivity cases. One needs VLF data to distinguish between the responses of a 20 cm outer diameter solid copper sphere, and a hollow one with wall thickness on the order of a cm or half cm. For a sufficiently small non-magnetic sphere, the Q component does indeed spread slightly into the MF zone. However, on the whole, only very small non-magnetic bodies with very thin walls will produce significant effects in the MF region. Still, over the complete EMI UWB one does see significant differences in signal for different wall thicknesses, within ranges of physical interest. It is notable that the results do not scale; meaning, we do not see the same picture when the external fields penetrate to the inner surface to any particular degree. Otherwise put, the results do not scale according to skin depth relative to shell thickness. This is because *two* scales are important here: only one is skin depth/outer radius, the other is shell thickness/outer radius. In all cases, we note that at resonance the shell thickness/ skin depth ratio is at most on the order of 1, and is usually less.

It is difficult to see much difference in signal from solid and hollow *magnetic* spheres, until the wall thickness is as small as a couple of mm, for an outer radius on the order of 10 cm. When differences do become apparently, they are strongly visible in the altered contrast between responses in the VLF zone and in the higher frequency domain. While there are significant differences between the magnetic and non-magnetic cases, they both show patterns in which the higher frequency portion of the spectral response remains relatively unchanged as walls become thinner. Not surprisingly, at high enough frequencies the thin walled bodies produce the same response as solids. For UXO shaped geometries with diameter of 40 mm, we see significant signal changes when wall thickness varies a few mm around the reference value of half a cm. Particularly in the vertical (axial) orientation, larger magnetic shells with thicker sides should produce visible wall thickness effects in the VLF zone. At the same time, the MF zone relation between the I and Q components is unaffected by these changes in magnetic shell thickness. This serves to highlight thickness effects in the lower frequency portion of the spectrum, a contrast that would not be clear without data in the MF zone.

For solid objects that are either compact or elongated in transverse orientation, increasing μ pushes f_p into higher frequencies. In hollow objects, decreasing wall thickness also raises f_p. However in

the latter case there are telltale signal features that distinguish the trend from the influence of μ. In particular, as wall thickness decreases one sees primarily a diminution of low frequency response only. Also, the quadrature peak becomes narrower, more symmetrical as wall thickness diminishes. This indicates shift to a single process system, that is, one with a single dominant circulation or preferred decay mode, which is logical for a thinner walled structure. This sort of peak shifting as a result of variation in wall thickness has some effects on the applicability of the frequency-based AR estimation. Still, reasonable approximations of AR are still obtained for all but the thinnest shells. In the examples considered, estimated AR differing from the actual AR only by about $\pm 1/3$, in cases where shell thickness was such that it had a visible effect on the signal pattern. More work is needed in this area. When one portion of the shell is much more substantial than others, as is commonly the case for a UXO nose section, it is noteworthy that the *more massive nose does not dominate the response*. Conversely, the relatively thinner sides appear to determine most of the spectrum, regardless of nose thickness.

Very small bits of clutter tend to produce weaker, higher frequency signals than UXO, other things being equal. But, frequently they are not equal. There may be very many clutter items, near the surface and much closer to the sensor. This can raise the magnitude of their signals to a point that severely damages SNR. At the same time, even quite small metallic objects produce maddeningly broadband spectra, so that it is difficult to keep the frequency range of their response from washing over into the locale for objects of interest. Analytical expressions are derived for the response of widely dispersed small clutter items, in surface layers or near-surface volume layers. These responses are evaluated relative to those from discrete larger objects, and are examined for the effect of changing sensor elevation. On the whole, raising the antenna is most beneficial when the target is relatively deep. In that case the signal from the clutter layer diminishes proportionally more rapidly than that of the target of interest, increasing the SNR.

One might sum up the overall laboratory and technology development mandate as a requirement to address the questions: Can consistent EMI measurements be made across the entire UWB? How? What does the success, failure, or difficulty of doing so reveal about future instrumentation possibilities? Do the new measurements harmonize with the theoretical predictions and modeling analyses? Do these, together, look useful?

The decision was made to stick with the basic GEM sensor head configuration and approach because 1) this has worked very well in the past, covering a heretofore unattainable broad band, and 2) the ultimate purpose was to produce measurements with some common calibration and consistent

implications. If entirely different devices or approaches were used for different parts of the spectrum, it would have been difficult or impossible to produce a continuous, consistent picture across the EMI UWB. Producing and investigating such a picture was our objective. Nevertheless, different coil and amplification components were employed to best address problems in different frequency ranges, as needed. Because the original GEM-3 was designed for a more limited bandwidth, the system response rolls of significantly above 100 kHz and SNR degrades, so a custom coil set was built with reduced Rx turns (from 100 to 27). Although the ideal sensitivity is reduced with fewer turns, the bandwidth associated with parasitic capacitance in the coil is improved, resulting in a system that rolls off at considerably higher frequencies. Tests verify the measuring system capability over the frequency range used, providing high SNR, repeatable data up to 390 kHz.

Measurements on UXO were made for the first time into the MF zone. An example demonstrates the capability of producing completely consistent spectra, across 4 or 5 decades (orders of magnitude) in frequency. In measured responses for a 61mm mortar, the inphase high frequency asymptotic limit is not approached until well above 100 kHz. The significance of the new, higher frequency zone for analyzing the quadrature components is revealed if one deletes the MF portion of the data. While Q peaks for all three (nose up, nose down, and horizontal) orientations reside below the old GEM-3 limit, that is not really clear in two of the cases without the more complete shape information from the MF zone. In any case, without the MF data the overall shapes of the Q components are quite unclear. Measurements on small ordnance items tend to show MF zone responses, e.g. quadrature peaks, in transverse but not in axial orientation. Thus MF information is needed to get the full picture of their response.

The VLF performance of the experimental apparatus was investigated for a relatively large target. In several cycles of the 5-55 Hz response measurement for a 105 mm UXO, repeatability was good enough to characterize the essential features of the target response. The peak of the Q component is visible, which it would not be without VLF data. Inherently, for a system in which the magnitude of received signal depends on the rate of oscillation of the magnetic field, low frequency data were weak and threatened by noise.

These lab experiments and the data displayed significantly strengthened our orientation to expand the usable bandwidth of FD EMI data into truly UWB dimensions. Some upward expansions of the GEM system operating bandwidth have already been implemented. The use of frequencies below the current 30 Hz GEM-3 capability is not a problem in principle. However it entails some

practical issues that must be considered because of the weak low frequency signals and vulnerability to sensor motion through the earth's field. These tend to affect any system of the general nature of the GEM. Inductive measurement systems have receiver input voltages that are proportional to frequency, and thus to achieve adequate SNR requires high transmitter current and long-duration measurement times. For high resolution, discrimination phase surveying, one may simply need to slow down or pause at points around an anomaly, to achieve complete EMI UWB data. However this study suggests that it is worth doing.

2. METHODS OF ANALYSIS

2.1 General Governing Relations.

Inevitably, the governing equations that form the basis for any pertinent analysis of EMI scattering physics are Maxwell's equations. These are typically simplified in induction problems to magneto-quasistatic (MQS) form, a maneuver that is immediately called into question by addition of the MF sub-band. Beyond that, different methods of analysis or modeling simply resort to different forms of these equations, or different approaches to solving them. In what follows we first review the equations themselves and the physical considerations that justify a number of simplifications that are suitable for addressing the problems at hand. This discussion is also designed to make comprehensible the subsequent material on specific methods and achievements in this project.

In both static and transient fields, Maxwell's magnetic field divergence equation must be satisfied.

$$\nabla \cdot \mathbf{H} \quad = \quad 0 \tag{3}$$

where this form of the equation assumes spatially uniform μ. In practice here we will assume that μ may vary between different portions of an object of interest, but that it is constant within any given section or sub-region. Thus (3) applies within every (sub)region, except on boundaries, where we apply a boundary condition instead.

The particular equation in Maxwell's complete set of that pertains most directly to induction is Faraday's Law,

$$\nabla \times \mathbf{E} \quad = \quad -\mu \frac{\partial \mathbf{H}}{\partial \mathrm{t}} \quad \text{(TD)} \quad \Rightarrow \quad i\omega\mu\mathbf{H} \quad \text{(FD)} \tag{4}$$

where **E** is the electric filed (V/m). For frequency domain expressions (far right), a time dependency of the form $\exp\{-i\omega t\}$ is assumed and its expression suppressed throughout in FD expressions. Throughout science and engineering, a different convention is sometimes used, assuming a positive

exponent in the time factor. We will occasionally make note that some FD results have a form assuming the alternative time exponent convention.

Equation (4) states that a transient or fluctuating magnetic flux (i.e. the right hand sides) induces a rotation or "circulation" of electric field (left hand side). This field rotation is tantamount to the generation of a non-zero voltage around a closed wire loop through which the magnetic flux passes. While for a legitimate solution we must draw on all of Maxwell's equations, at least by implication, we will use (3) and (4) primarily via substitution in some form of Ampere's Law:

$$\nabla \times \mathbf{H} \quad = \quad \sigma \mathbf{E} \; + \; \varepsilon \frac{\partial \mathbf{E}}{\partial \mathrm{t}} \quad (\mathrm{TD}) \; \Rightarrow \quad \sigma \mathbf{E} - \; i\omega\varepsilon \mathbf{E} \quad (\mathrm{FD}) \tag{5}$$

The quantity εE is called the electric displacement (C/m^2), where ε is the permittivity of the medium (farad/m). Note that, even in the frequency domain, ε as used here does *not* include any portion resulting from the electrical conductivity of the medium, σ, the effects of which will always be expressed separately. The first term on the right hand sides represents actual electric currents in the medium, and second term on the right is called the displacement current, through which the time derivative of the electric field performs a function like an electric current. We wish to examine the magnitudes of these terms, relative to each other and also relative to the various derivatives on the left side of the equation. We will do this by tracing the influence of each of the terms on the right hand side within an equation entirely in H, obtained by combining (5) with other of Maxwell's equations. Taking the curl of (5) and performing manipulations yields

$$\nabla^2 \mathbf{H} \quad = \quad - \; i\omega\sigma\mu \mathbf{H} - \; \omega^2 \mu\varepsilon \mathbf{H} \tag{6}$$

The first and second terms on the right in (6) descend from the first and second terms on the right in (5), respectively. Specifically, the relative magnitude of the first (second) term on the right hand side of (5) corresponds to the relative magnitude of the first (second) term on the right hand side of (6), and we will analyze the latter. The three parameter regions where this equation will be examined are those for air (free space), the soil, and the metallic scatterers.

All solutions in this study are based in part on two reasonable assumptions. The first is that, throughout the entire UWB EMI frequency band, electromagnetic phenomena are magneto-

quasistatic. While this may be taken as something of a foregone conclusion in LF EMI, we examine the assumption explicitly here because we are raising the upper frequency limits for EMI practice. This makes the magneto-quasistatic assumption more suspect. The situation is different in each of the three parameter regions.

In the air we assume that σ is approximately zero, so that the second term in (6) drops out. This leaves a classical wave equation with wavenumber *k* defined as

$$k = \frac{2\pi}{\lambda} = \omega\sqrt{\mu\varepsilon} \tag{7}$$

where λ is the wavelength. Higher frequencies produce shorter wavelengths. At the top of the MF-EMI band (300 kHz), this expression indicates that the electromagnetic wavelength is one kilometer. Typical distances over which we are concerned about electromagnetic interactions are on the order of 1 m. This means that, even at the highest frequencies considered, there is no phase difference or delay between the time pattern of magnetic activity in one air location relative to any other within the domain of interest. The fields have the same configuration (geometry) that they would in the static case, evolving over time only as they follow boundary or other imposed conditions. In structure, they are essentially static fields. This meaning of this is explained with reference to Figure 5.

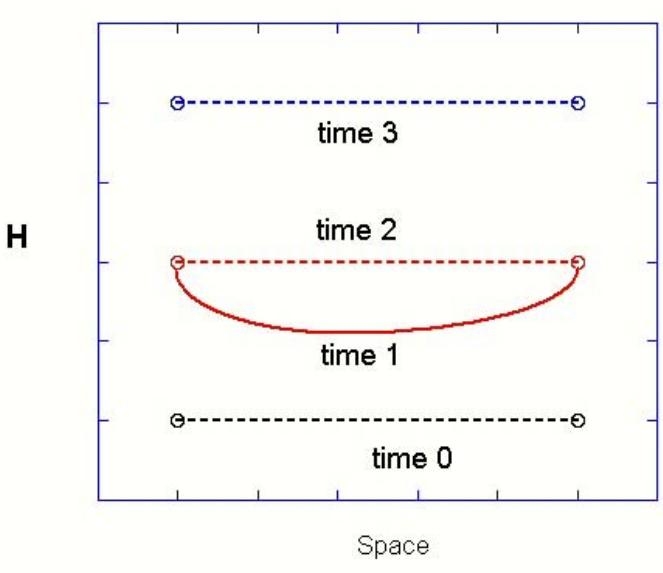

Figure 5. Schematic examples of H field distributions at different times, as the boundary values (circles) are changed.

Assume that the magnetic field distribution over space is initially flat (time 0). The boundary values rise quickly between time 0 and time 1, quickly enough so that the fields between the boundaries cannot keep up with the imposed change. As illustrated by the solid line in the figure, they lag behind in the region between the boundaries. The meaning of the observation above, in terms of wavelength, is that, for this to occur within the EMI UWB, the boundary values would have to change more quickly than rates implied by frequencies even at the top of the MF sub-band, e.g. we would have to operate at radar frequencies. If we hold the boundary values constant for a while after time 1, eventually the entire H distribution will even out to a static distribution, which is the flat distribution at time 2. Suppose we again change the boundary values, between time 2 and time 3, but this time much more slowly than before, in particular, at rates in line with the frequencies within the UWB EMI band. Now the H distribution between the boundaries always retains the static distribution between the boundaries, even as the field values change in time. That is, the time and space scales are such that internal fields always have sufficient time to distribute themselves in the steady state configuration as the boundary or other forcing values change. They may change in time, but always arrange themselves in the geometry of static fields between boundaries or around forcing functions.

The ultimate significance of this in connection with the equations above is that *both* terms on the right hand side of (6) are negligible, as both are FD expressions for time derivatives. Thus the corresponding terms in (5) are also negligible, and the H field is irrotational ($\nabla \times \mathbf{H} = 0$). An irrotational field may be represented as the gradient of a scalar potential, ψ (A/m^2).

$$\mathbf{H} = -\nabla \psi \tag{8}$$

Substituting (8) in (3) produces the governing equation for the air region.

$$\nabla^2 \psi = 0 \tag{9}$$

Within the soil, σ is nonzero and the ratio of the magnitude of the third to the second term in (6) is $\omega\varepsilon/\sigma$. As a "worst" case, i.e. the one that most threatens the MQS assumption, we assume ω ~10^6 rad/s, $\sigma \sim 10^{-3}$ S/m, and $\varepsilon \sim 10^{-10}$ F/m. This combination of parameters means that we would be operating at the extreme upper limit of the MF-EMI band and presupposes a particularly unlucky set

of soil properties, with low conductivity but rather high dielectric constant. Even this combination of parameters implies that the third (displacement current) term is not larger than the second (electric current) term. To estimate the significance of the electric currents in the soil, compare their magnitude to those induced in the metallic target. By general continuity conditions, the electric field E will be on the same order in the soil immediately surrounding the target and in the parts of the metal where the most significant currents are flowing. As the currents are equal to σE, the ratio of currents in metal and soil will be approximately equal to the ratio of their conductivities. A reasonable upper bound on soil conductivity is $\sigma \sim 10^{-2}$ S/m. A typical metal of interest has $\sigma \sim 10^{7}$ S/m. Thus the currents in the metal are about nine orders of magnitude stronger than those in the soil. Unless the metal scatterer is extremely small and simultaneously the sensor samples an enormously larger volume of soil, the fields in the soil will be dominated by those produced by currents in the metal. That is, the electric currents in the soil will not be a significant factor in determining the fields in the soil. Thus we conclude that the term containing the soil currents may be dropped (first term on the right in (6)). We have already concluded that the second term is less significant than the first; therefore the entire right hand side of (6) is again negligible. Thus, in the soil as in the air, we conclude that the magnetic fields are irrotational and can be represented using a scalar potential, i.e with the governing equation (9).

Within the metal, we again examine the quantity $\omega\varepsilon/\sigma$. Using the typical values cited above we immediately conclude that the displacement current term is negligible compared to the electric current term. However, the electric currents within the metal are by no means negligible; rather, they are a fundamental source of the scattered signals. Thus two terms remain in (6), which may be construed as a Helmholtz equation

$$\nabla^2 \mathbf{H} + k^2 \mathbf{H} = 0 , \qquad k = \sqrt{i\omega\sigma\mu} \tag{10}$$

where $k = \gamma + i\gamma$ is sometimes referred to as a wavenumber, by analogy with higher frequency solutions to the equation. However note that (10) is *not* a wave equation, as the second term $i\omega\sigma\mu\mathbf{H}$ is the frequency domain equivalent of $\sigma\mu$ times the *first* derivative H with respect to time, not the second derivative. We can create "traveling wiggles" within the metal by imposing sinusoidal behavior on its surface. However these are not true waves, e.g. they do not reflect. As in the wave case, fundamental solutions of (10) can be expressed as

$$\mathbf{H} \sim e^{ikx} = e^{i\gamma x} e^{-\gamma x} \tag{11}$$

Because the real and imaginary parts of k are equal, the spatially oscillating factor $e^{i\gamma x}$ decays by $1/e$ in less than one sixth of its spatial period.

In some important approximations that follow, we shall use the assumption of locally one-dimensional solutions of (10) of the form (11). Also, we may draw on (3) to recast the governing equation (10) as

$$\nabla \times \nabla \times \mathbf{H} - k^2 \mathbf{H} = 0 \tag{12}$$

This "double curl" equation will also serve as a governing equation in some places below. Lastly, the boundary conditions that must be satisfied on any surface between two regions (1 and 2) are the standard continuity conditions for tangential ("tan") magnetic field or normal flux:

$$\begin{aligned} H^1_{\text{tan}} &= H^2_{\text{tan}} \\ \mu_1 H^1_n &= \mu_2 H^2_{\text{n}} \end{aligned} \tag{13}$$

2.2 The Method of Auxiliary Sources (MAS)

Over the years, various numerical methods have appeared in order to address the kind of problem we consider here. These include 3-D Method of Moments (MoM) based on Magnetic Field Integral Equations (MFIE), which incorporates an impedance boundary condition (IBC) [6]; MoM for body of revolution (BOR) [7]; and MoM for body of revolution (BOR) with hybrid finite element - boundary element formulations (FEM-BEM) [8,9]. In first case the authors combined the MFIE with IBC, and solved for surface electric current. This approach has a limited and largely untested range of validity, in terms of (frequency dependent) skin depth relative to object dimensions. Further, the method does not solve for the internal fields. We are quite interested in these fields and associated currents, in order to understand the underlying mechanisms of response and their relation to object shape and composition. This is at the heart of what is needed for advances in discrimination.

In the most general MoM and FEM-BEM approaches [8,9], not reliant on the IBC, the Green function applicable to the target's internal material must be resolved on the surface mesh (beyond what relaxation of such resolution requirements is accomplished via singularity extraction). In [8] the authors use the MoM to solve the full low frequency EM field scattering for a BOR. As they have written, reasonable results are obtained when they use ten subsections per wavelength, in keeping with the requirements of the exp(ikr) type factor in the Green Function. This is unfortunate in that the quantities ultimately of interest (fields, currents) themselves actually change quite gradually and smoothly along the surface, and as such could be resolved well by a much coarser discretization, if other requirements did not apply. That is, the resolution requirements in the aforementioned integral formulations are dominated by the fact that the observation points for the Green function are placed on the same surface as the sources quantities to be approximated, and the Green functions often decay over extremely short distances. Similarly, for volume methods such as finite elements or finite differences, a comparable mesh constraint applies. The discretization interval or basis function size must be “much smaller than the skin depth” [9].

Our approach, the Method of Auxiliary Sources (MAS), locates sources off the physical surface. This means that the effects of source quantities are less concentrated, more smoothly spread over the mesh surface. That surface is also devoid of singularities, as source and observation points never coincide. There is no volume mesh. These facts allow use of many fewer subsections (elements, patches) on the surface, in keeping with the above-mentioned mild tangential gradients of dependent variables. By and large, numerical methods for our problem are computation intensive, limiting the ready application of modeling in problems of practical interest, particularly for general geometries. However, particularly when combined with the Thin Skin Approximation described below, the MAS is a, robust, accurate, easily programmed, and extremely efficient modeling system, over the entire UWB EMI range.

In the MAS, boundary value problems are solved numerically by representing the electromagnetic fields in each domain of the structure under investigation by a finite linear combination of analytical solutions of the relevant field equations. Each contributing solution corresponds to a hypothetical source, situated at some distance away from the boundaries of each physical domain. The "auxiliary sources" producing these analytical solutions are chosen to be elementary (infinitesimal) magnetic dipoles or charges, or in some cases are more continuous current configurations, located on fictitious auxiliary surface(s). These surfaces usually conform to the actual

surface(s) of the structure. In practice, at least in the simplest variant of the method applied to most of the problems here, we only require the identification of points, normals, and tangents on the auxiliary and actual surfaces, without resorting to the detailed mesh structures and connectivity required by other methods.

In general, auxiliary surfaces are set up inside and outside the scattering object ("target"), as in Figure 6. These are easily generated numerically simply by magnifying or shrinking the actual surface. The fields outside of the structure are considered to originate from a distribution of auxiliary magnetic charges placed inside the object, and the fields penetrating the object arise from a set of auxiliary magnetic current elements placed outside the object. The combination of these fields is required to obey fundamental electromagnetic interface conditions, i.e. (13), enforced at an array of subregions or selected points on the physical surface(s) of the structure. This produces a matrix equation from which the amplitudes of auxiliary sources are to be determined. Once the amplitudes of auxiliary sources are found, the solution is complete. All electromagnetic fields and related parameters can easily be computed throughout the interior and exterior domains.

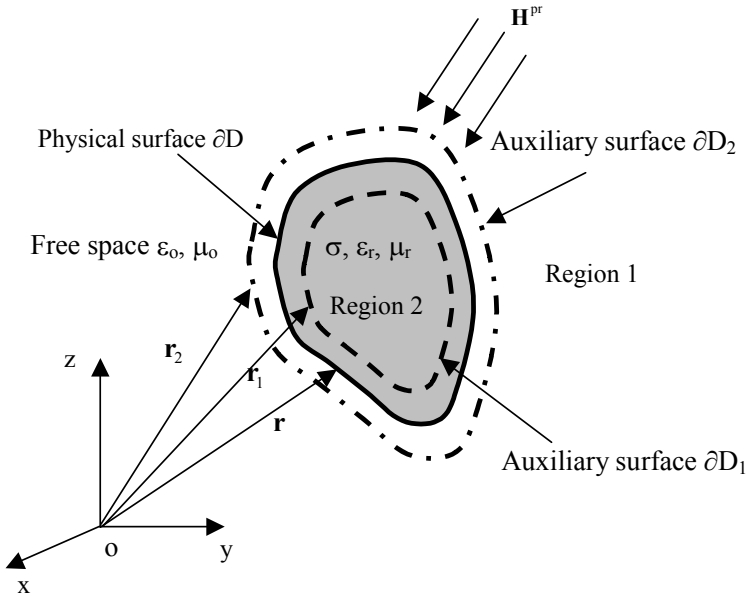

Figure 6. Geometry of scattering body, showing the relation of its physical and auxiliary surfaces

In sum, the MAS formulation we present here offers a number of advantages: Field singularities at source locations need not be confronted directly since the auxiliary surfaces containing the sources are separated from the physical surface where conditions are applied. The simplest version of the method, with infinitesimal sources, is extremely easy to program because the sources are expressed as delta functions, so evaluation of integrals is immediate. At the same time, the fields produced by these sources are relatively smooth on the surface of interest, because the sources are recessed from it. In more complex MAS formulations, we may trade the greater programming overhead involved in more elaborate mesh preparation, source specification, and error testing for higher resolution and efficiency.

Our variants of the method, together with their application and their performance assessments, are presented in a number of conference and journal papers [10-19]. Applications include materially heterogeneous objects, layered or hollow objects, and multiple objects. Here we only summarize enough of the simplest formulation to provide a sense of the method. Subsequent sections below report on our applications of the method, involving both measured data and theoretical constructs, designed to be revealing in connection with our assessment of UWB EMI.

For MAS purposes, the solution to (9) outside the target can be written as

$$\psi(\mathbf{r}) \;=\; \int_{\partial D_1} dS'\, Q(\mathbf{r}')\, G_Q(\mathbf{r}', \mathbf{r}) \tag{14}$$

where

$$G_Q(\mathbf{r}', \mathbf{r}) \;=\; \frac{-1}{4\pi\mu_0 \left|\mathbf{r} - \mathbf{r}'\right|} \tag{15}$$

and the internal integration surface ∂D_1 contains the initially unknown source distribution Q. Ultimately, combining (8) and (14)-(15) produces the final expression for the scattered field outside the object, $\mathbf{H}_1^{sc}(\mathbf{r})$

$$\mathbf{H}_1^{sc}(\mathbf{r}) \;=\; -\int_{\partial D_1} dS'\, Q(\mathbf{r}')\, \nabla G_Q(\mathbf{r}', \mathbf{r}) \tag{16}$$

When the source distribution Q is a collection of N point magnetic charges at locations r_j , each with scalar charge magnitude Q_j

$$Q(\mathbf{r}') = \sum_{j=1}^{N} Q_j \, \delta(\mathbf{r}' - \mathbf{r}_j) \tag{17}$$

then (16) is simply evaluated as

$$\mathbf{H}_1^{sc}(\mathbf{r}) = -\sum_{j=1}^{N} Q_j \, \nabla G_Q(\mathbf{r}_j, \mathbf{r}) \tag{18}$$

MAS expressions for the internal field follow an analogous scheme, taking into account the vector nature of the internal magnetic field and its sources, and the different governing equation. The total internal field $\mathbf{H}_2$ can be expressed as

$$\mathbf{H}_2(\mathbf{r}) = i\omega\varepsilon \int_{\partial D_2} dS' \, \mathbf{G}_H(\mathbf{r}', \mathbf{r}) \cdot \mathbf{P}(\mathbf{r}') \tag{19}$$

where the dyadic Green function is

$$\mathbf{G}_H(\mathbf{r}', \mathbf{r}) = \left[\mathbf{I} + \frac{1}{k^2} \nabla\nabla \right] \frac{e^{ikR}}{4\pi R}$$
$$R = |\mathbf{r} - \mathbf{r}'| \tag{20}$$

and the *external* integration surface ∂D_2 contains the initially unknown distribution **P** of magnetic currents. Note that the properties determining *k* in this equation correspond to those of the material inside the object. Again, restricting ourselves to point sources, i.e. infinitesimal current elements equivalent to point magnetic dipoles, one expresses **P** in (19) as

$$\mathbf{P}(\mathbf{r}') = \sum_{j=1}^{M} \mathbf{P}_j \, \delta(\mathbf{r}' - \mathbf{r}_j) \tag{21}$$

where $\mathbf{P}_j$ is the (vector) source strength of the j^{th} external source. This is immediately evaluated to obtain the expression for internal fields.

$$\mathbf{H}_2(\mathbf{r}) = i\omega\varepsilon\sum_{j=1}^{M}\mathbf{G}_H(\mathbf{r}_j,\mathbf{r})\cdot\mathbf{P}_j \tag{22}$$

The vectors $\mathbf{P}_j$ each contain two components, parallel to the surface ∂D_2, in the same way that current elements in the MoM or general Huygen's principle formulations are parallel to the integration surfaces. Thus there is a total of N + 2M unknown source coefficients to be solved for. These are obtained by enforcing the standard Maxwell equation interface conditions (13) at a sufficient number of points on the actual surface. As mentioned above, at the cost of greater programming complexity, a more efficient system can be obtained when (13) is applied continuously over each subregion of the surface, via selected "testing functions," and the sources Q and P also consist of continuous charge/ current sheets. However the source distribution and testing functions are defined, the result of applying the boundary conditions is a matrix equation that can be solved for the unknown source coefficients.

The accuracy of the method is illustrated here by comparison to the analytical solution for scattering from a hollow sphere [5]; and by comparison to measurements for solid cylinders of both magnetic and non-magnetic material (Figure 7 - Figure 9). Data were obtained with the GEM-3 before MF capabilities had been developed. Figure 7 shows the secondary magnetic field for the hollow sphere with $\mu_r = 100$, inner radius 45 mm, outer radius 50 mm, and conductivity $\sigma = 10^7$ S/m, when the target is exited by a primary field $\mathbf{H}^{pr} = H_0\hat{\mathbf{z}}$, with observation point x = y = 0, z = 1 m. The BOR code was used, with point sources and point matching. Agreement is excellent over the entire spectrum. For a solid body, Figure 8 compares measurements of the scattered (far) field with MAS simulations based on handbook values of the electrical parameters for brass. Excellent agreement was obtained from PC runs lasting at most a couple of minutes, usually much less. Simulations for the steel case (Figure 9) took a comparable amount of execution time, after preliminary runs were done to estimate σ and μ. The values ultimately chosen are reasonable for common steel, and we note excellent, detailed agreement over the entire GEM-3 frequency band, for both orientations, suggesting that the quality of results is not an artifact of parameter choice. As suggested by theory developed during this project [16], the response spectrum does not change significantly as a function of orientation for the non-magnetic (brass) case, except in overall

magnitude. By contrast, rotation of the steel cylinder into a transverse orientation shifts the frequency response notably higher, also expected from theory. Note that the fundamental reference point provided by the crossing of the in-phase and quadrature components lies in the new mid-frequency zone. Also, without the new higher frequency range one will not be able to produce reasonable estimates of the asymptotic value towards which the inphase response is heading.

A very advantageous feature of the MAS is its ability to provide easy and quantitative measures of the level of error in the numerical solution. The level of error can then be reduced by improving the source distributions over the auxiliary surfaces, either in terms of density in problem areas or overall number of coefficients. A direct error measure is possible because all parts of the formulation contain exact solutions to the governing equations and we only approximate the satisfaction of the boundary conditions (13). To see how precisely those conditions have been met, we need only integrate the right sides and left sides of (13) over the actual surface and note where or how much the equality is not met. This is an invaluable tool for guiding the numerical system towards convergence, for optimal numerical strategy (source distribution), and for evaluation of results. Other generally established numerical systems lack this facility.

We have made a user-friendly version of our MAS program available to the public, including some additional sophistications described below in Section 2.4. The user can select from a number of basic BOR target geometries, including a UXO-like shape, and can then specify the target's orientation and material properties. Before running the program, the user also specifies a tolerable level of error, which in turn determines the level of discretization source density. The mesh density and distribution are adjusted in an adaptive manner, as the program proceeds up through the frequency range requested. For basic geometries, common material parameters, and reasonable error tolerance, the program provides extremely accurate solutions covering the entire EMI UWB within a few seconds to a few minutes, on a PC.

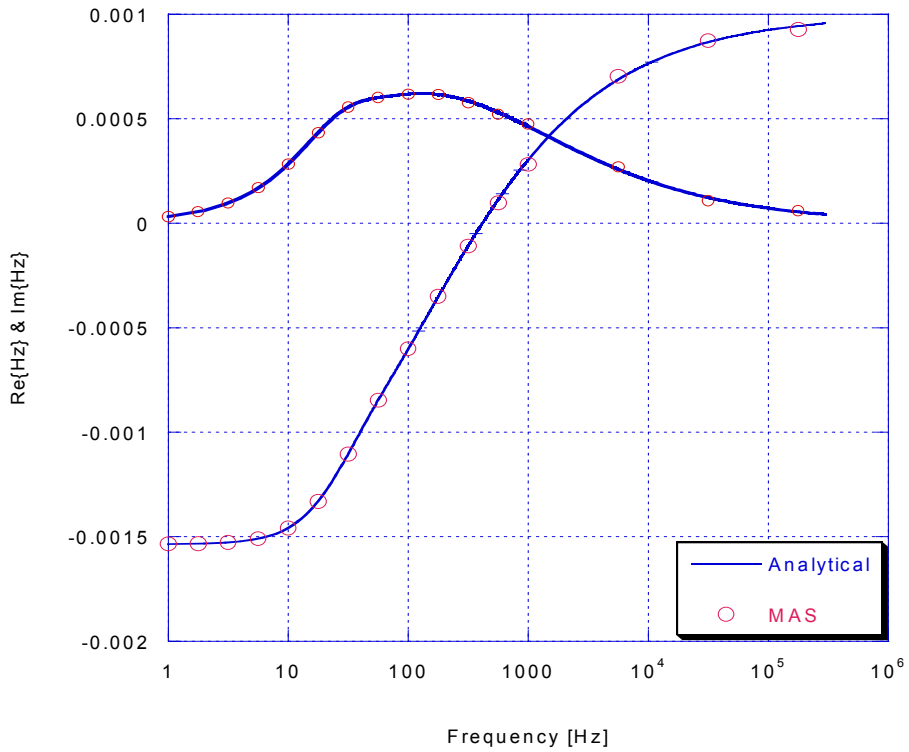

Figure 7. Scattered magnetic field from a hollow sphere vs frequency, comparing numerical MAS solution with analytical solution.

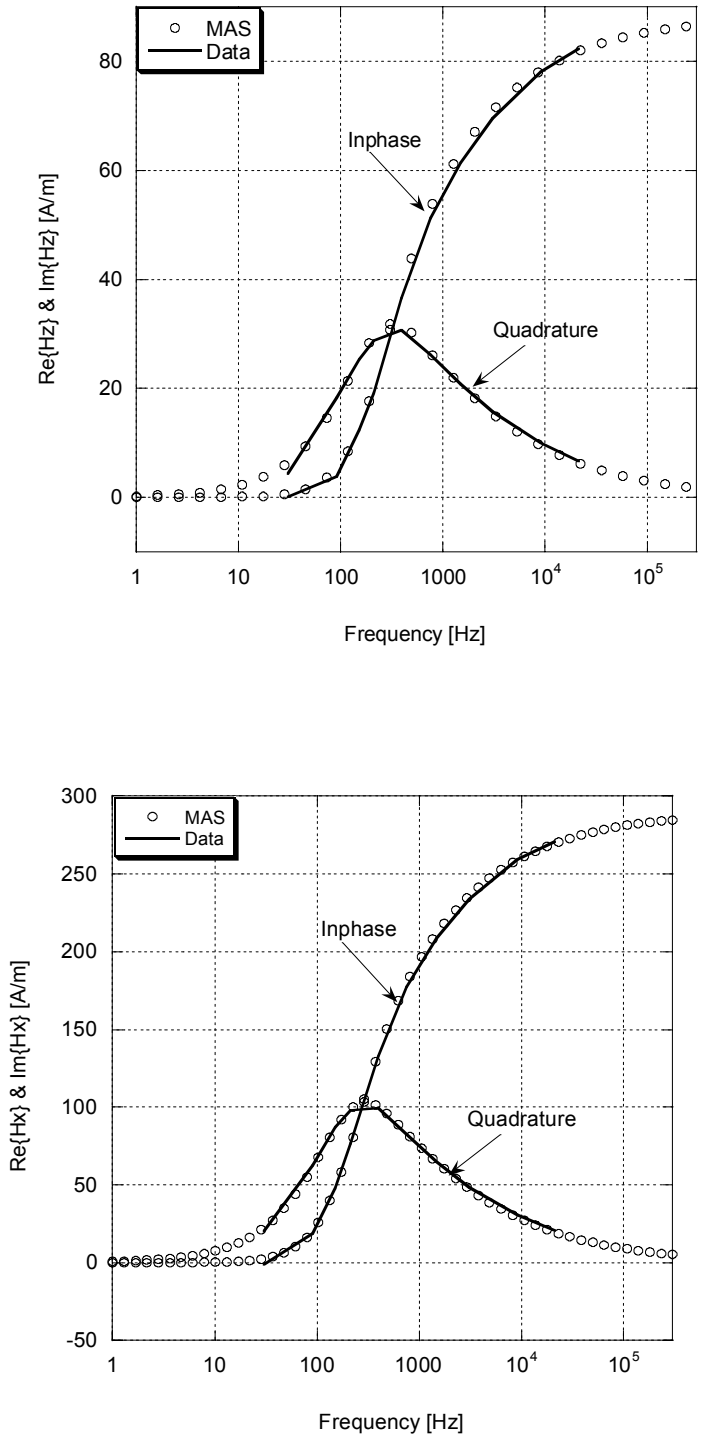

Figure 8. Normalized secondary magnetic field from a brass cylinder with length to diameter ratio 2.4, $\sigma = 1.2 \times 10^7$ S/m, $\mu_r = 1$, diameter = 3.175 cm. Circles = MAS, solid line GEM-3 measurements under axial excitation (top) and transverse excitation bottom.

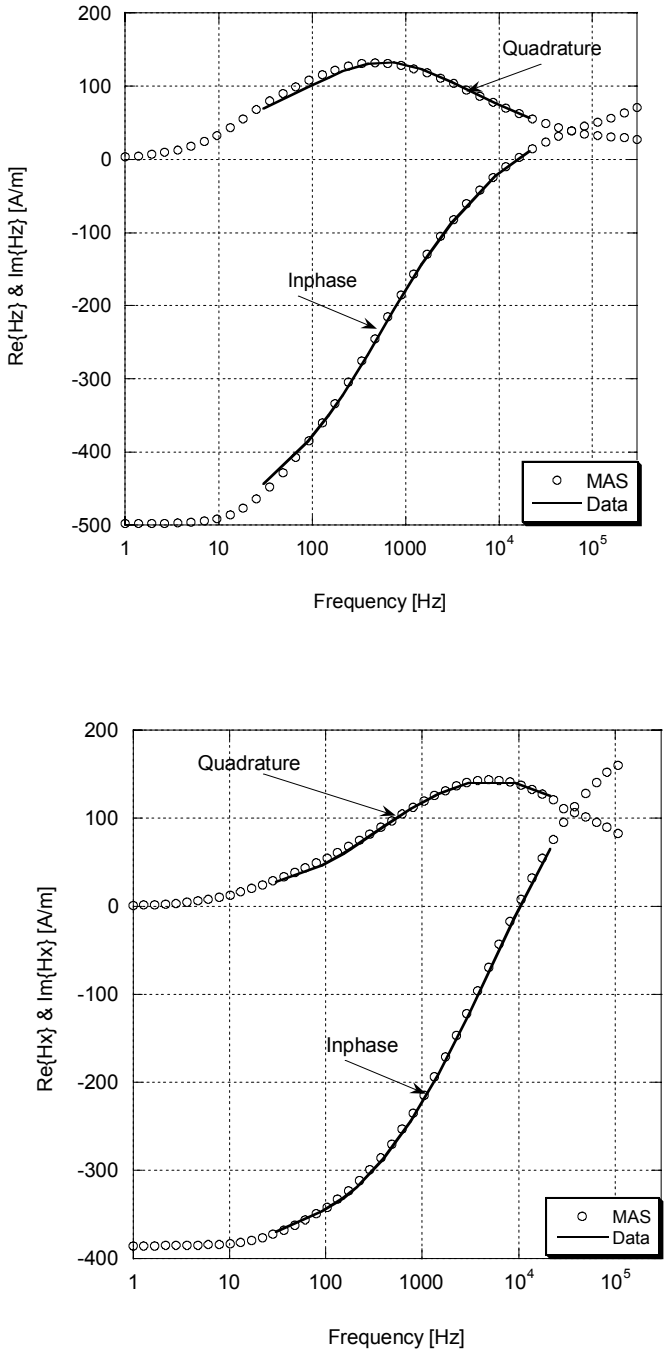

Figure 9. Normalized secondary magnetic field from a steel cylinder with length to diameter ratio 2.4, diameter = 3.175 cm, $\sigma = 4 \times 10^6$ S/m, $\mu_r = 50$. Circles = MAS, solid line GEM-3 data under axial excitation (top) and transverse excitation (bottom).

2.3 Exact and Approximate Analytical Solutions for Fundamental Cases

The paucity of EMI analytical solutions has hampered instrumental calibration, testing of numerical codes, understanding of the mechanisms underlying observed patterns of response, and, perhaps most important, the development of tractable inversion algorithms. Inversion work for UXO discrimination has been impeded in particular by a lack of reliable forward solution forms that can be examined for their implications in any given case, and that can be manipulated rapidly in the manner required by inversion processing. As we shall see in the sections below, objects with complicated geometrical detail can often be represented adequately by simpler, fundamental geometrical shapes with similar proportions. That is, the simpler shapes will produce response patterns that are virtually indistinguishable from those of the more complicated originals, while retaining important evidence of the finite size of the object, in contrast to representation by infinitesimal dipoles or other highly concentrated sources. Because all of the solutions we have developed are applicable and can be evaluated over the entire span of the EMI UWB, they can be used to assess effects in the newly expanded band. Also, analytical solutions can often be examined explicitly for functional dependencies and sensitivity to critical parameters. We exploit the analytical solutions in some of these ways in the material below, and apply them for general EMI scattering representation and inversion work elsewhere [e.g. 25].

At the inception of this project, the only analytical solutions available for EMI scattering from basic shapes were for the sphere and for the infinite cylinder oriented transverse to the primary field. These solutions had been established since around the mid-twentieth Century [e.g. 5,28]. Expert judgment of that time deemed solutions for general spheroids to be intractable because evaluation of the necessary vector spheroidal wave functions was not feasible [29]. And indeed no new solutions were forthcoming in the intervening years. To address this situation, a collaborative effort was undertaken with personnel from the Center for Electromagnetic Theory and Applications at MIT. Some ingenuity in terms of mathematical transformations, grouping of quantities, and other manipulations [32, 33] produced a solution for axial prolate spheroids, requiring only treatment of scalar wave functions and solutions for scalar quantities. This avoids very substantial complications of vector spheroidal wave function. Useful high and low frequency limiting forms are obtained, and for modest degrees of elongation or low permeability materials, all quantities can be evaluated over the entire UWB. For highly permeable, elongated objects, evaluation difficulties manifest themselves

in the middle of the band, and rational approximations are adduced to bridge the gap between the high and low frequency ranges where evaluation is solid. Further work treated the completely general cases, for both oblate and prolate spheroids, in both axial and transverse orientation. While this required us to deal with the full vector spheroidal wave functions, evaluations were comparably successful, with a problematical gap only in the middle induction numbers for some cases [36-38]. In follow-on work, also supported in part by SERDP, the remaining evaluation difficulties were resolved, and a sequence of three write-ups is now heading for submission.

Partly because they are all used below and partly just for completeness, the following sub-sections present all available EMI analytical scattering solutions, including the "classical" sphere and cylinder ones, together with our newer results.

The sphere.

This case provides the simplest of the EMI responses in that the sphere produces an external scattered field with essentially the same geometry of field lines and relative magnitudes as an infinitesimal magnetic dipole at the center of the sphere. That is, the expressions retain the same form in both the near and far field. Also, the direction of the induced magnetic dipole is always in (positive or negative) alignment with the primary field, assuming, as we do for this solution, that the latter is spatially uniform on the scale of the sphere. Both despite and because of its simplicity, this solution is very useful in gauging the form and frequency range of representative UWB EMI scattering. In terms of the conventions applied here, the scattered field can be expressed as

$$\mathbf{H}^{\mathrm{sc}}(\mathbf{r}) = \frac{3\hat{\mathbf{R}}\hat{\mathbf{R}}\text{-}\mathbf{I}}{4\pi R^3}\cdot\mathbf{m}_{\mathrm{sph}} \tag{23}$$

where $\mathbf{R}=\mathbf{r}-\mathbf{r}'$ and **r** and **r'** are the observation point and sphere location, respectively; $R=|\mathbf{R}|$, $\hat{\mathbf{R}}=\mathbf{R}/R$, $\hat{\mathbf{R}}\hat{\mathbf{R}}$ is a dyad, **I** is the identity tensor, and $\mathbf{m}_{\mathrm{sph}}=m_{\mathrm{sph}}\mathbf{H}^{\mathrm{PR}}$ with

$$m_{\mathrm{sph}} = 2\pi a^3\,\frac{(2\mu_{\mathrm{r}}+1)(1-ka\cot(ka))-(ka)^2}{(\mu_{\mathrm{r}}-1)(1-ka\cot(ka))+(ka)^2} \tag{24}$$

The radius of the sphere is a and it is understood that $R > a$. Notes in the next section on evaluation of trigonometric or Bessel function with large, complex ka values apply here as well. Ultimately, using large argument approximations, m_{sph} and related expressions for the cylinder can be evaluated without undue difficulty. This form of m_{sph} is based on an assumed (and suppressed) time expression of $\exp\{-i\omega t\}$. Beyond that, it retains a "physical" sign convention inherent in the derivation from Maxwell's equations, such that

$$\frac{m_{\text{sph}}}{2\pi a^3} = \left\{ \begin{array}{ll} \dfrac{(2\mu_r + 1)}{(\mu_r - 1)}, & ka \to 0 \\ -1, & ka \to \infty \end{array} \right\} \tag{25}$$

This is physically sensible in that the low frequency limit for magnetic materials is positive, when the induced dipole indeed aligns with the primary field; and at the high frequency limit it is negative, when the induced response opposes the primary field. For historical reasons, this sign convention is altered in the geophysical literature, so that the dipole moment is expressed using the *negative* of the *real part* of the expressions in (24), (25). When the $\exp\{+j\omega t\}$ time convention is used, with the notational convention that $j = i$, the negative of the entire moment expression above is usually employed to express m_{sph}. Go figure. In most of what follows, we will follow the geophysical-historical geophysical sign convention, with the $\exp\{-i\omega t\}$ time expression implied. This produces plots with the component patterns like those in Figure 2.

Note that the magnitude of the scattered field expressed by (23)-(24) falls off generally as $(a/R)^3$. The real and imaginary parts of (24) are the inphase and quadrature components of frequency response, respectively, as plotted in Figure 2. Basically, m_{sph} provides the frequency response, and the rest of the expression on the right hand side of (23) expresses the geometry and spatial dependence of the scattered field. As noted above, the geometry of the field produced by the sphere is the same, in detail, as that of a simple magnetic dipole, *in both near and far field* ($R > a$). This is not the case for any other geometry or (non-uniform) primary field, for which some near field effects will generally occur. The tensor form in (23) is useful in applying some of the results that follow because it does not depend on any particular coordinate system and is easily generalized. That is, the response of *any* object can be expressed in the far field using its dipole moment **m**, inserted in (23), whatever the shape of the object and whatever coordinate system is used to view it. Because many if

not most of our UXO sensors are at least approximately axisymmetric loops, a cylindrical coordinate system is often used. In the cylindrical system (23) becomes

$$\mathbf{H}^s(\rho,z) = \left[\hat{\boldsymbol{\rho}}\frac{3\rho z}{4\pi R^5} + \hat{\mathbf{z}}\frac{2z^2-\rho^2}{4\pi R^5}\right] m_{\text{sph}} \tag{26}$$

Figure 10 shows the normalized inphase and quadrature components of m_{sph} vs induction number $|k|a$. As is apparent from the form of (24), the m_{sph} pattern is fixed with respect to induction number for any given μ_r. Otherwise put, μ_r enters in two ways, only one of which is through induction number, while σ and ω can always be grouped together in the induction number for a single effect. Note that from variation of μ alone, the locus of signal activity can easily move about within a span of three orders of magnitude in induction number.

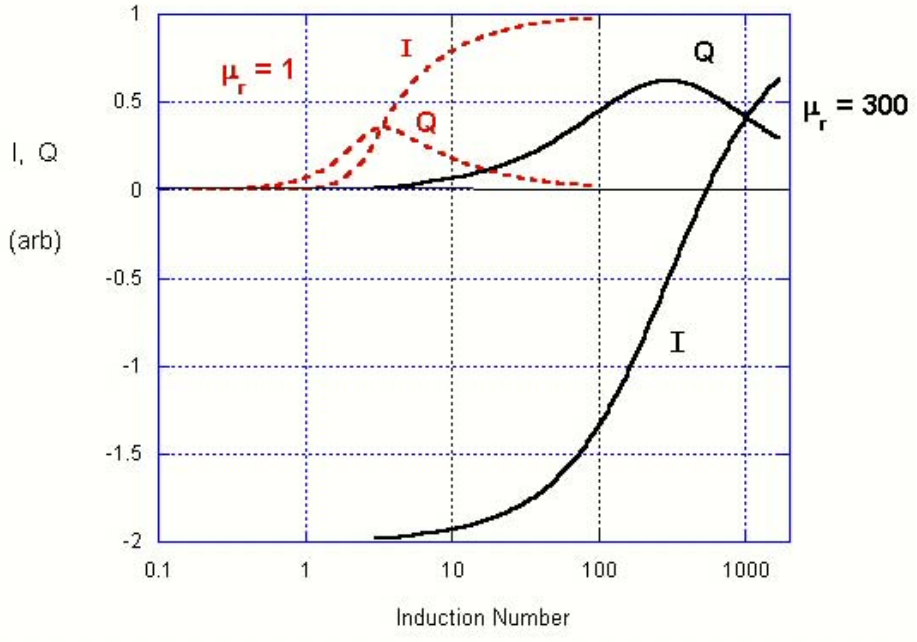

Figure 10. Normalized inphase (I) and quadrature (Q) components of the frequency response of a sphere, vs induction number $|k|a$, with historical geophysical sign convention applied, for lowest and highest permeabilities

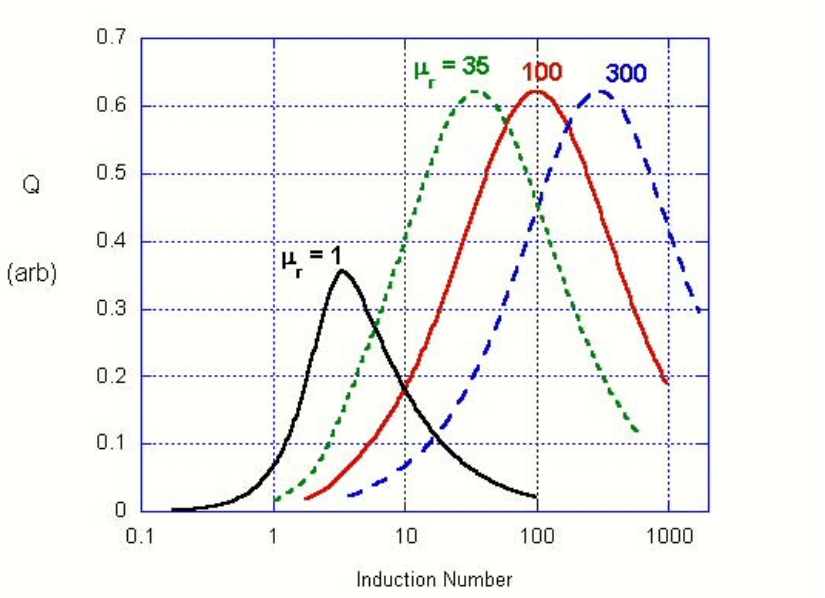

Figure 11. Dependence of Q component on μ_r, for the secondary field from a sphere, relative to induction number.

In their fundamental features, the component curves in Figure 10 are prototypes for the frequency response functions of many other objects. In the least, they serve as benchmarks for comparison. For the non-magnetic case, the I and Q curves have the same sign and cross at the peak of the Q component. The frequency point where the I and Q components are of equal magnitude is a fundamental defining feature of the frequency response, sometimes called the "resonance point." For the magnetic case, the curves are shifted notably to the right, other things being equal; the higher the μ_r value, the greater the shift. Also, for any $\mu_r > 1$, the inphase component crosses the Q component to the right of the peak in the latter.

The two values of μ_r selected probably represent the bounds on reasonable values that we may apply, and therefore these two sets of curves approximately define the extremes of frequency response, in terms of the induction number locale where the principal activity occurs. Relative permeability will not be less than unity for the ordinary materials we consider. And while certain cast irons can have μ_r values of thousands or millions, ordinary steels have been represented well in our studies by relative permeabilities no greater than about 50 to 250, in general not greater than 300. Because we are interested simply in representation of scattering behavior, we are not greatly troubled by the ambiguities in μ_r that can become an issue in very high permeability materials if one is

interested in intrinsic properties (non-uniqueness and hysteresis, non-linearity, frequency and time dependence, complex value…). In our frame of reference, increases of μ_r into the common "steel-like" range of 100 - 300 generally push responses into veritably asymptotic limiting behavior, so that the exact value of μ_r is not so important. Further, we have found that, for high permeability common materials, the effects of μ_r and σ cannot be separated entirely. Over much of the band, especially the MF-EMI portion, the same frequency response is obtained for any combination of μ_r and σ that produce the same ratio (μ_r/σ). Results in this regard are reported in [23]. Be this as it may, application of reasonable, constant values of μ_r and σ has allowed us to produce very good agreement between measured and modeled frequency response, for any distances from the object, all orientations, and non-uniform primary fields. That is, a *single, unvarying* set of μ_r and σ values applies consistently across the entire EMI UWB, for each of diverse bodies in varied dispositions and excitations.

Finite cylinders and plates

We show below that, for steel-like metal properties, solutions for finite cylinders and plates can be approximated well using other solutions we have developed, based on elongated or flattened spheroidal shapes. For non-magnetic materials, evaluation problems arise in the spheroidal solutions, and we therefore developed some generally adequate approximate analytical solutions. While the latter can be used in many cases for detailed solutions in the near field, we focus more on their use to determine the magnetic dipole moment induced in the scatterer. In the previous paragraphs, m_{sph} is the magnitude of the magnetic dipole moment of the sphere. We focus on its value as a scalar because it always has the same direction, i.e. that of the primary field at the location of the sphere. In general, however, an object may respond to an impinging magnetic field by generating a general vector magnetic dipole moment, with nonzero values in all three coordinate directions.

The dipole moment **m** can be used to represent the scatterer's response accurately when it is observed in the far field. In any case, it is a fundamental measure of the inherent scattering properties of a finite object, and frequently provides the same pattern of frequency response as the more complete solution that is needed in the near field as well. This is particularly true for homogeneous objects of modest size, such as clutter objects or portions of a UXO such as fins. Expressed as a vector, **m** registers the fundamental response in all component (coordinate) directions, when the object is subjected to any particular (locally uniform) primary field. In that sense, **m** is a function of

the primary field as well as of the scatterer's properties. If one computes **m** for unit values of the primary field in each coordinate direction, then the resulting set of three **m** vectors provides a fundamental measure of the scattering properties of the object. The complete vector far field response to any (locally uniform) primary field can be obtained from this set of three vectors. The eigenvalues of **m** represent the most fundamental, i.e. lowest order modes of response by the object, usually the strongest modes. Higher modes decay more quickly over space, as one moves away from the object.

The key to the new solutions presented in this section is the calculation of **m** using the fields within the object and on its surface, employing one or another of a variety of new ways developed under this project [33]. For reference below we provide one particular form, utilizing only fields internal to the object.

$$\mathbf{m} \quad = \quad \tfrac{1}{2}\int_{V} dV\, \mathbf{r}\times\mathbf{J} \quad + \quad \left(\mu_{\mathbf{r}} - 1\right)\int_{V} dV\, \mathbf{H} \tag{27}$$

where **r** is a position vector relative to any convenient reference point within the object, **J** is the internal induced electric current (A/m^2), and V is the volume of the object. As it stands, this relation is exact, assuming that the internal **J** and **H** fields are exact. However we wish to use it to compute **m** for finite objects by approximating the internal fields, because we don't know them exactly. In particular, we assume that the internal fields are the same, per unit length, area, or volume, as they would be for similar infinite objects. In using the exact solutions for infinite cylinders or plates in this way we avoid confronting the issues of the form of outer object boundaries or the possible non-uniformity of fields around those boundaries. We have shown that the failure to treat internal end effects causes unacceptable error for magnetic materials [34]; however this is not a factor in non-magnetic cases [35]. In any event, for the magnetic cases we can rely on our other solutions presented below. Therefore in what follows we restrict the application of (27) to non-magnetic cases ($\mu_r = 1$), so that the second integral drops out.

To proceed, consider the response of a uniform metallic plate, with thickness 2*a* in the Y direction and infinite extent in the other two directions (Figure 12). The sinusoidally oscillating, spatially uniform primary H field is oriented in the Z direction, ($\mathbf{H}^{PR} = \hat{\mathbf{z}}\, H^{PR}$, "into the page" in the figure), and in general H has only Z components.

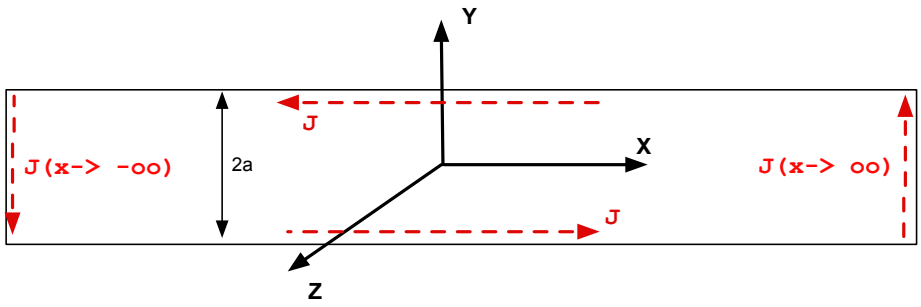

Figure 12. Schematic diagram of "parallel plate," infinite in the X and Z directions, with magnetic fields oriented only in the Z direction.

We call this the “parallel plate” case, because all magnetic fields are parallel to the sides of the plate. Within the main body of the plate, H will only have gradients in Y and thus only currents in the X direction. These currents will flow parallel to the plate’s surfaces, in opposing directions (anti-symmetrically) in the positive and negative Y regions. Note that this arrangement implies that the currents cross over at the plate’s ends, out of sight, so to speak, at positive and negative infinity in X. Our analysis pertains to the main body of the plate, away from its ends, though we will ultimately need to account for this crossing over of currents at the ends.

In general the solution for interior fields may be written as

$$H_z(y) = H_{zo}\left[e^{ik(a+y)} + e^{ik(a-y)}\right] \tag{28}$$

where the coefficient H_{zo} is to be determined. It is easily demonstrated that the secondary field along the sides of the plate is zero, i.e. for $|y| > 2a$. For an actual finite plate, however large its extent, secondary fields would emanate from the positive and negative Z ends. These secondary fields would form a magnetic dipole corresponding to the structure of the internal currents and fields, as reflected in (27).

Over the main side area of the plate, continuity of tangential H field implies that $H_z = H^{PR}$ for $|y| = a$; and the coefficient in (28) is readily evaluated to yield the solution

$$H_{zo} = \frac{H^{PR}}{1 + e^{ik\,2a}} \tag{29}$$

and thus

$$H_z(y) = H^{PR}\,\frac{\cos(ky)}{\cos(k\,a)} \tag{30}$$

The magnitude of cos(*k*y) in this expression typically increases exponentially, beyond the range of most computers, given the several orders of magnitude over which (complex) *ka* ranges. However an exponential factor may be extracted from both numerator and denominator; thus evaluation is not problematical, even for values of *ka* that confine induced activity to an extremely thin layer below the plate's surface.

To be useful, this solution must be manipulated to imply a secondary field beyond the ends of the plate in the Z direction. For this purpose we apply (27) as if the internal fields were uniform with respect to X and Z and normalize the dipole moment m_{pl} by the area of the plate.

$$\mathbf{m}_{pl} = \hat{\mathbf{z}}\,m_{pl} = 2\int_0^a dy\,(-\hat{\mathbf{z}})\,y\,\frac{\partial H_z}{\partial y} \tag{31}$$

Note that we have doubled the value of the integral. This must be done to account for the effects of the current crossings on the positive and negative ends of the plate in the X direction. While the end regions become vanishingly small relative to a limitlessly large plate, the currents across them must be of the same magnitude as those over the main plate region, by continuity (conservation of charge); and the long moment arm of these currents about the origin produces an effect equal to the X-directed currents over the main area of the plate. To see this note that, in a rectangular current loop, the current on each side produces the same contribution to the magnetic dipole moment of the loop, regardless of aspect ratio of the loop. For a given current, the moment depends only on the area of the loop, and all current segments contribute equally to that area, i.e. $A_{end} = A_{side}$ (Figure 13).

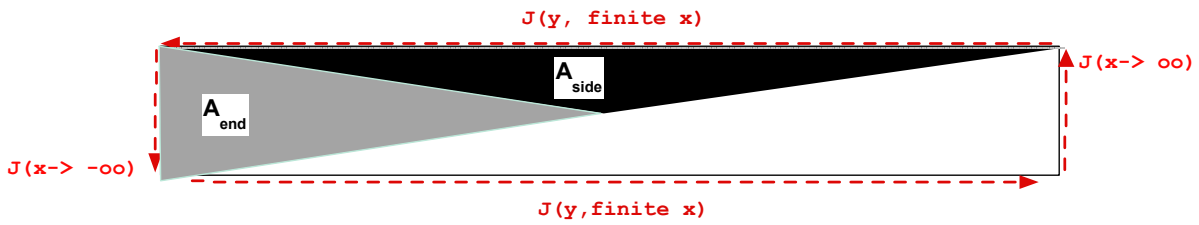

Figure 13. Cross section of a plate subjected to a primary magnetic field directed parallel to its sides, i.e. into the page, showing shaded areas that contribute equally to the induced dipole moment.

Carrying out the integrations yields

$$m_{\mathrm{pl}} = 2a\,\mathrm{H}^{\mathrm{PR}}\left\{\frac{\tan(ka)}{ka} - 1\right\} \tag{32}$$

Writing ka as $\gamma + i\gamma$, we may express the first term in brackets in (32) as

$$\frac{\tan(ka)}{ka} = \frac{i+1}{2\gamma}\left\{\frac{\mathrm{e}^{-2\gamma} - \mathrm{e}^{-2i\gamma}}{\mathrm{e}^{-2\gamma} + \mathrm{e}^{-2i\gamma}}\right\} \tag{33}$$

thus avoiding problems from exponential increase in factors within the numerator and denominator as γ becomes large. This form also provides directly the limiting values of the solution for magnetic dipole moment, namely $m_{\mathrm{pl}} \to -1 \quad as \quad \omega \to \infty$, $m_{\mathrm{pl}} \to 0 \quad as \quad \omega \to 0$, where the value of m_{pl} has been normalized by a factor of $\mathrm{H}^{\mathrm{PR}}\,2a$.

Figure 14 compares the solution (32) to rigorous and complete numerical solutions for circular disks, obtained using the MAS. Our approximate analytical solution presupposes no particular shape of the plate, but only characterizes it by its area and thickness. The circular disks in the MAS simulations were taken to have diameters 10 and 20 times the thickness. Regardless of the fact that two different disk aspect ratios were chosen, and the fact that they entail a circular geometry not drawn upon in the approximate analytical solution, their normalized solutions agree with one another and agree tolerably well with the approximate analytical result. This all implies that, for any broad non-magnetic plate (i.e. a body relatively wide in *both* transverse directions, as opposed to a

strip), its thickness is the controlling dimension for determination of the frequency response. We shall return to this in more specific tests below, using the MAS program and measured data. Equally notable in the figure is the fact that a plate thickness of an order that is reasonable for UXO fins, with handbook electrical parameters for stainless steel, produces essential signal features squarely in the MF-EMI range. Overall, results in this section show that, with negligible computational effort, the simple formula (32) can be used to estimate both the magnitude of secondary fields and the shape of the frequency response for non-magnetic parallel plates. On this basis and otherwise, we shall pursue a more detailed assessment of thin plate responses over the EMI UWB in Chapter 3.

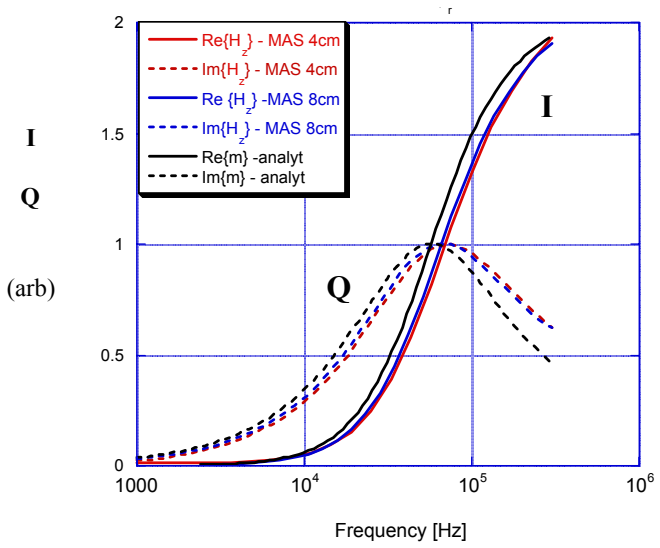

Figure 14. Normalized Inphase (I) and quadrature (Q) UWB EMI frequency responses from 4 mm thick stainless steel parallel plates ($\sigma = 1.4 \times 10^6$ S/m, $\mu_r = 1$), showing approximate analytical result (analyt) and MAS results for circular disks with two different diameters.

The Cylinder

Our detailed numerical simulations have shown that, under a transverse primary field, i.e. H^{PR} perpendicular to the cylinder axis, even a very short cylinder produces the same far field frequency response as an infinite cylinder (this is not the case for the axial orientation). Thus we may use solutions in the literature for the far field response of transverse infinite cylinders to compute the dipole moment per unit length of comparable finite cylinders. Using the $\exp\{+j\omega t\}$ time convention, Ward and Hohman [28] express the dipole moment as

$$m_{ctr} = H^{PR} a^2 \left\{ \frac{ka\,J_o(ka) - (\mu_r+1)J_1(ka)}{ka\,J_o(ka) + (\mu_r-1)J_1(ka)} \right\} \quad (34)$$

In practice, for $\mu_r > 1$, we would likely employ one of our other prolate spheroid solutions to obtain the response of a transverse elongated BOR, particularly in the near field. Be that as it may, for the far field and for the overall frequency response, (34) suffices.

For a cylinder subject to axial excitation (H^{PR} parallel to its axis, the Z axis) we must proceed in a manner similar to that in the previous section to obtain a dipole moment, viewed from some position beyond well beyond the ends of the cylinder. We will exploit the internal field solutions for a unit length of infinite cylinder, in axial orientation. As for the infinite plate, the secondary field alongside the cylinder is negligible; the only non-zero component of **H** is H_z and $H_z = H^{PR}$ on the surface $\rho = a$, where a is the cylinder radius. For the same reasons as before, relating to end effects, we must restrict ourselves to the non-magnetic $\mu_r = 1$ case. The solution may immediately be written as

$$H_z = H^{PR} \frac{J_o(k\rho)}{J_o(ka)} \quad (35)$$

where J_o is the zero order Bessel function of the first kind. To obtain the magnetic dipole moment, we again perform the integrations in (27), leading to

$$m_{cax} = H^{PR} 2\pi a^2 \frac{J_2(ka)}{J_o(ka)} \quad (36)$$

Figure 15 shows a comparison between the moment calculated using (36) and that obtained from full MAS solution. Agreement is generally good, from the low frequency limit up essentially to the high frequency asymptotic limit.

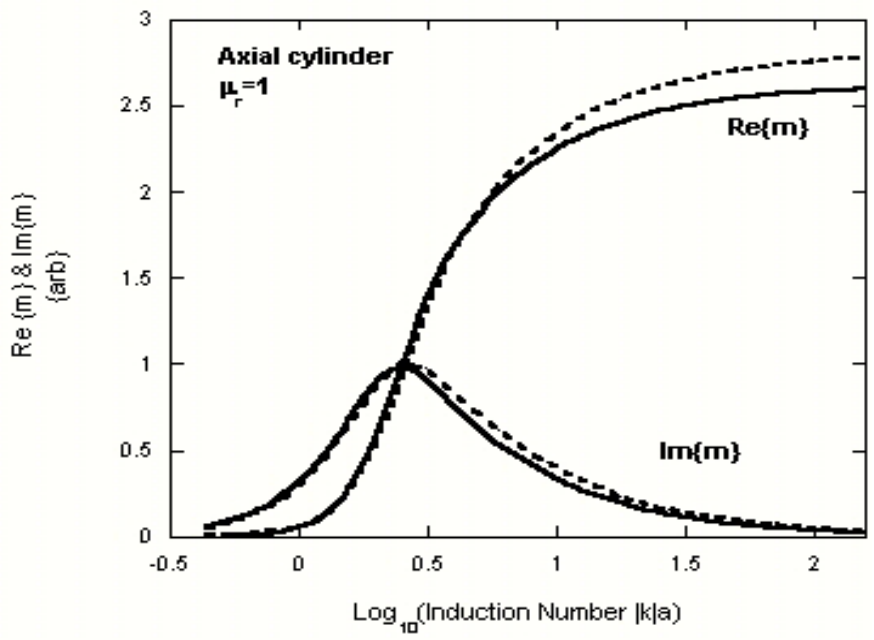

Figure 15. Comparison of approximate analytical solution for axially oriented, non-magnetic cylinder, with rigorous calculations using MAS algorithm

General Spheroids

Particularly for magnetic materials, we still require solutions valid in both near and far fields, for non-spherical shapes of arbitrary proportions. Our initial progress in this regard consisted of new analytical solutions for the axial orientation of a prolate spheroid [32, 33]. The approach ingeniously took advantage of the azimuthal symmetry of the problem to produce a scalar spheroidal wave function formulation. Here we present the more general, but more difficult vector spheroidal wave function formulation, which was completed more recently [36-38]. Figure 16 shows the geometry of oblate and prolate spheroids, and their relation to the general spheroidal coordinate system.

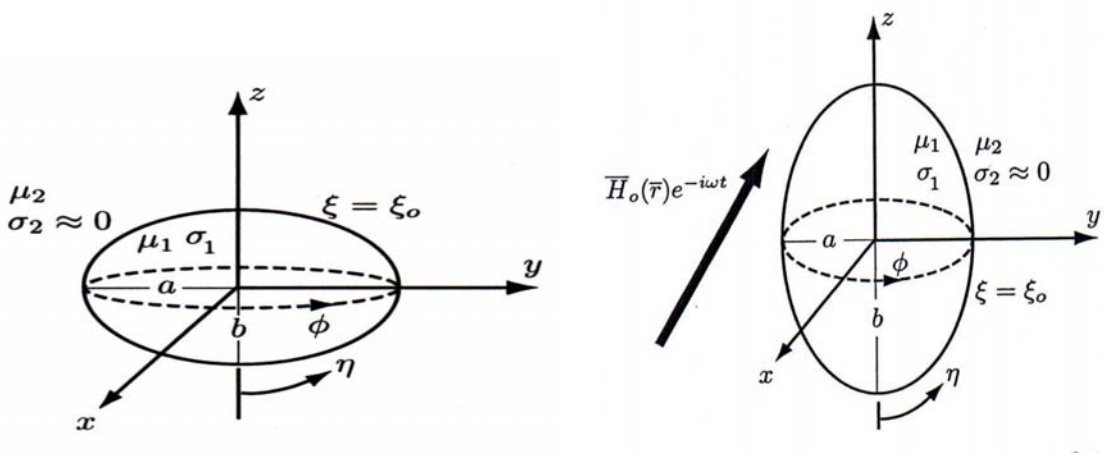

Figure 16. Geometry of an oblate spheroid (left) and prolate spheroid (right), with indication of the spheroidal coordinates (ξ,η,ϕ). We assume that μ_2 in the soil is equal to μ_o.

The rotational axis of symmetry coincides with the Z axis, and the cross sections of the object in the (X,Y) plane are circles of radius *a*. In keeping with the discussion in Section 2.1, the fields outside the object are expressed using scalar potentials, denoted ψ^{PR} for the primary field and ψ^{s} for the scattered field. For the prolate case,

$$\begin{aligned} \psi^{\mathrm{PR}}(\eta,\xi,\phi) &= \frac{H_o d}{2}\sum_{m=0}^{\infty}\sum_{n=m}^{\infty}\sum_{p=0}^{1} b_{pmn}\Phi^{(1)}(\eta,\xi,\phi) \\ \psi^{\mathrm{s}}(\eta,\xi,\phi) &= \frac{H_o d}{2}\sum_{m=0}^{\infty}\sum_{n=m}^{\infty}\sum_{p=0}^{1} B_{pmn}\Phi(\eta,\xi,\phi) \end{aligned} \tag{37}$$

where

$$\Phi^{(1)}(\eta,\xi,\phi) = P_n^m(\eta)P_n^m(\xi)\begin{cases}\cos m\phi, & p=0\\ \sin m\phi, & p=1\end{cases} \tag{38}$$

$$\Phi(\eta,\xi,\phi) = P_n^m(\eta)Q_n^m(\xi)\begin{cases}\cos m\phi, & p=0\\ \sin m\phi, & p=1\end{cases}$$

$P_n^m(\eta)$ and $Q_n^m(\xi)$ are Associated Legendre functions, and are readily evaluated. The oblate solution can be obtained from the prolate case by transformation, i.e. inserting certain well-established substitutions and equivalences. For example, for the oblate case, (37) becomes

$$\begin{aligned} \psi^{PR}(\eta,\xi,\phi) &= \frac{H_o d}{2}\sum_{m=0}^{\infty}\sum_{n=m}^{\infty}\sum_{p=0}^{1}\left(-ib_{pmn}\right)\Phi^{(1)}(\eta,i\xi,\phi) \\ \psi^{s}(\eta,\xi,\phi) &= \frac{H_o d}{2}\sum_{m=0}^{\infty}\sum_{n=m}^{\infty}\sum_{p=0}^{1}\left(-iB_{pmn}\right)\Phi(\eta,i\xi,\phi) \end{aligned} \tag{39}$$

Because the transformations from the prolate to oblate shapes do not present problematical considerations, we will just proceed below in terms of the prolate case. The coefficients b_{pmn} in these equations are known in the sense that they are calculated from the primary field, while the unknown B_{pmn} must be solved for. Obtaining the B_{pmn} constitutes solving the problem, given that the associated Legendre functions P_n^m and Q_n^m are readily evaluated. A set of b_{pmn} can be obtained for essentially any primary field. We have obtained and used them for uniform fields, dipole fields, and fields from actual experimental instrumentation (GEM-3).

Overall, while certain beneficial maneuvers had to be devised to complete the formulation, the basic scheme is straightforward. After expressing the interior fields in terms of series appropriate for the material properties in that domain, we match tangential H field components and normal B field components. Manipulations of those relationships provide the governing algebraic equations for the unknown coefficients in the series, and in principle the system can be solved. The challenge lies primarily in evaluating quantities pertaining to the interior of the object, where we express the magnetic field as

$$\mathbf{H} = \sum_{m=0}^{\infty}\sum_{n=m}^{\infty}\sum_{p=0}^{1}\left[A_{pnm}^{(M)}\mathbf{M}_{pmn}^{r(1)}(c_1;\eta,\xi,\phi) + A_{pnm}^{(N)}\mathbf{N}_{pmn}^{r(1)}(c_1;\eta,\xi,\phi)\right] \tag{40}$$

where $c_1 = kd/2$ and d is the interfocal distance, so c_1 is analogous to "ka" ; and, by definition

$$\left\{\begin{array}{l} \mathbf{M}_{pmn}^{r(1)} = \nabla\psi_{pmn}^{(1)}\times\mathbf{r} \\ \mathbf{N}_{pmn}^{r(1)} = \dfrac{1}{k}\nabla\times\mathbf{M}_{pmn}^{r(1)} \end{array}\right\}, \qquad \psi_{pmn}^{(1)} = S_{mn}(c_1;\eta)\,R_{mn}^{(1)}(c_1;\xi)\,T_{pm}(\phi) \tag{41}$$

where $T_{pm}(\phi)$ is $\sin(m\phi)$ or $\cos(m\phi)$, as in (38). Here the unknown coefficients are $A_{pnm}^{(M)}$ and $A_{pnm}^{(N)}$. By convention $S_{mn}(c_1;\eta)$ is called the angular function, and $R_{mn}^{(1)}(c_1;\xi)$ the radial function (first kind). It is the evaluation of these latter two functions over the relevant parameter range that makes the problem extremely difficult, such that authorities in the field at one time considered the problem intractable [29]. While much work has been done in evaluating spheroidal wave functions, for the most part it has involved only real arguments or quantities with small imaginary parts, or a limited range of values for the argument. In our case, c_1 is proportional to *k*, and as such has equal real and imaginary parts. Thus as the wavenumber increases, the locus of calculation proceeds out from the origin in the complex plane, on a 45^o line. And it is a very long line, given that the relevant *k* range spans perhaps four orders of magnitude.

Despite these challenges, solutions were obtained, valid over the entire frequency range of interest for modest degrees of elongation and for either non-magnetic or slightly magnetic materials [36-38]. Further, using small penetration approximations (SPA, next section below), a large class of additional cases was also solved [37,38]. Interestingly, these SPA solutions are applicable over the entire induction number range for high μ materials (e.g. steel), for both large and small elongation. This has far reaching importance. It means that extremely fast, accurate analytical solutions can be obtained for magnetic materials, for both elongated and flattened spheroidal shapes, using relatively simple algorithms, whatever the skin depth relative to the object's dimensions. Still, a certain "no mans land" remained, for cases with significant elongation, in the mid-induction numbers, for slightly magnetic materials. We have suggested ways to bridge this gap, using rational approximations that link up with the valid solutions in the high and low induction number regions [32, 33]. Since the completion of this project, all evaluation problems have been overcome, in follow-on work at MIT, also sponsored by SERDP.

2.4 Thin Skin Depth Approximations

In modeling work to elucidate the physics and phenomenology in the higher reaches of the EMI UWB, one quickly confronts some problems that have frustrated modelers heretofore. In fact, we shall see that these same problems await even those analysts attempting to avoid the high frequency end of the band. Overall, note that, as induction number increases, the skin depth in the target's metal decreases (see discussion of induction number and skin depth in Chapter 1). Modeling of EMI responses is very much complicated by this rapid internal decay of magnetic field changes that are imposed from outside the target. While penetration of the target can be complete, near the magneto-static limit, it will typically be slight or extremely slight over most of the EMI band and relevant parameter space. And though slight, the effect of this penetration also typically has a non-negligible effect on the scattered field.

Consider the requirements of modeling the essential internal fields using a domain method, e.g. finite difference or finite element method applied to differential equations. One would have to discretize the scatterer volume using numerical intervals below the target surface that are some fraction of the skin depth, while that scale is also frequency dependent. Based on the standard expressions in Chapter 1, the skin depth δ is on the order of $0.1/\sqrt{f\mu_r}$ (meters), where f denotes frequency (Hz) and we have assumed (reasonably) that the order of magnitude of σ is about 10^7 S/m. Even for a non-magnetic material, the greatest skin depths, i.e. for f ~ 10's or ~ 100 Hz, are only about a centimeter, and are only a few millimeters at about 1 kHz. Targets of interest are typically on the order of 0.1 m to 1 m. Worse yet, for a typical steel μ_r on the order of 100, the skin depth will range from only about 1 mm at 100 Hz down to an extremely small fraction of that up through the rest of the UWB. Lastly, as noted in Section 1.2, μ values typical of steel push the essential signal activity up into the higher induction number and into the higher frequency portions of the UWB. Altogether, this imposes very stringent mesh requirements indeed. It is for this reason that some recent modeling algorithms are not applied to magnetic materials. But we must treat those materials, over the entire UWB, to deal with the problem at hand.

Integral equation approaches, such as MoM, do not require meshes over the object interior. However, resorting to any of the various recognized integral equation formulations will not free us from the resolution problem. As has been noted for Method of Moments (MoM) and hybrid MoM formulations applied to this problem [7], one must use sufficient mesh refinement over the target

surface to resolve the Green function for the target's material. Because the Green function applied at a point on the scatterer surface decays as $\exp\{ikR\}$, where R is distance from the point on the surface, mesh resolution must be tighter than the skin depth. Failure to observe this constraint will mean that the Green function will decay virtually entirely between surface mesh point and another, and the points will not be numerically connected. Solutions will not be stable or will not be feasible at all, due to algorithmically singular matrices.

In general, trying to observe this resolution requirement will impose an enormous computational burden, for UWB simulation with arbitrary, realistic metal properties. For example, for the basic case of a sphere, responses approach high frequency asymptotic limits in the induction number region greater than about $\chi \sim 20\ \mu_r$. It has been suggested [7] that when penetration is only a small fraction of the target's characteristic dimensions, the resolution problem does not arise because the scatterer may be treated simply as a perfect reflector, with appropriate boundary condition on the external field. Unfortunately this is not so. Examination of the aforementioned analytical solutions for the sphere shows very significant (non-asymptotic) signal activity essentially all the way up to the $\chi \sim 20\ \mu_r$ domain. That is, the effects of volume currents and imperfectly conducting material are quite significant up to that induction number range. For steel with $\mu_r \sim 100$, a ratio of target size to skin depth of 10, 100, or even 1000 still does not take one into the induction number range above $\chi \sim 20\ \mu_r$ where the limiting, i.e. perfectly reflecting behavior occurs. The overall point is that, though the skin depth may be quite small in relative terms, its effect can still be quite significant, particularly for magnetic materials. Using the recommendation in the literature to the effect that mesh increments be $\sim \delta/10$ means that numerical surface element areas will be $\sim \delta^2/100$. The area of the sphere of radius a is $\sim 10\ a^2$. This means that, as one approaches $a/\delta \sim \chi \sim 20\ \mu_r$, approximately 4×10^8 surface elements would be required for adequate resolution, when $\mu_r = 100$. Fugheddaboudit! In recent numerical EMI work, using MoM or finite element - boundary element hybrid formulations, simulations are avoided over domains that entail these problematical constraints [9]. However, for full simulation capability over the whole UWB, we must in some way include the electromagnetic activity below the surface of the target in our model, over *all* regions of significant signal activity.

Not only is the level of numerical discretization cited above unlikely to be achieved, even with sophisticated measures to increase efficiency dramatically. It is unnecessary. In most cases we are primarily interested in the scattered field *outside* of the metallic object, which has only mild gradients relative to size of the object. Thus we seek to deal with the abovementioned challenges by

devising some simplifying treatment of the field inside the object or on its surface. In the high induction number range, tangential gradients of the internal field near the surface of the object are very much less than gradients normal to the surface. This suggests that the field structure inside of the object might be approximated locally as a 1-D field variation in the direction normal to the surface. That is, gradients normal to the surface locally dominate the gradient term in the interior governing equation (10), just inside its surface. For the normal field component, the 1-D solution corresponding to this is

$$\mathrm{H_n}\left(n\right) \approx \mathrm{H_n}\left(0^-\right)e^{ikn} \tag{42}$$

where $H_n(0^-)$ is the value of H_n on the inside of the surface, i.e. as n approaches zero from the interior; it is a function of location on the surface. We have developed a number of variations of techniques using this kind of assumption, in analytical and numerical solutions, applied to tangential field components or to normal components. All the approaches have in common the fact that they implement a Small Penetration Assumption (SPA,[37,38]) or Thin Skin Approximation (TSA[21-23]) by applying the gradient of an equation such as (42), then taking the limit as n approaches zero, i.e. approaching the scatterer's surface from the inside. That is,

$$\frac{\partial \mathrm{H_n}}{\partial \mathrm{n}}\left(0^-\right) \approx ikn\ \mathrm{H_n}(0^-) \tag{43}$$

To understand the implementation of these approximations, consider Figure 17. Beneath some patch of area on the object surface, A_{n+}, we construct a thin volume. The bounding lines of the volume along the surface may coincide with coordinate lines of some sort, in the analytical treatments, but in general need not do so. The figure shows only a schematic representation of some segment of the surface geometry, with curved surface and four edges, i.e. four lateral sides of the volume, A_{s1}, A_{s2}, A_{s3}, and A_{s4}. However these particulars are not essential. The surface patch may have piecewise flat subsections and the volume may have any number of lateral sides. The thin volume is constructed to have uniform thickness d, and the edge areas A_{si} are perpendicular to A_{n+}, so that the interior surface, A_{n-}, is parallel to A_{n+}. Thus the unit normal vectors along the edge areas, $\hat{\mathbf{s}}_i$, are tangential to the object surface.

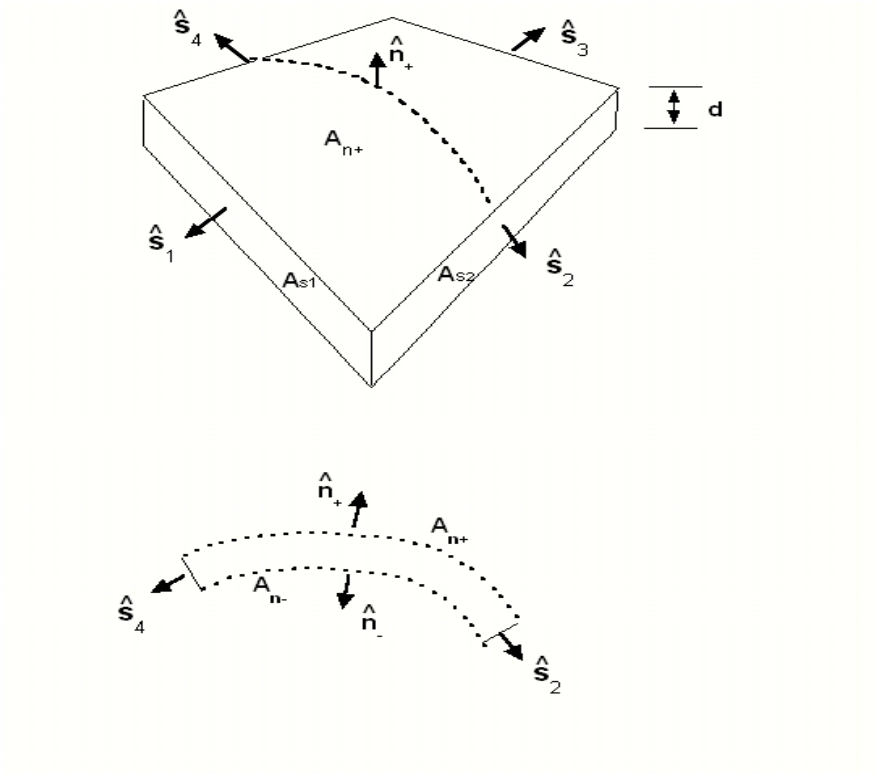

Figure 17. Top: Thin volume below a surface patch, where the outer surface of the object coincides with A_{n+} . Bottom: Cross section of the volume, normal to the surface, through the dotted line on A_{n+}.

While the double curl equation (12) may also be used to derive some versions of the method [37] here we illustrate it using the divergence equation (3), applied within the volume. The integral of (3) over the thin volume

$$\int_V dV \nabla \cdot \mathbf{H} = 0 \tag{44}$$

can be re-expressed with Gauss's theorem as

$$\langle H_{n+} \rangle A_{n+} + \langle H_{n-} \rangle A_{n-} + \sum \langle H_{sj} \rangle A_{sj} = 0 \tag{45}$$

where <> denotes an average value over the associated surface. Expressing the lateral side areas as a line length times their depth d in the n direction

$$A_{sj} = \ell_{sj}\, d \tag{46}$$

one then divides (45) by d and takes the limit as d approaches zero, i.e. as A_{n-} approaches A_{n+}, to obtain

$$H_n \frac{\partial A_n}{\partial n} + A_n \frac{\partial H_n}{\partial n} + \sum \langle H_{sj} \rangle \ell_{sj} = 0 \tag{47}$$

As the thickness d of the volume shrinks to zero, equation (47) contains only quantities pertaining to a point or patch on the (interior side of the) object's surface. Re-expressing $\partial H_n / \partial n$ using (43), then (47) removes the normal field derivative, so that the result contains only geometrical factors and field values on the interior of the object's surface. Each of these interior field values can be re-expressed in terms of corresponding exterior field values on the surface, using the standard electromagnetic interface conditions. Thus all interior electromagnetic activity has been absorbed into a boundary condition on the exterior **H** field components, and we need only solve the exterior problem.

How well does this method work? Figure 18 and Figure 19 show numerical simulation results for prolate and oblate spheroids at various μ_r values, subject to spatially uniform axial and transverse excitation, using a physically consistent sign convention with the $e^{+j\omega t}$ time factor. Results from a MoM-like boundary integral formulation using the TSA [21-23] are compared to those from the MAS, based on the full Maxwell equations. The quantity a in the induction number is always the smallest semi-minor axis of the object, and r is the distance to an observation point. By increasing r, we eventually reach a limiting set of curves (i.e. limiting values of r times **H**), tantamount to the dipole moment, which does not depend further on observation point. As some theoretical investigations suggest should be the case [22], we see that in the least the TSA algorithm does well for induction number (i.e. a/δ) values greater than about 20, even in the worst cases. This makes sense: the skin depth must be more than an order of magnitude smaller than a (small) characteristic dimension of the object. Most astonishing, however, is how well the TSA algorithm performs for high μ cases, as for steel, across the *entire* UWB. Even when some slight error appears in the middle of the band, note that the TSA still tends to converge to the proper static value, as ka approaches zero. Our theoretical analyses show why this is so [23], and reassure that it is not some sort of numerical

happenstance. Basically, the accuracy of the scattered field patterns depends on an interplay of how good the approximation (43) is, and how sensitive the system of equations is the quality of the approximation. High μ values move the region of high sensitivity into the higher induction numbers, where the approximation is more accurate. Further, the structure of the numerical formulation is such that, as *k* approaches zero, the formulation collapses to the proper static formulation, at least for simple shapes in a uniform field. Thus the correct low frequency limiting values are obtained. *These remarkable results suggest that, for steel-like properties, one can perform accurate 3-D simulations across the entire UWB, solving only an exterior scalar problem, with no greater mesh resolution than is needed to resolve the object's geometry.*

Similar procedures may be employed in analytical solutions for the prolate and oblate spheroids, by-passing much of the complexity or intractability of the complete solution, particularly at the high induction number end of the spectrum [37,38]. As noted, we term the approach the Small Penetration Approximation (SPA), to distinguish it from the strictly numerical TSA. A version of the SPA using the divergence equation in the object interior has been developed, along the lines of the material above, but taking some advantage of the specific geometry and coordinate system of the spheroids. Here we give a few details for an alternative rendition, more accurate over the middle LF frequencies, in which the same kind of thinking behind (43) is applied to the *tangential* field components, producing a similar algebraic problem in the end. After various appropriate simplifications of the governing double-curl equation, application of the basic SPA, and reduction of the system using testing functions from the original basis, one obtains a governing algebraic system

$$\frac{ic_1}{\mu_r} B_{pmn'} \frac{dQ_{n'}^m}{d\xi_o} - \frac{1}{\xi_o^2 - 1} \sum_{n=m}^{\infty} B_{pmn} Q_n^m(\xi_o) \Gamma_m(n', n)$$

$$= \frac{ic_1}{\mu_r} b_{pmn'} \frac{dP_{n'}^m}{d\xi_o} + \frac{1}{\xi_o^2 - 1} \sum_{n=m}^{\infty} b_{pmn} P_n^m(\xi_o) \Gamma_m(n', n) \tag{48}$$

where p, m, and n' are free indices. The function $\Gamma_m(n', n)$ only involves straightforward algebraic expressions and quantities related to the spheroidal coordinate system or Associated Legendre Functions. That is, *one can evaluate all the necessary expressions using only simple programming with library functions typically available in current systems libraries*. No spheroidal wave functions are involved. While one must still ultimately solve a matrix equation (i.e. (48)), the matrix is

typically quite small, of order perhaps 35 to 70. This means that one can obtain extremely fast, accurate, and easily programmed analytical solutions, for steel-like properties, across the entire EMI UWB. Some user-friendly programs employing the method, produced during this project, are now publicly available.

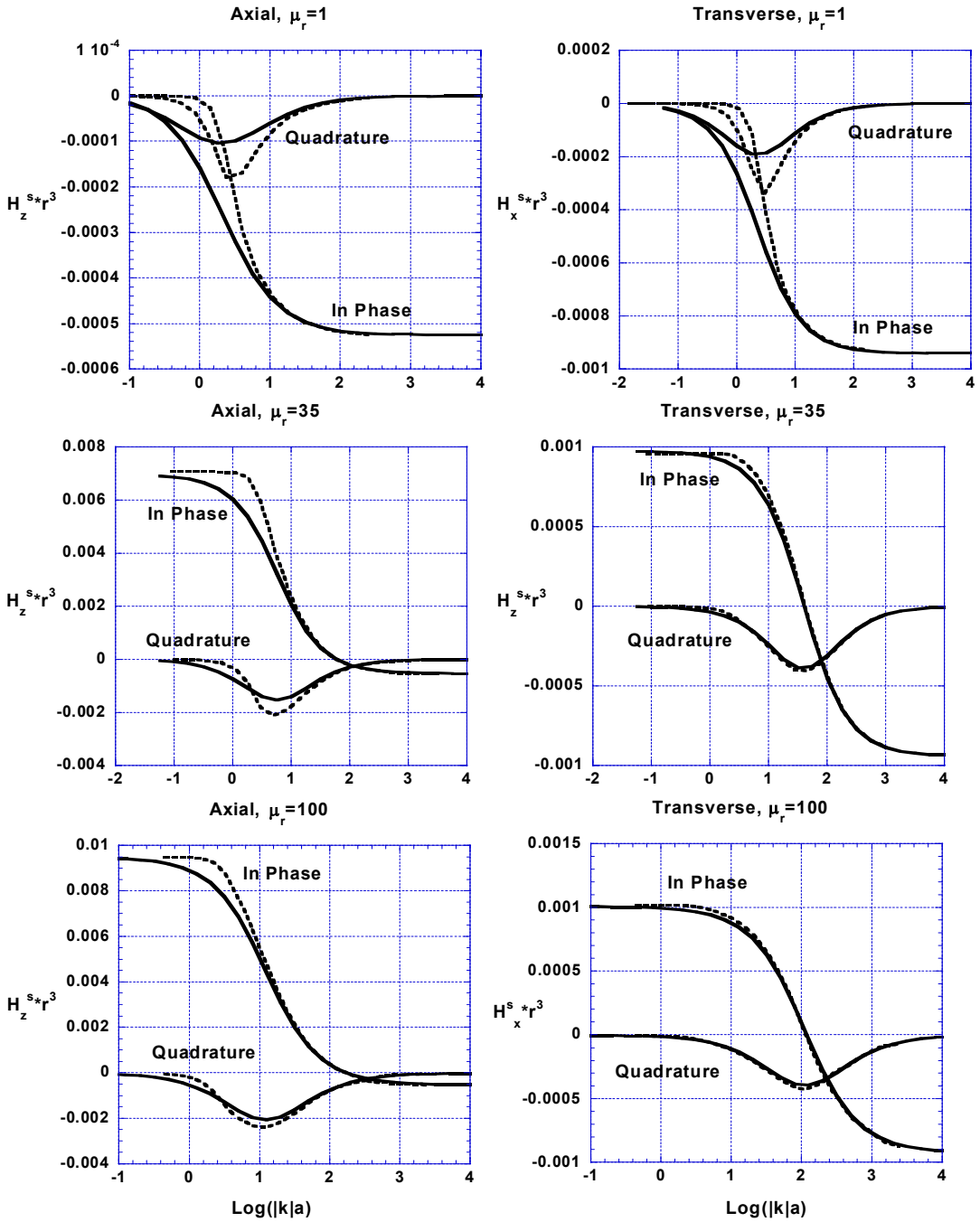

Figure 18. UWB frequency response for 1 x 6 prolate spheroid, with solid lines for TSA results and dashed lines for MAS, units on vertical axis are (A m2).

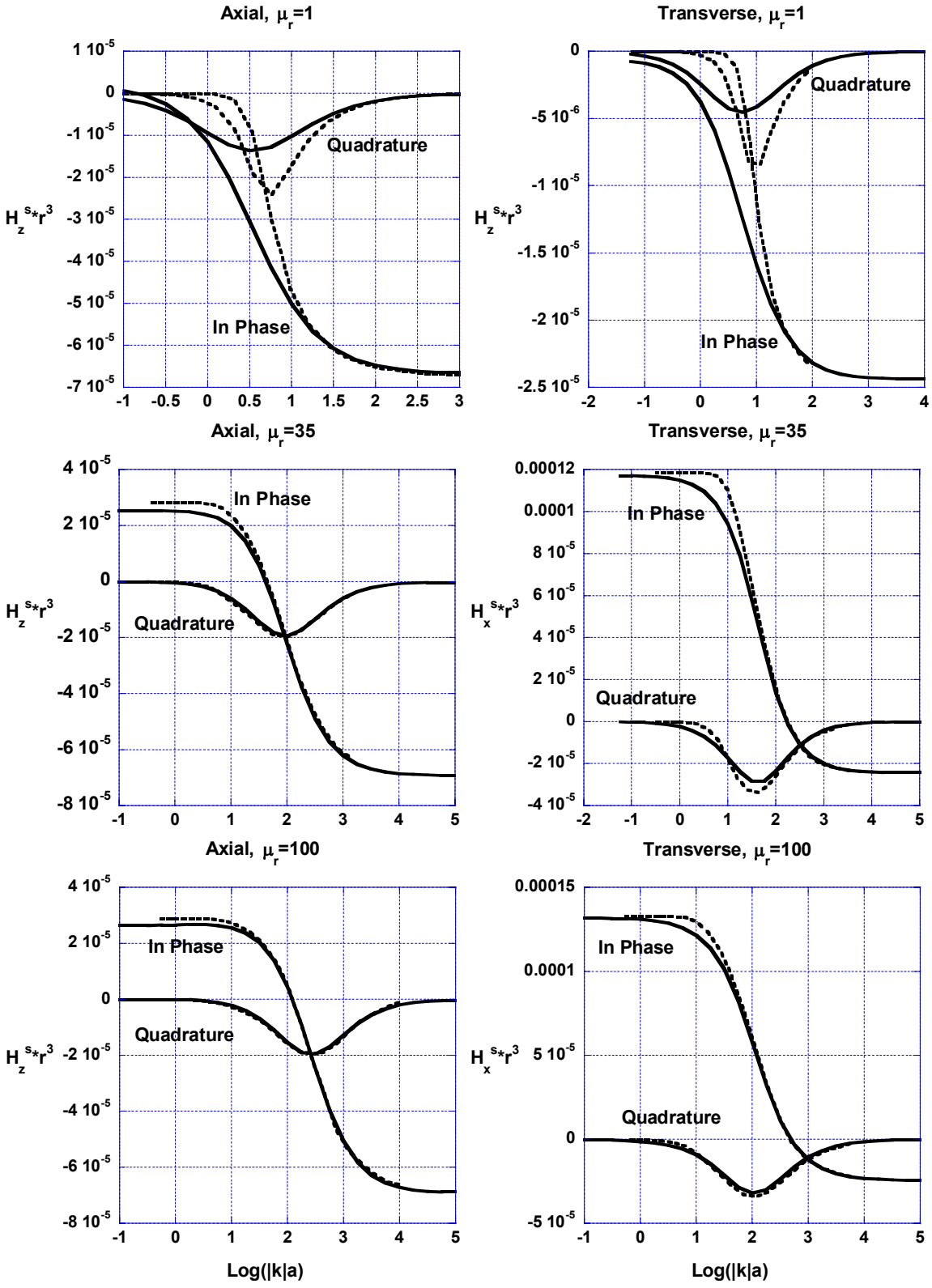

Figure 19. UWB frequency response for 4x1 oblate spheroid, with solid lines for TSA results and dashed lines for MAS. Units on vertical axis are (A m2).

2.5 Translation of Results from Frequency to Time Domain (TD)

Occasionally in what follows we will indicate some specific implications in the time domain for content that has been developed in the frequency domain. However for the most part we will proceed in terms of the frequency domain (FD). The pro's and con's of FD vs TD can be debated, in both measurements technology and associated signal analysis. In the latter realm, we prefer FD for a variety of reasons. 1) The resulting data and patterns therein seem to us to be richer and more revealing: fundamental signal character, peak frequencies and dominant modes are often more apparent; important limiting or asymptotic values can be identified at extreme ends of the spectrum; and inphase and quadrature components can be tracked, as well as their relationship, containing important indications of physical mechanisms underlying the response. 2) TD systems entail a particular input spectrum resulting from the square-wave primary field pattern, which may not provide good representation of important phenomena over all areas of the spectrum,; and 3) All the information that would be seen in the available TD signals is present in our FD results - and more. Each spectral pattern discussed below can be translated readily into TD equivalent by inverse Fourier transformation, as detailed in this section. Further, the frequently range successfully attained in this project allow us to use such translation to infer TD results at both much earlier and much later times than has been possible via direct TD measurement. Our UWB EMI spectrum ranges from a few Hz up to some 100's of kHz. This corresponds to time ranges on the order of tenths of a second on the one end, down to microseconds on the other. As discussed in other sections of this report, various signal parameters in the high frequency/ very early time and low frequency/ very late time regimes hold significant discrimination potential. Typically, the TD measurement systems can't shut off the transmitted signal fast enough to catch the very early time response, and also can't record signals long enough to obtain the very late time record. We have noted that progress is being made in pushing the frontiers in TD, and we watch such development with interest. Even if an extreme time range of measurement is ultimately, we still prefer to examine the implications of the data through a FD rendering of it, for the reasons mentioned above.

To assist in the FD-TD translation, we pursue a few alternative analytical maneuvers geared specifically towards translating the general FD results into corresponding responses that would be obtained for the specific input pattern that is typical of time domain devices. In particular, most TD devices first transmit a constant magnetic field, until the target and environment are "saturated." Then the transmission is terminated, and the receiver is turned on. The sudden withdrawal of the

supporting transmitted field causes the magnetic field in the target to collapse, but with resistance. That is, swirling eddy current loops form on the metal surface, to maintain compatibility between conditions inside and outside the object. These gradually diffuse into the object interior, slowing and weakening. Eventually they penetrate the object completely, circulating ever more slowly, until all activity ceases. Then the receiver is shut off and the transmitter is again activated, and the process is repeated. Simply put, the primary field input from the TD device consists essentially of a repeated step function, which we will construe here as a downward step from unity to zero. The sensor signals constitute measurements of the fields produced by the response to this that is induced in the object.

The EMI response spectra typically shown for UXO related work are essentially the impulse response I(f) of some object, that is, I(f) is the response that would be obtained if all possible frequencies were transmitted with equal amplitude. (Note a certain historical inconsistency in notation: Above and in much of the current literature, I and Q are used for the frequency domain inphase and quadrature components, represented below and in some of the literature as M and N, respectively, while I below denotes the impulse response. Use of this (M,N) convention is employed only in this subsection). By convention this is written

$$I(f) = M(f) - i\,N(f), \qquad \textit{where} \quad M(-f) = M(f) \qquad N(-f) = -N(f) \tag{49}$$

The latter two equalities must hold because the ultimate signal must be real valued, hence the negative frequency spectrum must be the complex conjugate of the positive spectrum. Because this is understood, we normally only examine the more physically intuitive positive frequency spectrum, as shown in Figure 2. Note that one typically obtains these spectra in terms of data at discrete points, so that the analytical maneuvers in what follows presuppose either interpolation between the points or, better, some kind of simple function fitting.

Let's consider the general case in which the actual primary field is not a perfect impulse, with a perfectly flat spectrum, but rather has some Fourier transform P(f). Then the spectrum of the response will be the impulse response weighted, frequency by frequency, by the value of the actual input spectrum. That is, the actual response spectrum will be simply I(f) P(f), with the time domain equivalent expressed by IFT as

$$H(t) \;=\; \int_{-\infty}^{\infty} df\, I(f)\, P(f)\; e^{i\,2\pi ft} \;=\; 2\int_{-\infty}^{\infty} df\; Re\left\{ I(f)\, P(f)\; e^{i\,2\pi ft} \right\} \tag{50}$$

in which, as through the rest of this section, we assume an $e^{i\omega t}$ time factor, for consistency with historical Fourier Transform expressions. When the input equals a downward unit step in time, U_o, then

$$P(t) \;=\; U_o(t) \;=\; \left\{ \begin{matrix} 1, & t < 0 \\ 0, & t \geq 0 \end{matrix} \right\}, \qquad P(f) \;=\; U_o(f) \;=\; \frac{1}{2}\delta(f) \;+\; \frac{i}{2\pi f} \tag{51}$$

Evaluation of the integral in (50) involving the delta function is immediate, and we focus on the more challenging portion involving the singularity 1/f, with a lower integration limit of zero. This part of the integral may be written

$$H_t(t) \;=\; 2\int_0^{\infty} \frac{df}{f} \left\{ N(f)\cos(2\pi ft) - M(f)\sin(2\pi ft) \right\} \tag{52}$$

One approach to this integral is to write $M(f) = M_o + M_1(f)$, where M_o is a constant offset; then express $M_1(f)$ and $N(f)$ in terms of sine series, and thus cast all integrations into terms of cosine transforms, sine transforms, and direct integrals of the *sinc* function, where *sinc*(x) is defined as *sin*(πx)/πx. These are readily evaluated. The drawback of this approach derives from the fact that, against a linear f scale, M(f) and N(f) rise extremely steeply near zero frequency. It will typically be quite difficult to obtain sine series for M and N that apply over the whole domain and yet do not overshoot near the steep part of their curves (Gibbs phenomenon). Nevertheless, if one obtains adequate sinusoidal series in linear f for M and N, the problem can be solved.

An alternative method is inspired by the observation that the typical impulse responses are quite smooth, tame functions relative to ln(f), see Figure 2. Thus we use the variable transformation $v = \ln(f)$ to recast (52) as

$$H_t(t) \;=\; 2\int_{-\infty}^{\infty} dv \left\{ N(v)\cos(2\pi t\, e^{v}) - M(v)\sin(2\pi t\, e^{v}) \right\} \tag{53}$$

This succeeds in eliminating the singularity altogether; further, sine and cosine series for M(v) and N(v) are much easier to obtain relative to v. Because N(f) is typically negligible and M(f) constant at frequencies less than 1, the entire negative frequency region of the integral can probably be well approximated by

$$\int_{-\infty}^{0} dv\, M(v)\, \sin(2\pi t\, e^{v}) \quad \square \quad 2\pi t\, M_o \int_{0}^{1} df\, sinc(ft) \tag{54}$$

leaving only the positive v region to be dealt with, with all integrands containing readily evaluated sine and cosine functions. However one pays for the benefits of the transformation of variables by the appearance of e^v in the arguments of two of the factors. As v increases, these factors oscillate more and more rapidly. Either some sort of asymptotics must be employed, or at least sufficient brute force quadrature to evaluate the integrals without accumulation of too much error over many, many cycles. Again, with sufficient resourcefulness, this can be accomplished. Clever evaluators will note that high e^v factors should only be influential for low t values, and high t factors should only engage relatively low values of e^v in the arguments. Thus, overall, really attentive quadrature is only necessary over tolerable ranges of the complete argument $2\pi t\, e^{v}$.

A third alternative probably combines the best features of the approaches above; we recommend this approach and provide a computer program to implement it as part of this report. In this approach, M and N are fit by simple functions over finite intervals in linear f, in each of which the integrations can be carried out easily and exactly. First we must presuppose that the user supplies data for M(f) and N(f) containing sufficient low frequency resolution to allow smooth polynomial fitting between sets of each 3 adjacent frequency points. In measurement practice with the GEM-3 this has always been possible, and in simulation we can specify any such resolution. Writing the integral (52) as a summation over subdomains between f_{i-1} and f_{i+1} produces

$$H_1(t) = \frac{1}{\pi} \sum_{i=2}^{n-1} \int_{f_{i-1}}^{f_{i+1}} \frac{M(f)}{f} \sin(2\pi ft) df - \frac{1}{\pi} \sum_{i=2}^{n-1} \int_{f_{i-1}}^{f_{i+1}} \frac{N(f)}{f} \cos(2\pi ft) df \tag{55}$$

Approximating M and N as

$$M(f) = A_m f^2 + B_m f + C_m$$
$$N(f) = A_n f^2 + B_n f + C_n \tag{56}$$

yields tractable integrals over each [f_{i-1}, f_{i+1}] interval. For the terms involving M:

$$\int_{f_{i-1}}^{f_{i+1}} \frac{f^2 \sin(2\pi ft)}{f} df = \left\{ -\frac{f}{2\pi t}\cos(2\pi ft) - \frac{1}{4\pi^2 t^2}\sin(2\pi ft) \right\}\Bigg|_{f_{i-1}}^{f_{i+1}} \tag{57}$$

$$\int_{f_{i-1}}^{f_{i+1}} \frac{f \sin(2\pi ft)}{f} df = -\left\{ \frac{1}{2\pi t}\cos(2\pi ft) \right\}\Bigg|_{f_{i-1}}^{f_{i+1}} \tag{58}$$

and

$$\int_{f_{i-1}}^{f_{i+1}} \frac{\sin(2\pi ft)}{f} df = \pi \int_{x_{i-1}}^{x_{i+1}} \mathrm{sinc}(x)\, dx \tag{59}$$

can be calculated from typical function libraries, by simple quadrature, or by series:

$$\pi \int \mathrm{sinc}(x)\, dx = \sum_{n=1}^{\infty} (-1)^{n-1} \frac{(\pi x)^{2n-1}}{(2n-1)\cdot(2n-1)!} \tag{60}$$

For the terms involving N:

$$\int_{f_{i-1}}^{f_{i+1}} \frac{f^2 \cos(2\pi ft)}{f} df = \left\{ \frac{f}{2\pi t}\sin(2\pi ft) + \frac{1}{4\pi^2 t^2}\cos(2\pi ft) \right\}\Bigg|_{f_{i-1}}^{f_{i+1}} \tag{61}$$

$$\int_{f_{i-1}}^{f_{i+1}} \frac{fco\mathrm{s}(2\pi ft)}{f} df \quad = \quad \left\{ \frac{1}{2\pi t} \sin(2\pi ft) \right\} \Bigg|_{f_{i-1}}^{f_{i+1}} \tag{62}$$

$$\int_{f_{i-1}}^{f_{i+1}} \frac{co\mathrm{s}(2\pi ft)}{f} df \quad = \quad \int_{x_{i-1}}^{x_{i+1}} \frac{\cos(x)}{x} dx \quad = \quad \left[\ln(x) + \sum_{n=1}^{\infty} (-1)^n \frac{x^{2n}}{2n \cdot (2n)!} \right]_{x_{i-1}}^{x_{i+1}} \tag{63}$$

where, again, the last integral can also easily be evaluated by quadrature or use of mathematical library packages. Note that, for small f, $I(f) \sim C_m$, so that only the *sinc* integral in (59) need be treated, eliminating problems with the singularity. In practice, one may simply integrate down to a very low but finite frequency. Approaching the singularity or choosing relatively large intervals [f_{i-1}, f_{i+1}] over which the sinusoids oscillate intensely does not pose any problem here, because all the integrals may be evaluated analytically or via very tractable expressions.

3. UWB RESULTS AND ANALYSIS

3.1 Factors That Determine Spectral Response Properties, From Low to High Frequency Limits

Gross Size

The EMI response from a sphere furnishes a good general idea of the pattern of response associated with the sheer size and the electromagnetic properties of a metallic target, that is, without significant influence from fine features or directional characteristics. We demonstrate below that, even in the MF-EMI region, fine surface features (as opposed to thin elements) have little effect on the spectral response. This means that, more than not, we may take the sphere response to be reasonably representative of that from any compact object of the same material. By "compact" we mean that the object lacks predominant elongation in any particular direction. The lines in Figure 20 show the quadrature component of the sphere dipole moment, vs induction number. This compresses all Q information for the sphere into a single plot. Figure 21 provides explicit translation into size and electrical properties vs frequency, for some representative dimensional examples.

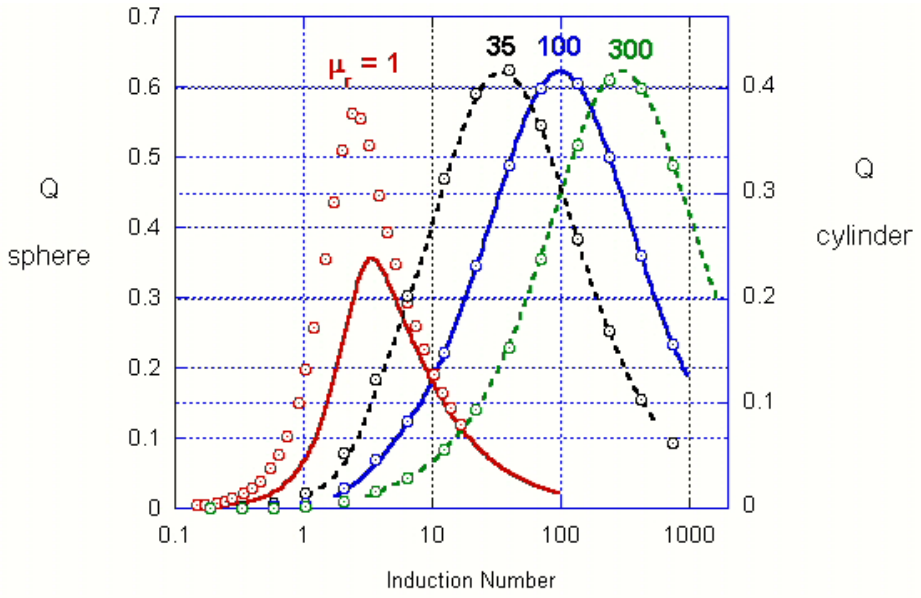

Figure 20. Quadrature component of frequency responses for the sphere (lines) and transverse infinite cylinder (markers), vs induction number, for different values of μ_r.

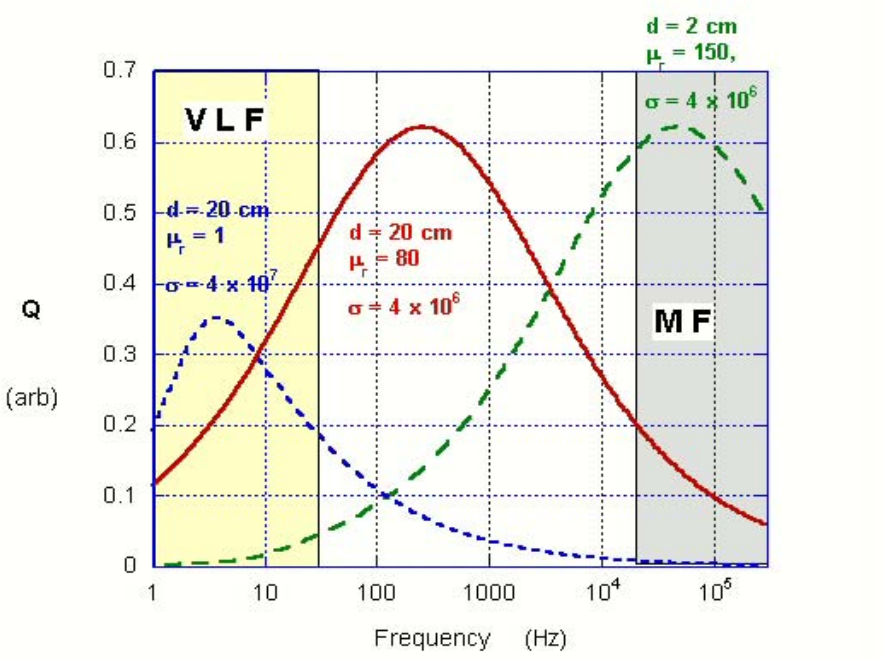

Figure 21. Quadrature responses from spheres with different properties and diameters *d*, relative to the full EMI UWB.

Recall that induction number χ may be written

$$\chi = \left[a\sqrt{2\pi\sigma\mu} \right] \sqrt{f} \tag{64}$$

where, to emphasize the effect on frequency range, we have grouped the other factors together. Increasing σ will shift the curves to the *left*, i.e. into a lower frequency region. If its only effect were through the induction number, increasing μ would also shift the curves to the left. However, independent effects of μ overbalance this influence. Increases in μ shift the curves to the right, into higher frequencies, in a manner similar to the effect of μ on the pattern relative to χ. Increasing the radius or characteristic dimension *a* shifts the curves to the left, linearly in proportion to the square root of *f*.

Bearing these patterns of influence in mind, one gains some assessment of the relation between gross object characteristics and frequency locale of response by pondering Figure 21. A

relatively large object made of a high conductivity, low permeability metal (e.g. copper) will produce responses squarely in the VLF range. At the other extreme, a relatively small, lower conductivity, high permeability object produces its response squarely in the MF region. The parameters chosen in the second case correspond roughly to those that might apply to a 20 mm UXO, and indeed measurements show responses for such ordnance in this range (see below). Note particularly that halving or doubling *a* does not take the frequency locale of response for these items out of the VLF or MF regions, respectively. Even if shifts in these parameters take the much of the Q pattern out of these regions, without the additional VL or MF information it would be difficult to locate the peak very well. Also, one wouldn't be able to define the shape of the Q curve. See discussion below on symmetry of the Q curve, aspect ratio inference, and interference between signals from high frequency and low frequency targets (Sections 3.2 and 3.4).

For *magnetic* objects of interest here, it's unlikely that *gross size alone* will cause the main portion of the Q response to be in the VLF region. This is illustrated by the middle curve in Figure 21. Assuming "typical" steel parameters for a rather large object, we see a significant portion of the curve still appears in the VLF. However one can at least locate the Q peak rather well and infer much of its shape without VLF information. To define the asymptotic limit of the inphase response, however, one is very likely to need the VLF range. In one orientation or another, most magnetic objects of interest are likely to produce inphase curves between the two shown in Figure 22. The curves for the real part of the dipole moment are effectively normalized, so that they both converge to(wards) -2 as *f* approaches zero. However to infer the actual (non-normalized) low frequency asymptote for arbitrary, compact magnetic bodies, we generally need to see sufficient indication that the low frequency part of the curve is flattening out. This will frequently require VLF information. While simple dependencies cannot be stated, overall the magnitude of the low frequency limit is strongly influenced by magnetic content and object elongation (see the following sub-Section). At the same time, the high frequency limit depends on quite different fundamental properties, i.e. only on shape, and the relation (e.g. crossing) of the inphase and quadrature components relates magnetic content, elongation, and axial vs transverse orientation. Figure 22 and the preceding material show that, for a range of gross sizes and material parameters characteristic of UXO, any processing system that fails to access the complete UWB picture will lack some of the most fundamental response information on which classification can be based.

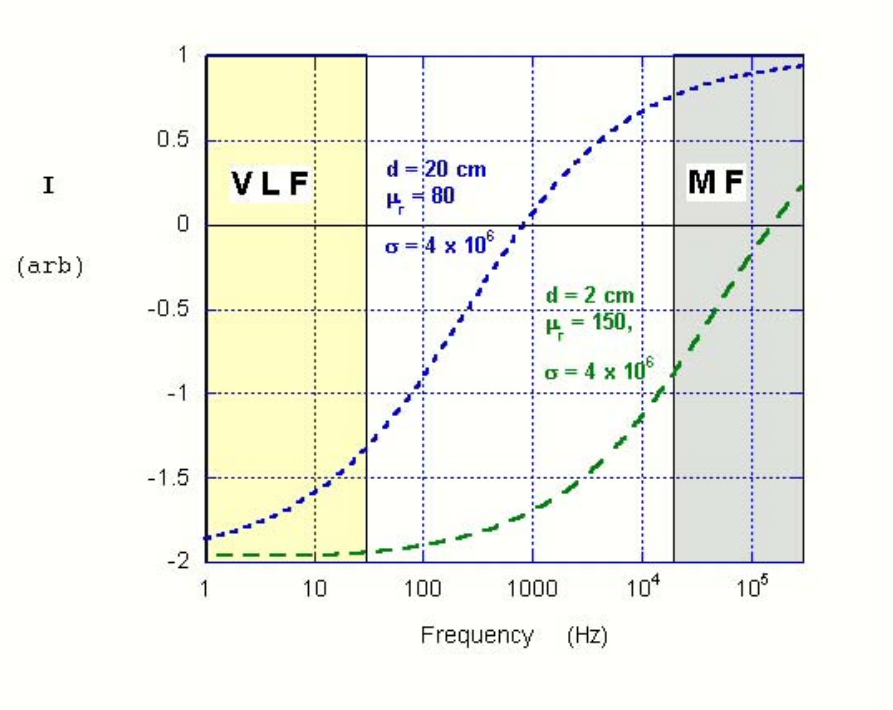

Figure 22. Inphase response patterns for the two magnetic cases in Figure 21.

While the results above apply to "compact" objects, they also pertain to an elongated object when the primary field impinges on its sides, i.e. on anything generally cylindrical in shape, in transverse orientation. Figure 20 shows markers for Q solutions based on (34) for the infinite circular cylinder in transverse orientation. In this orientation, the infinite cylinder provides a good guide to the frequency response of even rather short finite length cylinders. Even for the $\mu_r = 1$ case, the locations of the peaks for the sphere and transverse cylinder are close. And clearly, as soon as μ_r is significantly greater than 1, the normalized sphere and cylinder curves coincide. Detailed numerical investigations show this to be the case for transverse orientations of other elongated BOR's. See [16] and Section 3.1. It will even be the case for a cylinder with square transverse cross section, with any rotation about its long axis. Despite its angularity, the transverse square cylinder will still produce approximately the same results as the circular cylinder; and similarly the cube will produce the same general response as a sphere of comparable size. Figure 23 shows the secondary field from a cube, with both the uniform, unit magnitude primary field and observation direction oriented at various angles in the XoZ plane, where the coordinate axes are perpendicular to the cube faces. The cube is 20 cm on each side and the observation point is a meter from the center of the cube. Clearly the response changes little as a function of angle of view. Response from a sphere large enough to

circumscribe the cube, with the same material properties, clearly has about the same frequency range of response (Figure 24).

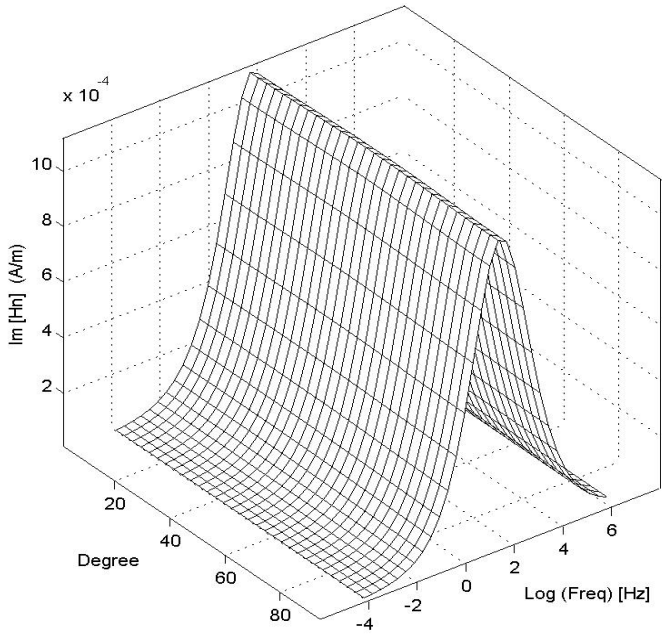

Figure 23. Quadrature response of a 20 cm square cube, as a function of angle of primary field in the X0Z plane, for $\sigma = 10^7$ S/m, $\mu_r = 150$.

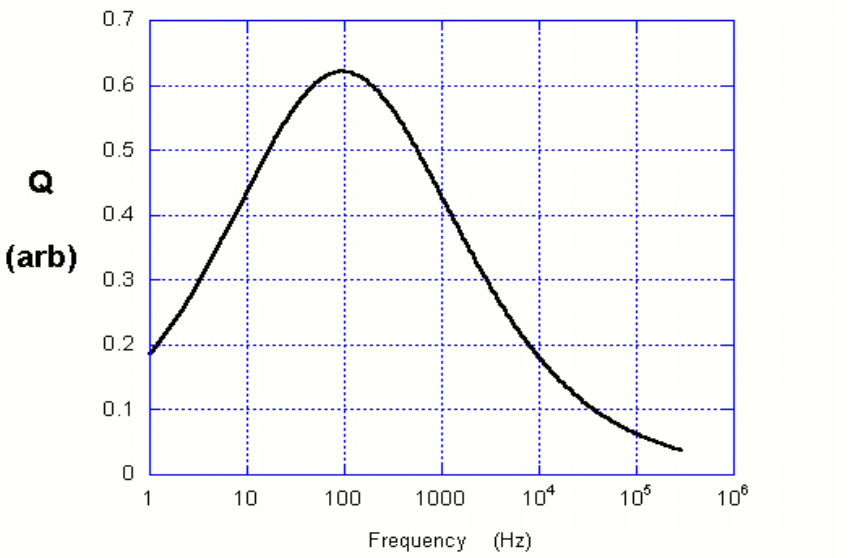

Figure 24. Normalized response from a sphere of about the same size as the cube in Figure 23, with same material properties.

For more in this connection, the reader is referred to the discussion in Sections 3.1 and 3.2 on the effects of fine features, surface detail, and shape/elongation, some results of which we anticipate here for the following generalization: A*s long as a single characteristic length is the only controlling dimension of the response*, we expect the conclusions in this section regarding the frequency range of response to apply. The emphasis in the preceding sentence is designed to foster caution in application to plates and rods, where *for magnetic materials* the still central role of the transverse dimension can be modified by the body's length in the axial or "parallel" direction. While this and other basic spectral effects of thickness and length, aspect ratio, orientation, and material properties are explored below, to illustrate our caution here we just note the results in Figure 25, obtained using the SPA algorithm (Section 2.4).

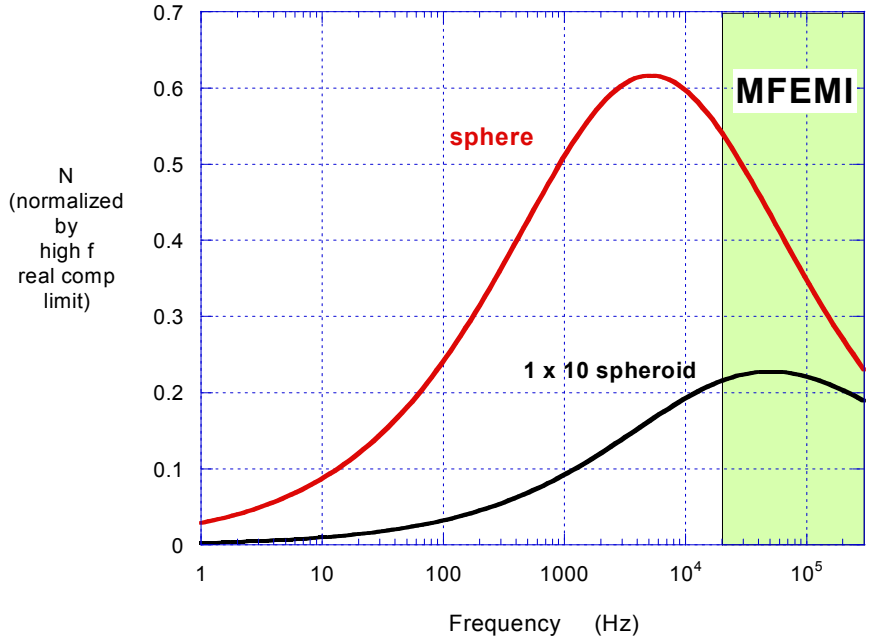

Figure 25. Analytically computed axial (broadside) responses of spheroids 5 cm in diameter, μ_r = 100, $\sigma = 5 \times 10^6$ S/m, for a perfectly spherical and a flattened (oblate) shape.

For the cases in this figure, both the sphere and spheroid have the same diameter "facing" the sensor. Induction tends to excite strongest currents towards the outer edges of the body, more or less in a plane perpendicular to the direction of the primary field. In the sphere, the currents on the poles (facing towards and away from the sensor) have very small magnitudes and moment arms, hence they have very little influence on the dipole moment near resonance. Both maximum currents and current

moments are produced near the "equator." These currents determine the Q component. All this might lead one to expect approximately the same resonance pattern for the sphere and for the oblate spheroid under axial (broadside) excitation, with the same diameter. Both would seem likely to produce dominant current rings of about the same radii and hence the same resonant frequency. However for the flattened shape the responses are modified by the role of a second dimension, namely the thickness. With steel-like properties, the 5 cm diameter sphere shows a resonant peak at a few kHz, whereas the 5 cm diameter oblate spheroid with 1 x 10 aspect ratio resonates squarely in the MF-EMI range.

Spectral Effects of Basic Shape and Material Properties

We have already shown above that the response of a long *transverse* cylinder behaves very much like that of a sphere. This is true more or less regardless of degree of elongation. Here we look at the effect of degree of elongation and of permeability for axial excitation of cylinders, all 5 cm in diameter. The effect of electrical conductivity is not considered separately, because its influence is relatively simple in every orientation, primarily shifting the response spectrum as noted above. Consideration of a short cylinder under axial illustration serves to illustrate further the assertions made above regarding "compact" objects. In particular, Figure 26 shows that for this case one sees the same sensitivity to μ as for a sphere, in that increasing permeability drives up the frequency of its region of peak response. The reverse is true for an elongated cylinder (Figure 27), for which higher μ drives its response down in frequency. In addition, Figure 28 shows that increasing the elongation of a magnetic cylinder also lowers its range of peak response. These two factors together can thus easily conspire to produce significant responses in the VLF range, for axial orientations or elongated objects. Detailed examination of results over very large parameter ranges shows that, at least in the case of μ, the trends shown in these figures continue for more extreme parameter values, e.g. $\mu_r \sim$ 1,000 and 10,000, etc. That is the trend in response to log(μ) extends out indefinitely. However, for our purposes, best served by the linear scale for μ_r and the limits shown, the trends flatten out, both with respect to μ_r and elongation. Overall, for aspect ratios greater than about 6, the spectral behavior approaches that of the infinitely elongated case.

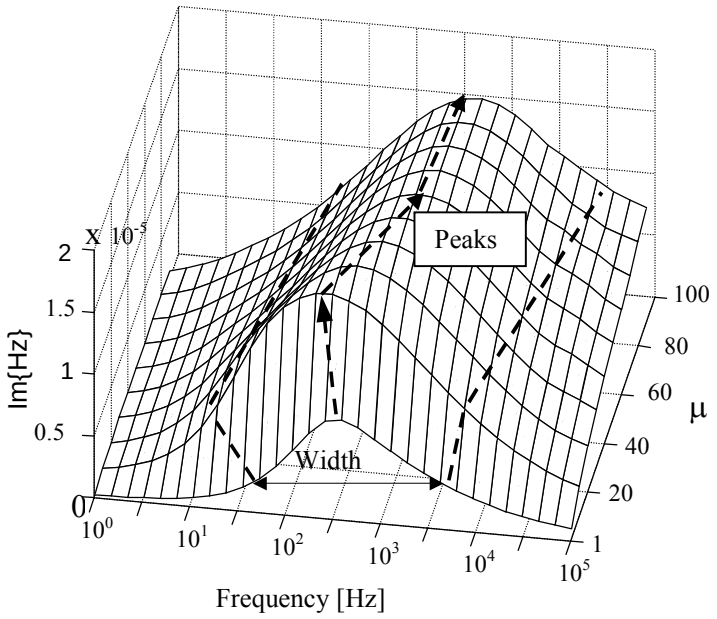

Figure 26. Quadrature component for spectral response of a very short cylinder (L/2a = 1.2), as a function of permeability. Axial excitation, $\sigma = 5.5 \times 10^6$ S/m

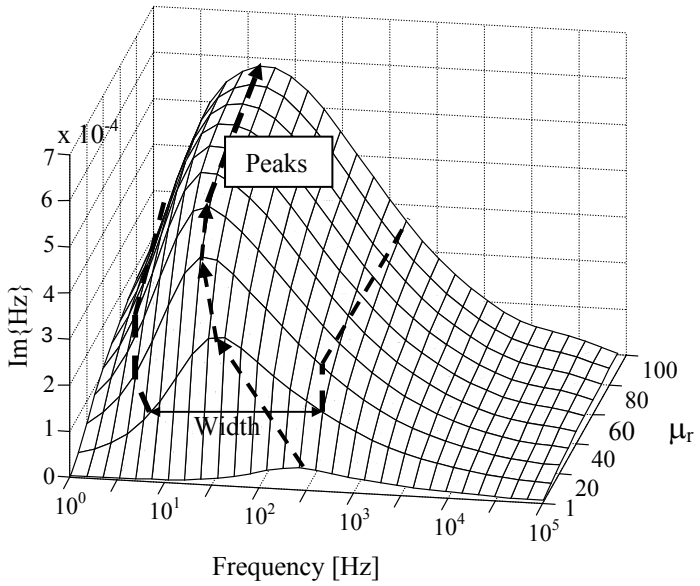

Figure 27. Quadrature component for spectral response of a long cylinder (L/2a = 7), as a function of permeability. Axial excitation, $\sigma = 5.5 \times 10^6$ S/m

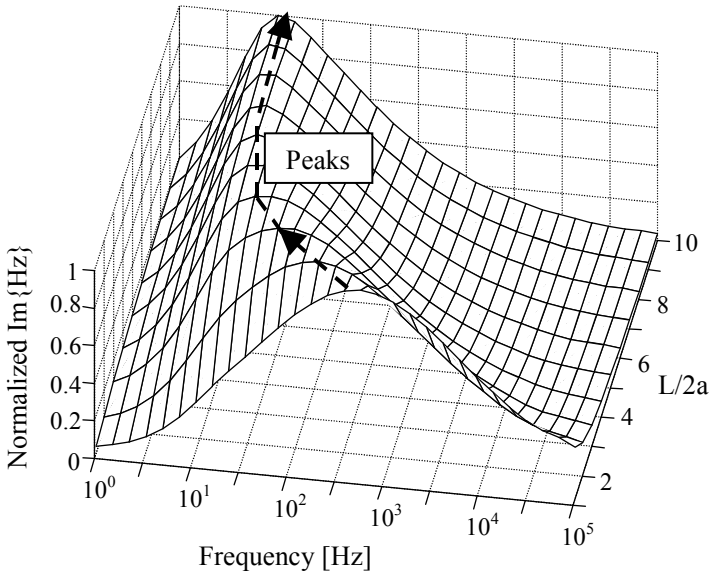

Figure 28. Normalized quadrature component of the spectral response of a cylinder as a function of elongation. Axial excitation, $\sigma = 5.5 \times 10^6$ S/m, $\mu_r = 40$.

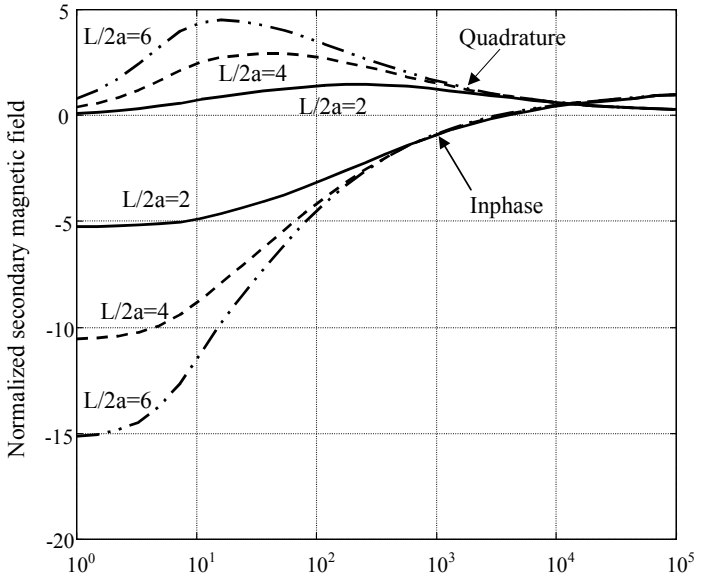

Figure 29. Both inphase and quadrature component spectra for the cases in Figure 28, normalized with respect to high frequency limit, as a function of elongation.

Figure 29 shows a different view of the effect of elongation by including both I and Q components in the plot. This reiterates the point that we may need the VLF sub-band to see the quadrature peak and the low frequency limit. Only a full view of the EMI UWB shows the change in the relation between the components in the high vs low frequency range. Note that that the relation in the higher frequency portion does not change as the cylinder is elongated. This suggests that one might infer degree of elongation by observing the relation between the pictures of the I and Q components in the high and low frequency portions of the spectrum.

UWB Data and Uniqueness in Parameter Estimation

Developments in this project permit the examination of parameter effects across the EMI UWB. They also indicate that, in fact, we *must* examine the effects across the UWB to obtain unique values for basic electromagnetic parameters. At the most general level, uncertainties in geometry and material composition can play together to create ambiguities, or threaten non-uniqueness or non-invertibility of EMI signals. With wideband information and some general knowledge of the geometry that is being considered, this can often be dealt with, e.g [20]. However, even when the object at hand has a well defined, known, and simple shape with uniform composition, substantial uniqueness problems can arise in connection with material parameters. To illustrate this, we will draw on measurements, simulation, and some of the expressions developed in the analysis of the TSA formulation. Figure 30 shows comparisons of normalized calculated responses and the measured data, in the physically consistent sign convention. The target is a small steel cylinder, 3.8 cm by 7.6 cm, with unknown conductivity and permeability, and its responses were measured up into the beginning of the MF zone with an upgraded GEM system developed during the project. Because the material is high permeability, we'll assume that the TSA will be sufficiently accurate to model its response over the entire frequency range. By adjusting the parameters around reasonable quantities, we succeed in zeroing in on adequate values. Because the values apply well for all frequencies, for both components and for both axial and transverse orientations, it seems unlikely that there could be any uniqueness issue.

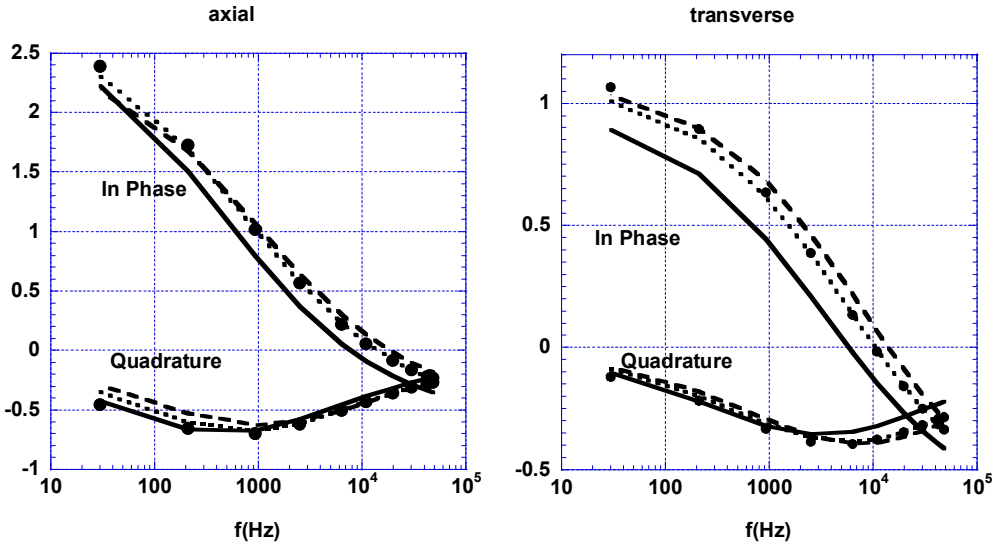

Figure 30. Measurements (solid markers) and responses obtained using the TSA algorithm, for a small steel cylinder. Solid lines: $\mu_r = 55$, $\sigma = 5.5 \times 10^6$ S/m. Dotted lines: $\mu_r = 95$, $\sigma = 5.3 \times 10^6$ S/m. Dashed lines: $\mu_r = 95$, $\sigma = 4.0 \times 10^6$ S/m.

However an examination of the pattern of error between measured and calculated H^s is revealing (Figure 31). While the parameters ultimately chosen on the basis of the results in Figure 30 do indeed point to a minimum, it is a rather weak minimum. That is, there is a long "trough" of low error, running at roughly a 45° angle from lower left to upper right in the figure.

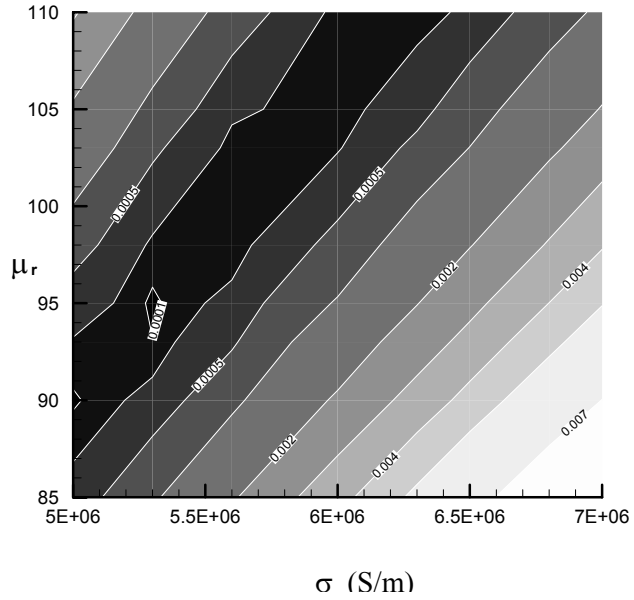

Figure 31. Error contours in (σ,μ) space, for the small steel cylinder.

Systematic pursuit of this reveals that the valley in the error surface is indeed more or less linear, at the 45^o angle, over a much larger parameter range than appears in the figure. Figure 32 shows that, as long as some high permeability value may be assumed, the results are almost entirely insensitive to changes in parameter values when a fixed ratio of σ and μ is maintained. The generality of this result is apparent if one examines the analytical expressions developed for investigating the domain of validity of the TSA. For both spheres and transverse cylinders, the scattered far field can be expressed as

$$\psi^s(\mathbf{r}) = a_1\left(\frac{a_2}{1+\frac{1}{\mu_r}(a_3+ika\alpha_n)}-1\right) \tag{65}$$

where a_1 and a_2 are constants. The constant a_3 equals 2 for the sphere and equals 1 for the cylinder and is basically just a frequency independent expression of geometry, i.e curvature of the object surface.
For these basic shapes subjected to smooth excitation fields, one can in principle always specify a value of α_n between about zero and one that will make this relation *exact*. Therefore, we can investigate the behavior of the solution by examining this expression, whether we know the exact value of α_n or not. In other cases involving relative simple shapes and primary fields, we have also seen the TSA system perform in the manner predicted by (65). In particular, as *k* increases, the influence of the product containing it becomes dominant. Including the $1/\mu_r$ factor, that product may be rewritten as

$$a\sqrt{i^3\alpha_n\omega\mu_0\frac{\sigma}{\mu_r}} \tag{66}$$

Systematic investigations [23] have shown that, for μ_r much greater than one, two trends come together, namely: 1) ψ^s is sensitive to the quantity (66), at higher induction numbers, in which regime this quantity is the only variable that determines the solution, overshadowing the influence of the a_3/μ term. This means that the solution depends only on the ratio σ/μ_r, other things in (66) being fixed. Or, 2) at lower induction numbers ψ^s is fundamentally insensitive to the term in (66), and the system ultimately boils down to the static formulation, in which the a_3/μ term dominates.

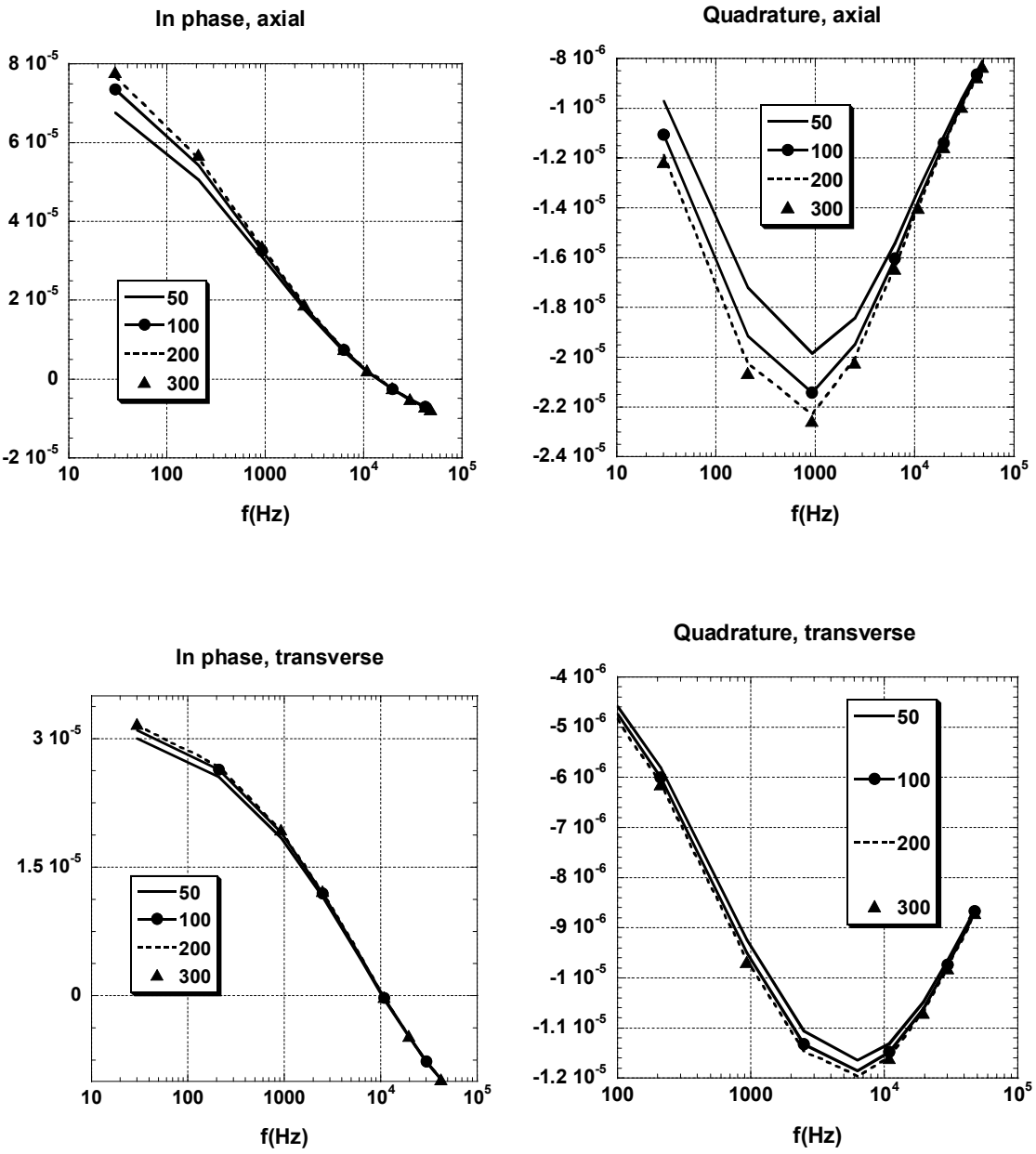

Figure 32. Scattered fields calculated for a 1x2 permeable cylinder, with μ_r = 50, 100, 200, and 300, with σ adjusted in each case to maintain $(\sigma/\mu_r) = (5/9) \times 10^5$ S/m.

This is to say, for steel-like properties, either the solution is strongly determined by the ratio σ/μ_r or the value of that ratio is irrelevant to the solution, with very little intermediate territory in the middle of the EMI UWB. Section 2.4 above shows a sample of results in which there is very good agreement between TSA results and the correct solutions, for steel-like properties, over *all* induction numbers. The analyses

in [23] show that this is because of the virtually seamless transition between the conditions 1 and 2 described above, for any induction numbers significantly above the zone of essentially static response. In this state of affairs, inversion cannot identify any unique combinations of σ and μ that apply.

For some purposes, this may not matter. If our requirements are only that we be able to represent the scatterer's behavior successfully, as in Figure 30, then we will be happy with any workable combination of σ and μ, however physically incorrect. But for many applications one must pin down some estimate of the separate values of these parameters, in order to isolate the influence of other factors of greater consequence. Also, note that the results discussed immediately above apply specifically to spheres and cylinders in transverse orientation. In follow-on work, also supported by SERDP since the conclusion of this project, we have seen strong suggestions in measured data that separate applicable values of σ and μ may be necessary to match successfully the important near field patterns from a steel cylinder, for more arbitrary excitation and observation angles. This is essentially an argument for inclusion of the VLF sub-band for full UWB analysis. In the VLF zone, μ is often the only variable other than geometry that influences the response. To the extent that the VLF extends low enough to catch the quasi-static asymptote of the inphase component, it will necessarily include the zone in which *only* geometry and μ can influence the data. Therefore inclusion of the VLF in the EMI UWB would provide a sufficient basis for inference of unique electromagnetic parameters.

Fine Surface Features

Both measurement and rigorous simulation agree that changes in ordnance orientation shift the locus of frequency response. Results in the section below on measurements also show this dramatically for small ordnance items. To investigate this phenomenon we will use the MAS program, which is tested against GEM-3 measurements for a small UXO, in

Figure 33. Agreement with data is very good; both measurements and simulations agree on the pattern shift with orientation.

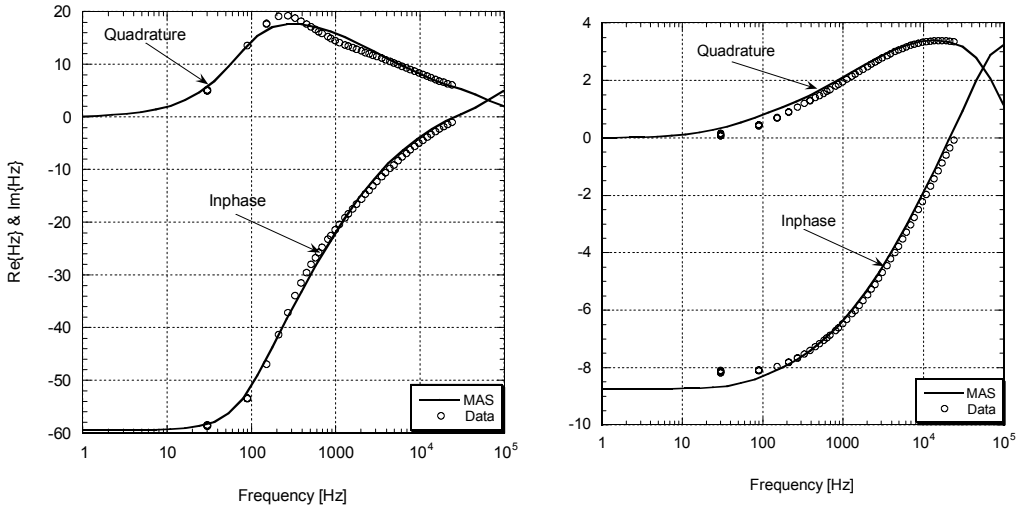

Figure 33. GEM-3 measurements of response from 20 mm UXO, in axial (left) and transverse orientation (right), showing excellent agreement with numerical simulations.

Note that we could not ascertain the crossing point of the curves, nor really define the peak shape in the transverse case, without the MF-EMI band. Why does the quadrature peak shift to such higher frequencies when the object is rotated from axial to transverse orientation? We will use the simulation programs, validated in many tests such as that above, to test hypotheses about the cause of this low to high frequency shift. The models allow us to vary particular parameters and target features systematically and thereby isolate links between target characteristics and signal content.

The first, obvious hypothesis is that change in orientation forces the induced currents into different paths over the object, in the course of which they encounter features that are more responsive at higher frequencies. Recall that an impinging primary magnetic field generates current loops in the target circulating more or less in planes perpendicular to the direction of the primary field. This means that, in the axial orientation, currents circulate around the barrel of an elongated object. In the transverse orientation the currents must flow along the sides and over or around the ends. Consider the scatterer geometries in

Figure 34 which, together with those of the sphere and spheroid, will be used in the following tests. The UXO-like geometry is like that used to simulate the 20 mm shell, and is chosen for further probing here because it contains a number of suggestive features, namely both relatively sharp edges at the tail end and a relatively sharp, pointed nose. In the transverse orientation, currents must flow around the profile of the projectile, i.e. around or over the edges of the object in the plane of the picture. We know that small spheres provoke much higher frequency response than larger spheres. Is it possible that flow over small radii of curvature in a larger object also produces higher frequency response? At higher electromagnetic frequencies, e.g. for ground penetrating radars operating in the hundreds of MHz, the incident fields provoke electric currents on the target surface which tend to produce intense electric charge concentrations at sharp points, edges, etc, sometimes causing large effects in the scattered electric fields. Is it possible that magnetic currents in the EMI range are forced into higher concentrations when they confront surfaces that converge, producing the equivalent of high magnetic charge concentrations, with commensurately large effects on the scattered magnetic field? This sort of thinking underlay the main hypothesis that was reported as a going proposition earlier in this project, which we now lay to rest.

Axial Cases

First we examine the effects of varying the radius of curvature in cylindrical geometries, when the object is oriented so that the induced currents must flow around (i.e. along) an edge, but not across it. Figure 35 shows scattered magnetic field vs frequency at a far field observation point (x = y = 0, z = 1 m, with length of cylinder about 0.2 m), for permeable and non-permeable cylinders under an axial primary field, $\mathbf{H}^{pr} = \hat{\mathbf{z}}$. The radius of curvature of the edges of the cylinder varied from case to case (R in

Figure 34). Clearly, variations in the cylinder end geometry, from flat and sharp, to slightly rounded, to very rounded, produce very little effect on the scattered field. Responses are virtually the same in all cases. Figure 36 shows the far field frequency response for the axially oriented UXO shape, for both non-permeable and permeable cases. The overall aspect ratio (length to diameter ratio L/2a) is 4.5 and the largest diameter 2a = 5 cm.. The figure shows the broadband scattered H_z field at the observation point x = y = 0, z = 1 m. Different tip curvatures were investigated, with the radius of curvature as large as the radius of the uniform section, and as small as 1/10 that value. Here, as the tip becomes more blunt, the overall shape of the target changes more than when the edge curvatures were reduced in the cylinder cases. The UXO shows some slight difference between the different curvature cases, at lowest frequencies, in the inphase component at low frequencies. This can probably be attributed to a slight difference in volume between the different shapes, with the smaller volume shapes producing slightly less static response. The surface area is almost same in all three cases, and correspondingly in all cases the scattered field remains relatively unchanged at high frequencies, where penetration of the target is slight, only the inphase component appears, and only the exterior surface is important. Note some slight downward shift in the location of the quadrature peaks for these magnetic cases, as the sharpness of the edges is reduced. However this change is very small. In the non-permeable cases it is not even quite monotonic relative to reduction of sharpness, suggesting that the pointedness per se has less effect than other secondary geometrical traits that are altered as we attempt to blunt the tip. In the permeable case, the peak shifts from about 300 Hz to 200 Hz, which is quite small relative to the overall spread of the peak; its overall locus remains about the same. In any case, the shift is not enough to be useful for discrimination purposes, and is certainly not on the scale of effects seen in

Figure 33, for example.

Transverse cases

While none of the cases above shows significant high frequency effects from sharpness in edges or points, the tests all entailed axial orientation. This does not force the currents to "confront" the sharpness in the same way that the transverse orientation does, so we investigate the latter orientation next. For transverse orientation the primary field is $\mathbf{H}^{pr} = \hat{\mathbf{x}}$ and three different targets are oriented transverse to it: a prolate spheroid, a cylinder, and a UXO shape, all with the same largest diameter $2a$ = 2.5 cm. Results for a sphere of diameter $2a$ are also included, for reference. This diversity of shapes is chosen in order to enlist the broadest possible array of curvature distribution possibilities, for the orientation where we expect the greatest sensitivity. The prolate spheroid has large semi-axis c and small semi-axis a, with c/a = 6, while the cylinder has L/2a = 6 and the UXO shape has L/2a = 4.5. Figure 37 shows the secondary field calculated for non-magnetic cases and also for μ_r = 50. To aid in comparisons, values are normalized with respect to the maximum quadrature response in the non-permeable case. The figure shows that all the non-permeable case targets have very similar frequency response patterns, with quadrature component peaks in the same vicinity and convergence between the cases at higher frequencies. In the middle frequencies the pattern for the sphere is shifted slightly to the right. The general result is that, for any of the elongated non-magnetic cases, the details of geometry have little effect. Because responses to permeability are absent, all of the patterns are due to induced electric currents as they flow over and through the sharp or smooth edges and points. Clearly substantial differences in the distribution of those features and in their radii of curvature have little on the frequency response pattern.

It is remarkable that the pattern for the sphere in Figure 37 is as close to the others as it is, given its radically different shape, much more compact and with a single, relatively large radius of curvature over all parts of the surface. This suggests that the shortest distance across the object, i.e. $2a$, dominates the frequency pattern of the magnetic moment in all these non-permeable cases. We explain this by examination of the internal current patterns in a longitudinal cross section of a representative elongated object, namely a long transverse cylinder, assumed to respond as an infinite transverse cylinder, at any cross section away from its ends. The well-established analytical solution for this case appears in above (Section 2.3), and has a maximum in the quadrature component at a $|k|a$ value of 1.77. Note that for a non-magnetic cylinder the location of this maximum is a function *only* of $|k|a$, that is, of induction number, and $|k|a/\sqrt{2} = a/\delta$, where δ is the skin depth. Thus at f_p, δ is about half the radius. The current distribution across the cylinder, at f_p, in a plane perpendicular to the primary field, is given by $k^2 J_1(ka\xi)$, where $\xi = \rho/a$. The distribution of field strength and especially its gradients thus imply that, at f_p, the strongest currents are in the outer region of the cylinder,

necessarily flowing parallel to its surface. In particular, three-quarters of the contribution to the current moment comes from about the outer third of the current distribution ($\xi > 2/3$). This current moment distribution will always be the same at f_p; that is, the picture will always be the same relative to ξ, and the total moment will depend only on a. At higher induction numbers the current will be more intense and will be even more concentrated near the surface. However, the combination of reduced area over which the current acts and the only marginally increased radius to its region of intensity ultimately mean a diminished moment. For lower induction numbers (lower frequencies than f_p) the region of significant current will spread over a greater portion of the cylinder cross section. However its intensity will be diminished and the radius over which most of it acts reduced, so that ultimately its moment will be less than for the distribution at f_p.

Inspired by these observations we may construct a schematic representation of the overall current pattern in an elongated object at f_p (Figure 38). The moment of each current element traveling parallel to the sides is proportional to aJ. Viewing the system of currents in terms of current loops, note that current elements subtending equal areas around the object center produce equal contributions to the moment. In aggregate, the currents crossing over at the ends contribute the same amount to the moment as those passing parallel to its sides, as the areas of the two shaded triangles in the figure are equal. Therefore, the contribution to the magnetic moment from each set of (side, end) current elements peaks at the same induction number, regardless of the object's length, and the moment is proportional to a.

For the permeable objects in Figure 37, the inphase components are similar in all cases, with the sphere shifted somewhat away from the rest into higher frequencies. The quadrature component peaks are again in about the same location for all cases. Further, the normalized quadrature components virtually coincide over the whole frequency spectrum for the sphere, prolate spheroid and the cylinder, with the crossing of the components shifted higher for the sphere. This is strong evidence that sharp edges or other details of surface geometry at that scale have very little visible effect on even the higher frequency portion of the spectral responses. While the UXO ‘s normalized quadrature component coincides with those of the other shapes at frequencies below the peak, it shows a dramatic departure at higher frequencies. Presumably this has to do with its relatively long, tapered nose. At lower frequencies than f_p currents circulate within the object's volume and are not constrained to follow *the details* of its surface. As frequency increases above f_p, the currents reside only in a thin layer near the surface, and are thus required to confront more of the surface geometry. While the results indicate that sharpness of surface features is not influential, apparently intermediate

scale characteristics, such as the converging lines of the tapered nose, may indeed have some effect. Forcing the currents to follow the converging sides apparently makes the overall circulation into a less efficient radiator, relative to the situation (and the other shapes) at lower frequencies. This effect underlines the importance of being able to obtain ultra-wideband data to discriminate different geometries adequately, with instruments adequate to obtain results in the higher frequency realm.

Overall, we see very little sensitivity to sharp edges and points. For a physical understanding of this, consider first that the wavelength outside the body is many, many orders of magnitude larger than the scattering structure. Thus small surface alterations are unlikely to affect them. Further, as mentioned above, inside the target the electromagnetic fields are governed by a diffusion equation. Diffusion is insensitive to small details of geometry, tending to dissipate concentrations in any region, including those with irregularities and sharp curvature. Because diffusive fields do not reflect, we also do not see any influence on resonance behavior caused by sudden geometrical changes, such as might appear at higher (i.e. radar) frequencies. Sharp changes in surface geometry are not prone to reflect, deflect, or divert currents in the diffusive MQS realm.

So, can we still obtain information of distinguishing geometrical features from UWB observations? The answer is "yes," with some important qualifications and remaining effects to be investigated. In the next section we describe some fundamental UWB parameter sensitivities that should be very useful in inversion, including tests of some new theory that identifies simple signal effects that are linked to target aspect ratio. We also explore the notable effects of slender structures, i.e. plates, shells, and fins, which we have excluded from the category "fine surface features."

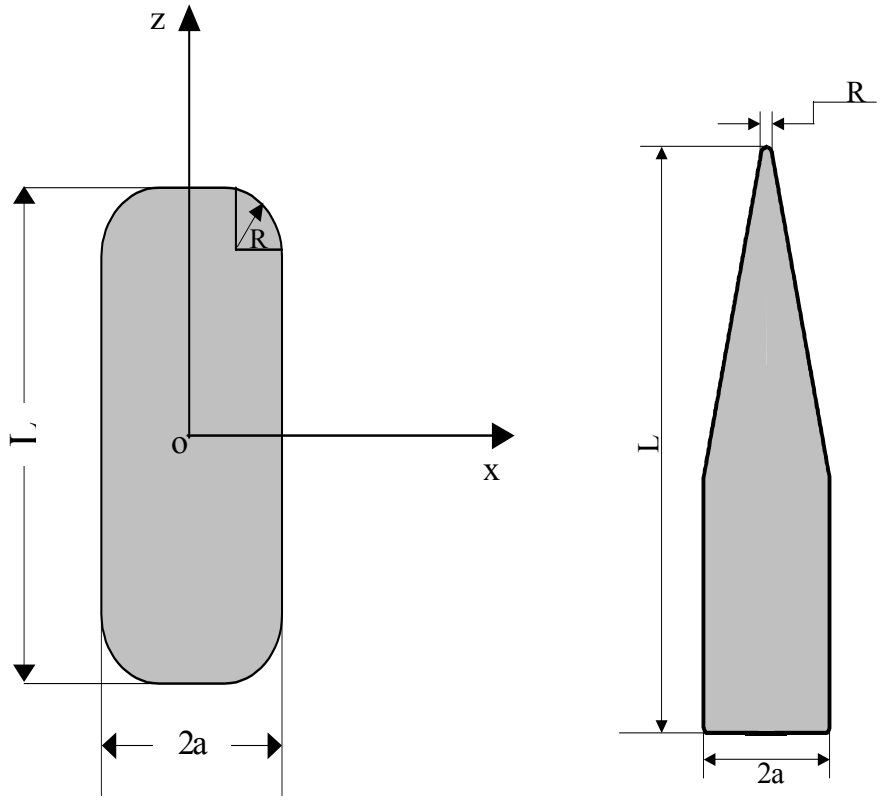

Figure 34. Geometry of cylinders (left) and UXO-like shape (right).

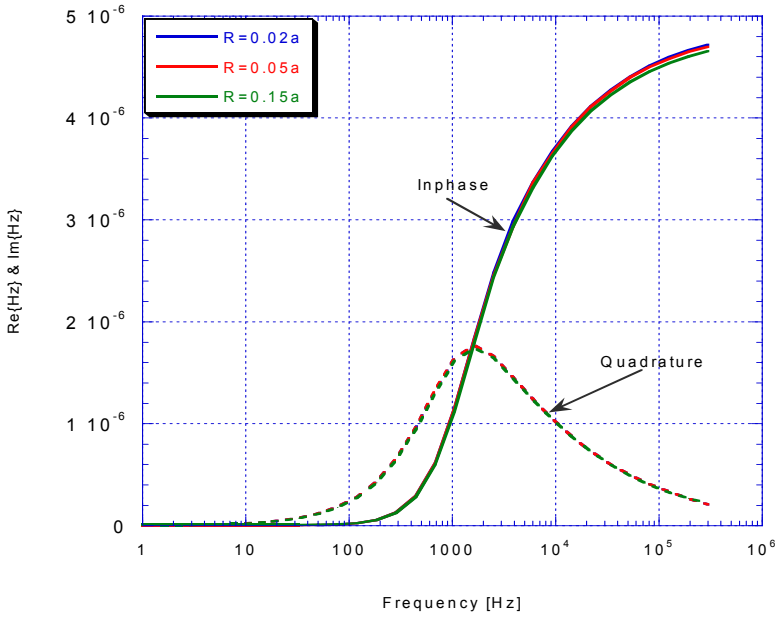

a)

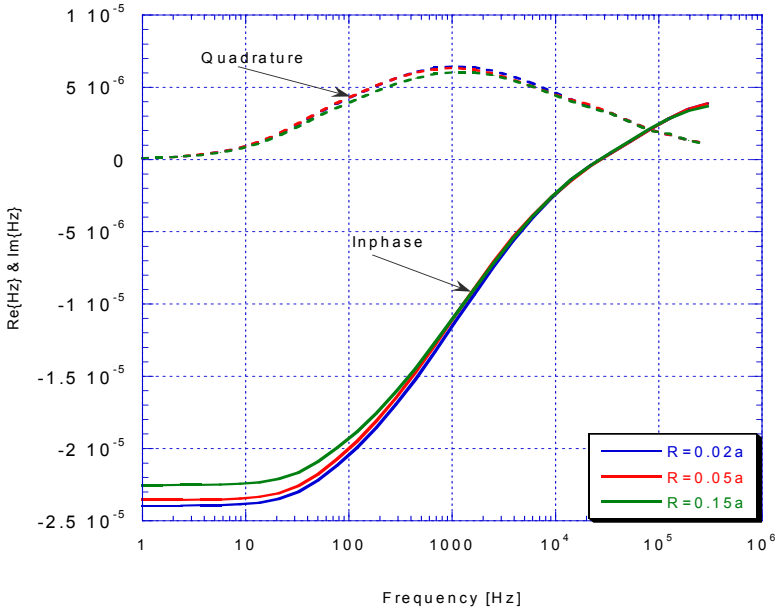

b)

Figure 35. Scattered magnetic field vs frequency for a cylinder under axial excitation, for different radii of curvature R at the edges. a) non-magnetic case, b) $\mu_r = 50$

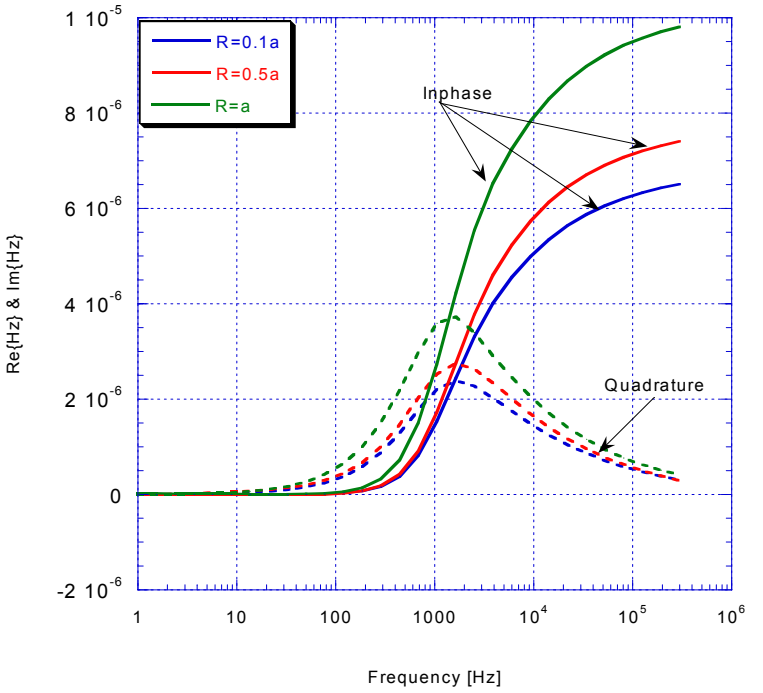

a)

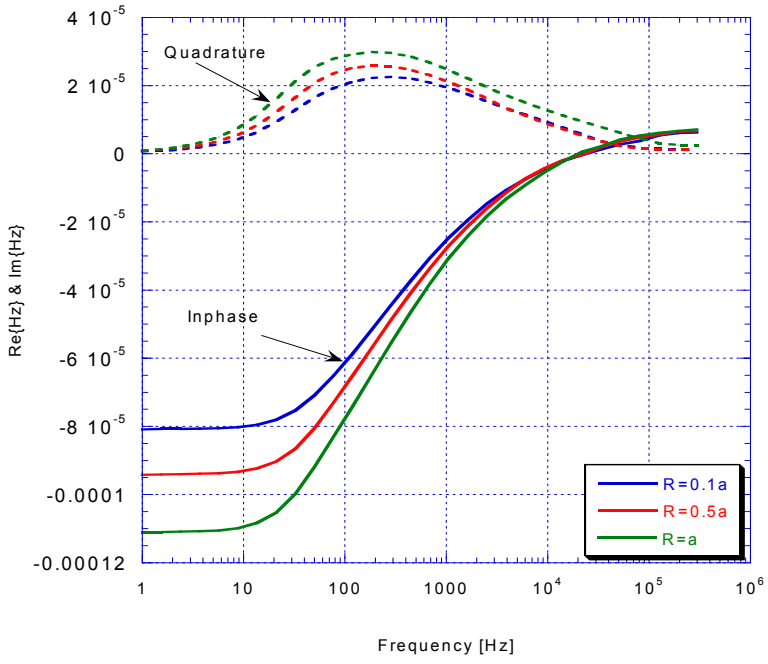

Figure 36. Scattered magnetic field vs frequency from UXO shape under axial excitation, with $\sigma = 4\ 10^6$ S/m, for a) non-magnetic case and b) $\mu_r = 50$.

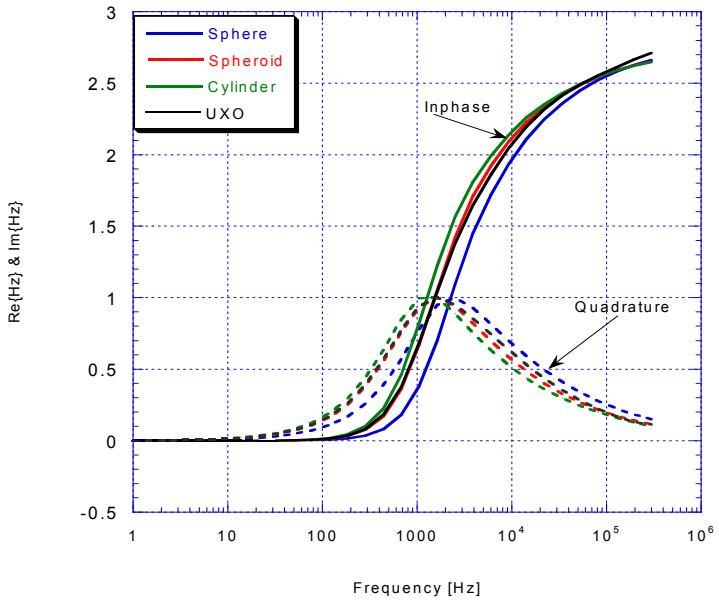

a)

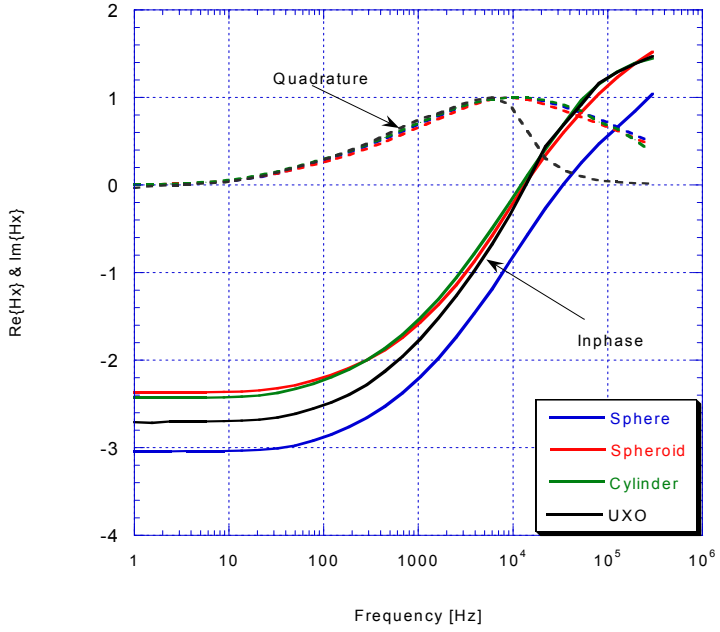

b)

Figure 37. Transverse responses of variously shaped objects, with $\sigma = 4x10^6$ S/m, a) non-permeable, b) permeable with $\mu_r = 50$.

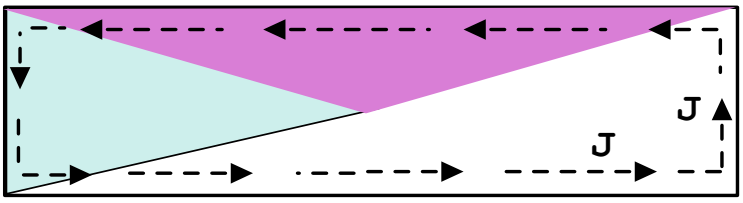

Figure 38. Current pattern within the cross section of a cylinder under transverse excitation (primary magnetic field pointing into the page), at f_p.

3.2 Inference of Aspect Ratio (AR)

Magnetic Resonance Theory for Frequency Based AR Estimation

In electromagnetic surveying of a buried metallic object, e.g. for UXO cleanup, inferring its aspect ratio is an extremely important discriminant. Both UXO and common clutter fragments can have an infinite variety of shapes. However, intact ordnance and clutter items rarely possess comparable aspect ratios, defined here to mean the ratio of principal characteristic dimensions. Further, in terms of shape inference, we have seen above that it is frequently impossible to discern any effects in scattered signals due to details of shape beyond gross proportions, i.e. aspect ratio.

When an incident radar wave impinges upon a metallic scatterer, complex natural resonances are excited [39-41]. These occur as the incident wave tends to produce current patterns on the target corresponding approximately to electric dipoles. This means that the currents run back and forth in more or less linear patterns along the object, and do not form the closed loops characteristic of currents induced in the EMI band. On an elongated target illuminated by radar, for example, late time resonant currents will travel back and forth along its length. Loosely speaking, these "bounce" back and forth between the ends of the object. A pattern of electric current magnitudes along the length with nulls at the ends, where the currents must stop and reverse, fits naturally on the object. Such electric dipole type current elements reside on the outer surface of the object, and radiate most efficiently when their path lengths along the surface are integral multiples of half the electromagnetic

wavelength in the outer (surrounding) medium. Thus, by observing the real part of the resonant radar frequencies, one can sometimes infer the dimensions of an unseen target, particularly its longest dimension [39-41].

By contrast, in EMI we are dealing with much lower frequency *magnetic* fields impinging on the targets, tending to produce *magnetic* dipoles in them. These are *inside* the surface of the object and are most intimately connected with interior electromagnetic activity. By analogy with the radar case, we propose here that magnetic current elements that naturally fit the target's dimensions will likewise tend to resonate. While we emphasize that the interior electromagnetic phenomena are diffusive oscillations, not waves, it remains true that the fundamental solutions to the governing Helmholtz equation have the form (11) in the frequency domain, in particular for the interior field $\mathbf{H} \sim e^{ikx} = e^{i\gamma x}e^{-\gamma x}$. That is, resonant *magnetic* currents should still appear at frequencies such that the current element lengths *within* the penetrable scatterer are $\lambda/2$, where λ is obtained from $\lambda = 2\pi\gamma$. But what *is* the length of a magnetic current element? Otherwise put: what is the physical meaning of the mathematical fact that characteristic values of k exist?

In approaching the answer to this question, we first remind the reader of the relation between these resonant frequencies and the patterns observable in wide band EMI data. (See the remarks on this subject in Section 1.2, following Figure 2). In terms of real valued frequency, for simple (single pole) systems, identification of the peak in the quadrature component, f_p, in the frequency domain corresponds to identification of b in a simple exponential decay in the time domain, of the form e^{-bt}, with $2\pi f_p = b$. While complex structures may produce responses containing combinations of modes, it is often the case that the single, lowest mode dominates most of an object's response. Inversion work often seeks to identify the most fundamental response mode of an object, whether by identifying a dominant b in e^{-bt} in the time domain, or by noting f_p in FD data. Our FD strategy here will be to estimate f_p and relate it to the confining dimensions of the target in different orientations relative to the primary field. From this we will infer scatterer aspect ratio.

To relate all this to aspect ratio, consider an elongated scatterer with length to diameter ratio AR = L/2a. Under axial excitation the primary field impinges upon it from the end, inducing a magnetic response corresponding to a magnetic current element oriented more or less along the long axis of the object. For reasons explained below, for magnetic objects we expect the magnetic current element to be "confined" by the ends of the object, so that the lowest mode of resonance occurs when

$$L = \frac{\lambda}{2} = \frac{2\pi}{Re\{k\}} = \frac{2\pi}{\sqrt{\sigma 2\pi f_a \mu / 2}} \tag{67}$$

where f_a is the real part of the resonant frequency for the fundamental mode, under axial orientation. Under transverse excitation, the primary field impinges upon the object from the side. By the same reasoning we expect resonance for

$$2a = \frac{\lambda}{2} = \frac{2\pi}{Re\{k\}} = \frac{2\pi}{\sqrt{\sigma 2\pi f_t \mu / 2}} \tag{68}$$

where f_t is the real part of the resonant frequency for the fundamental mode, under transverse orientation. Taking the ratio of these two expressions produces a relation between aspect ratio and the two fundamental frequencies.

$$\frac{L}{2a} = \sqrt{\frac{f_t}{f_a}} \tag{69}$$

Note that the discussion above about "confinement" of the magnetic current elements suggests that this conceptual framework for resonant frequencies should not apply to both magnetic and non-magnetic objects. Detailed observation of solutions has shown that, for magnetic objects, whether spherical or elongated, the maximum exterior magnetic field that forms around the induced North and South poles is generally on the order of 2 or 3 times the primary field, but no greater. For values of μ_r much greater than one, this means that the interior field is forced down in magnitude, by virtue of the fundamental condition (13). This creates (approximate) nulls near the poles of the object, in the interior, thereby "confining" the induced magnetic current. By contrast, referring to the expressions above for cylinder magnetic dipole moments when $\mu_r = 1$ (Section 2.3), one can easily show using standard Bessel function identities that both the axial and transverse moment expressions can be put into the same form, namely

$$m \sim a^2 \beta \left[1 - \frac{2}{ka} \frac{J_1(ka)}{J_o(ka)} \right], \tag{70}$$

where β is a constant. For different cylinder lengths, the dipole moment based on (70) would be obtained simply by multiplying the expressions times the length of the cylinder. Altogether this means that, for $\mu_r = 1$, the frequency (induction number) at which the quadrature peak occurs does not depend on object length, and the right side of (69) is always unity. In what follows we evaluate the applicability of (69) vs (70) in different cases.

Figure 39 shows a plot of aspect ratios predicted by equation (69) compared to those for shapes used in MAS simulations from which f_a and f_t were determined. The objects considered were solid cylinders and spheroids of various sizes and shapes. Results shown in Section 3.1 indicate that increasing μ_r in elongated objects shifts the transverse response somewhat higher while it shifts the axial response lower in frequency. While this suggests that the frequency ratio in (69) should depend on μ_r, note that μ_r does not appear explicitly in (69). Thus the numerical tests were performed for variations of μ_r between 1 and 100, with aspect ratios between about 1.5 and 6, for both a flat-ended cylinder and a spheroid. Even though the cylinder and the spheroid have very different degrees of sharpness around the ends, both of them generally demonstrate similar peak frequency patterns relative to aspect ratio inference. For the low permeability magnetic case ($\mu_r = 10$) the difference between the theoretically inferred aspect ratio and actual aspect ratio is significant for both object shapes, with similar patterns of variation for both. As relative permeability increases to 50 and 100 this difference becomes small and stays almost the same for both permeabilities. Further investigations indicate that permeability effects level off, once the material is as magnetic as most iron and steel materials. For the non-magnetic case (69) fails completely as the peak frequency ratio remains around unity over a range of aspect ratios.

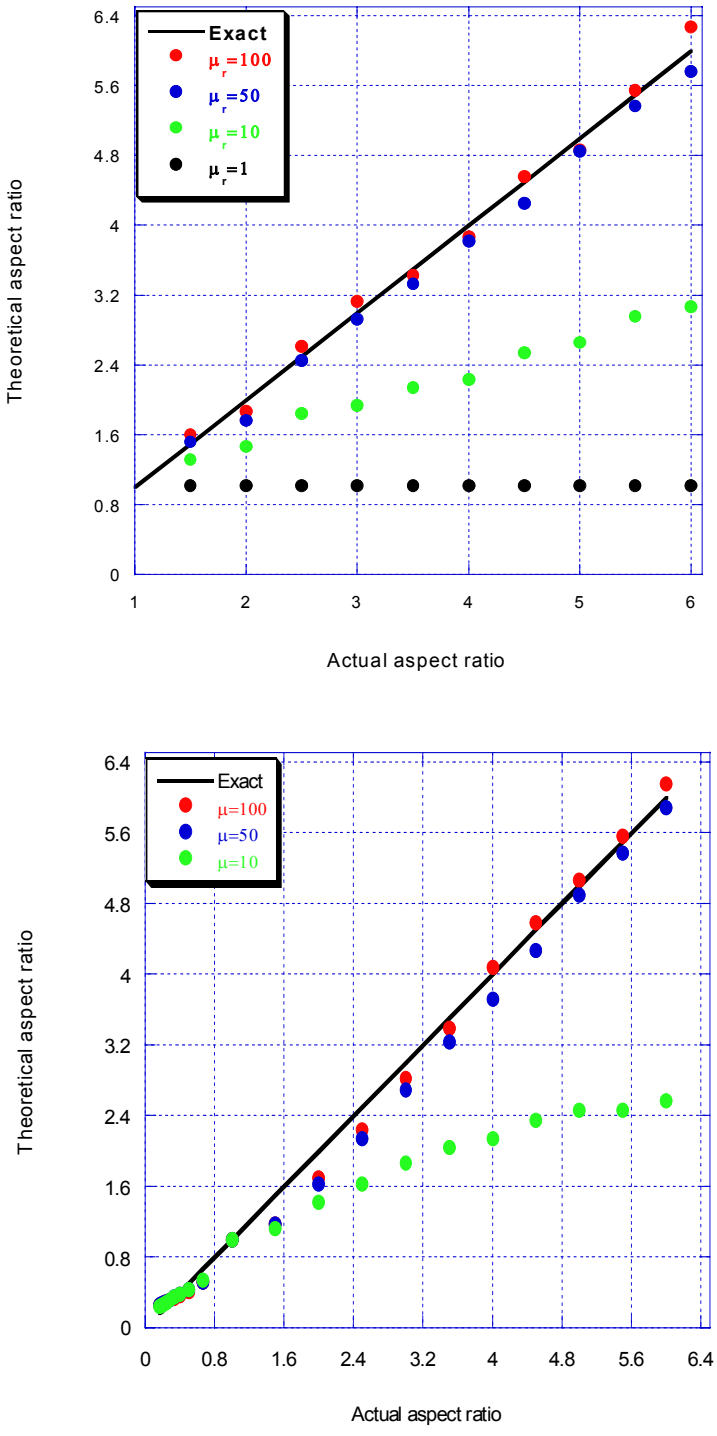

Figure 39. Theoretical aspect ratio from (69) vs actual aspect ratio, for different values of μ_r. Top:cylinder, Bottom: spheroid.

Figure 39 verifies that, for a non magnetic cylinder, both f_a and f_t are the same regardless of elongation, as predicted by (70). Figure 40 shows computed results for non-magnetic cylinders of a given diameter with length varied so that aspect ratios span the range from 1.5 to 6. When elongations are greater than about 4, the cylinders behave approximately like infinite cylinders, meaning that the ratio of magnitudes of the transverse and axial magnetic dipole moments converges to a constant (β in (70)).

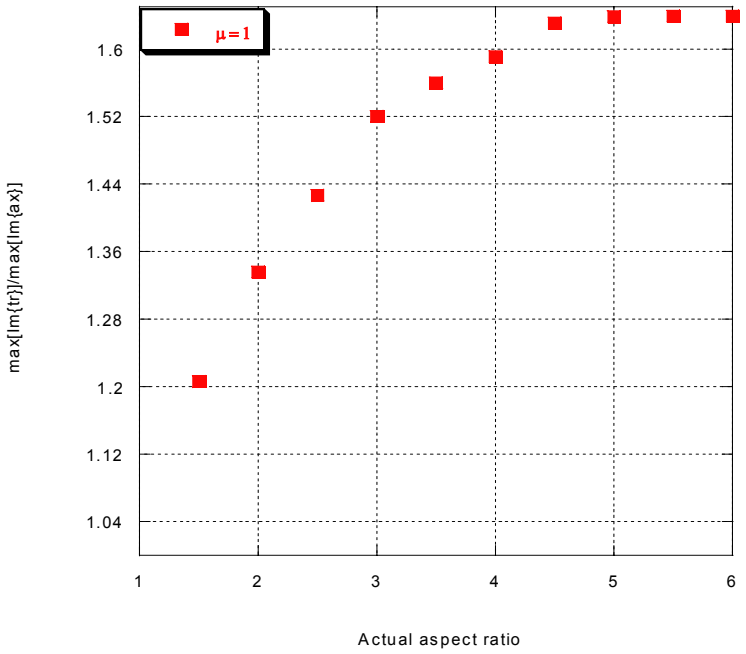

Figure 40. Ratio of magnitudes of the transverse to axial magnetic dipole moments vs actual aspect ratio, for cylinder with $\mu_r = 1$.

In principle, the relationship in Figure 40 could be used to infer AR for elongated non-magnetic bodies. However, in realistic situations one must deal with the complications added by near field effects, necessary antenna motion to gain different viewing angles, and the uncertainty of object location in fields that fall off very sharply. Fundamental axial and transverse responses are estimated by moving the antenna around in the vicinity of an unseen object, then doing some modeling, inversion, or at least inferential calculation. All this makes it doubtful that one could infer axial response magnitudes well enough to obtain the inherent eigenvalue ratio with sufficient accuracy. For the magnetic objects, perhaps the greatest importance of these results lies in the fact that they depend only on the shape of the frequency response pattern, not on the magnitudes of the response. Whenever possible, it is advantageous to

proceed in terms of frequency as opposed to magnitude patterns. In the AR approach for magnetic objects, one need only note the peak frequency for the different inferred orientations, whatever the associated magnitudes are. As a further development of this approach, it would be advantageous to infer f_p by determining a best fit of the entire Q peak to single prospective fundamental mode patterns. This might lessen vulnerability to the disturbances of f_p values when they are obtained by the somewhat precarious business of "peak picking." Many influences can complicate the details of the shape of the Q component, and values close to its peak value may be spread over quite an extensive frequency range. For this reason it is probably better to infer the fundamental response mode by treating the entire component shape.

Importance of VLF for Aspect Ratio Estimation

In an emphatic parenthesis, we note here how these AR tests reveal the importance of being able to see the peak in the quadrature component, and how they highlight the importance of the VLF sub-band.

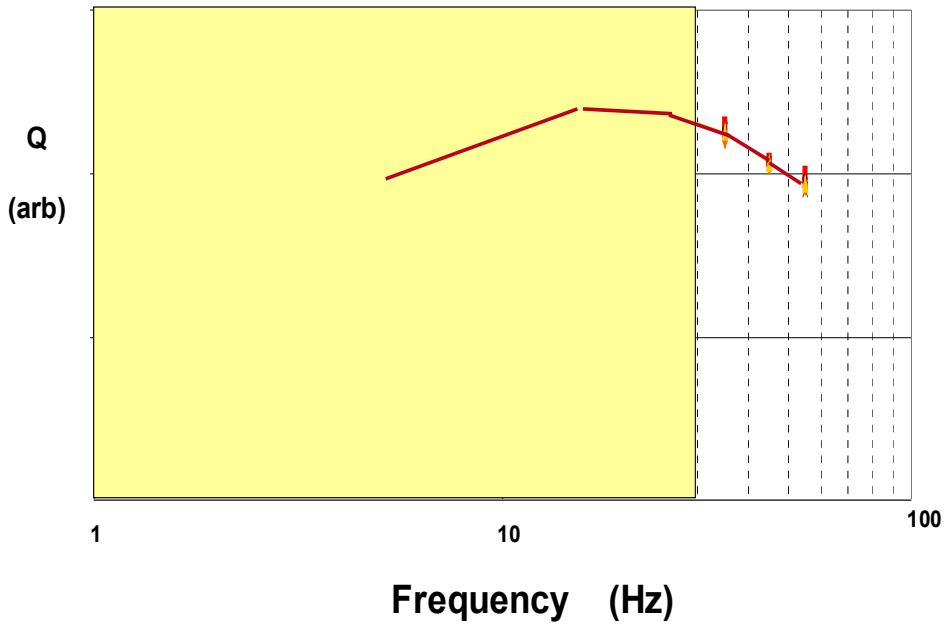

Figure 41. Quadrature frequency response of 105 mm projectile, nose down, measured with the experimental setup constructed during this project. VLF area is shaded on the left.

Figure 41 shows the quadrature component for a 105 mm projectile, measured in the course of this project, in the new VLF zone. Data in the lowest frequency portion of the measurements show considerable spread, as the signal becomes quite weak in that domain. This could not be overcome with the system as constructed for these measurements. Nevertheless, it is quite clear that the quadrature peak lies within the VLF sub-band. The parameter sensitivities shown in Section 3.1 indicate that other ordnance or elongated magnetic objects of at all comparable dimensions and materials should also produce peaks in the same VLF locale. To apply the aspect ratio system illustrated above, we must see enough of this peak to locate its tip or infer its overall shape. As mentioned, the latter is valuable because it allows better estimation of the fundamental resonant frequency than "peak picking" does.

Exploitation of the Full UWB for Magnitude Based AR Estimation

While noting the dangers mentioned above in connection with use of signal magnitude for target classification, we also present an alternative AR estimation system that exploits transverse vs axial response magnitudes. Others have done this kind of thing e.g. [43], though results have been complicated by material heterogeneity, standoff ambiguity, and selections of particular time or frequency ranges. The particular method suggested in this section has the advantage that it relies on the shape of response over the entire UWB and does not depend so crucially on a single signal characteristic or a feature in one frequency or time locale. Figure 42 shows the calculated magnitude ratio of the transverse and axial responses of a prolate spheroid, for different standoff distances from the center of the target, obtained from the validated TSA algorithm described above. The quantity b is the semi-major axis length. Thus $r = 3b$ implies observation at one object length from the tip of the scatterer when it is axially oriented. In terms of permeability, the object is steel-like. The clarity of the pattern across the EMI UWB is quite striking. At all but the closest observation point, the ratio reverses, relative to unity, between the lowest and highest induction number zones. At the lowest frequencies, the transverse response is distinctly smaller, while at the highest frequencies it is larger. This is fundamentally characteristic of an elongated object, i.e. one with high aspect ratio. Figure 43 shows results from comparable simulations, using the TSA program, but for a flattened shape, i.e. an oblate spheroid. In this case the pattern of the transverse to axial magnitude ratio is reversed relative to that for the elongated object. In some cases, the actual high and low frequency limiting values, for reasonable standoff, could also be used to estimate the degree of elongation: Note the systematic evolution of the relation between those values in Figure 3.

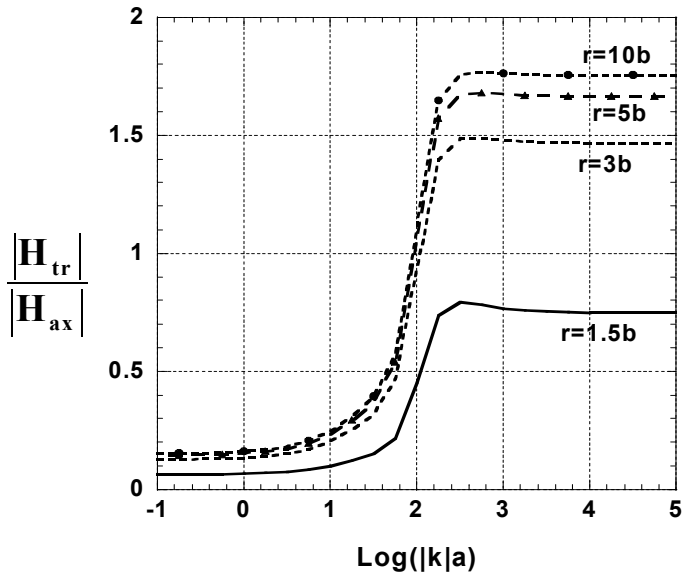

Figure 42. Magnitude of the ratio of transverse to axial response for 1x5 prolate spheroid, at different observation distances. $\mu_r = 100$

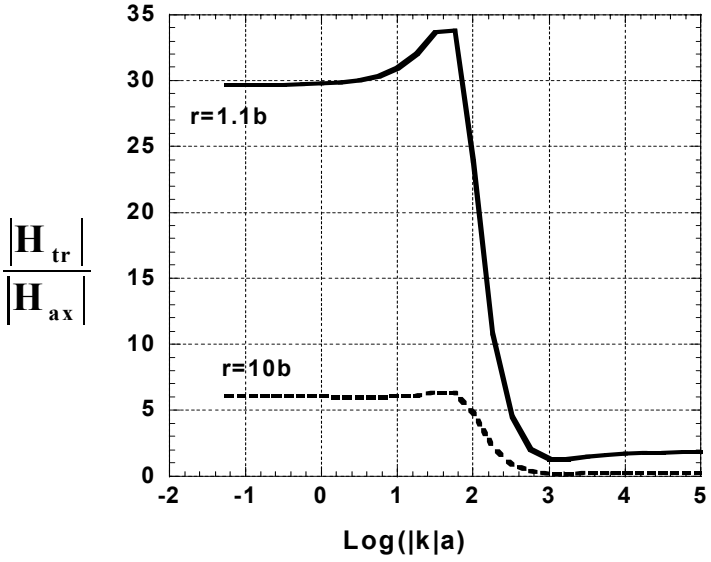

Figure 43. Magnitude of the ratio of transverse to axial response for 1x5 oblate spheroid at near and far field. $\mu_r = 100$

For the sake of generality, the results in Figure 42 and Figure 43 are plotted vs induction number, where *a* is the smallest semi-minor axis length. Assuming typical values for electrical

conductivity, one can readily translate these results into dimensional terms for different object sizes, i.e. different *a* values. Doing so reveals clearly that the MF and VLF regions are needed to see at least the edges of the high and low frequency plateaus, for objects of interest. Examples in the next section, with measurements relative to frequency, also illustrate this fact.

Altogether we have introduced two systems for inferring AR, one based on resonant frequency ratio, the other on UWB magnitude ratios. Especially when combined, these form a powerful resource for AR inference, at least for homogeneous objects, or heterogeneous objects dominated by one component.

Aspect Ratio Inference and More Complicated Objects

The main challenge that surfaces in more detailed tests of the AR inference approaches does not reside in complications caused by more diverse scatterer geometries per se. Rather, it is the association of material heterogeneity with such geometrically variable objects. This is implied by the information in Figure 39 and Figure 40. Both the f_t/f_a ratio and the associated response magnitude ratio behave fundamentally differently for magnetic and non-magnetic materials. Thus a combination of the two material types may produce a muddled pattern, from the point of view of aspect ratio inference. We will illustrate the problem using the magnitude based system.

Figure 44 shows GEM-3 measurements for a magnetic steel cylinder screwed about 1.2 cm into an aluminum cylinder, each with length of 7.6 cm and diameter 3.8 cm. The axial response was measured with the steel section facing and closest to the sensor head (i.e. "up"). The pattern over the UWB is similar to that was observed for the homogeneous prolate spheroid, with steel-like characteristics. Note that, with information into the edge of the MF region (up to 50 kHz), we are just barely able to see the edge of the high frequency plateau, for this relatively small target. A sufficiently larger composite target would also push the edges of the UWB, but on the VLF end. In any event, the results in the figure encourage one to pursue the AR estimation method outlined in the previous section, for composite as well as homogeneous targets, at least when steel dominates the axial response. Unfortunately, when the aluminum section is closest to the sensor, the steel does not appear to dominate the response. Instead, there is a bi-modal pattern, with a peak in the ratio in the lower frequency region (Figure 45). Attempts to apply the frequency based AR inference system will run into related difficulties. For the magnitude based system, detailed explication of the contributions by the different, interacting components to the total picture are possible. However, this is little consolation. The PI's ongoing investigations into composite target responses may ultimately

yield a sufficiently complete yet sufficiently simple approach for employing AR estimation systems like those here, but when targets are heterogeneous. For now we suggest only that the two present systems will succeed when the steel portion dominates the signal. Among other things, it may be possible to estimate from the UWB signal characteristics *when* the steel in a composite target is the dominant influence. See results emerging from the current composite object project.

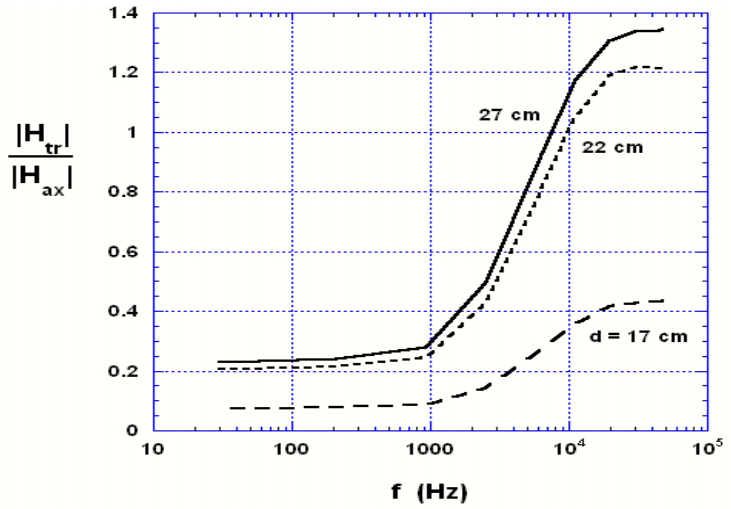

Figure 44. Magnitude ratio of scattered transverse to axial response vs frequency, measured for a cylinder composed of aluminum and magnetic steel parts, with steel towards the sensor in the axial orientation.

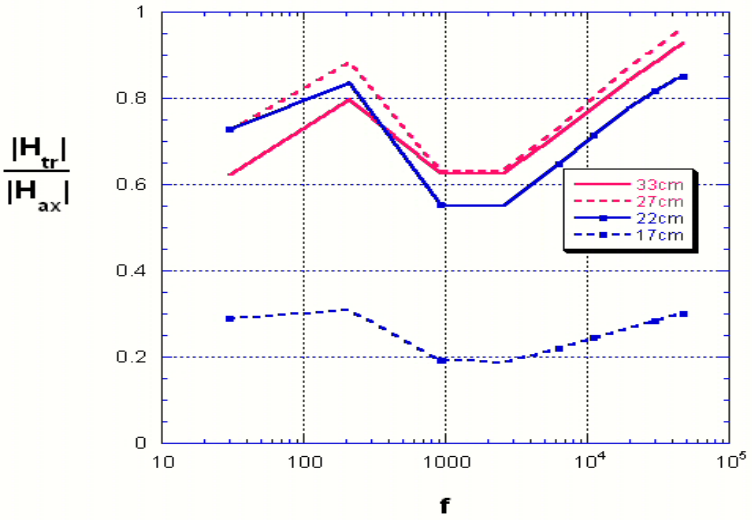

Figure 45. Same as Figure 44 but with the AL up, at different observation distances from the object center.

Results in the previous section near the high frequency limit are particularly interesting. In this (MF) part of the EMI band, the externally imposed field influences do not penetrate the metal significantly. This means that the response does not depend on metal type, rather just on overall object shape. Figure 46 shows the ratio of transverse to axial response, for objects with different aspect ratios (length/diameter). These were calculated with a version of the TSA formulation specialized for obtaining the high frequency limit of responses. The curve for the cylinder is slightly different from that for the spheroid, since they have different volumes at the same nominal aspect ratio. Despite this small difference, for a given axial to transverse response ratio at the high frequency limit, it is possible to estimate the aspect ratio of the object.

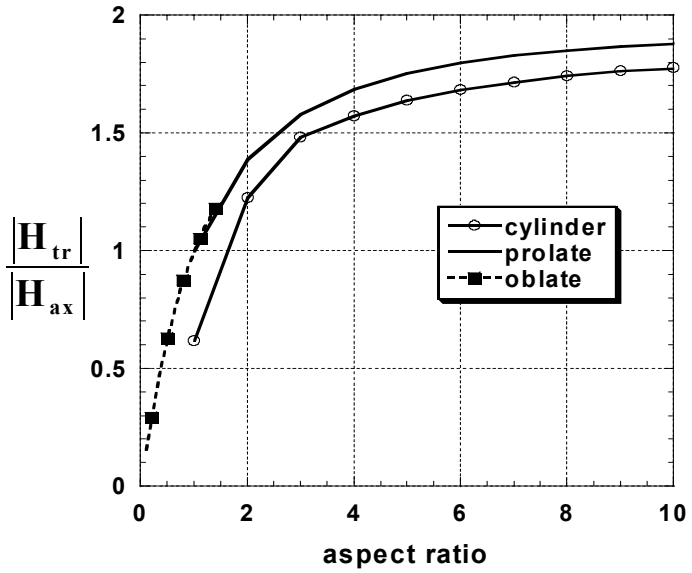

Figure 46. Ratio of computed transverse to axial response magnitude at the high frequency limit, for objects with different aspect ratios.

So, have we solved the problem of target heterogeneity in AR estimation? Probably not, unfortunately, though continued optimism is encouraged. The results in Figure 46 are indeed intriguing because they suggest we might infer aspect ratio from different look angles, even when objects are composites of different metals. Unfortunately the range of the transverse/axial response ratio shown is not very large, and the sensitivity of field magnitudes to distance between the target

and sensor is very great. As noted above, this ratio might easily be lost in measurement uncertainty and clutter, as an antenna is moved through different look angles and positions. Experiments are now underway to see whether this difficulty can be overcome, at least under certain circumstances, by obtaining data over a volume above the target, i.e. for diversity in both antenna elevation as well as horizontal shift and tilt.

3.3 Spectral Responses of Thin Elements

Flattened Shapes

First we examine the non-magnetic "parallel" plate response, that is, the response spectrum of a flat metal plate, of uniform thickness, with primary field oriented parallel to its flat surfaces and impinging on its edges. Such responses may appear in EMI data either from isolated fragments or from UXO fins still attached to the ordnance. Figure 47 shows analytical results for non-magnetic cases, obtained from (32), for some thin stainless steel slabs. Figure 48 shows the same, for aluminum slabs. Tail fin thicknesses on some medium sized UXO have been measured in the size range considered in the figures. Both metal types produce signals well into, if not essentially entirely within the new MFEMI band. Overall, the thinner the plate, the higher the frequency of the response, other things being equal. Note that the stainless steel plates produce higher frequency responses because their electrical conductivity is over an order or magnitude lower than that for the aluminum plates.

Clearly non-magnetic fins can produce significant response in the MF-EMI range. A remaining question is how strong that response will be relative to that from the material in the main body of the ordnance item. Data (Section 4.4) show substantial signal effects associated with non-magnetic tail sections that include fins, particularly when the ordnance is close below the sensor head with fins up, a realistic configuration. These signal effects appear in both the MF-EMI range and in lower portions of the EMI band. It is as yet unclear how much these signal effects are due to the fins themselves, as opposed to the rest of non-magnetic tail structure. This is now being determined in our ongoing work that centers on composite targets.

All these considerations may be summed up by plotting (32) in terms of induction number (Figure 49). To distinguish the higher frequency responses from that of the heftier, steel UXO body, we probably do best to examine the quadrature component. This is because the inphase component from the main body levels off at a fixed, asymptotic value as frequency increases, whereas the quadrature response from that part of the target should die down within the MFEMI range, leaving that of the fins more visible. Figure 49 shows that, for any "parallel" non-magnetic plate, peak response should be at an induction number of about 1, and significant response appears between induction numbers of about 0.4 to 4. We have seen in the previous figures that, for thin plates of stainless steel or aluminum, the peak or the upper half of the curve extends over the MF-EMI zone. To consider the other extreme, note that Figure 49 implies that the quadrature response would extend from about 2.5 Hz to about 250 Hz, with peak at about 16 Hz, for a thick, highly conductive non-magnetic parallel slab (d = 1 cm, $\sigma = 4.0 \times 10^7$), very much in the VLF domain. The induction number is directly proportional to $\sqrt{f}\,d$, so that this Q peak range for the 1 cm sheet is $1.6 < \sqrt{f} < 16$. Thus one can translate this last result for a copper-like material to results for any other thickness by simply shifting the computed $\sqrt{f}$ range by a factor of thickness/1cm. This suggests that, at least for parallel plate excitation, copper sheeting thinner than about 3 mm will have little effect in the VLF range, and that only a copper sheet that is about a millimeter or less in thickness will affect the MF-EMI domain. Aluminum has somewhat smaller conductivity than copper, and conductivity enters into the induction number as $\sqrt{\sigma}$. Thus relative to these results for copper, the $\sqrt{f}$ ranges cited will be shifted higher, but not greatly. This means that aluminum sheets of a mm or two produce effects in MF-EMI, and sheets on the order of a cm in thickness will still produce effects in the VLF.

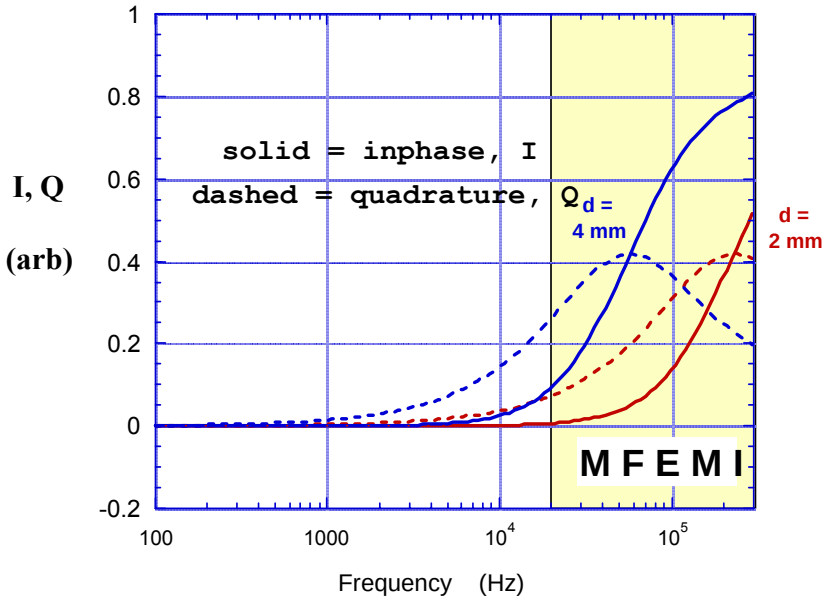

Figure 47. Normalized induced magnetic dipole moment for vertical plates of stainless steel ($\sigma = 1.4 \times 10^6$ S/m) of thickness d.

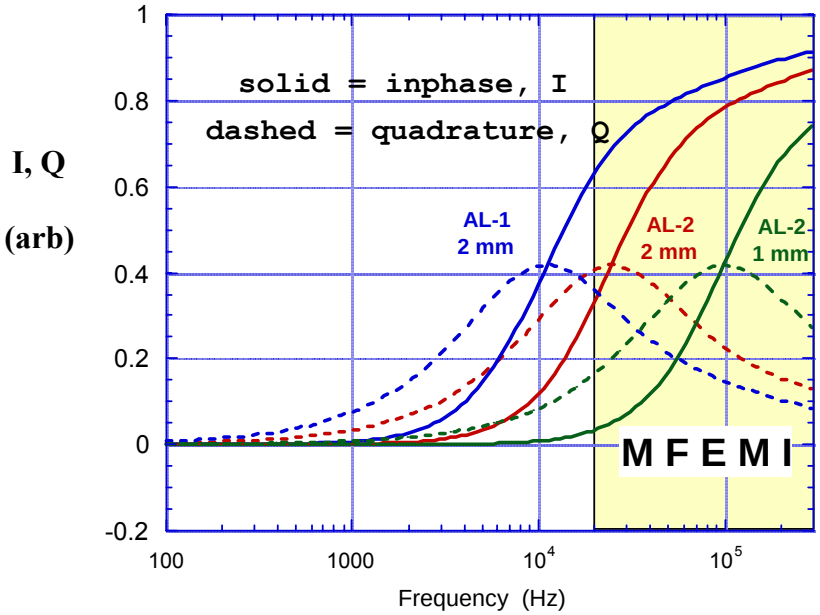

Figure 48. Normalized induced magnetic dipole moments for aluminum parallel plates of 1 mm and 2 mm thicknesses. Two different types of aluminum are considered: AL-1 ($\sigma = 2.9 \times 10^7$ S/m) and AL-2 ($\sigma = 1.3 \times 10^7$ S/m)

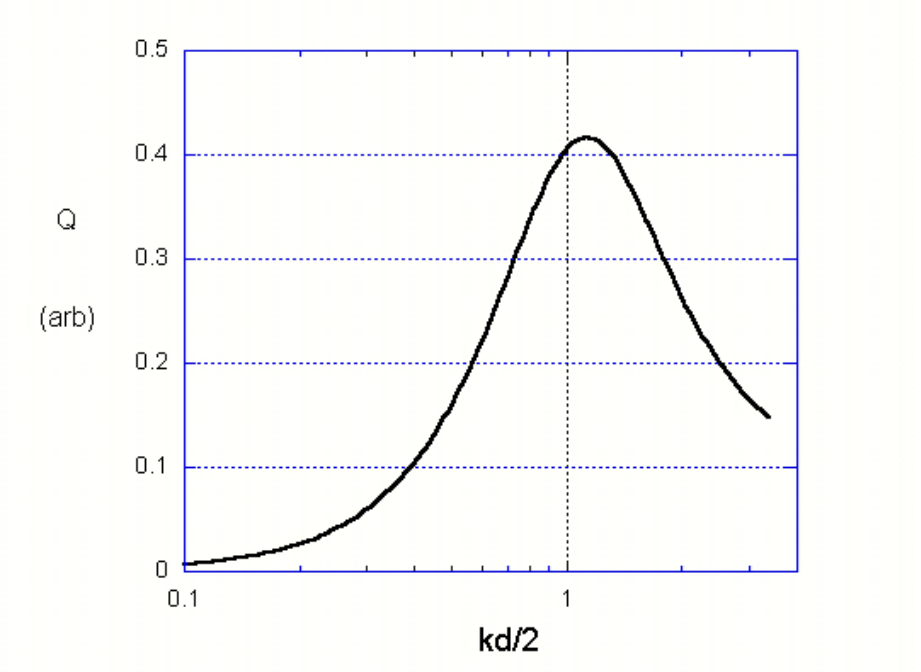

Figure 49. Normalized quadrature component of response from non-magnetic parallel plate, vs induction number.

As explained in Section 2.3, magnetic cases cannot be analyzed with the parallel plate solution, so we exploit the SPA specialization of the analytical spheroid solutions (Section 2.4). For the cases considered in the next two figures, steel-like parameters are assumed, namely $\mu_r = 100$, $\sigma = 5 \times 10^6$ S/m, with a diameter (major axis length) 2a of 10 cm. The aspect ratio a/b = 10 (see Figure 16), so the "plate" (flattened sphere) is 1 cm thick. Recall that the transverse orientation means “edge on” illumination, with the direction of the primary field perpendicular to the axis of rotation, not perpendicular to the long dimension of the object.

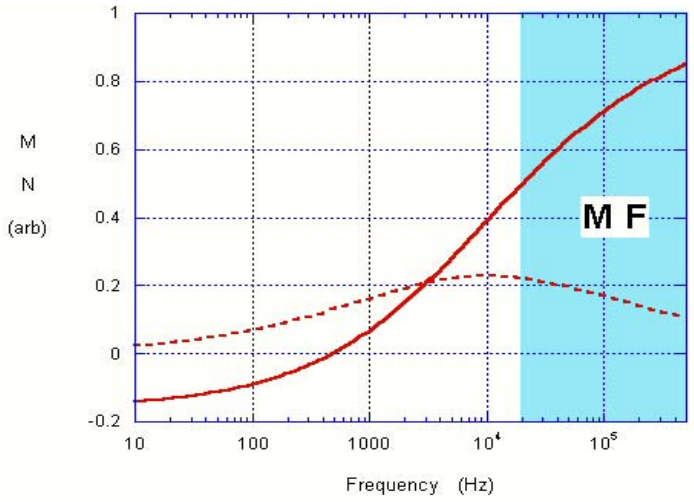

Figure 50. Normalized scattered field (dipole moment) for a magnetic oblate spheroid subject to axial excitation.

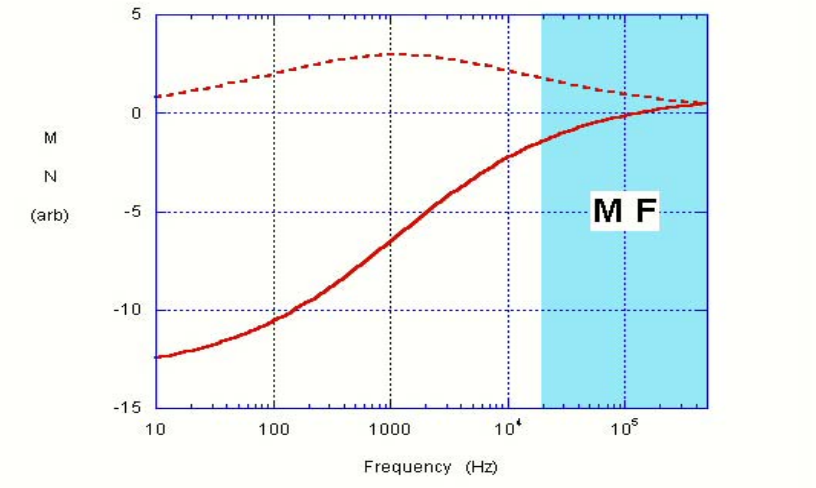

Figure 51. Same case as in Figure 50, but for transverse primary field.

The magnetic moment values are normalized to be unity at the high frequency limit, which, interestingly, one still does not see entirely, even though the upper frequency limit is 500 kHz. The new MF zone is shaded.

The similarities and contrasts between these and previous figures are quite striking. For the transverse case, the object is elongated in the direction of the sensor's view (the direction of the primary field). As in the case of elongated cylindrical magnetic bodies in axial orientation, the edge-viewed

oblate spheroid shows a downward shift in Q peak, relative to that seen for the orthogonal orientation. With the same normalization, the secondary field from a sphere converges on a low frequency value of -2, as μ_r increases. Compared to that, the inphase component magnitude in Figure 50 is remarkably small as we approach the static limit. Further, it rises steeply from its low frequency value, *crossing the quadrature component before the peak in the latter*, and converging on a relatively high value as one approaches the PEC limit. To our knowledge, this relation between the components has never been documented before. In terms of relations between the components, the situation is reversed for the transverse orientation (Figure 51). In that case, the inphase component heads for a much smaller value near the PEC limit, relative to both the height of the Q peak and the magnitude of the low frequency limit. It's almost more accurate to say that the I and Q curves converge as frequency increases, instead of crossing. These distinguishing details of response could not be observed very well, without the MF range.

As a final note on the oblate spheroid solutions, we examine the effect of increasing the spheroid diameter, while maintaining the same thickness. The material parameters are the same as above. Figure 52 and
Figure 53 show results in terms of the Q component, when the diameter of the oblate spheroid changes from 10 to 20 cm. In the axial case, this pushes the Q peak lower, as induced currents form larger loops. In the transverse case, the sinking of peak Q peak frequency is reminiscent of that occurring for magnetic cylindrical bodies, when their elongation is increased in the direction of the primary field (Section 3.1). At least for these parameters, for the oblate spheroid both peak frequencies decline in proportion to the square of the change in diameter. This proportionality is particularly logical for the axial case, as we expect the resonance frequency of current loops to be proportional to their radius squared. Relative to our VLF and MF interests, it seems unlikely that enlargements of the object within the size range of interest would shift its responses into the VLF range. However, modest changes in diameter and/or thickness can easily move some response further into the MF zone, and the MF zone will likely be needed to view the approach to the high frequency asymptote.

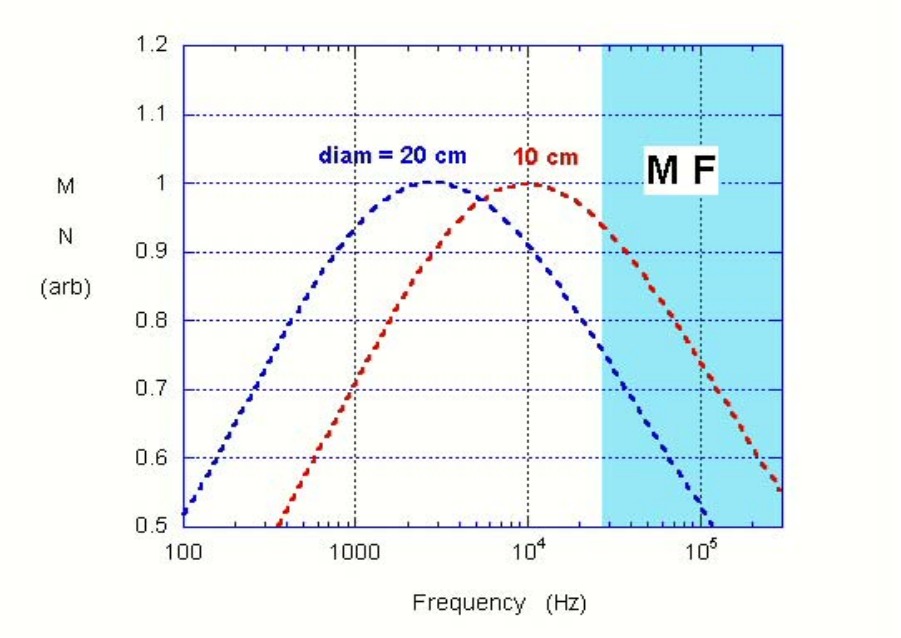

Figure 52. Comparison of Q components from 1 cm thick oblate spheroids, with AR = 10 and 20, for axial excitation, normalized by peak Q value.

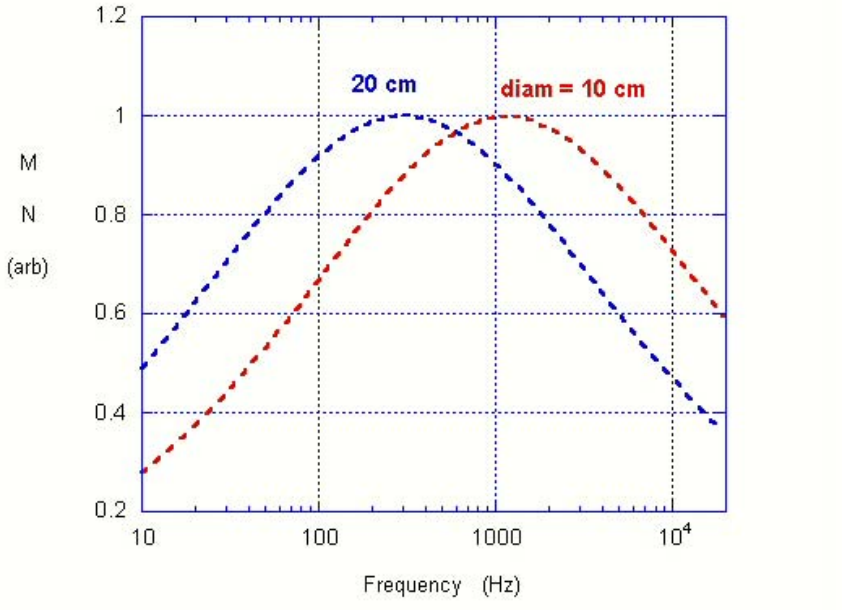

Figure 53. Same as Figure 52, for transverse excitation.

Effect of Degree of Flatness

We have seen in Section 3.1 (Figure 25) that, over the broad band, the same cross sectional area facing the sensor may haved markedly different effects if the target is flattened in other dimensions, that is, if the overall aspect ratio is changed. And the immediately preceding section demonstrates broadband effects associated with changes in aspect ratio, for magnetic materials. Overall, we have seen that aspect ratio can affect the response pattern from different viewing angles, and the responses from the different viewing angles may be quite different. This section illustrates how changes in aspect ratio may or may not affect the higher frequency portion of a target's response, particularly near the PEC limit when material properties are unimportant and only shape matters. In particular, we investigate different degrees of flattening of an initially rounded shape (Figure 54). The shape on the left in the figure is a prolate spheroid, with circular cross sections in planes of constant Z. From this condition (b=a), the object is flattened laterally so that its volume is retained but b = 2a and b = 3a (shape on right in the figure). Figure 55 shows that this has no effect on the high frequency scattered field from an "axial" or end view, i.e. for monostatic observation with $\mathbf{H} = \hat{\mathbf{z}}$. Ultimately, the cross sectional area of each constant Z plane presented to the sensor is the same; the size (area) of current loops in those planes are the same; and apparently the corresponding current moments are the same. However when the same three shapes are viewed from the sides, with primary field and receiver aligned with the X and Y axes, the responses are quite different (Figure 56 and Figure 57). In terms of magnitude, the ordering of the responses reverses between the narrow side and broad side viewing angles. This illustrates how high frequency responses can be correlated with an object's cross section facing the sensor. For UXO discrimination, this holds the possibility of inferring object proportions, i.e. shape alone, without complication by material property effects.

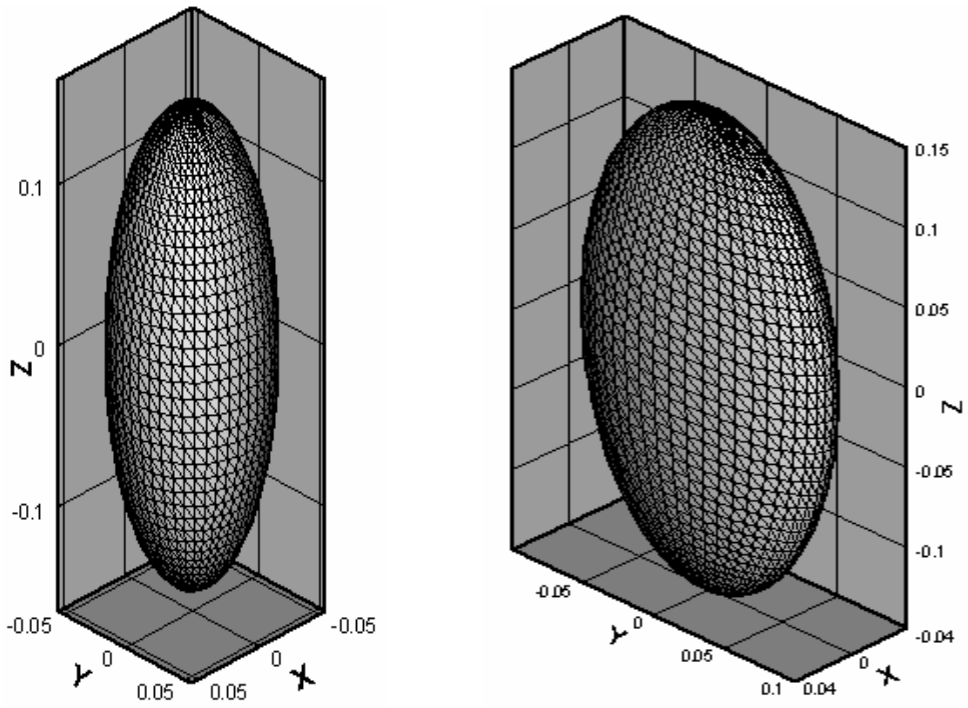

Figure 54. Ellipsoids with fixed length *c* and same volume, but different aspect ratios in the (X,Y) plane. Shading is added only to highlight the shapes.

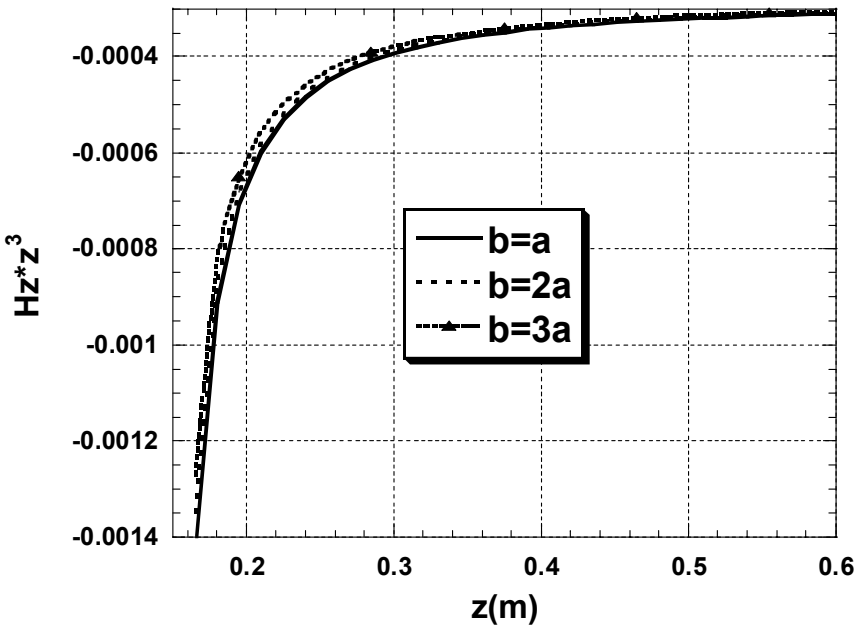

Figure 55. End view of ellipsoids: Scattered fields, scaled by r^3, along Z axis, for the axial excitation case, for the set of three ellipsoids with different aspect ratios but same lengths and volumes.

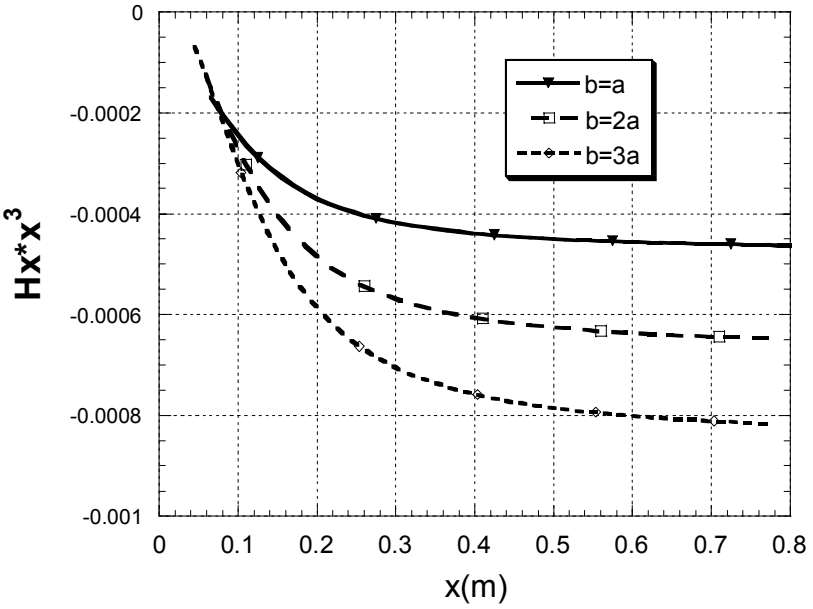

j

Figure 56. Broad side view of the three ellipsoids: Transverse case scattered fields, scaled by r^3, for observation points and primary field orientation along the X axis.

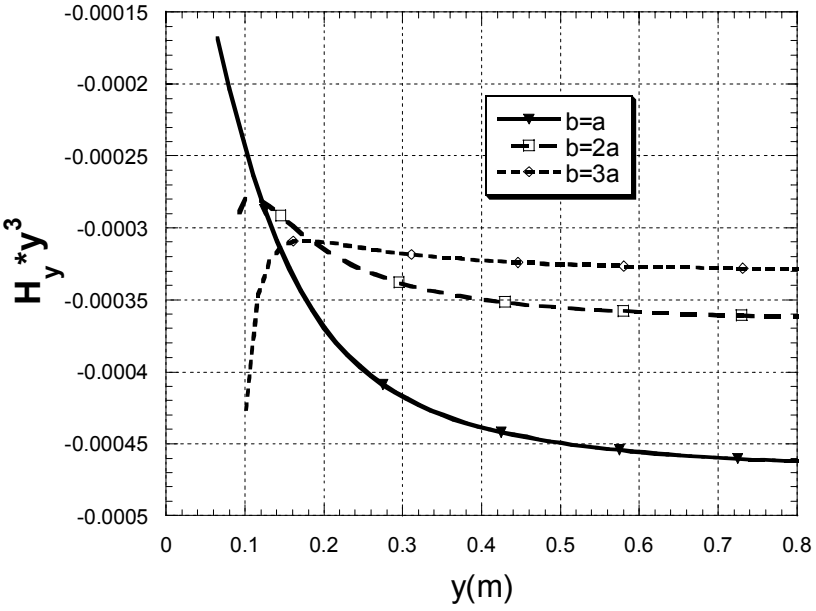

Figure 57. Narrow side view of the three ellipsoids: Transverse case scattered fields, scaled by r^3, for observation points and primary field orientation along the Y axis.

Bent Plates

While some of the objects considered in the last section had curved surfaces, e.g. the oblate spheroids, in overall shape they constituted flat plates. In this section we consider curved plates, beginning with a pipe shaped annulus (with color added only for visual clarity). Simulations at the PEC limit illuminate the basic phenomenology. These are easily executed and provide maps of surface currents that show the nature of the object's response. While at lower frequencies these currents will penetrate the object, over much if not most of the EMI band the induced currents will follow the overall patterns of these high frequency surface currents. The figure shows currents stimulated by "broadside" illumination of the annulus, together with those induced on a similarly shaped solid cylinder. Both similarities and differences between the two cases are apparent. In both cases, the overall current flow is up one side, over the top, down the other side.

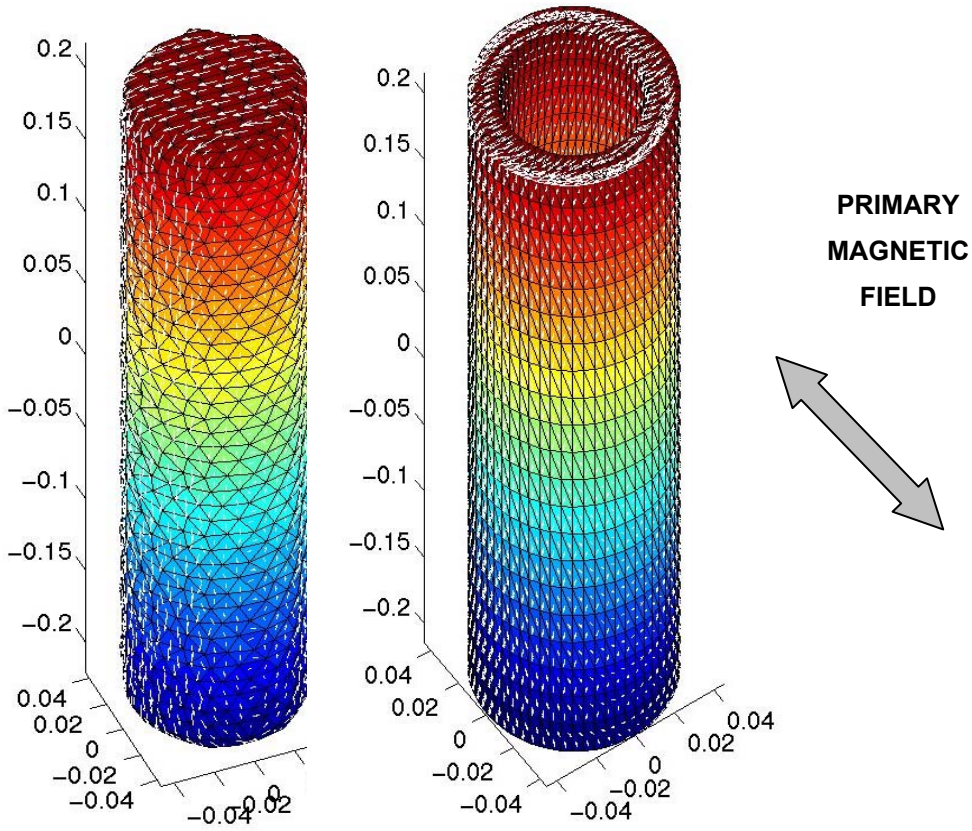

Figure 58. Solid cylinder and comparably sized cylindrical shell, with primary field impinging from the side, showing surface current currents (white arrows) at the PEC limit.

While there is some electrical activity within the pipe interior, for the most part the currents "prefer" not to shortcut by forming loops that travel up the outside, over the top of the pipe wall, and down the *interior*. Instead, the currents from the pipe exterior flow predominantly over the top of the pipe to the opposite *exterior* surface, crowding onto the relatively narrow path over the ends of the pipe to do so. Evidently, by pursuing this route, the currents best satisfy Lentz' Law, which says that they will dispose themselves so as to maximize their opposition to the stimulating actions of the primary field within the cross section presented by the target. By taking the outermost route, the currents form a radiator with the greatest possible magnetic dipole moment; that is, with the strongest response contrary to the excitation (primary) field from our sensor.

Orientation of the primary field in the same direction as the targets' long axes produces distinctly different current patterns. When the primary field passes directly in and out the pipe ends and interior, its scattered field is notably different from that of the solid cylinder (Figure 59).

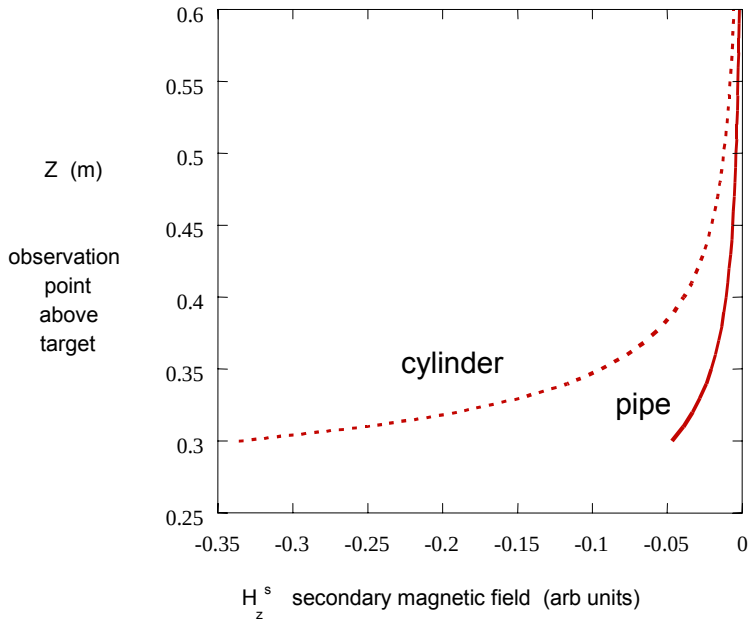

Figure 59. Contrast in induced high frequency secondary fields from axially oriented pipe and solid cylinder, both about the size of a 105 mm projectile.

Here, for the annulus, axial excitation induces the interior and exterior current circulations of the sort shown in Figure 61 and Figure 61. Overall dimensions are the same as in the previous two figures, but in Figure 61, as in Figure 58, the axes have been scaled separately for display purposes.

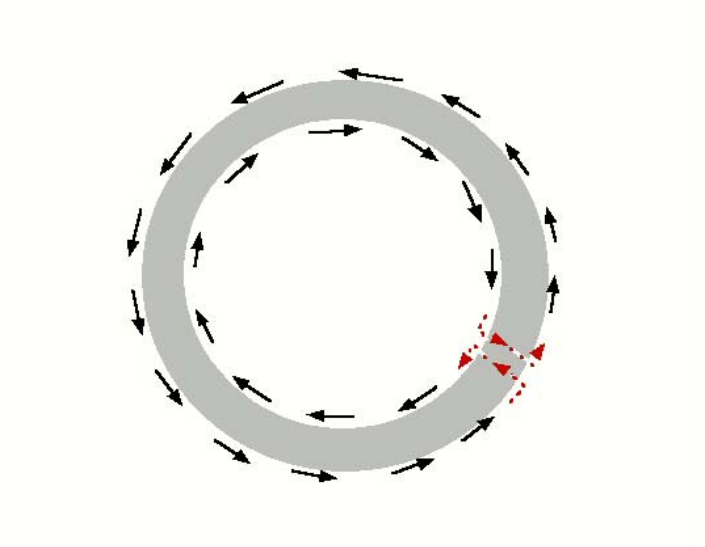

Figure 60. Inner and outer counter circulations of induced current (solid black arrows) on surfaces of an axially oriented annulus, with (dashed, red) cross currents passing through the cut in the case with longitudinal gap.

To illuminate the response tendencies further, the intact annulus case is also compared to one with a longitudinal cut or gap in the pipe (Figure 61). When the vertical gap in the sidewall of the pipe is closed, detailed examination or animation of the current patterns shows two contrary horizontal circulations: one on the outside and another, in the opposite direction, on the inside. Simulations over lower frequency ranges, where the currents penetrate the pipe's metal slightly, show similar current patterns with altered phase. That is, the inner and outer currents are no longer perfectly out of phase (opposite) as they are here in the PEC case. However they remain persistently, substantially out of phase, each oriented so as to minimize total fields within the interior of the metal walls.

The measured response to each target would consist of the secondary magnetic field produced by these currents, as observed above the open ends. For a wall thickness on the order of that shown relative to the outer diameter, what difference does it make if a vertical gap is cut in the sidewall? In terms of our preoccupations, could we distinguish the open end of a UXO from a bent plate? Over much of the EMI band it turns out that the gap produces virtually no difference in the secondary fields. The reason for this is that in both (cut, uncut) cases the currents form virtually the same contrary flows on the inner and outer surfaces, flowing through the gap if necessary in order to complete their loops. Below we investigate this further, over the broad band.

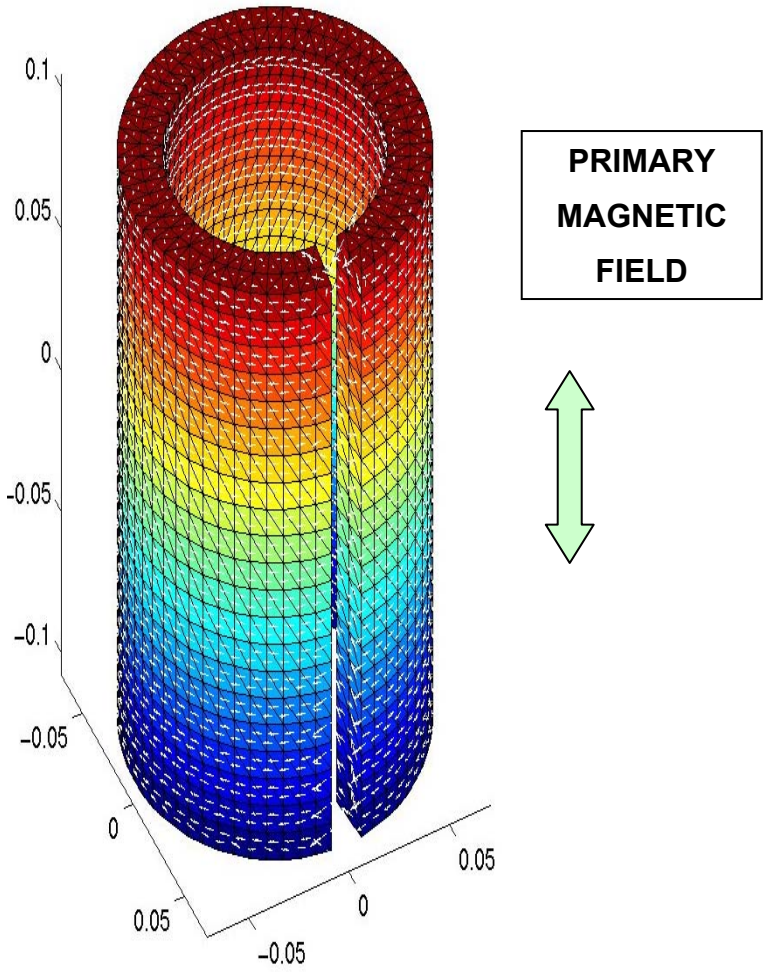

Figure 61. Annulus under axial excitation, with and without longitudinal cut. Shading/ color added only for visual clarity.

Suppose we take something like the cut pipe (annulus with gap in Figure 61) and unbend it, that is, widen the gap further and further? Consider the shapes shown in Figure 62.

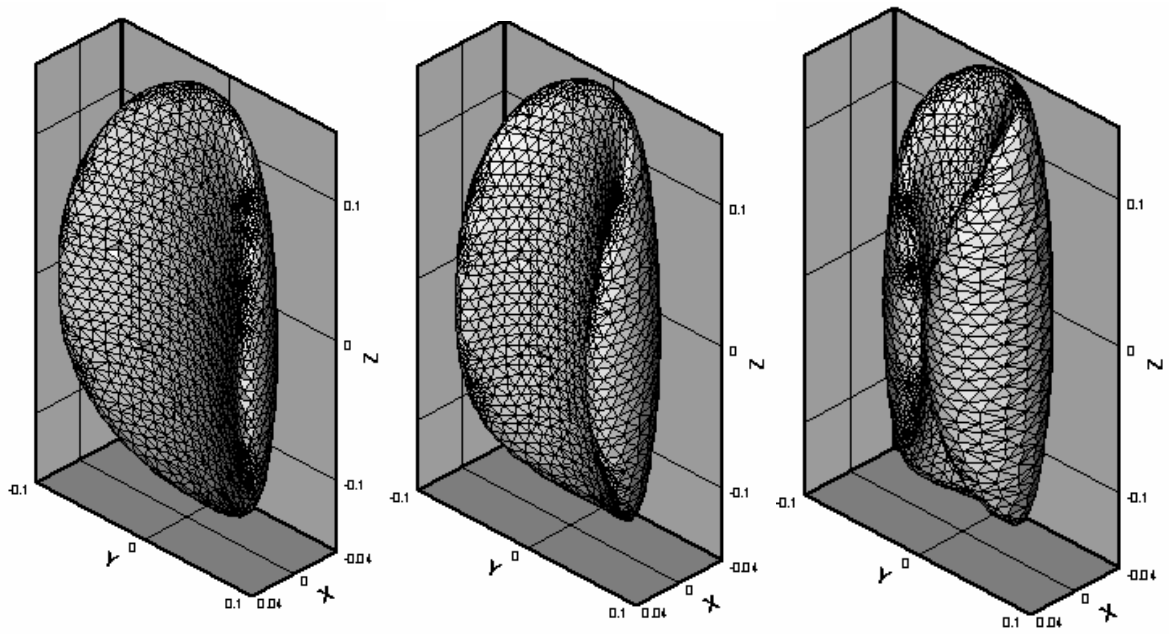

Figure 62. Three bent ellipsoids, with shading added only to highlight shape.

Each shape in the figure is produced by bending a "flat" ellipsoid with a given long axis and shorter axes b = 3a (Figure 54, right). The ellipsoid is bent about its long axis such that the original longitudinal center (X, Z) plane is bent into a circular cylindrical arc, with a different radius of curvature in a each case: $\rho_1 = 0.1$, $\rho_2 = 0.06$, or $\rho_3 = 0.035$. The horizontal cross-sectional areas (at each Z value) remain the same during bending. Subjecting these shapes to a uniform primary field $\mathbf{H}^{PR} = \hat{\mathbf{z}}$ produces the secondary fields at the high frequency limit shown in Figure 63. Very near the end of the object the scattered fields are quite different, even reversing in sign between the cases with different curvatures. However very quickly as a function of distance above the object, all responses converge to the same value. The cross sectional area of the object at each plane of constant Z is the same, regardless of its degree of bending. Current loops around each such cross section therefore have the same area, and it appears that each has the same magnitude. Thus the response for all degrees of bending is the same. We expect that this pattern will prevail over most of the EMI UWB. Of course transverse responses will be different for the different shapes. Thus for discrimination purposes it is vital to obtain multi-angle looks at an object, as opposed to relying on data just from the strongest (here: Z directed) response. Overall, bending has little effect on the high frequency response from a flat plate, when the sensor view is edge-on, oriented along the axis around which the plate is bent.

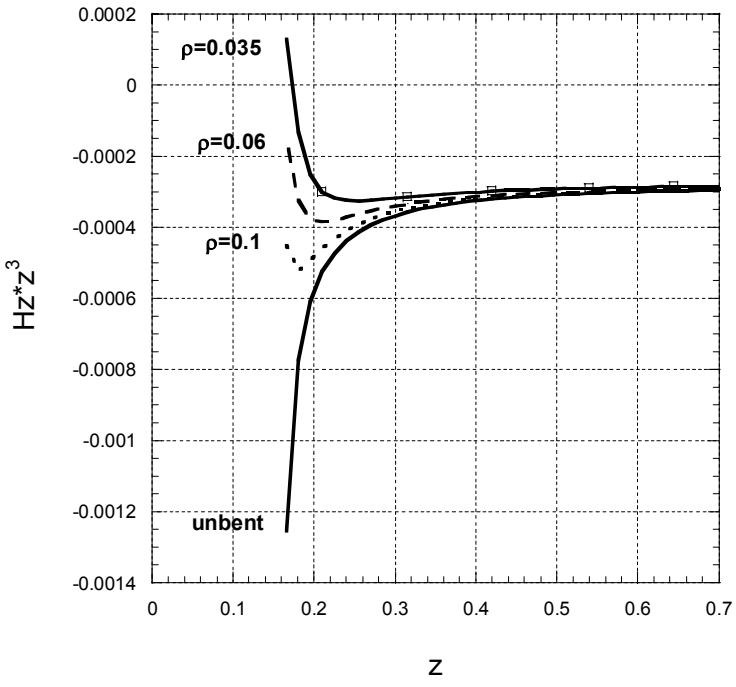

Figure 63. Axial scattered field from bent and unbent flattened ellipsoids, scaled by Z^3, vs axial coordinate Z (m)

Above we have seen that "squashing" a rounded shape (e.g. Figure 54) can leave the high frequency response unchanged. At the same time, other sections of this report demonstrate that that thinned profiles can produce marked changes across lower frequency portions of the spectrum. Such findings hold potential for distinguishing different shapes through inversion processes. In the same vein, let us return to the cut and uncut annuli and note an interesting clue to the presence of the gap, inapparent at high frequency but evident at low frequency, e.g VLF. Along the way we illuminate some basic EMI phenomenology.

Virtually every electromagnetic text displays the basic, prototypical induction case featuring a steady or oscillating current loop with magnetic field passing through the area surrounded by the loop. If an applied magnetic field is the primary forcing feature, then the current is the *effect* and is *induced* by the oscillating field. Texts usually illustrate induction with reference to a wire loop or thin walled tube. The immediately striking thing about this common picture, in light of the discussion and results above, is that it involves *an* induced current; that is, a single, uni-directional current, or at

least a clear net flow of current *in only one direction* around the responding metal structure. If this well established picture holds true, how can one resolve it with the higher frequency EMI picture painted here for the annulus under axial excitation, featuring two distinct and contrary current flows? Or, otherwise put, how do you get from one picture to the other?

For the annulus without gap, Figure 64 demonstrates the sequence of events leading from counter-circulating currents on opposite surfaces at high frequency to a single uni-directional circulation at low frequency. Analytical solution for the case of an infinite, axial annulus provided the curves shown. At high frequency (100 kHz), the currents are quite intense and very close to the surface (note the log scale on the vertical axis). As frequency decreases, the skin depth grows until the currents on opposite surfaces threaten to encounter one another. Eventually the outer circulation expands, at the expense of the inner one, until there is a single circulation (40 Hz).

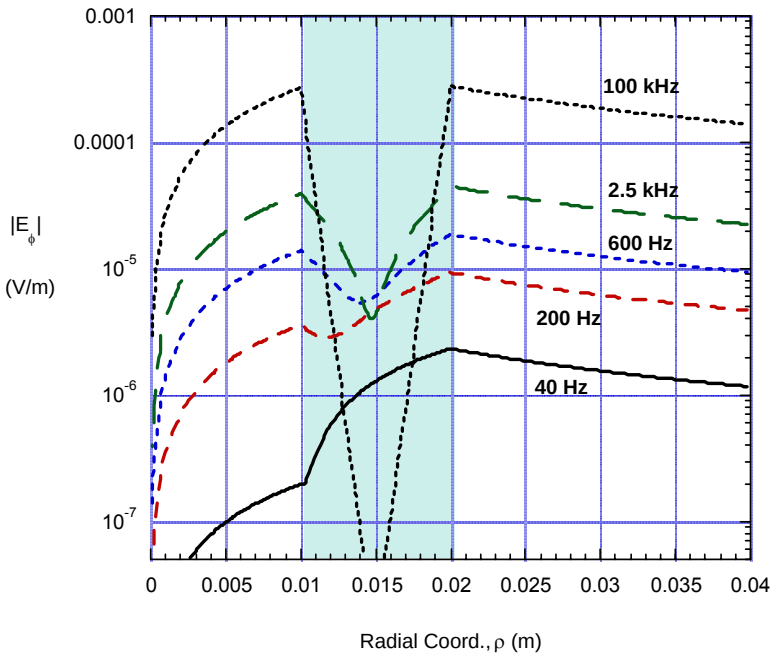

Figure 64. $|E_\phi|$, proportional to electric current, with an annulus interior (left area), the annulus wall itself (shaded region), and the exterior region (right area), for axial excitation at different frequencies. Non-magnetic, $\sigma = 10^7$ S/m.

The analyses above regarding the annulus with a gap generated some controversy amongst study participants in the course of the project. Some felt that any longitudinal cut should kill all circumferential circulation. OK, seeing is believing. Two essentially identical sections of a steel pipe were subjected to axial excitation and the responses recorded, using a GEM-3. Figure 65 shows the piece of cut pipe that was used, and

Figure 66 shows the measured responses. Consider first the quadrature peaks, which reflect volume currents. The higher frequency portion of the Q component for the cut pipe resembles that of the uncut pipe, which harmonizes with our figures and reasonings above: In this frequency region, while the fields and currents penetrate the surfaces somewhat, they flow near the surfaces, following the surfaces. In the case of the cut pipe, they produce secondary fields similar to those from the uncut pipe because the current loops are quite similar, given the cross over currents through the gap. The only way that the pipe with gap could produce a response similar to that of the whole pipe would be via this cross over flow. That is the only way that a similar global circulation could be achieved in both cases. At lower frequencies both objects will "try" to shift to the kind of low frequency current distributions shown in Figure 64 at 40 Hz. However the cut pipe cannot succeed beyond a certain point. In particular, it cannot form a flow across the whole wall thickness, all in one direction. The gap prevents this. Hence the lowest frequency portion of the Q curve for the cut pipe is suppressed, (

Figure 66), relative to that of the whole pipe. The inphase component for the cut pipe also begins to flatten at the lowest frequency measured (30 Hz), indicating that it is converging to its static condition. We cannot see the flattening very clearly however, because VLF data are lacking.

Note two additional things in conjunction with the results in

Figure 66. Our modeling above indicates that the inphase curves for the cut and uncut axial pipes should converge to about the same high frequency limit. Also, the figure suggests that the I and Q components for the two cases will likely cross at quite different frequencies. However, we cannot see this. This is because MF region data were not obtainable at the time these measurements were made. Also, note that use of larger diameter objects, more on the order of most UXO in diameter, would shift the curves to the left, into lower frequencies. A shift of only one frequency decade would mean that we would not be able to see the distinguishing Q curve suppression in the cut case at all, without the VLF sub-band.

Figure 65. Section of steel pipe with longitudinal cut.

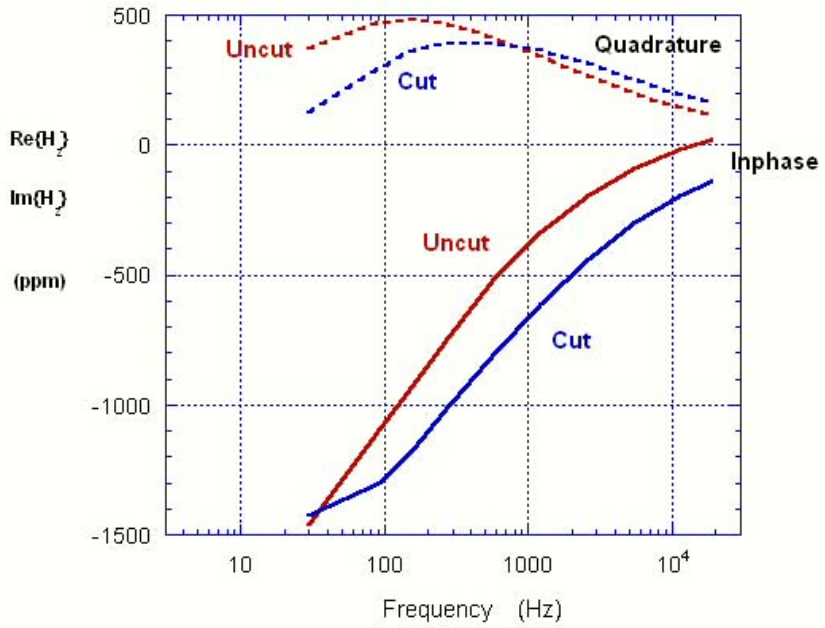

Figure 66. GEM-3 measurements of spectral response from samples of steel pipe, in axial orientation, with and without a longitudinal cut.

Fin Structures

UWB experimental investigations have shown distinctly different responses when a UXO is oriented so that either its tail section or nose section is nearer the sensor, under axial excitation [e.g. 42 and measurements shown below]. The main body of the object consisted of magnetic steel, while the tail and fins were non-magnetic, probably aluminum. In our ongoing work, we are analyzing the response of such geometrically complex targets including their heterogeneous composition. Here we pursue the indication in the data that the fin structures themselves may play a significant role, despite their small volume. To clarify this we investigated EMI responses from 3 objects (Figure 67): a plate, two plates (fins) attached at a right angle, and three fins attached together with equi-angular spacing in their orientations, i.e. each one forming a 120 deg angle with the others. For these irreducibly 3-D cases, numerical results were obtained from an MAS code employing a highly efficient Galerkin formulation [14]. To test the validity of the code, numerical results were compared to data obtained with a GEM-3 EMI sensor, for a right angle structure with two aluminum fins ($\mu_r = 1$). The electrical conductivity was taken from handbook values as 1.2×10^7 S/m, and in terms of the geometrical parameters in Figure 67b, t = 0.25 in, d = 1.25 in, and h = 4 in, with observation point always 1 m from the center of the structure. Figure 68a shows results for a primary magnetic field oriented parallel to the z-axis, i.e parallel to the flat sides of the fins. Figure 68b shows the pattern obtained when the primary magnetic field is parallel to the x-axis, aligned with one fin and perpendicular to the other. Numerical and measurement data agree very well over the entire spectrum.

Figure 69 shows comparisons between the scattered magnetic field from the plate, the two fins, and the three fins, in different orientations. Electromagnetic properties, dimensions of the fins, and observation point parameters were the same as above, where we emphasize that *non-magnetic material* is being considered. In the first orientation (Figure 69a) the primary field is parallel to the flat sides of all fins, and we note that f_p is approximately the same for all three geometries. Amplitude of both components increases as number of fins increases. The quadrature part does not scale by surface area or volume, presumably because of the complexity of current flow around the different angles at the joints. In the real part, the high frequency limit scales approximately as surface area for the two and three fin cases. The primary field orientation for results in Figure 69b is always parallel to the side of at least one fin, but for the two and three fin geometries it also has components perpendicular to other fins. The magnitude of scattering is significantly larger here for the multi-fin cases, in which this orientation induces currents that flow in loops on the fin sides. These current

loops are larger than the flattened loops formed in the previous orientation, producing greater magnitude of response and the commensurately lower f_p that we expect from larger loops. Note that both the spectral pattern *and component magnitudes* are essentially the same for the single fin (plate) in these two orientations, though it presents different edge lengths to the sensor. Together with the small variation of f_p for the first orientation, this underscores the fact that the fin thickness (t) is the controlling dimension when the primary field is only parallel to the fin sides, and it is the controlling factor overall, for a given non-magnetic material.

Figure 69c shows results when the primary field is oriented along the y axis. For the plate this represents excitation perpendicular to its broad side. The shift in its magnitude of response and of f_p value are comparable to those for the multi-fin geometries when they experienced some side excitation. Rotated through the three orientations, the plate produces somewhat more distinct sensitivities than the other shapes, showing slightly higher f_p for excitation parallel to its sides and lower f_p for excitation perpendicular to its surface. Notably, the responses of the other two geometries are essentially unchanged between the second and third (side) orientations. While this is expected for the right angle structure, it is less intuitive for the three-fin geometry. Because responses from any rotation of side excitation can be synthesized (for a spatially uniform field) from linear combinations of orientations b) and c), this implies that the multi-fin response is rotationally symmetric for a "transverse" primary field. The responses for orientation a) are also independent of rotation about the (z-axis), for all three structures. Taken together these observations suggest that we might consider the orientation sensitivities of a UXO with multiple fins to mimic those of a rotationally symmetric object: Despite strongly directional geometrical features, i.e. the fins, rotation about its axis has negligible effect, from all vantage points. At the same time, note that the difference in f_p between side and edge-on orientation is much greater than one expects for a solid elongated BOR (e.g. Section 3.2). This will all be explored in an upcoming publication, for cases with fins attached to a UXO body, with different metals in head and tail.

Figure 70 shows responses from the three fin structures in Figure 69, for the permeable case, with $\mu_r = 50$ and $\sigma = 4 \times 10^6$ S/m. In terms of the geometrical parameters in Figure 67, again t = 0.25 in, d = 1.25in, and h = 4 in, with observation point always 1 m from the center of the structure. The objects are excited by a uniform magnetic field with the same three orientations as in the non-permeable case above. Note here that, for most part, the inphase and quadrature component curves cross at a point on the quadrature component well to the right of its peak. Experience leads us to expect this in the response from an elongated or rounded permeable object. Overall, the flat plate

offers the greatest contrast to the dominant trends, with a large difference between response curve values and patterns for side as opposed to edge-oriented excitation. Compared to the non-permeable case, the plate shows some slight difference in response when the primary field is directed at different edges. That is, in this case the depth in the direction of excitation plays a role, not just the plate thickness. This difference is quite small however, particularly in comparison to the variation of its response when the primary field impinges only on its side (Figure 70c): Here f_p shifts to a *higher* frequency and the magnitude of response is much smaller, all in marked contrast to the non-permeable case. The peak appears much broader and the component curves cross near the quadrature peak. This last, very interesting point is consistent with the pattern noted in the oblate spheroid analytical results, in which the axial case curve crossing was shifted to a much lower frequency, relative to the Q peak, than is seen for most magnetic object shapes in most orientations.

One of the most important observations here is that both magnetic and non-magnetic multi-fin structures show almost no change in response for the different "transverse" excitations. They behave like BORs in the sense their spectral responses show very little sensitivity to rotation about their long or "parallel plate" direction. This has significant implications for the modeling required in inversion calculations, where repeated forward problem solutions are generally required. It is very, very much quicker to produce solutions for something that can be represented as a BOR than for an irreducibly 3-D object.

While multi-fin structures indeed have some response features in common with BORs, can we discriminate single or multi-fin geometries, taken by themselves, from elongated BORs? Based on the material regarding BORs presented in the previous two sections, the answer is *yes*. The three principal directions of the non-magnetic plate exhibit two higher f_p values and one lower f_p one. The non-permeable multi-fin cases produce two principal directions with lower f_p, while a single principal direction shows a higher f_p. Both of these contrast with the non-magnetic elongated BOR case, in which f_p is essentially invariant with change in orientation. In the permeable cases, contrast between the flat plate's response and that from a BOR is immediate: The plate produces signals for *two* orientations with lower frequency peaks that are also notably stronger than that for the single higher frequency orientation. Also, the magnetic plate has two principal directions in which the I and Q components cross far out in the higher frequency portion of the pattern, a characteristic we have seen for magnetic bodies when their elongated directions are aligned with the primary field. In sum, in both the number of lower vs higher frequency orientations, their relative magnitudes, and the relations of the inphase and quadrature components to one another, the plate's response is quite distinct from

the elongated BOR cases. The three-fin magnetic structure shows very little shift in f_p with orientation. Therefore it is unlikely to be confused with a true BOR. Because it only shows slight shift in f_p with orientation, the two-fin structure could probably be distinguished from a magnetic BOR as well. However it does show at least some shift to higher frequency, for two principal directions, and therefore at least some potential for ambiguity exists. In addition, the I and Q components for the two-fin structure cross near the high frequency end of the pattern for only one of the principal directions, namely the one with slightly lower f_p. In effect, this is at least reminiscent of a magnetic BOR. Overall, for the two-fin magnetic structure, discrimination from an elongated BOR would have to be based on 1) the only very slight upward shift in f_p for transverse principal directions for the right angle structure; in fact, it is probably more accurate to say that the peak broadens more that it shifts upwards, as both parallel plate and broadside plate scattering mechanisms are mixed in the "transverse" orientation. And, 2) the contrast between the magnitudes of the peaks in all three principal directions is slight for the finned structure, whereas we frequently see an order of magnitude difference for a magnetic elongated BOR.

The importance of the MF and VLF zones for identifying the signal features discussed above will be case dependent. In the cases examined, most of the fundamental signal characteristics of interest occurred roughly in the mid-band, away from the VLF and MF ends. However even in some of these cases the picture would be incomplete without the new zones. For example the inphase component of the magnetic 3-finned structure in Figure 70a only converges to its low frequency asymptote in the VLF. And the distinguishing features of the I and Q curve relation (crossing) occurs at the edge of the MF zone. For fins thinner than the ~ 6 mm considered, this crossing will occur up within the MF zone. Overall, to obtain the full picture that we need to distinguish between cases like these, and between cases like these and solid bodies, one needs the full EMI UWB.

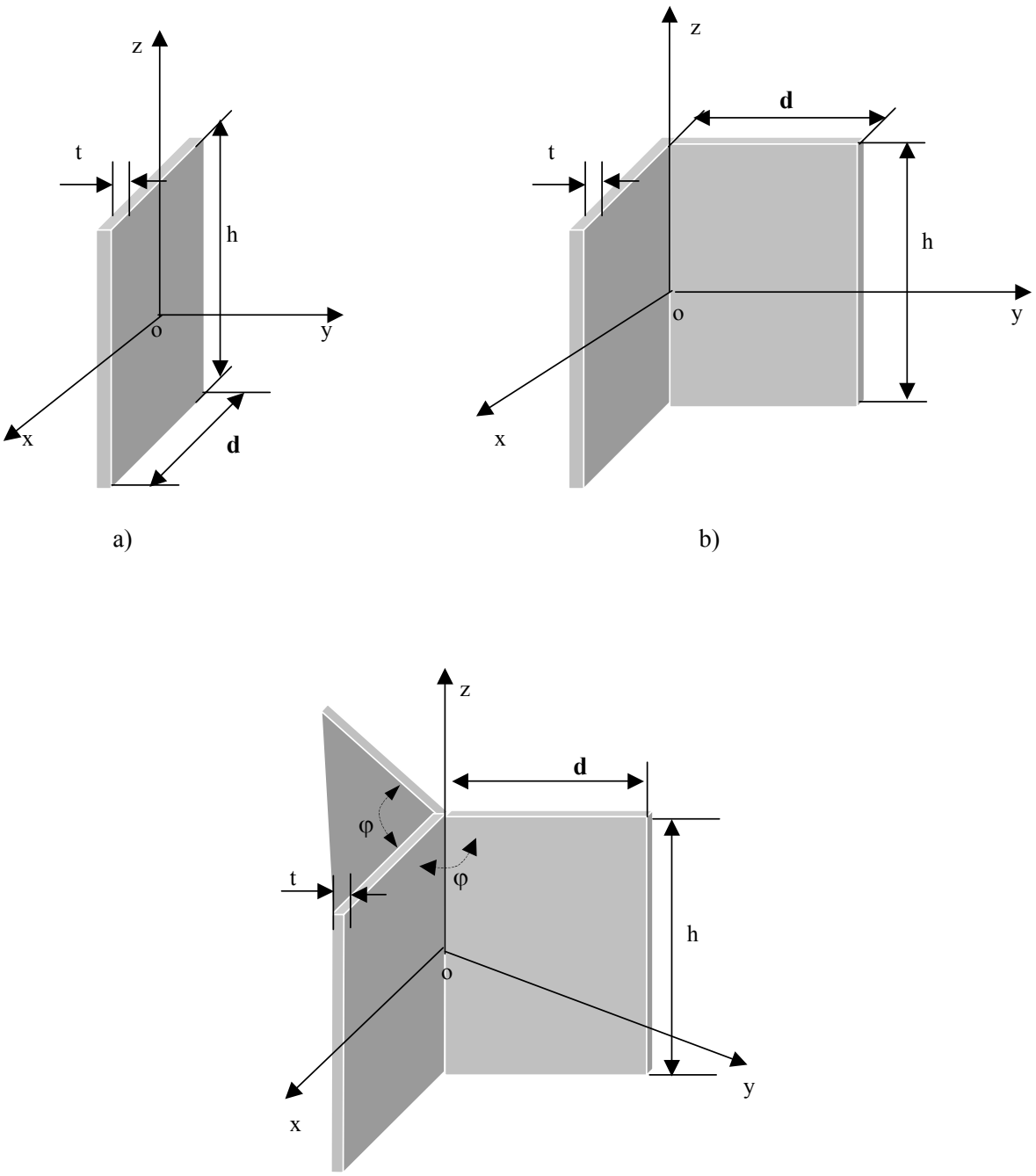

Figure 67. Geometry of plate and fins. In case c, the y axis is not parallel to any fins.

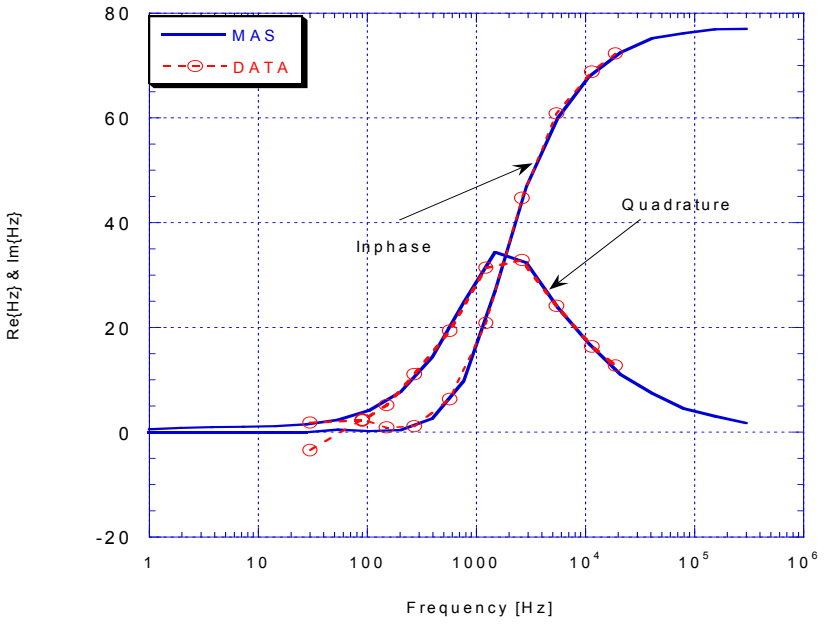

a)

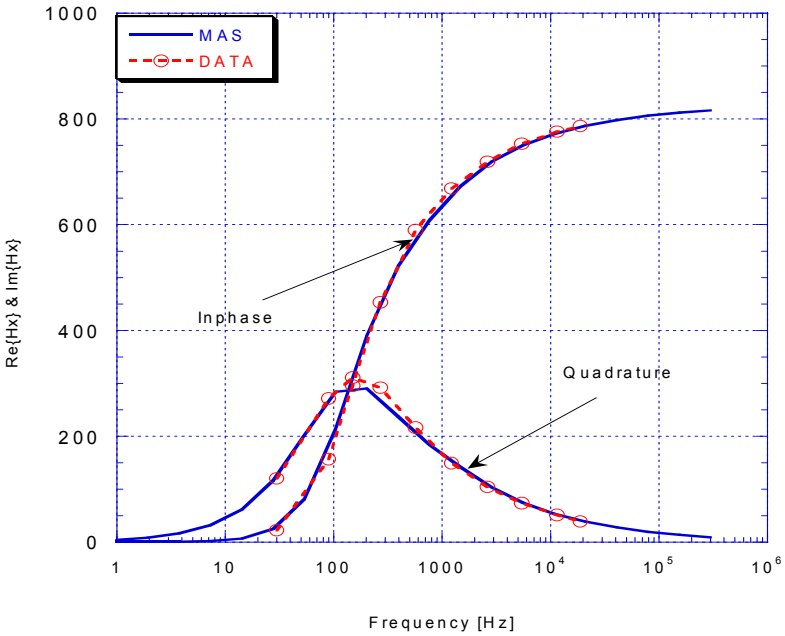

b)

Figure 68. Modeled and measured secondary magnetic field from an aluminum right angle fin structure, under a) end excitation, b) side (x axis) excitation.

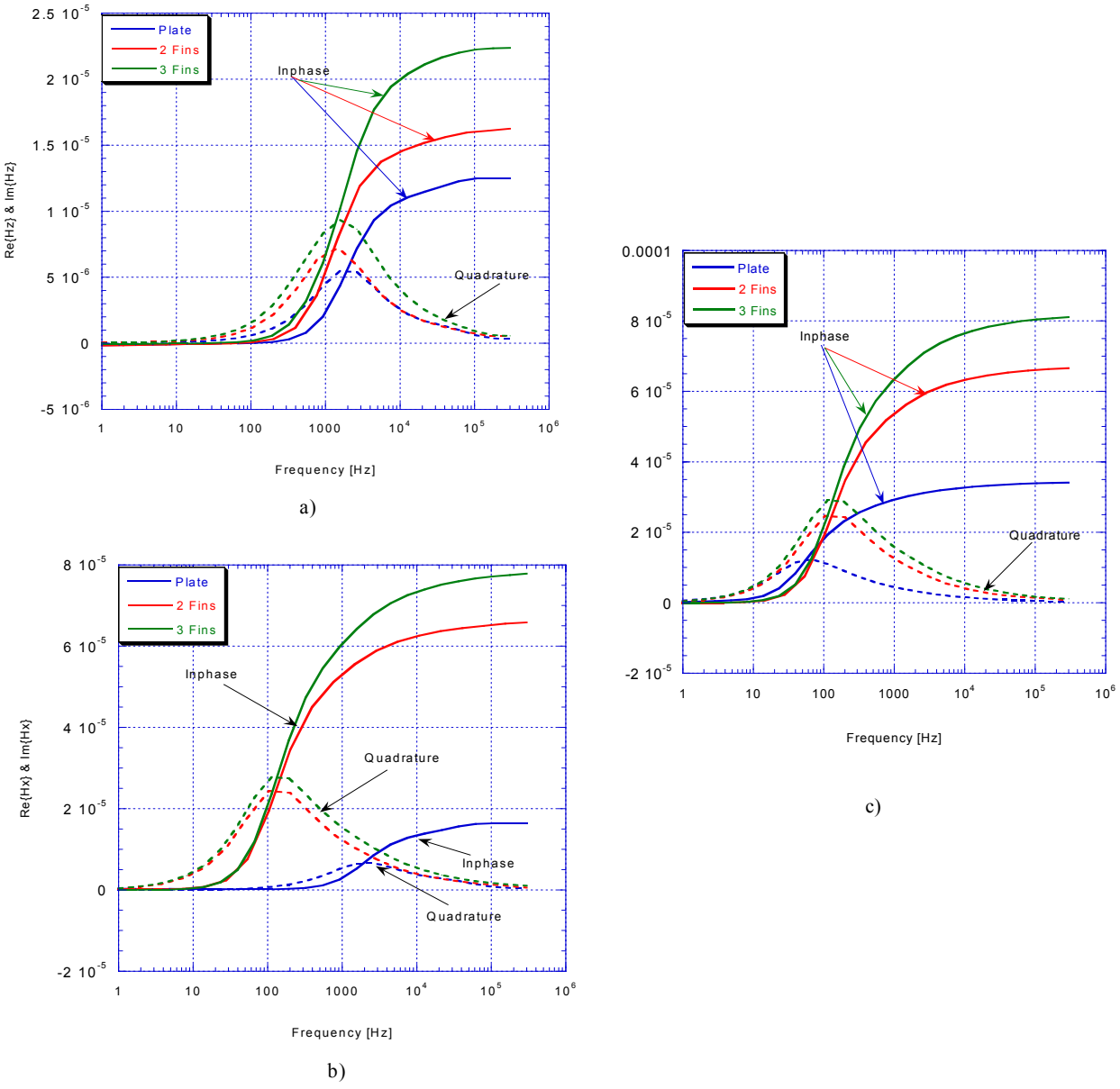

Figure 69. Secondary magnetic field from the three fin structures, for non-permeable material, under primary magnetic field parallel to the a) z-axis, b) x-axis, and c) y-axis.

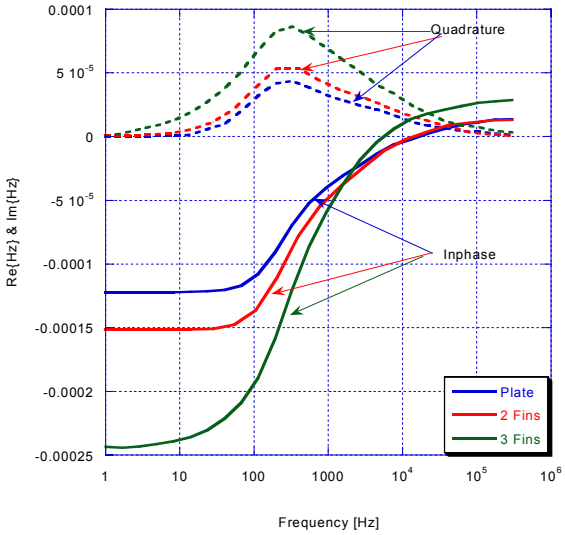

a)

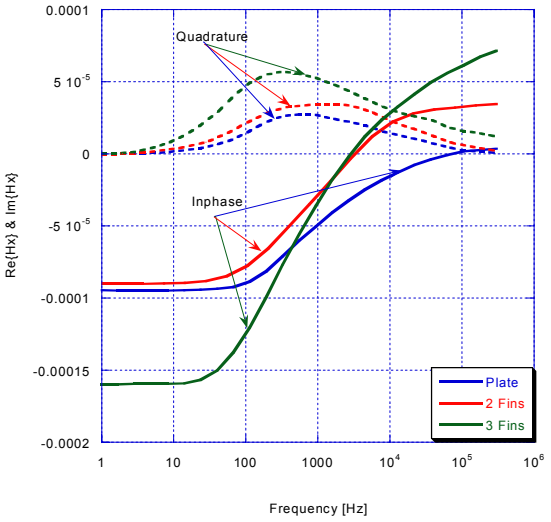

b)

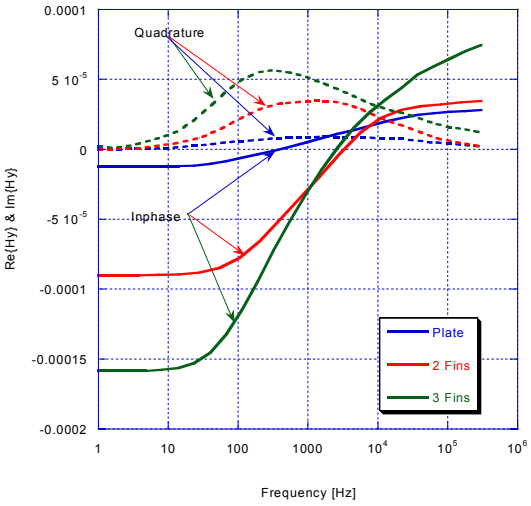

c)

Figure 70. Secondary magnetic field from the three fin structures for the permeable case, under primary magnetic field parallel to the a) z-axis, b) x-axis, and c) y-axis.

Hollow Objects

Even though they do not protrude like fins, producing a relatively independent response, and also do not constitute "fine surface features" as treated above, thin walls in a shell may produce notable signal effects. The figures immediately below show normalized scattered magnetic field values over the combined LF+MF-EMI spectrum, obtained from an analytical solution [e.g. 5], for various wall thicknesses of a metallic spherical body. For a representative non-magnetic material, we have chosen conductivity $\sigma = 10^7$ S/m. The figures show that, to produce much movement in the curves, i.e. to register as "thin," smaller wall thicknesses are required in smaller objects than in larger objects. For a large non-magnetic sphere (Figure 71), seeing the VLF zone allows one to compare the peaks that would appear for solid and thin shell structures. Assuming a conductivity characteristic of copper would move the action further into the VLF; assuming a smaller outer diameter would move the signal activity further out of the VLF. Overall, for non-magnetic rounded bodies, it seems that the VLF will only be relevant to discrimination of wall thickness effects in large, thick-walled, high conductivity cases. For a small non-magnetic sphere (Figure 72), the Q component spreads into the MF zone. However, on the whole, only very small non-magnetic bodies with very thin walls will produce significant effects in the MF region. At the same time, as discussed below in the section on collections of objects, very high frequency scatterers also produce signals that spread over into the lower frequency regions, and therefore may need to be distinguished in some way.

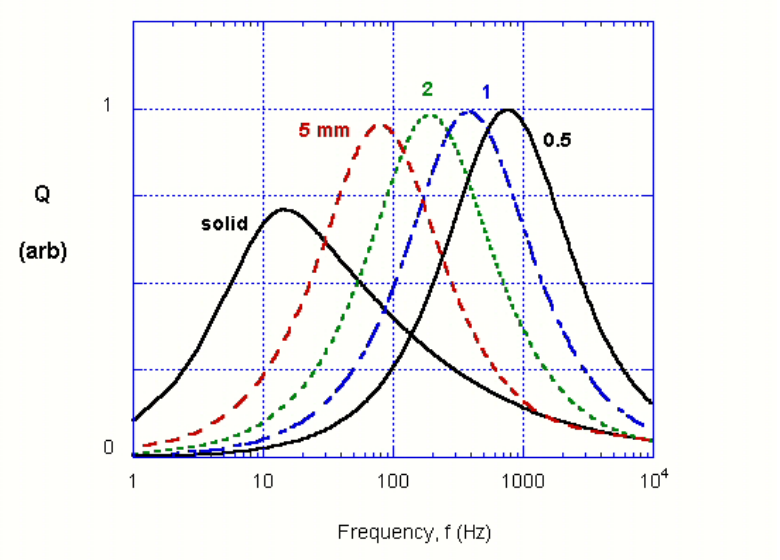

Figure 71. Normalized quadrature component in the scattered field spectrum from a non-magnetic spherical shell with 20 cm outer diameter, $\sigma = 10^7$ S/m, for different shell thicknesses

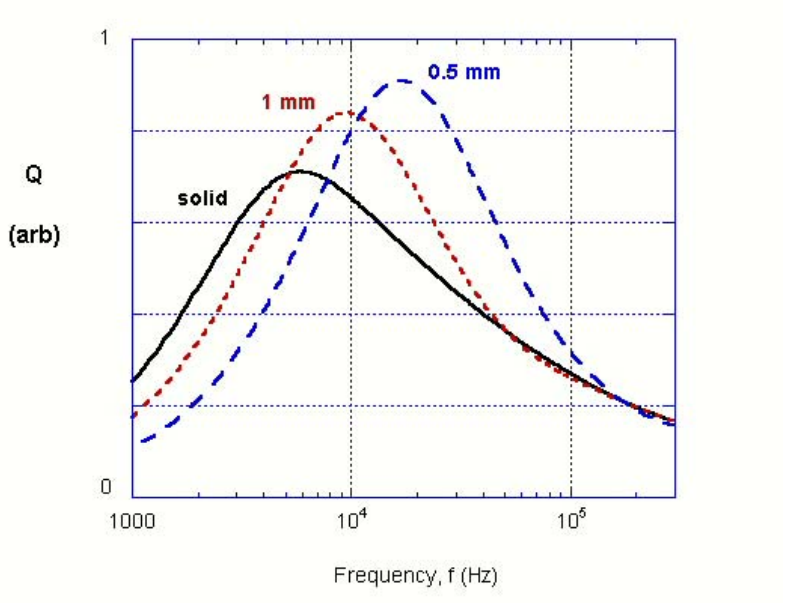

Figure 72. Normalized quadrature component in the scattered field spectrum from a non-magnetic spherical shell with 1 cm outer diameter, $\sigma = 10^7$ S/m, for different shell thicknesses

All cases shown in the figures present the same kind of pattern in which, for a given gross size of the body, i.e. a given outer radius, both quadrature and in-phase components (the latter not shown) approach the same respective high frequency asymptotic values, regardless of shell thickness. That is, at a sufficiently high frequency each sphere behaves like a solid with no internal cavity. For a given size of sphere, i.e. given outer radius, decreasing the shell thickness produces a shift of activity into the higher frequency ranges. For the variations of shell thickness chosen, the overall span of the curves with respect to frequency remains about the same in all cases, on a log scale, i.e. spanning about one decade or so of frequency, regardless of outer radius. Thus for any outer radius these curves might permit one to infer shell thickness by comparing to results from a solid sphere. As the curves shift higher in frequency, they become more symmetrical, indicative of a single dominant circulation resonance.

We define the normalized shell thickness as the ratio of shell thickness Δ to electromagnetic skin depth δ. As a general trend, the value of f_p relative to normalized shell thickness shifts upward with decreasing sphere size. Figure 73 shows results from solutions such as those shown above. Interestingly, this means that we do not see the same picture when the external fields penetrate to the inner surface to any particular degree. Otherwise put, the results do not scale according to skin depth relative to shell

thickness. This is because two scales are important here: only one is Δ/δ, the other is Δ/a. In all cases, we note that at resonance the shell thickness/ skin depth ratio is at most on the order of 1, and is usually less.

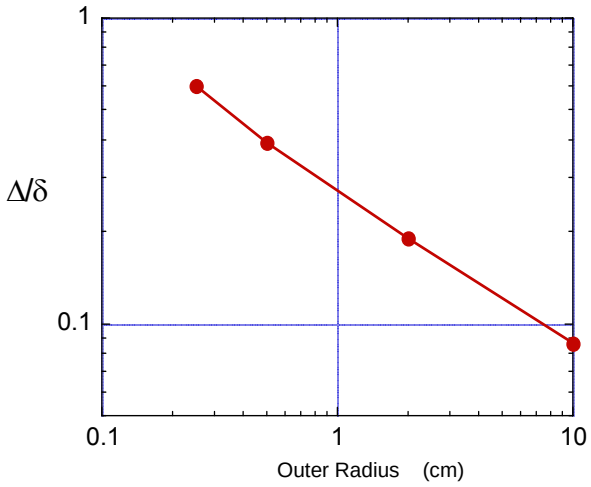

Figure 73. For larger spheres, resonance occurs when the shell thickness is a smaller fraction of the skin depth, other things being equal.

Magnetic spherical shells present a rather different picture (Figure 74). Overall, the higher frequency portion of the curves remains unaffected as shell thickness is reduced, while outer diameter remains fixed. As the amount of material is reduced, the depth of the inphase response near the static limit declines. The low frequency portion of the Q component is also lost, such that the peak eventually shifts higher. It is notable that, for this 10 cm diameter sphere, a shell thickness of 5 mm causes changes in response that are barely visible, relative to the response from a solid. Larger outer diameters will shift this picture to the left; smaller diameters will shift it to the right. Object (outer) diameters on the order of 1 cm or less are required to produce significant pattern activity in the MF zone, as a result of shell thickness. At the same time, especially for smaller objects, one needs the MF region to get a clear view of the invariable higher frequency portion of the pattern, for comparison with the changing lower frequency part. Comparing the low frequency limits of the solid and hollow bodies requires a view of the VLF zone; lower permeability would increase this requirement.

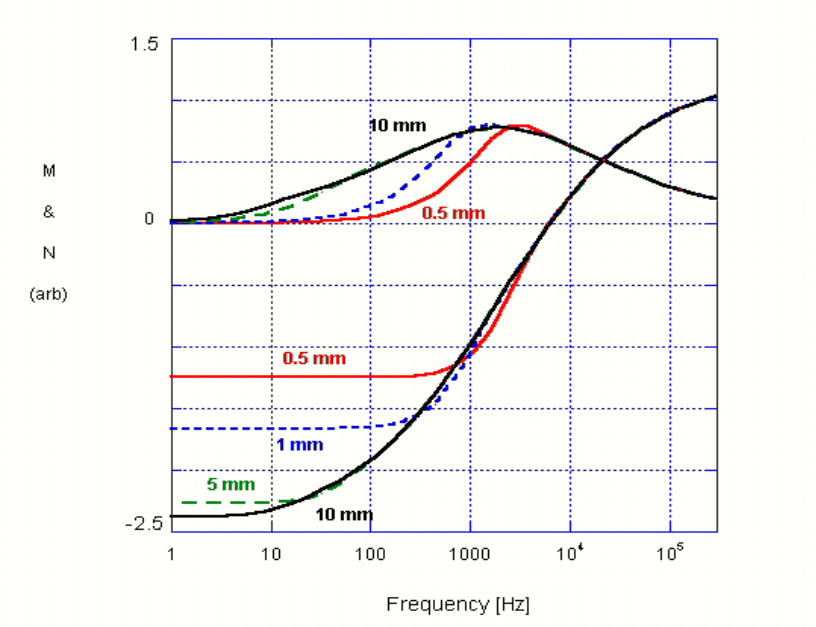

Figure 74. Normalized spectral response from magnetic spherical steel shells with outer diameter of 10 cm, $\sigma = 4 \times 10^6$ S/m, $\mu_r = 150$, for different shell thicknesses.

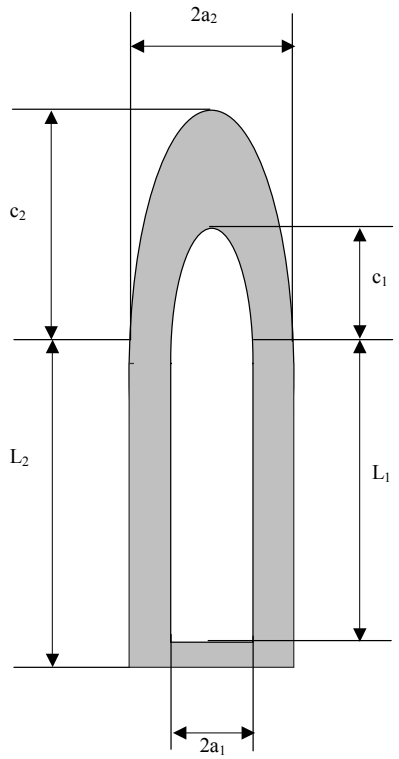

Figure 75. Hollow, UXO-like shape used in simulations

In the preceding examples, in addition to its electromagnetic properties, only the gross dimensions of the object and its wall thickness played a role. We now consider the response of a hollow object more representative of a UXO, with non-uniform wall thickness and elongated shape. For the hollow shell geometry in Figure 75, the MAS code provided broadband simulations for different wall thicknesses, with outer diameter $2a_2 = 40$ mm, length $L_2 = 2.75\ a_2$ and $c_2 = 3a_2$, $c_1 = 3a_1$. We assume that the interior of the object has the characteristics free space. Figure 76 clearly shows significant effects in the secondary magnetic field due to wall thickness at a far field observation point ($x = y = 0,\ z = 1$ m), under axial excitation. When wall thickness decreases, the peak in the quadrature component moves into higher frequencies, increasing in magnitude for the non-magnetic case but decreasing for $\mu_r > 1$. For $\mu_r = 1$ the real part is tied to the peak of the quadrature component, in the middle frequencies. This inphase component shifts along with that peak while maintaining its low and high frequency asymptotic limits. In the magnetic case (Figure 76b), the real part changes primarily near its low frequency, static limit. The transverse orientation shows a similar, though less pronounced pattern (Figure 77). For all thicknesses of magnetic shell, the inphase and quadrature curves converge to the same patterns at higher frequencies and cross at the same point in each case, reminiscent of the pattern noted for the sphere. These patterns indicate that the relation between f_p, the shape of the quadrature peak, the low frequency limit, and the relation of these to the higher frequency portions of the curves, together contain information as to the wall thickness of the shell.

In what parameter ranges might these signal trends find application? It is unlikely that any UXO will have wall thicknesses on the order of 1 mm. Thus a pattern corresponding to that case in the figure would rule out a UXO. For application to thicker shells, note that a larger outer radius will shift the signal activity to lower frequencies. In such cases, noticeable effects of wall thickness will be seen for greater thickness values than for the relatively small item examined in Figure 76 and Figure 77. The MF zone relation between the I and Q components is unaffected by shell thickness. This serves to highlight thickness effects in the lower frequency portion of the spectrum, a contrast that would not be clear without data in the MF zone.

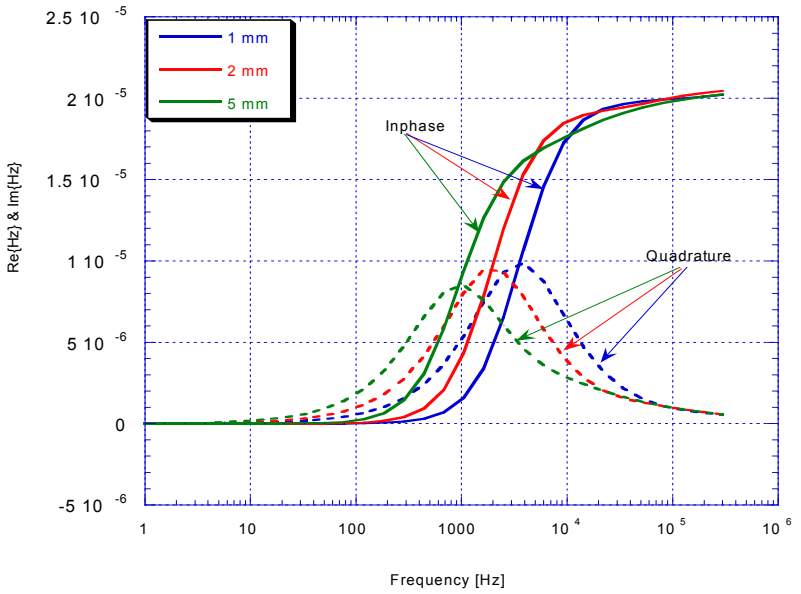

a)

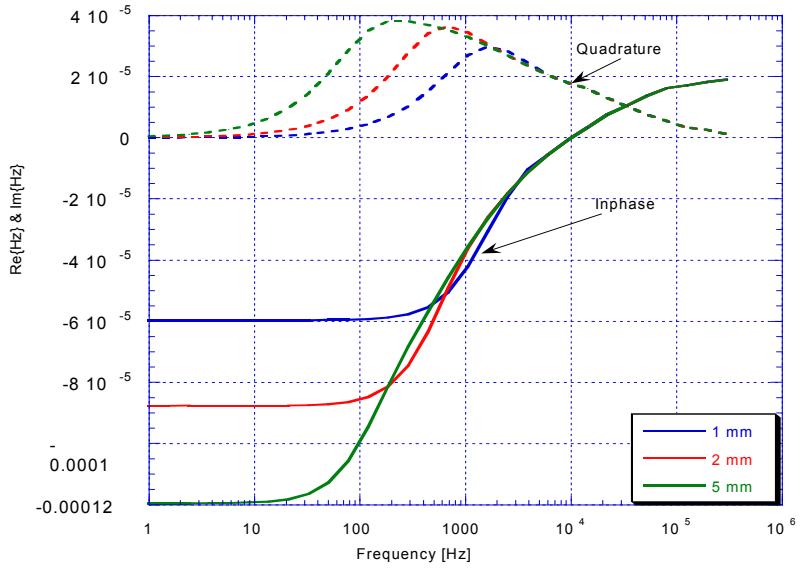

b)

Figure 76. Secondary magnetic fields from the UXO shaped hollow shell, vs frequency, with $\sigma = 4x10^6$ S/m, under axial excitation. a) $\mu_r = 1$, b) $\mu_r = 50$. Different lines correspond to different shell thicknesses $L_2-L_1 = a_2-a_1$.

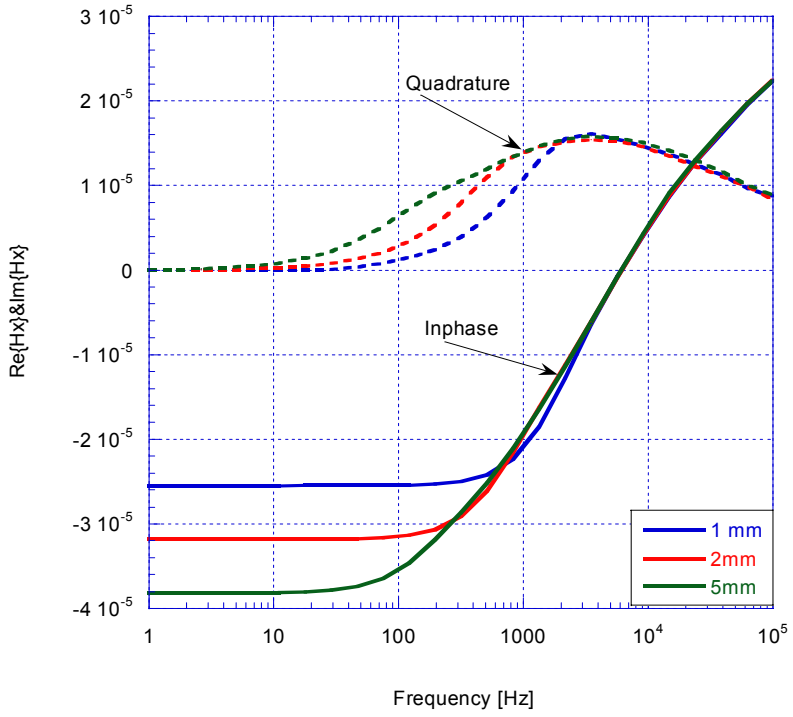

Figure 77. Secondary magnetic fields from the UXO shaped hollow shell, vs frequency, with $\sigma = 4x10^6$ S/m, under transverse excitation, $\mu_r = 50$. Different lines correspond to different shell thicknesses L_2-$L_1 = a_2$-a_1.

In Section 3.1 we have shown that, when elongated solid objects are excited by axial primary magnetic fields, f_p moves rapidly down as target's permeability increases. For example, for a solid cylinder with elongation L/2a = 7, f_p moves from about 500 Hz down to 20 Hz as μ changes from 1 to 100 (Figure 27). For both solid spheres and elongated objects under transverse primary fields, increasing μ pushes f_p into higher frequencies. In the axial magnetic shell cases in Figure 76 and, to a lesser extent, for transverse shell cases in Figure 77, decreasing the wall thickness also increases f_p; however, this does not occur in the manner accomplished by an increase in μ in some of the solid cases. In particular, for decreased wall thickness the only change is in the lower frequency portion of the peak. Also, in the axial shell case, as f_p shifts higher the peak becomes much more symmetrical. This latter trend indicates movement into a single mode type of response and highlights the long, high frequency tail that is present for thicker walls or solids.

How does all this affect the applicability of the frequency-based AR inference system (Section 3.2)? Comparison between f_a (Figure 76, axial) and f_t (Figure 77, transverse) verifies that, for a magnetic hollow shell, equation (69) implies target aspect ratio reasonably well, except for the thinnest hollow shell. For the 2 mm and 5 mm shell thicknesses, (69) implies total length to diameter ratios of about 3.9 and 2.3 respectively, relative to the actual value of about 2.9. More work is needed to treat aspect ratio inference for such geometrically complex shapes, as it also is for composite structures.

Next we consider what happens when one portion of the shell is much more substantial than others, as is commonly the case for a UXO nose section. Again, the shell geometry is that in Figure 75, with geometrical parameters $L_2 - L_1 = a_2 - a_1 = 6$ mm, $c_2/a_2 = 3$, $2a_2 = 40$ mm. The nose thickness, c_2-c_1, is varied from being the same as the wall thickness, 6 mm, up to 40 mm, which also changes c_1/a_1 from 3 to 10/9. Figure 78 shows the response curves for axial excitation. Overall, little changes in these spectra as a function of nose thickness, including f_p. For the non-magnetic cases, the quadrature peak magnitude increases slightly for the thinner nose while the more massive nose only deepens the response slightly at the static limit in the magnetic case. Simulations for transverse orientation of the same case show very similar patterns of response to nose thickness variation (Figure 79). It is noteworthy that the *more massive nose does not dominate the response*; conversely, the relatively thinner sides appear to determine most of the spectrum, regardless of nose thickness.

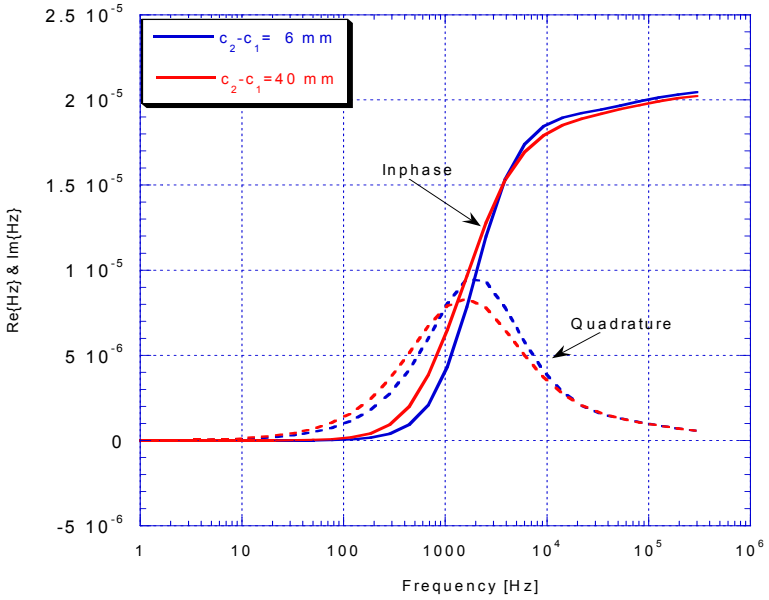

a)

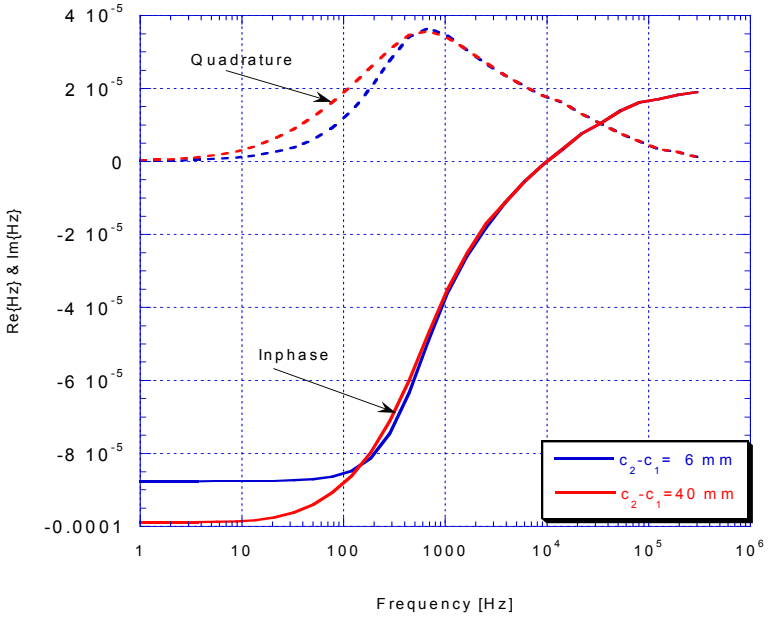

b)

Figure 78. Secondary magnetic field vs frequency, from the hollow shell with varied nose thickness, under axial excitation, with $\sigma = 4 \times 10^6$ S/m and nose thicknesses of 6 mm and 40 mm a) $\mu_r = 1$, b) $\mu_r = 50$

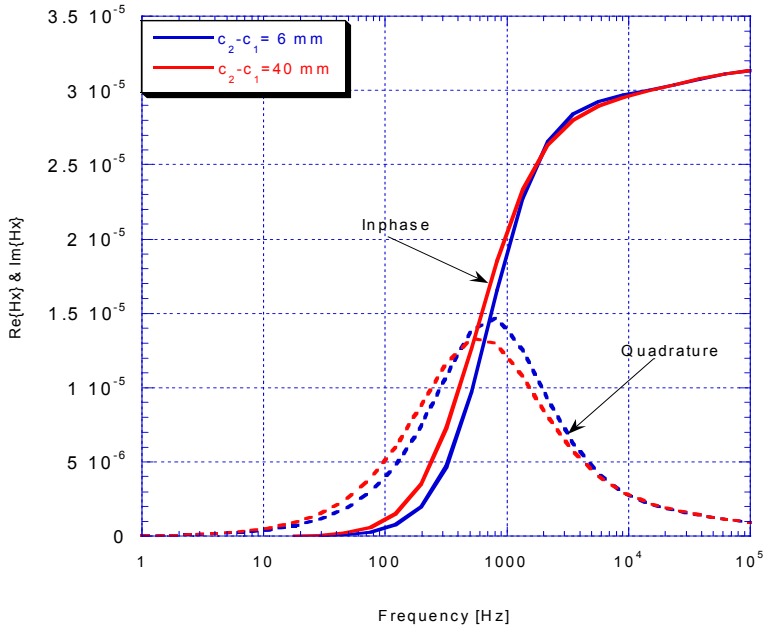

a)

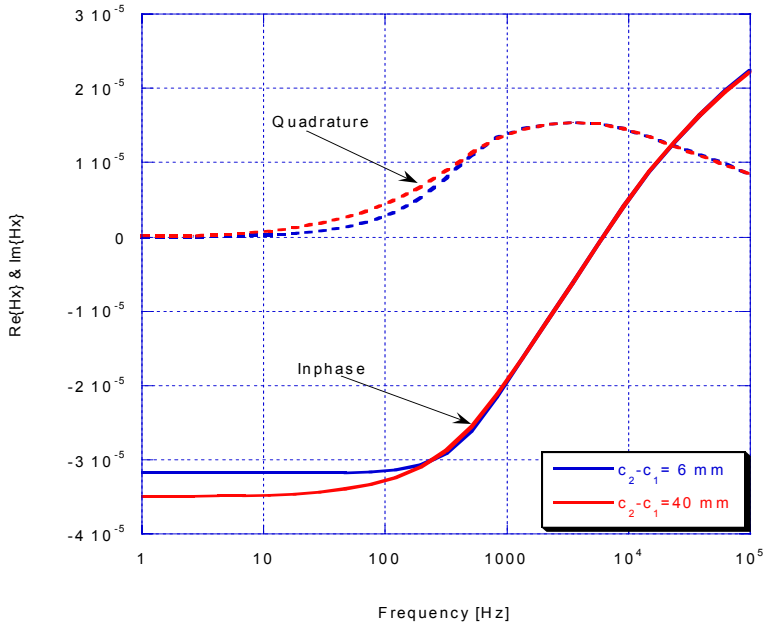

b)

Figure 79. Secondary magnetic field vs frequency, from the hollow shell with varied nose thickness, under transverse excitation, with $\sigma = 4 \times 10^6$ S/m and nose thicknesses of 6mm and 40 mm a) $\mu_r = 1$, b) $\mu_r = 50$

Obscuration of Large Low Frequency Targets by Dispersed High Frequency Clutter

We have seen that the MF region can be relevant to UXO discrimination because some UXO show significant signal content there, including, for small items, resonance peaks. Also, parts of larger UXO may produce relatively high frequency responses, e.g. fins. In some instances the identification of Q peaks within the MF zone can be taken to support the classification decision that the target is not a larger UXO. This last point merits some further discussion in connection with obscuration. The overwhelming reality of real field survey conditions (emphasis on "overwhelming") is the prominence of clutter. While identification of high Q peaks may suggest that an unseen item is not some larger UXO we seek, a more significant issue may be the overlapping of higher frequency responses from small clutter items and lower frequency responses from UXO. Should we be concerned about this? Other things being equal, small items will produce smaller EMI responses. A quite approximate but still useful rule of thumb is that, at least from some reasonable range, equi-distant objects with comparable composition will produce responses in proportion to their volume. By this standard, an item with, say, one-tenth the diameter of another would only produce 1/1000 as strong a response. So how could smaller clutter items be a problem? For two reasons: 1) there may be many, possibly *very many* small items, the extreme being nearly invisible but densely distributed micro-fragmentation; and 2) clutter items, e.g. a "cloud" of clutter items may be near the surface, much closer to the sensor. Using the usual EMI $1/R^6$ signal decay rule of thumb, we note that a near surface object one-tenth as far from the sensor as a deeper object will produce one million times the signal strength, other things being equal. Thus a distribution of small clutter items near the surface may obscure a larger deeper item of interest, even though the inherent response of each clutter item is small.

But can't we distinguish between the spectra of the smaller, near-surface items relative to the larger item, as long as the former do not saturate the signal (compare two curves on the right in Figure 21)? All too frequently, no, although combination of sensing modes may help [26]. The problem is that so many objects produce such broad band EMI responses. It is instructive to consider the *sum* of the two curves on the right in Figure 21, shown in Figure 80. The sum of the two curves produces, more or less, a single slightly muddled peak. Further, any linear combination of the two original curves is possible, and for slightly different object sizes or material parameters, the original two peaks could easily be closer together, with greater overlap. This means, unfortunately, that even small clutter items that produce resonance peaks two order of magnitude higher in frequency than a UXO can obscure the crucial signal features of interest.

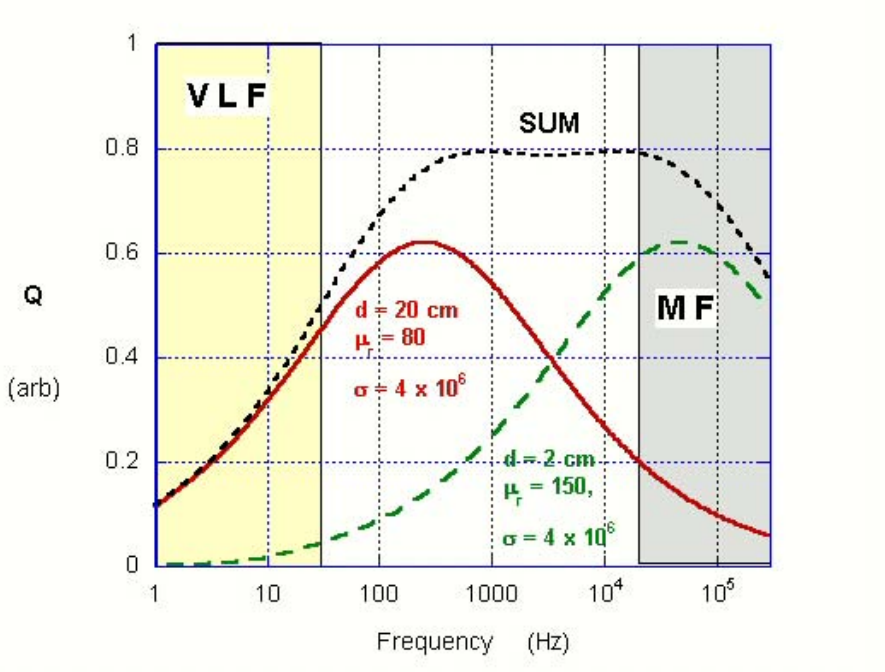

Figure 80. Same as Figure 21, showing the sum of the right-most curves.

This makes it all the more important to achieve good signal definition over the entire EMI UWB, if we are to have any chance of disentangling UXO and clutter responses. As a first step towards distinguishing the responses of small, widespread clutter from single larger objects, we offer the material in the remainder of this section. This material has been developed further and tested against measurements in a follow-on SERDP project. In brief, we adduce some new analytical theory to estimate the sensitivity of widespread clutter responses to antenna height, and contrast that with the standoff sensitivity of larger discrete items. The scheme is to try to identify different spatial dependencies in the behavior of different contributing classes of targets, and also to see when or how different antenna positions might help or hurt SNR.

We begin by assuming that the small clutter items are "well distributed," by which we mean here that they are small and widespread enough so that any surface or volume sub-region contains a statistically representative collection of them. Thus, below, we determine the response from elements of surface or volume based on the number of a class of scatterers per unit area or volume, given the intrinsic response of each scatterer. That is, we assume that *any and every* such sub-region contains enough of the scatterers to produce a statistically meaningful response. We also assume, reasonably, that each small object scatters independently of the others. Thus each sub-region of space produces

average scattering behavior for items in the class, for the sub-region's location and excitation, weighted by the number of small scatters in the sub-region. By "small" we simply mean that each object has dimensions significantly less than that of the overall problem geometry, including antenna height and depths of interest. By contrast, the "target" is a larger scale, non-clutter object of interest.

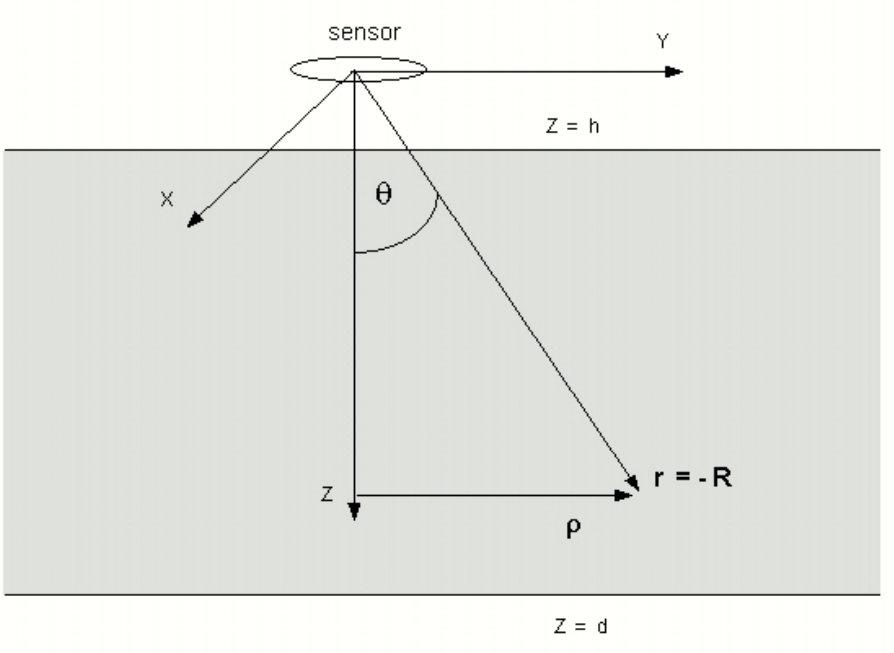

Figure 81. A sensor resides at the origin, below which at distance h is the ground surface. A surface layer extends down to a depth d, relative to the origin.

Figure 81 shows the setup assumed. For a single object, located at **r**, with polarizability matrix **M**(**r**), subject to the primary field $\mathbf{H}^{PR}$, the scattered magnetic field at the observation point $\mathbf{r}_o$ is [44]

$$\mathbf{H}^{s}\left(\mathbf{r}_{o}\right) = \frac{3\hat{\mathbf{R}}\hat{\mathbf{R}}\text{-}\mathbf{I}}{4\pi R^{3}} \cdot \mathbf{M}\left(\mathbf{r}\right) \cdot \mathbf{H}^{PR}\left(\mathbf{r}\right)$$

$$\mathbf{R} = \mathbf{r}_{o} - \mathbf{r}, \quad R = \left|\mathbf{R}\right|, \quad \hat{\mathbf{R}} = \mathbf{R} / R \tag{71}$$

For many, well-distributed such objects, the response to $\mathbf{H}^{PR}$ is

$$\mathbf{H}^{s} = \int dV\, p(z) \frac{3\hat{\mathbf{R}}\hat{\mathbf{R}}\text{-}\mathbf{I}}{4\pi R^3} \cdot \mathbf{M}(\mathbf{r}) \cdot \mathbf{H}^{PR}(\mathbf{r}) \tag{72}$$

where $p(z)$ specifies the spatial distribution of the particles as a function of depth, assumed (statistically) uniform in the horizontal plane. Here we only consider two such distributions,

$$p(z) = \begin{Bmatrix} 0, & z < h \\ n_v, & d \geq z \geq h \end{Bmatrix} \quad volume\, layer$$

$$or \tag{73}$$

$$p(z) = n_s\, \delta(z-h) \quad surface\, layer$$

where n_v and n_s are the number of scatterers per unit volume or per unit surface area, respectively. In these equations and what follows, we assume that the sensor is located at the origin of the coordinate system, i.e. $\mathbf{r}_o = 0$. The vertical coordinate Z is positive downwards and the ground surface is at z = h. The first equation above means that the objects are spread uniformly through a volume beginning at the surface and ending at some depth, d, where $d \to \infty$ implies a half space. The second equation in (73) means that the scatterers are distributed only over the ground surface.

As a further simplification, let us assume that all the scatterers in the i^{th} class are identical, i.e.

$$\mathbf{M}(\mathbf{r}) = m_i\, \mathbf{I} \tag{74}$$

where **I** is the identity tensor, and is not a function of **r**. We will proceed in terms of the scattered field from the i^{th} class, with the understanding that a number of classes of scatterers may be intermixed, without significant interaction, so that their combined effect may be obtained by superposition.

Within a good approximation, EMI sensors emit axially symmetric primary fields, with significant H_z and H_ρ components, but negligible H_ϕ. Thus, if the clutter particles are distributed uniformly in the horizontal plane, they will produce no net H_ρ at the sensor. This is one of the reasons for our current interest in vector receivers in EMI sensors, in which horizontal scattered field

components from discrete targets of interest may tend to stand out. Applying the equations above for the vertical received component H_z^s and assuming an axisymmetric H^{PR}, we obtain

$$H_z^s = m_i \int_{z=h}^{d} dz\, p(z) \int_S dS \frac{1}{4\pi R^3} \left\{ 3\cos(\theta)\sin(\theta) H_\rho^{PR} + \left(3\cos^2(\theta) - 1\right) H_z^{PR} \right\} \qquad (75)$$

This is the expression we use in what follows for evaluating the scattered field produced by a collection of scatterers subjected to representative primary fields. Figure 82 shows a single frequency GEM-3 response magnitude as a function of antenna height, measured above a dispersed layer of coated steel BB's on the ground surface. A numerical expression for the details of the GEM-3 primary field in (75) was used in a numerical evaluation of the integral by quadrature. Agreement with the data is very good, validating the overall formulation.

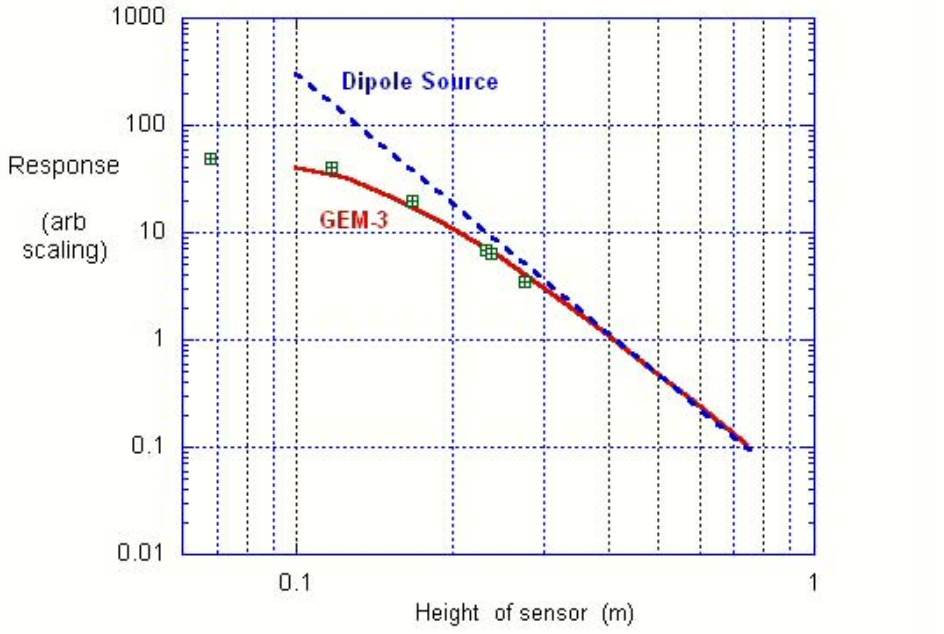

Figure 82. EMI response magnitude vs antenna height above a surface layer of randomly dispersed BB's, measured with GEM-3 (markers), calculated from (75) using numerical expressions for the GEM-3 primary field (solid red line), and for a comparable magnetic dipole source (dashed blue line), as derived below.

Analytically, we consider two other cases, namely the uniform primary field and a dipole excitation field. Large loop systems are currently being considered for a next generation of UXO sensors, which produce an approximately uniform primary field. Alternatively, the dipole is often a good fundamental representative of the kinds of sources in existing instrumentation. In Figure 82 we also compare the GEM-3 results to analytical expressions using two oppositely directed magnetic dipoles to represent the two mutually opposing transmission coils in the GEM-3. The analytical solution for a dipole source is derived below. This dipole representation of the GEM-3 is considerably simpler to apply and is reasonably accurate, on this log-log scale, for antenna elevations above about 20 or 30 cm. Also, in follow-on work, also under SERDP auspices, we represent the GEM-3 field arbitrarily accurately with a collection of dipoles, usually modest in number.

Uniform Primary Field

While a completely uniform primary field cannot be achieved, current proposals and field measurements sometimes resort to very large excitation loops around a section of ground surface, e.g. [45]. At the scale of a localized receiver and the typical depth of interest here, H^{PR} may then be regarded as uniform. In this case,

$$\begin{aligned} H_\rho^{PR} &= 0 \\ H_z^{PR} &= 1 \end{aligned} \tag{76}$$

and (75) becomes

$$H_z^s = \frac{m_i}{2} \int_{z=h}^{d} dz\, p(z) \int_{\rho=0}^{\rho=\infty} \rho\, d\rho \frac{3\cos^2(\theta)-1}{\left(z/\cos(\theta)\right)^3} \tag{77}$$

Over each horizontal plane S in (75), z is constant and

$$\begin{aligned} \rho &= z\tan(\theta) \\ d\rho &= z\frac{d\theta}{\cos(\theta)} \end{aligned} \tag{78}$$

so that

$$H_z^s = \frac{m_i}{2}\int_{z=h}^{d} dz\,\frac{p(z)}{z}\int_{\theta=0}^{\theta=\pi/2} \mathrm{d}\theta\,sin(\theta)\left(3cos^2(\theta)-1\right) = 0 \tag{79}$$

Thus, when subjected to a uniform primary field, a statistically uniform distribution of particles over a surface or a half space will produce null response in localized receiver. This is true for both p(z) in (73); that is, it is the zero value of the integration with respect to θ, at each Z value, that nullifies the entire integration.

This suggests that such a large excitation loop will minimize the response of widespread clutter relative to a target of interest, as long as the clutter is uniformly distributed at least over the footprint of the sensor. It also suggests the main limitation of this result, namely the fact that the clutter may not be sufficiently uniform in its horizontal distribution, and the integration with respect to θ may produce some nonzero value, say V. Then, for the surface layer

$$H_z^s = V\frac{n_s m_i}{2}\frac{1}{h} \tag{80}$$

and for the volume layer

$$H_z^s = V\frac{n_v m_i}{2}\ell n\left(\frac{d}{h}\right) = V\frac{n_v m_i}{2}\left[\ell n(d)-\ell n(h)\right] \tag{81}$$

Thus when the clutter is spread entirely on the surface, any effect on the received signal will decline in inverse proportion to the height of the antenna. When the clutter is spread over a volume layer, the signal will be proportional to the natural log of the depth to which the clutter is found, offset by the log of the height of the antenna. Equation (81) does not converge to (80) as $d \to h$ only because, in the former, we assume that the scatterers are volumetrically distributed with n_v per unit volume, so that a layer of zero thickness contains zero scatterers. Note that the signal from the volume layer declines as the antenna is raised, because both d and h increase but $d/h \to 1$. However this decline is very slow. Figure 83 shows the pattern of signal strength (i.e. $|H_z|$) as a function of h produced by

the volume layer, the surface layer, and by a discrete object at the bottom of each volume layer considered. All signal strengths are normalized so that they are the same at the initial antenna height (0.1 m). The object is assumed to respond as a point target, with signal decaying as $1/d^3$. We see that, as the antenna height ranges up to 1 m, the deeper target's response decays at a rate between that of the 0.25 m and 1 m thick clutter layer, and decays less rapidly than the signal from the surface layer. However the response from the shallow target, at 25 cm below the ground surface, decays most rapidly of all, fading about an order of magnitude more than the others. Overall, the figure suggests that changing the antenna height has little effect on the relative strength of the deeper target's signal relative to clutter responses.

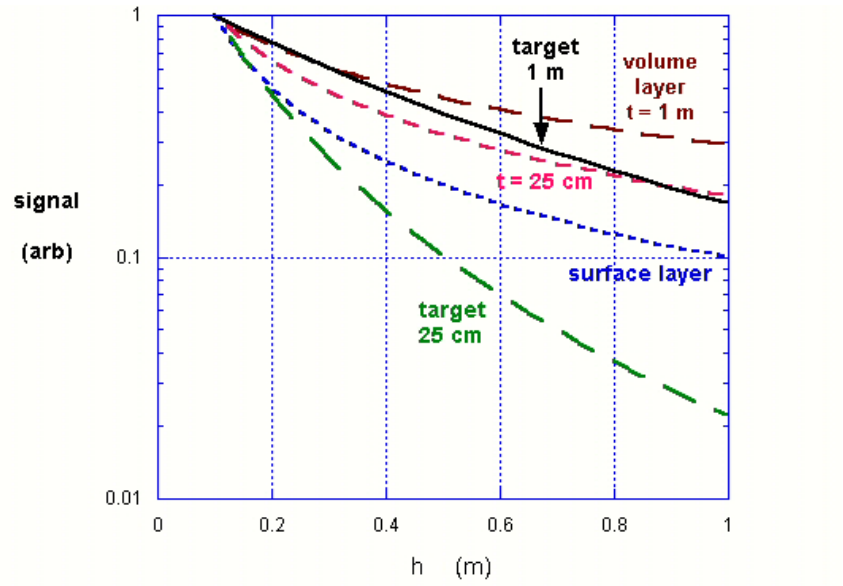

Figure 83. Received signals as a function of antenna height h, under uniform primary field, for different clutter layer thicknesses t and from a target at the bottom of the layer

We see that, as the antenna is raised from 0.1 m to 1 m, the various clutter layer signals decline as the antenna is raised, between about a factor of 3 (1 m thick layer) and an order of magnitude (surface layer). However the shallower discrete target's signal has declined by 2 orders of magnitude. Overall, under these conditions, raising the antenna generally only maintains or decreases the signal to clutter ratio.

Dipole Primary Field

At least in its general features, a magnetic dipole produces a good representation of the kind of primary field emitted by a sensor with transmit coils that are small relative to the field of interest. In this case, the primary field is of the form

$$\mathbf{H}^{\mathrm{PR}} = \hat{\rho}\frac{3\rho z}{4\pi R^5} + \hat{\mathbf{z}}\frac{2z^2-\rho^2}{4\pi R^5} \tag{82}$$

When (82) is used in (75) and the various geometrical relations above are employed, all integrations can be carried out by elementary methods, yielding

$$H_z^s = \frac{17m_i}{192}\int_{z=h}^{d} dz\,\frac{p(z)}{z^4} \tag{83}$$

so that

$$\begin{aligned} H_z^s &= \frac{17m_i n_s}{192}\frac{1}{h^4}, \qquad surface\,layer \\ H_z^s &= \frac{17m_i n_v}{576}\frac{1}{h^3}, \qquad half\ space\,(d\to\infty) \end{aligned} \tag{84}$$

In these cases, as the sensor is elevated, the signal received from the clutter declines much more rapidly than in the previous case, but so does the signal from the target. Treating the latter as before, we assume a here a $1/z^6$ dependency. Figure 84 shows some scattered field strengths for different target depths and clutter distributions. Interestingly, the deeper target signal declines least rapidly and the surface layer response most rapidly. Raising the antenna provides the same or better signal to clutter ratio in all cases involving the surface layer, until the target is as shallow below the surface as the initial antenna height above the surface. Relative to the half space clutter response, the shallowest target fades more rapidly with antenna height, and all others fade less rapidly as the antenna is raised.

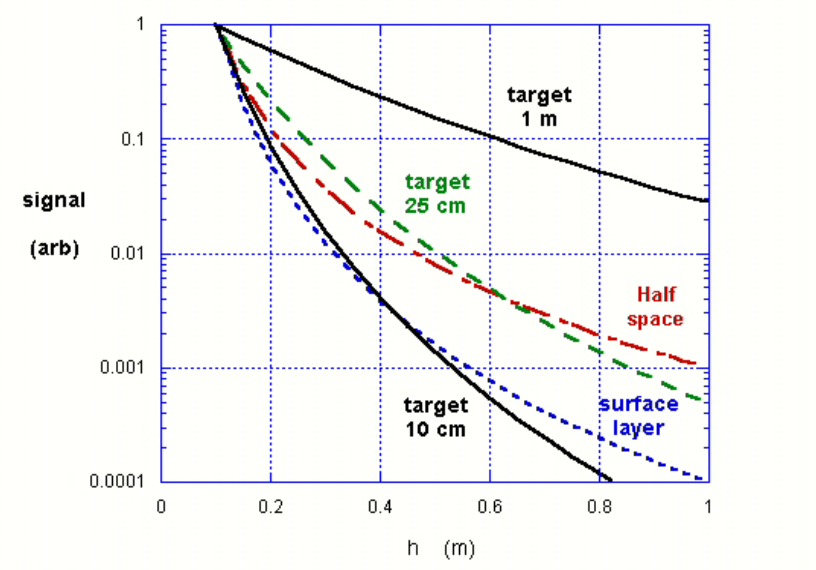

Figure 84. Received signals as a function of antenna height under dipole primary field, for surface and half space clutter layers, and from a target at indicated depths below ground surface.

4. TECHNOLOGY DEVELOPMENT AND FIRST UWB MEASUREMENTS.

4.1 Objective

At the time that this project was undertaken, the Geophex GEM-3 electromagnetic induction sensor represented the state of the art in FD surveying and field measurement capability. It certainly offered the broadest band, operating between 30 Hz to 24000 Hz. Some users, including this PI, considered the signal a bit unreliable above about 18 to 20 kHz, and a high frequency limit of about 20 kHz is often reflected in the preceding sections of this report. While this bandwidth is broad in the context of EMI sensors designed for near-surface geo-engineering applications (i.e. detection of buried pipes, drums, and UXO), the potential benefit of extending that range for UXO identification and UXO/clutter discrimination merited investigation. In particular, we undertook an experimental program to utilize the GEM-3 type coil configuration, with laboratory electronics capable of driving the transmitter (Tx) current as well as measuring the receiver (Rx) coil over an additional decade above the standard GEM-3 range. At the completion of the high-frequency experiments, we modified the setup to operate below the normal GEM-3 frequency range in order to investigate very low frequency (VLF) EMI potential. The decision was made to stick with the basic GEM sensor head configuration and approach because 1) this has worked very well in the past, covering a heretofore unattainable broad band, and 2) the ultimate purpose was to produce measurements with some common calibration and consistent implications. If entirely different devices or approaches were used for different parts of the spectrum, it would have been difficult or impossible to produce a continuous, consistent picture across the EMI UWB. Producing and investigating such a picture was our objective. Nevertheless, as recounted below, some modifications of the system or components of it were employed to best address problems in different frequency ranges, as needed. While we strove for greatest consistency in the measurement system across all sub-bands, the ultimate purpose of the work was the UWB picture that would emerge. In particular, the object was not (necessarily) to produce a handy or integrated system for application.

One might sum up the overall laboratory and technology development mandate as a requirement to address the questions: Can consistent EMI measurements be made across the entire UWB? How? What does the success, failure, or difficulty of doing so reveal about future instrumentation possibilities? An ultimate consideration is addressed primarily in the preceding sections, but is also effectively involved here as well, namely: Do the new measurements harmonize with the theoretical predictions and modeling analyses? Do these, together, look useful?

4.2 Instrumentation and Its Application

Hardware

The primary tool utilized to achieve the extended frequency range of the GEM-3 coil was a Hewlitt-Packard 89410A Vector Signal Analyzer, with a baseline operating range of 1 Hz to 10 MHz, digital control of the current source and digital recording and signal processing capabilities. Some of the features of this instrument include a real-time graphical display capable of simultaneous multiple plots of raw and processed data, current source with built-in digitally controlled waveforms including sine wave and broadband chirp with 0.1 amp at 5 volt output drive, 4 MB recording RAM, two-channel input with auto-gain ranging, and programmable processing capabilities including built-in FFT for spectral analysis and built-in data stacking for signal/noise enhancement.

Initially, a standard 40 cm radius (outer Tx) GEM-3 coil set was used as the EMI sensor [46], consisting of three concentric coils – a primary Tx (outermost), and a bucking Tx coil designed to counteract the primary field around the innermost Rx coil (6.25 cm radius). A preamplifier is built into the Rx coil to reduce signal corruption along transmission cables. A small reference coil is built into the annular region between the Tx coils which provides a phase reference and signal normalization (with respect to primary field); this is brought into the analyzer channel 2. Because the GEM-3 was designed for a more limited bandwidth, the system response rolls of significantly above 100 kHz and SNR degrades, so a custom coil set was built with reduced Rx turns (from 100 to 27). Although the ideal sensitivity is reduced with fewer turns, the bandwidth associated with parasitic capacitance in the coil is improved, resulting in a system that rolls off at higher frequencies (Figure 85).

The HP analyzer signal source is low power and intended to drive low power instrumentation or provide input to signal generators. Much of the data were collected by driving the GEM-3 coils directly with the HP analyzer source. However, we also experimented with two power amplifiers in an attempt to increase signal/noise. The first was an off-the-shelf audio amplifier, which did not perform adequately at the frequencies of interest. The second was an Apex PA05 Power Operational Amplifier with an output voltage limit of 100 Volts, and current range of 30 Amp, and bandwidth determined by the slew rate of 100V/μs. Unexpected non-linear behavior resulted in unstable

performance when it was driven by the high-frequency broadband chirp (the performance for single sine waves was linear). However, this amplifier was essential for the very low frequency (< 50 Hz) experiments, because inductive systems have a signal linearly proportional to frequency and the current directly from the HP analyzer is inadequate at these frequencies.

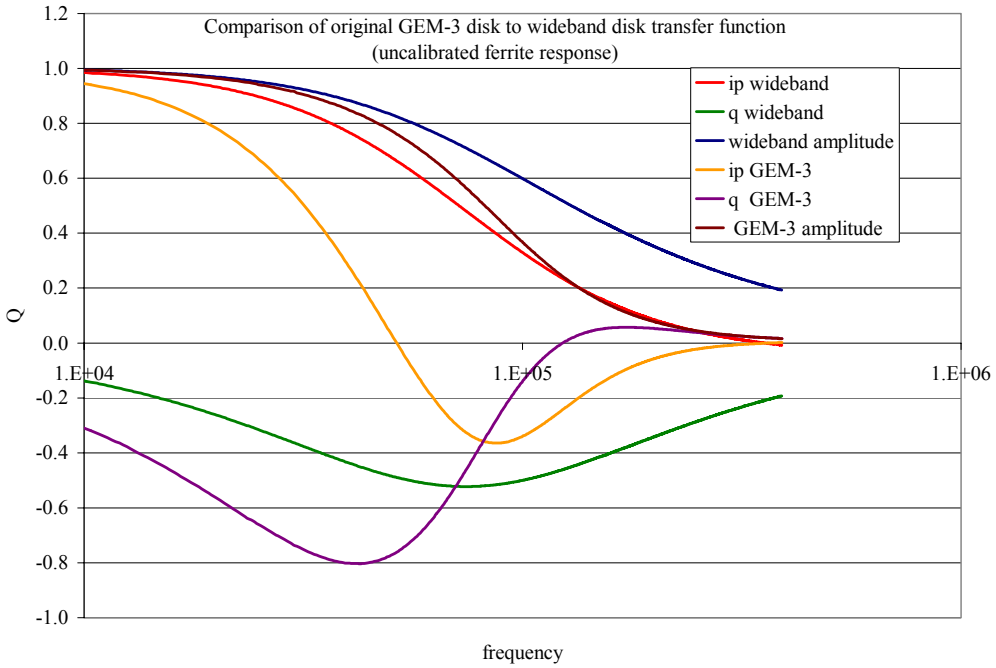

Figure 85. Theoretical coil frequency responses for the standard GEM-3 and the wideband GEM-3 coils, showing the greater attenuation above 100 kHz for the standard coils.

Experimental Procedure

A broadband chirp signal generated by the HP analyzer was used for the high-frequency experiments. The chirp waveform is formulated by a built-in function, with user settings available to define the frequency band, frequency resolution (or alternatively chirp signal duration), and stacking number. Data were stacked (averaged) for typically 200 pulses (about a minute) simultaneously from the Rx and reference coil channels. The HP analyzer automatically performs an FFT and stores the spectrum for each, and was programmed to perform a complex division providing inphase and quadrature (with respect to the primary field) spectrum. A background spectrum is recorded and the analyzer programmed to subtract it from subsequent target measurement spectra. The system was calibrated by recording the spectrum of a ferrite rod. Removing the background from the ferrite

response, changing the sign (i.e. multiply by –1) gives the system transfer function, since the ideal ferrite response is a constant negative inphase, zero quadrature response over the entire frequency range. The transfer function is stored in the analyzer, and subsequent target spectra (background removed) are divided by the transfer function automatically by the analyzer, to remove the sensor system response. This provides spectra from the target over the measurement frequency band. Although the chirp Tx waveform is broadband, its spectrum is not flat. This is not a problem because normalization relative to the reference coil signal removes the chirp frequency dependence. The frequency range used during the first phase of experiments, using the standard coil, was 1.9 kHz to 300 kHz, and for the second phase, initially with the standard coil, and subsequently for the high-frequency coils, was 6 kHz – 390 kHz. The chirp generates weak signal below 10 kHz and during the second phase, data below 10 kHz was corrupted by environmental noise.

The sensor coil was mounted on a wooden stand in the shop at Geophex in Raleigh, North Carolina, cabling taped in place, and targets placed directly below the coils on a height adjustable wooden shelf, using various foam, plastic, or wooden blocks to hold the target in the desired position and orientation. Spectra were displayed on the analyzer scope, and also stored on standard pc diskettes for transfer to a pc for analysis and plotting.

An example of the spectral response of a chrome-steel sphere (2” diameter) is shown in Figure 86, with a theoretical model fit. Conductivity and permeability were not known a priori, and were inferred from these data. Similar model parameters were obtained using a standard GEM-3 over the 30 Hz – 24 kHz range. The discrete spectral spikes were repeatable (the high frequency spikes are harmonics of the lowest) and represent environmental narrow-band noise. This test verifies the measuring system capability over the frequency range used, providing high signal/noise, repeatable data up to 390 kHz. A few narrow-band noise peaks from environmental sources are visible, but do not obscure the broadband response of the target sphere.

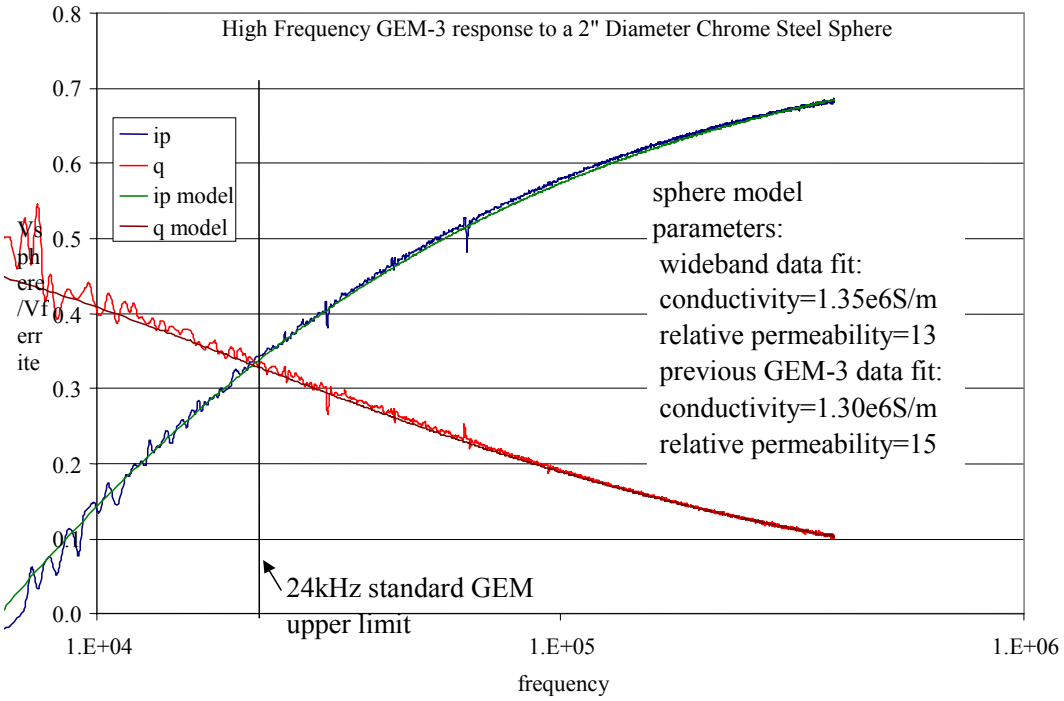

Figure 86. Measured spectrum of a chrome-steel sphere compared to a fit model.

The methodology was modified for the low-frequency experiments, below the 30 Hz limit of a GEM-3. While initially the network analyzer had the appeal that it operated over the entire UWB in which we are interested, ultimately it exhibited significant limitations for the VLF measurements. The chirp signal is not viable at such low frequencies, and the current capability of the analyzer is not adequate for an inductive sensor that depends on the time derivative of magnetic fields. This dependence is characteristic of any receiver system that uses coils and depends on the oscillation of the secondary magnetic field to generate currents in those coils, to provide the signal. The strategy was to make measurements at a small number of frequencies to as low as 5 Hz, with some overlap of the GEM-3 operational frequencies. Single sine wave generation at low frequencies is viable, and the Apex power amplifier was used to provide the required current (requires a high-power DC power supply), driven by the analyzer signal current source. The amplifier was saturated to produce an approximate square wave; this turned out to be stable and repeatable, with sharply clipped sine waves providing ample power at the 5 Hz base frequency and its odd harmonics up to 55 Hz.

Acquisition of VLF data included background removal and ferrite calibration as above. The low frequency data were processed in the same fashion as the high frequency, with the analyzer FFT frequency resolution of 0.5 Hz determined by the recording time interval of 2 s for each sample to be stacked.

Experimental Performance

An example of the capability of the spectrum analyzer setup to provide extended-bandwidth (up to 390 kHz) EMI measurements of an ordnance item (61mm mortar) is shown in Figure 87. Note that the inphase (ip) high frequency asymptotic limit is not approached until well beyond 100 kHz. The significance of the new, higher frequency zone for analyzing the quadrature components is revealed if one covers the MF portion of the plot. While Q peaks for all three (nose up, nose down, and horizontal) orientations reside below the old GEM-3 limit, that is not really clear in two of the cases without the more complete shape information from the MF zone. In any case, without the MF data the overall shapes of the Q components are quite unclear. As in the sphere measurements, data quality up to 390 kHz is excellent.

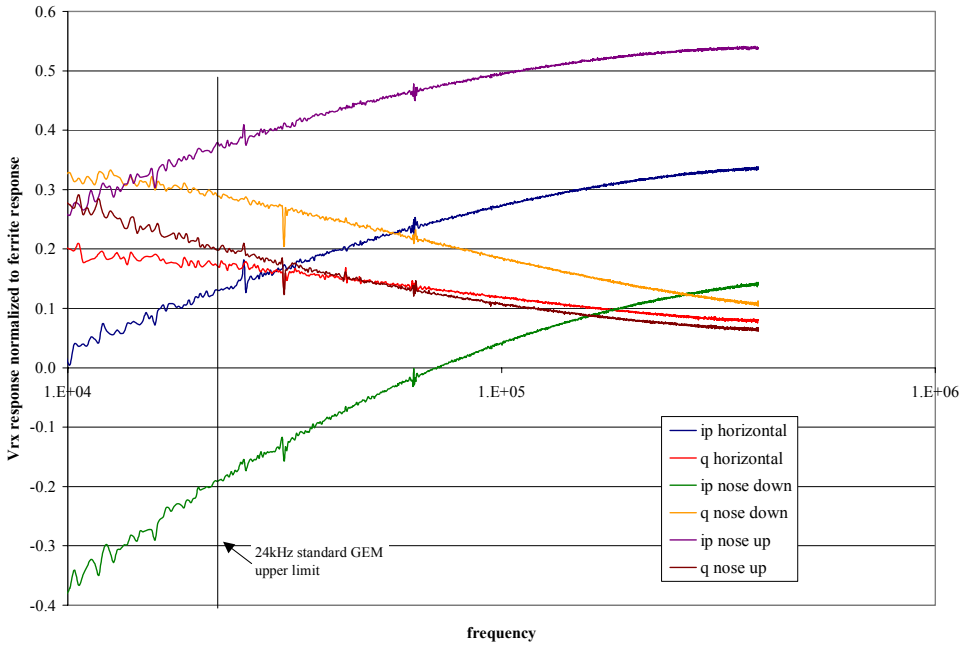

Figure 87. Extended frequency response of a 61mm mortar in three orientations, showing that the inductive limit (high-frequency inphase asymptote) is not reached until well beyond the GEM-3 bandwidth at the time of these experiments.

The extended low-frequency bandwidth performance of the experiments is shown in Figure 88, in which several repeats of the 5-55 Hz response of a 105 mm ordnance in the nose-down orientation are compared along with the average. The measurements required the use of a high-power amplifier driven by the spectrum analyzer sine-wave signal generator at 5 Hz. By saturating the

amplifier, a clipped current waveform approximating a square wave provided odd-harmonics, and the GEM-3 coil provided target responses that could be measured with the spectrum analyzer. Repeatability was good enough to characterize the essential features of the target response. These measurements just catch the peak region of the Q component, more vividly displayed in Figure 41.

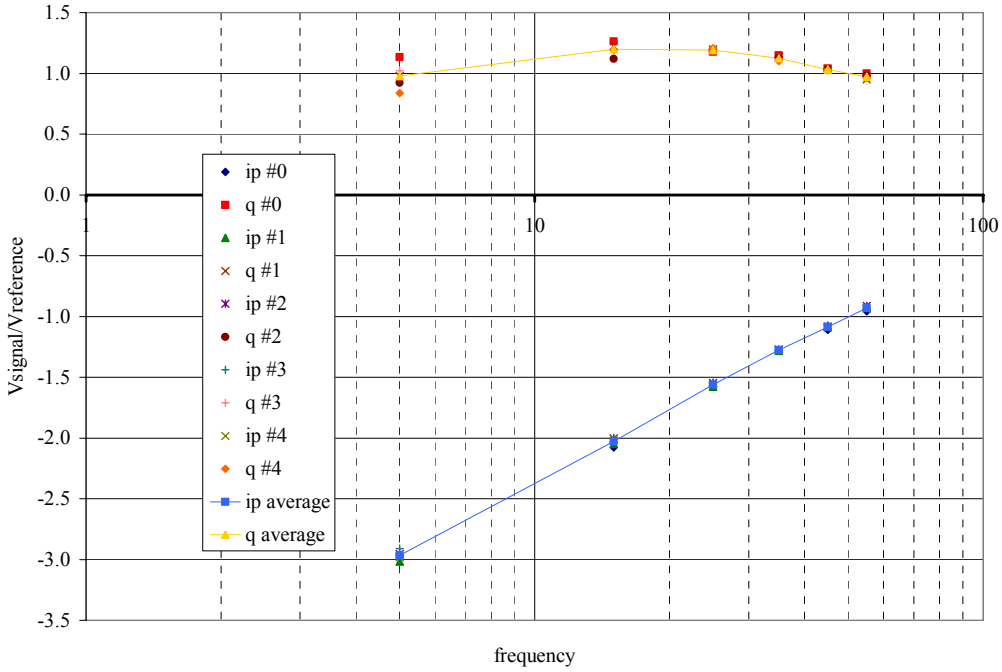

Figure 88. An example low-frequency measurement of the response of a 105 mm UXO, nose down, using the spectrum analyzer, with amplified drive current.

4.3 Implications for EMI Sensor Advancements

These lab experiments and the data displayed below significantly strengthened our orientation to expand the usable bandwidth of FD EMI data into truly UWB dimensions. Since the beginning of this project, Geophex has doubled the GEM-3 bandwidth through the use of improved commercial electronic technology, in particular faster A/D converters that retain the required features of the GEM console. Further increases are planned, with the required investment motivated in part by the experiments performed in this study.

The use of frequencies below the current 30 Hz GEM-3 capability instrument is not fundamentally a problem, but has some practical issues that must be considered for any system depending for signal on the current generated in a receiving coil by the secondary field oscillations ($\partial \mathbf{B}/\partial t$). Inductive measurement systems have input voltages that are proportional to frequency, and thus to achieve adequate SNR requires high transmitter current and long-duration measurement times. Also, sensor motion in the Earth's field can generate noise at these frequencies. This may limit the use of these frequencies to static measurements. However, for discrimination purposes this may simply mean either re-acquisition of targets for a second phase of variously shifted static measurements, or pauses for static acquisitions when targets are detected during a "search and flag" scenario. If discrimination performance is significantly enhanced, the cost effectiveness of such a procedure would still be reasonable. Adding that basic capability to the GEM-3 would be primarily a software change (without increasing the transmitter power). The experimental procedure used in this study allowed assessment of what could be gained.

4.6 Example UXO Measurements over the UWB

UWB measurements were made at different stages of the project, sometimes with loaned equipment, and with different levels of implementation of the ultimate approach and instrumental findings outlined above. In presenting the following material we do not attempt to indicate the details of the hardware arrangements and procedural maneuvers employed for each of them, except to note that, throughout, the overall picture of the measurement system and approach is the same. In these figures the components from different orientations are also normalized so that the greatest magnitude of each quadrature component is the same (within the frequency range shown). This was done primarily to make the weaker components more visible.

Figure 89 shows results for a 61 mm projectile, with non-normalized values in the upper plot and normalized values in the lower one. It is not unusual for the magnitude of the transverse ("horizontal") response of an elongated object to an order of magnitude less than the axial response. In terms of normalized components, the quadrature responses of all three orientations are not readily distinguishable within the frequency limits that apply. While the shape of the "nose up" Q curve suggests that its peak is lower than the others, one cannot tell without a view of the full UWB. The axial inphase curves appear to be converging on their high frequency asymptotes, something we can

only just begin to see by virtue of the MF zone data. The "nose-down" and horizontal Q curves are remarkably similar, more or less by coincidence: their relations to their respective inphase components reveal that quite different materials are dominating the responses in each of the orientations. Evidently the fins are steel and contribute to the kind of pattern we have identified as coming from very elongated or thin, magnetic bodies (see Sections 3.1 and 3.3). In particular, the I and Q curves cross quite far out in the spectrum, near the tail of the Q component. By contrast, when the nose is up, the components cross quite near what appears to be the peak of the Q component, probably reflecting the fact that there is a sizeable aluminum tip on the nose. For the horizontal orientation, the curves cross at about the point that we frequently see for horizontal, elongated, magnetic bodies. Note that we would not be able to form a good picture of these relations between the I and Q components, particular in the nose down case, without the MF zone.

Figure 90 shows results for a "small projectile" (this and all data in the subsequent figures are normalized as described above). Note that without the MF zone one would hardly be able to distinguish between the patterns from the two orientations. The peak for the horizontal orientation lies squarely in the MF zone, and lower frequencies than those in the plot are required to see the peak of the axial orientation. Again, without the full UWB picture, one cannot form a clear picture of the essential signal features which we have seen related to fundamental target characteristics (Chapter 3).

Figure 91 shows data with the lower GEM-3 range added, producing a vivid picture of the peak frequencies and distinguishing the fundamental modes associated with the different orientations, for this object. This quite remarkable picture includes, for the first time, data from five decades of EMI frequency. It also includes an interesting feature, one that idiosyncratically makes the MF portion particularly relevant. Without the latter sub-band, one might well conclude that the vertical inphase curve was becoming relatively flat as it passes above 10 kHz. However we see it rise again beyond that, crossing the Q curve in a manner we associate with elongated objects. Other research has shown that the copper band around the projectile has a counter-intuitively large effect, causing a strong perturbation of the overall pattern between about 100 Hz - 1000 Hz. This is discernible as a distinct or local influence, because one can see the entire LF + MF band.

In Figure 91 through Figure 93, the objects are small enough so that they tend to produce a single axial response pattern, regardless of which end faces the sensor. Therefore only a single "vertical" signal is shown. In the last two of these, the UXOs are generally similar in size, but different in shape and composition. The 30 mm has a tapered nose section of a different material

from that of the body of the projectile. The quadrature components appear quite similar for the two cases, as do the patterns involving both components for the horizontal orientations of each. However the relation between the inphase and quadrature components is quite different for the vertical orientation of each target. This is revealed by the addition of the MF zone.

Figure 94 and Figure 95 show results for larger UXOs, namely an 81 mm with and without tail section in the former figure, and a 105 mm in the latter. The inphase components head for quite different limits in the MF zone for the different targets and orientations. It appears that some of them only begin to level out around their high frequency limits at the end of the MF sub-band, e.g. vertical cases in Figure 94. In other cases the leveling off at an upper limit is less clear, particularly for the horizontal components. It is likely that this last point is inaccurate. The horizontal components are very much weaker than the vertical ones, and because of their sizes the targets were placed much further away from the sensor than in the preceding examples. The very highest frequency data may also challenge the measurement system the most. Presumably the high frequency end of the inphase data in Figure 95 should show the same kind of trend that the corresponding components do in Figure 94. While all this suggests that more development work is needed to make the highest frequency measurements more reliable, it is at least clear that, even for these rather large UXO, one cannot estimate the asymptotes towards which the inphase components tend without the MF zone. At the same time, it is clear in the figures that the Q peaks and central features of the signal shapes are out of the picture, lower in frequency than the roughly 2 kHz lower limit on the data in these plots. All this emphasizes the need for the entire UWB picture for adequate characterization of the signals and of the objects to which they correspond.

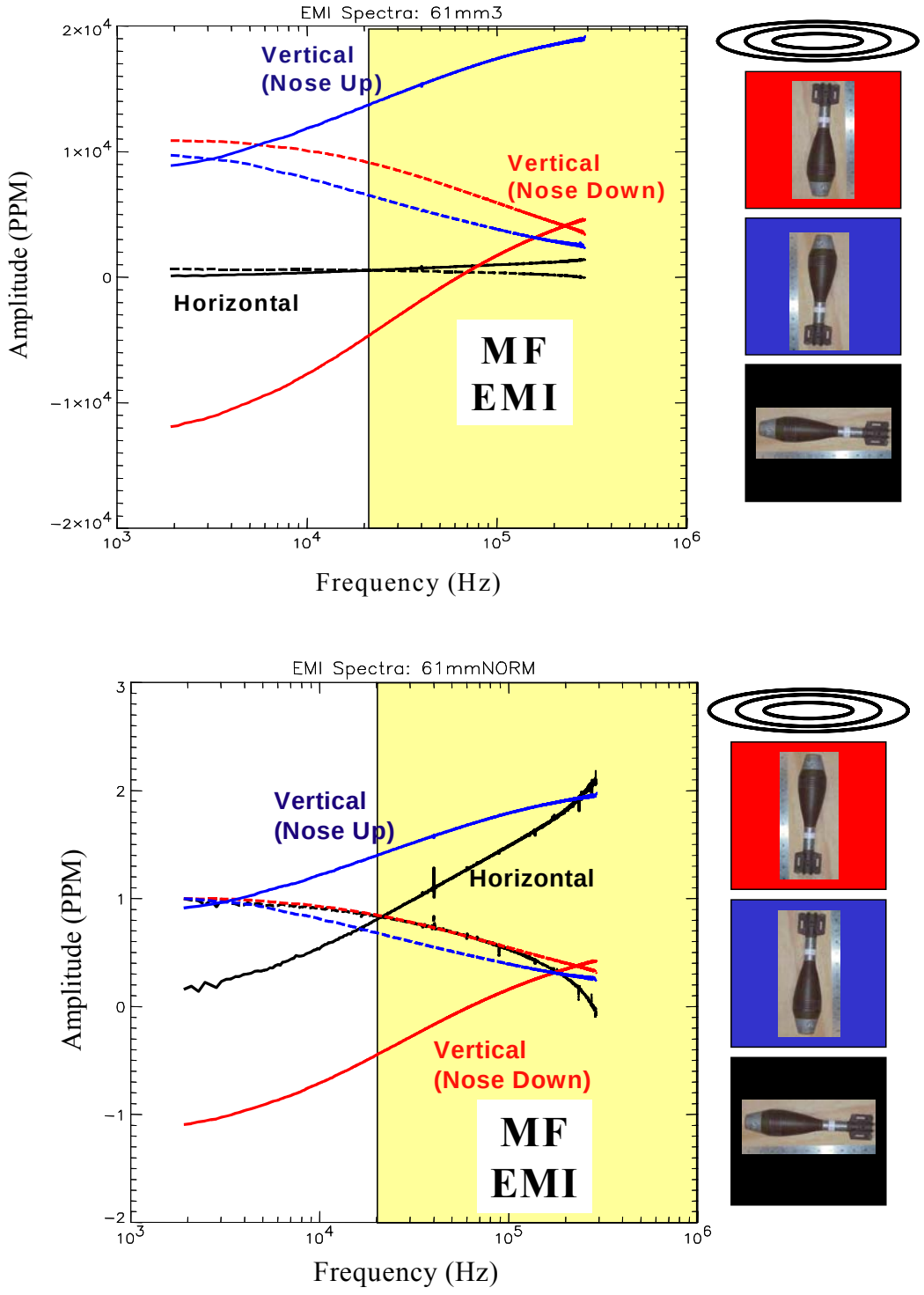

Figure 89. Measured responses of 61 mm projectile, into MF-EMI sub-band, with (bottom) and without normalization (top).

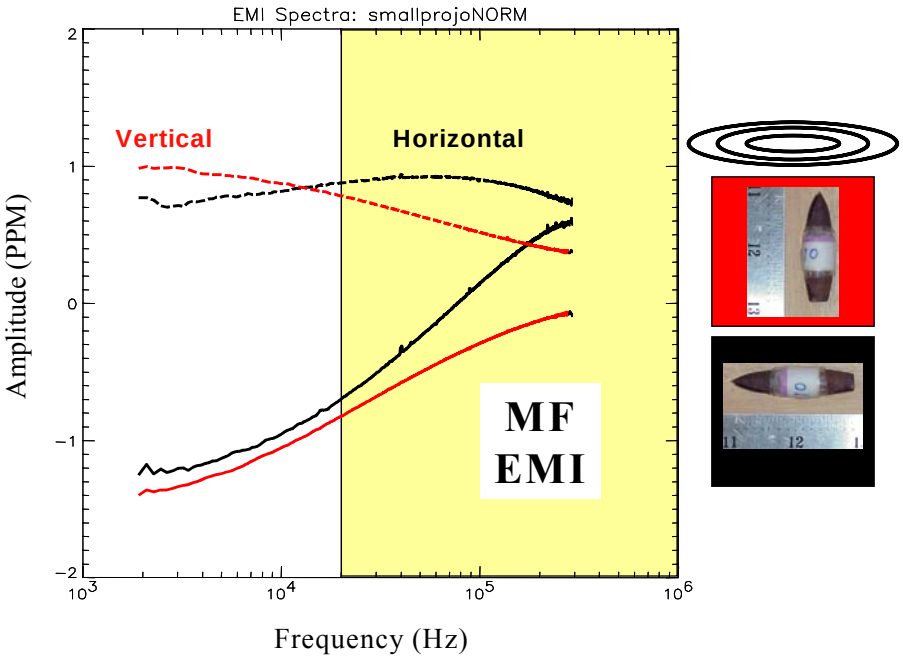

Figure 90. Measured response into MF-EMI range, from "small projectile" with dimensions revealed by the meter stick.

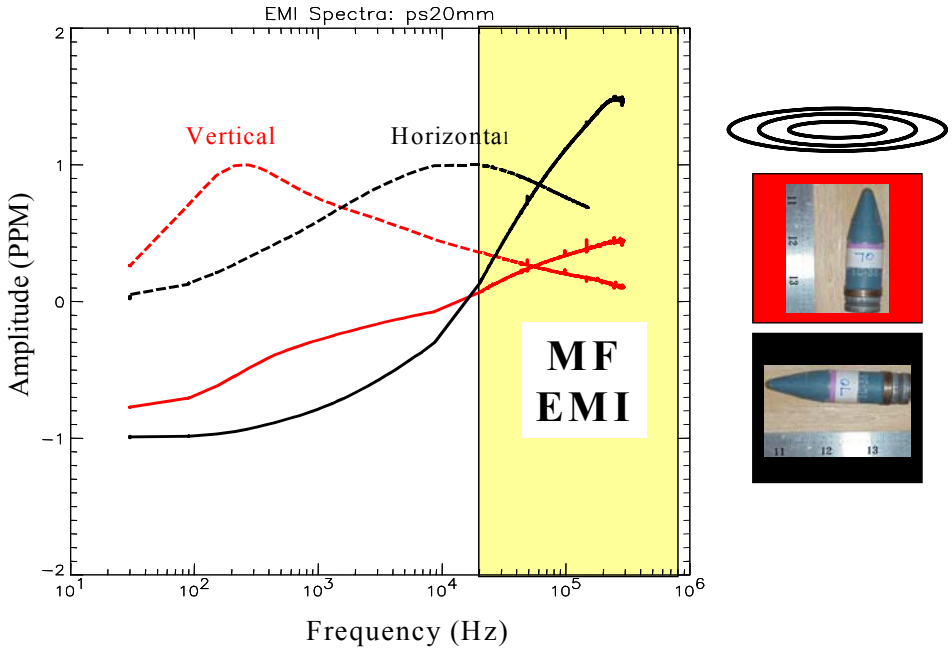

Figure 91. EMI data within five decades of frequency, including MF-EMI sub-band, for 20 mm shell.

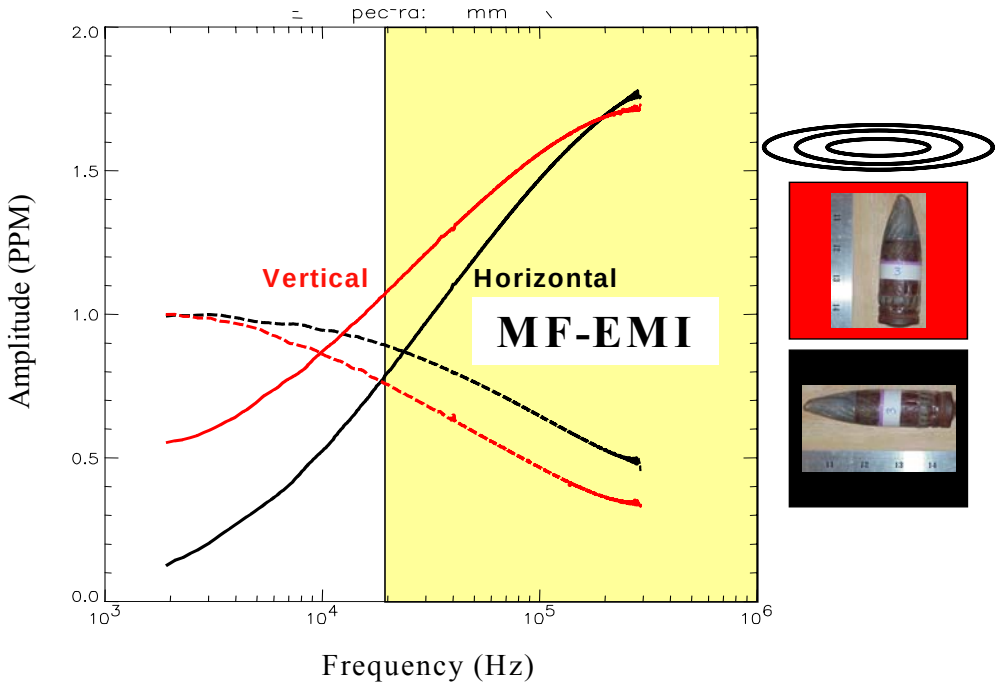

Figure 92. Measured response from 30 mm projectile, into MF-EMI range.

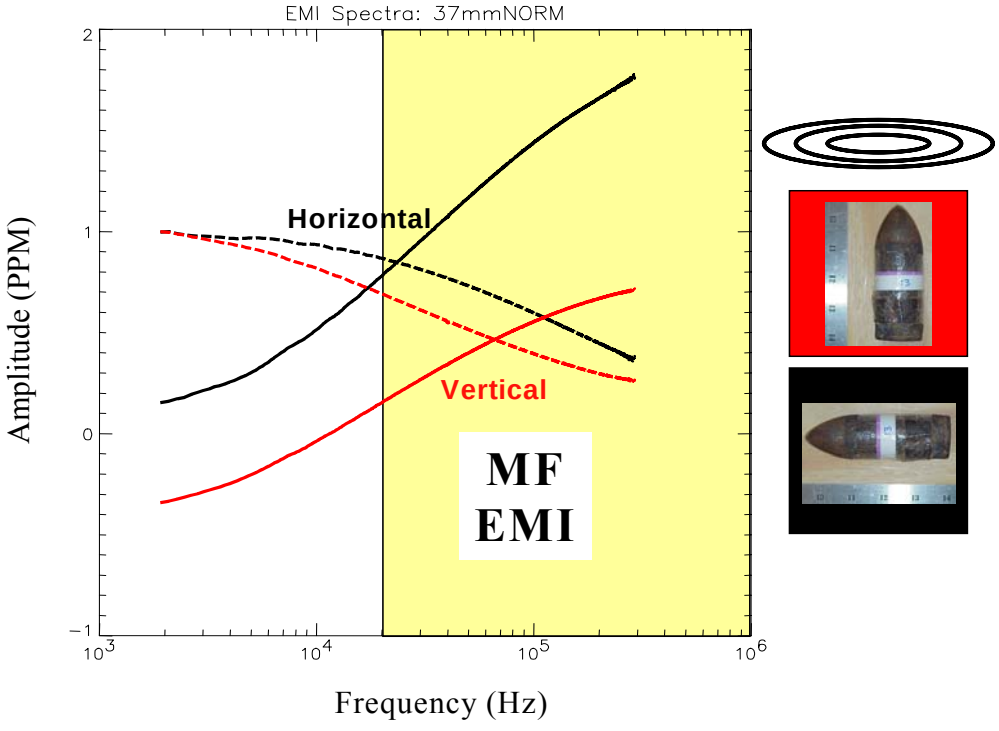

Figure 93. Measured response from 37 mm projectile, into MF-EMI range.

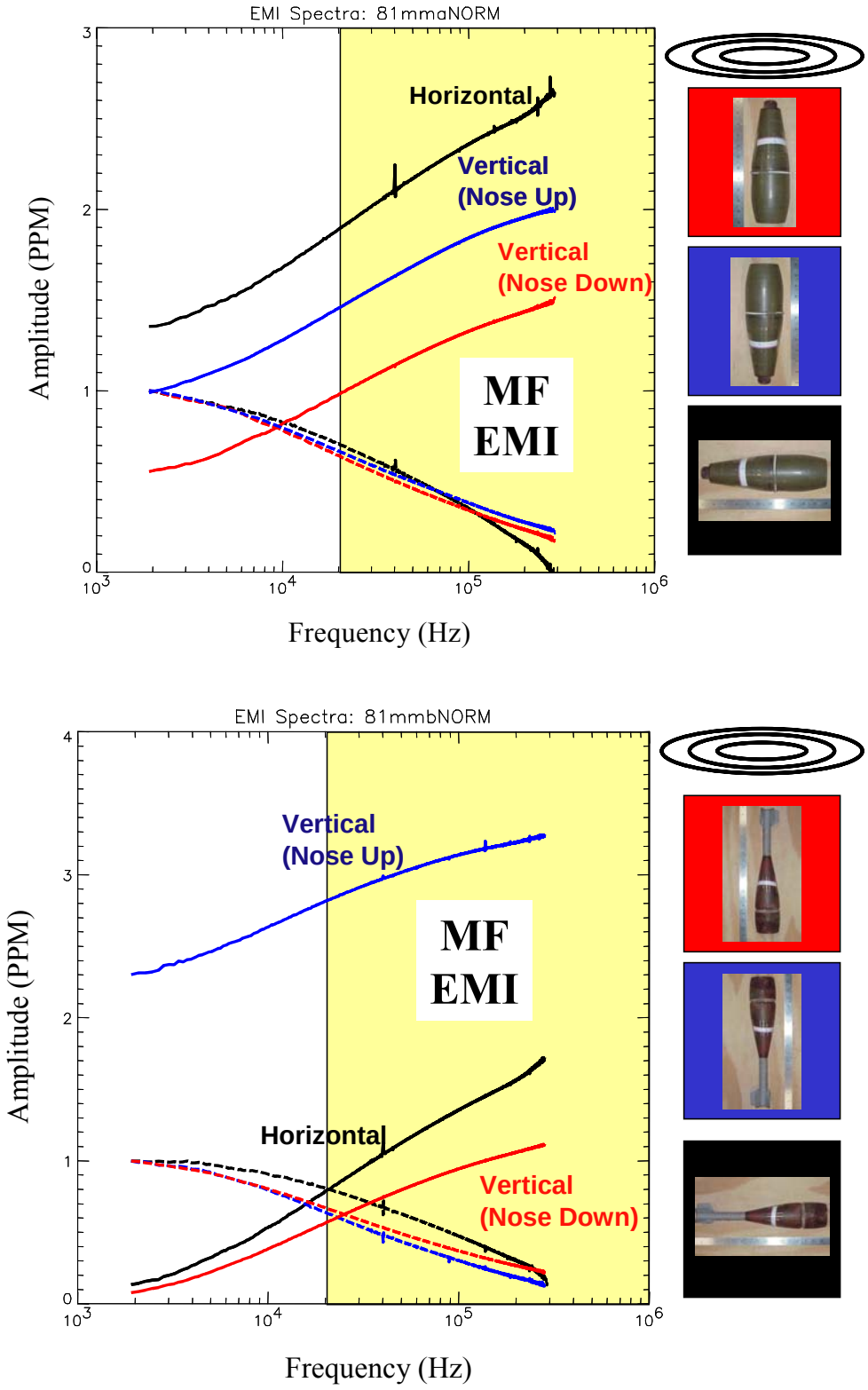

Figure 94. Measured response from 81 mm projectile, into MF-EMI range, with (bottom) and without tail (top).

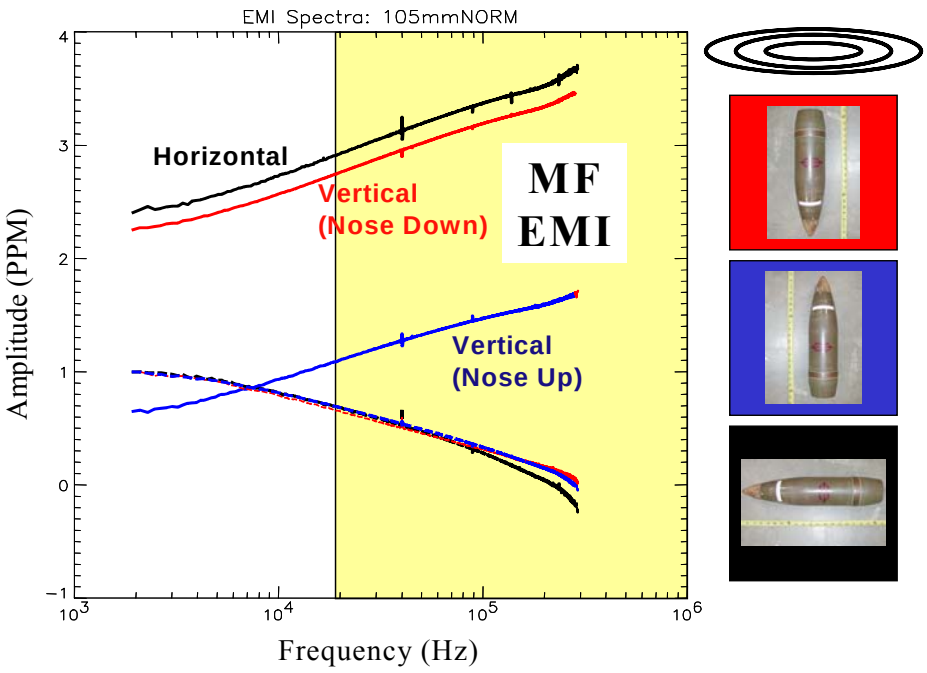

Figure 95. Measured response from 105 mm projectile, into MF-EMI range.

5. REFERENCES

Bold (blue) publications report work supported by this project.

1. Proc. UXO/Countermine Forum, Apr 9-12, 2001, New Orleans

2. Proc. UXO/Countermine Forum, Sept 3-6, 2002, Orlando.

3. D. D. Snyder, D. C. George, S. C. MacInnes, and K. L. Zonge, Demonstration of a fast 4D TEM system at the NRL baseline ordnance test site, UXO Forum, 2002.

4. L. R. Pasion, S. D. Billings, and D. W. Oldenburg, UXO discrimination using time domain electromagnetic induction, UXO Forum 2001.

5. J.R. Wait, A conducting sphere in a time varying magnetic field. Geophysics, vol. 16, pp. 666-672, 1951.

6. Sebak and L. Shafai, Near Zone Fields Scattered by Three Dimensional Highly Conducting Permeable Objects in the Filed of an Arbitrary Loop, IEEE Trans. Geoscience Remote Sensing, Vol. 29. No1. pp –15. Jan. 1991.

7. N. Geng, K. E. Baum, L. Carin. On the low frequency natural responses of conducting and permeable target IEEE Trans. Geosci. Remote Sens., Vol. 37, pp 347-359, 1999.

8. P. Gao, L. Collins, P. Garber, N. Geng, L. Carin Classification of landmine like metal targets using wideband electromagnetic induction , IEEE Trans. Geoscience Remote Sensing, Vol. 38. No. 3. pp 1352-1361 May 2000.

9. L. Carin, H. Yu, Y. Dalichaouch, A.R. Perry, P.V. Czipott, C.E. Baum On the wideband EMI response of a rotationally symmetric permeable and conducting target, IEEE Transactions Geosci. & Remote Sensing, Vol: 39 No 6 , pp: 1206 –1213, June 2001

10. **F. Shubitidze, K. O'Neill, S. Haider, and K.D. Paulsen (2000). Analysis of low frequency response from metal objects using the method of auxiliary sources, 2000 International Conference on Mathematical Methods in Electromagnetic Theory, September 12 - 15, 2000, Kharkov, Ukraine, 468-470.**

11. **F. Shubitidze, K. O'Neill and K. Paulsen The Method of Auxiliary Sources for analysis low frequency EM field scattering from composite objects. 2001 IEEE Antennas and Propagation Society International Symposium, July 8-13, Boston MA, pp. 522-525, 2001.**

12. **F. Shubitidze, K. O'Neill, S.A. Haider and K. Paulsen, The Method of Auxiliary Sources for analysis of low frequency electromagnetic induction sensor response URSI National Radio Science Meeting, January 8-11, 2001, Boulder Co (Abstract).**

13. **F. Shubitidze, K. O'Neill, K. Sun and K. Paulsen (2002). Application of broadband EMI responses to infer buried object's aspect ratio, Proc. IGARSS'02, Toronto, June 24-28, 2002, Vol III, 1542-45.**

14. **F. Shubitidze, K. O'Neill, S. Haider, K. Sun, and K.D. Paulsen (2002). Application of the method of auxiliary sources to the wideband electromagnetic induction problem, IEEE Trans. Geosci. Remote Sensing, vol 40, No 4, 928-942, 2002.**

15. **K.O'Neill, F. Shubitidze, I. Shamatava, J. Curtis, and J. Simms (2002). UXO discrimination: near field, heterogeneous and multiple objects, UXO/Countermine Forum, Sept.3-6, 2002, Orlando, FL.**

16. **F. Shubitidze, K. O'Neill, K. Sun, and K.D. Paulsen (2002). Investigation of broadband electromagnetic induction scattering by highly conductive, permeable, arbitrarily shaped 3-D objects, submitted, IEEE-Trans. Geosci. Remote Sensing.**

17. **F. Shubitidze, K O'Neill, K. Sun, and I. Shamatava (2003). Interaction between highly conducting and permeable metallic objects in the low frequency EMI range, ACES (Applied Computational Electromagnetics Symp) 2003, submitted.**

18. **F. Shubitidze, K O'Neill, K. Sun, and I. Shamatava (2003). A combined MAS-TSA algorithm for low frequency broadband electromagnetic induction problems, ACES'03, submitted.**

19. **F. Shubitidze, K. O'Neill, K. Sun, I. Shamatava and K.D. Paulsen (2003). Analysis of EMI Scattering to Support UXO Discrimination: Heterogeneous and Multiple Objects, SPIE'03, Orlando, April 03 (submitted).**

20. **S.A. Haider, K. O'Neill, F. Shubitidze and K.D. Paulsen Efficient use of analytical methods in analyzing low-frequency responses from buried UXO, URSI National Radio Science Meeting, January 8-11, 2001, Boulder Co. p. 330 (Abstract).**

21. **K. Sun, K. O'Neill, S.A. Haider & K. Paulsen. Numerical modeling of Electromagnetic Induction Scattering from Target with Small but non-negligible Skin Depths, Proc. IEEE Geosci & Remote Sensing Symp, Honolulu, July 24028, 2000, Vol. 4, pp 1411-1414.**

22. **K. Sun, K. O'Neill, F. Shubitidze, S.A. Haider & K. Paulsen, Simulation of electromagnetic induction scattering from targets with negligible to moderate penetration by primary fields, Proc. IEEE Geosci & Remote Sensing Symp., Vol 40, pp 910-927, 2002**

23. **K. Sun, K. O'Neill, F. Shubitidze, I. Shamatava and K.D. Paulsen (2002). Theoretical analysis of TSA formulation and its domain of validity, submitted for publication.**

24. **F. Shubitidze, K O'Neill, I. Shamatava, K. Sun and K.D. Paulsen (2002). Implementation of hybrid MAS and SPA algorithm for broadband electromagnetic induction problems, Proc. 8th International Workshop on Direct and Inverse Problems of Electromagnetic and Acoustic Wave Theory (DIPED-2002) , Tbilisi, Georgia, October 10-13, 2002.**

25. **K. Sun, K O'Neill, I. Shamatava, F. Shubitidze (2003). Use of Prolate Spheroid Solutions for Simulation of EMI Scattering with Realistic Sensors and Objects, ACES'03, submitted.**

26. K. O'Neill, K. Sun, F. Shubitidze, I. Shamatava, L. Liu, K. D. Paulsen, Chi-Chih Chen, and R. Lee (2003). Dealing with Clutter in Inversion and Classification Schemes for Buried UXO Discrimination, SPIE'03, Orlando, April 03 (submitted.

27. K. Sun, K. O'Neill, Lanbo Liu, F. Shubitidze , I. Shamatava and K.D. Paulsen (2003). Analytical Solutions for EMI Scattering From General Spheroids with Application in Signal Inversion for UXO Discrimination, SPIE'03, Orlando, April 03 (submitted)

28. S. Ward and G. Hohmann, Electromagnetic Theory for Geophysical Applications, in Electromagnetic Theory in Applied Geophysics, Tulsa OK: Soc. Exploration Geophys., 1987.

29. C.Flammer, *Spheroidal Wave Functions*, Stanford University Press, Stanford, 1957.

30. C.E Baum, (ed) *Detection and Identification of Visually Obscured Targets*, Taylor and Francis 1998.

31. L. Collins, P.Gao, J. Moulton, L. Makowsky, R. Weaver, D Keiswetter, I.J. Won. Detection of Low metal mines using frequency domain EMI. UXO forum 1999, Alexandria, Virginia May 24, 1999.

32. H. Braunisch, C.O. Ao, K. O'Neill, and J.A. Kong, Magneto-quasi-static response of a distribution of small conducting and permeable objects, proc. IGARSS2000, Honolulu, July, Vol 4, 1424-1426.

33. H. Braunisch, C.O. Ao, K. O'Neill and J.A. Kong, Magneto-quasistatic response of conducting and permeable prolate spheroid under axial excitation, IEEE Trans. Geosci. And Remote Sensing, vol. 39, pp. 2689-2701, 2001.

34. I. Shamatava, K. Sun, F. Shubitidze, and K. O'Neill, Evaluation of new approximate analytical solutions for EMI scattering from fundamental shapes, in prep.

35. I. Shamatava, K. O'Neill, F. Shubitidze, K. Sun and C.O. Ao (2002). Evaluation of approximate analytical solutions for EMI scattering from finite objects of different shapes and properties, Proc. IGARSS'02, Toronto, June 24-28, 2002, Vol III, 1550-52.

36. C.O Ao, H. Braunisch, K. O'Neill, and J.A. Kong, Quasi-magnetostatic Solution for a Conducting and Permeable Spheroid. Proc. Int'l Geosci & Remote Sensing Symposium, Honolulu, July 24-28, 2000. vol. 4 pp. 1418-1420.

37. C.O. Ao H. Braunisch, K. O'Neill, J.A. Kong, Quasi-magnetostatic Solution for a Conducting and Permeable Spheroid Object to Arbitrary Excitation, IEEE Geosci & Remote Sensing, Vol 40, no 4, pp.887-897.

38. C.O. Ao, H. Braunisch, K. O'Neill, J.A. Kong, L. Tsang, and J.T. Johnson (2001). Broadband electromagnetic induction response from conducting and permeable spheroids, Proc. SPIE, vol.4394: Detection and Remediation Technologies for Mines and Mine-like Targets VI, Orlando, April 16-20, 2001, pp1304-1315.

39. L. Peters, Jr, and C-C. Chen, in C. Baum (ed*), Detection and Discrimination of Obscured Objects*, Elsevier, 1999.

40. C-C. Chen and L. Peters Jr., Buried unexploded ordnance identification via complex natural resonances, IEEE Trans. Ant. & Propagat., vol. AP-42, pp. 1645-1654, Nov. 1997.

41. K. O'Neill (2001). Discrimination of UXO in soil using broadband polarimetric GPR backscatter, IEEE-Trans. Geosci. Remote Sensing, vol 39, No.2, 356-367.

42. D. Keiswetter, I.J. Won, B. Barrow, T. Bell, Object identification using multi-frequency EMI data, UXO forum 2000.

43. J. Miller, T. Bell , D. Keiswetter, and D. Wright, Feature-based characterization of uxo-like targets using broadband electromagnetic induction, Proc. UXO/Countermine Forum, Apr 9-12, 2001, New Orleans

44. D.J. Jackson, *Classical Electrodynamics*, Wiley, NY, 3rd Edition, 1999

45. J. M. Stanley and S. M Griffin, Sub-Audio Magnetics - Simultaneous magnetic and electromagnetic detection of UXO, UXO/Countermine Forum, Sept 3-6, 2002, Orlando

46. I.J. Won, D.A. Keiswetter, D.R. Hanson, E. Novikova, and T.M. Hall, 1997, GEM-3: a monostatic broadband electromagnetic induction sensor, Journal of Environmental and Engineering Geophysics, v. 2, Issue 1, p. 53-64.

Other publications reporting work supported by this project:

K. O'Neill, S. Haider, F. Shubitidze, K. Sun, C.O. Ao, H. Braunisch and J. A. Kong, Ultra-wideband Electromagnetic Induction Spectroscopy, UXO Forum, April 8-11, 2001, New Orleans.

I. Shamatava, K. O'Neill, F. Shubitidze, K. Sun and C.O. Ao (2002). Evaluation of approximate analytical solutions for EMI scattering from finite objects of different shapes and properties, Proc. IGARSS'02, Toronto, June 24-28, 2002, Vol III, 1550-52.

K. Sun, K. O'Neill, F. Shubitidze, and K. D. Paulsen (2002). Applicability of the TSA approximation in magneto-quasistatic scattering over the entire induction frequency band, for high permeability objects, PIERS'02, Cambridge, MA, July 1-5, 2002 (abstract).

I. Shamatava, K. O'Neill, F. Shubitidze, and K. Sun (2002). Evaluation of approximate analytical solutions for magneto-quasistatic scattering from both high and low permeability objects, PIERS'02, Cambridge, MA, July 1-5, 2002 (abstract).

F. Shubitidze, K. O'Neill, K. Sun and K.D. Paulsen (2002). Analysis of UXO classification capability with low frequency EMI sensor responses, PIERS'02, Cambridge, MA, July 1-5, 2002 (abstract).